

COMPUTATIONAL STUDY OF HEAT TRANSFER IN FLUID-SOLID FLOWS

By

LIKE LI

A DISSERTATION PRESENTED TO THE GRADUATE SCHOOL
OF THE UNIVERSITY OF FLORIDA IN PARTIAL FULFILLMENT
OF THE REQUIREMENTS FOR THE DEGREE OF
DOCTOR OF PHILOSOPHY

UNIVERSITY OF FLORIDA

2013

© 2013 Like Li

To my parents and my wife

ACKNOWLEDGMENTS

I would like to express my most sincere gratitude to my advisor, Professor Renwei Mei, and my co-advisor, Professor James F. Klausner, for their constant advice, support, inspiration and encouragement. This dissertation would have been impossible without their expert guidance and enthusiasm on the subject.

I would like to express my sincere gratitude to my committee member, Professor David W. Hahn, for his concern and help with Chapter 2 about the heat conduction computation between colliding particles. I would also like to express my sincere gratitude to my committee member, Professor Jörg Petrasch, for his guidance and help with the material presented in Chapter 6 about the coupled radiation-conduction model.

My sincere gratitude also goes to Professor Jason E. Butler, from the Department of Chemical Engineering at the University of Florida, for serving as an external member in my committee and for his valuable advice and suggestions regarding the particle-level simulations.

I would like to thank Abhishek Singh in our department for developing the radiation model and providing me the required heat flux boundary conditions for the coupled radiation-conduction model in Chapter 6. We have discussed and collaborated a lot and learned from each other during the process. I would also like to take this opportunity to thank my labmates: Drs. Richard Parker, Fotouh Al-Raqom, Ayyoub Mehdizadeh, Nicholas AuYeung, Bradley Bon, Chang-kang Guan, and Fadi Alnaimat, and those who are on the way of pursuing a Doctor's degree, including Nima Rahmatian, Chen Chen, Kyle Allen, Benjamin Greek, Prasanna Venuvanalingam, and Amey Barde.

Finally, I am deeply grateful for the enduring and endless support and love of my wife, Jing Hu, my parents, and my brother.

TABLE OF CONTENTS

	<u>page</u>
ACKNOWLEDGMENTS.....	4
LIST OF TABLES.....	10
LIST OF FIGURES.....	11
LIST OF ABBREVIATIONS.....	17
ABSTRACT.....	18
CHAPTER	
1 INTRODUCTION TO HEAT TRANSFER IN FLUID-SOLID FLOWS.....	20
1.1 Background and Motivations.....	20
1.2 Objectives.....	21
1.2.1 Heat Transfer between Colliding Solid Particles.....	22
1.2.2 Thermal Boundary Conditions on Curved Boundaries.....	22
1.2.3 Heat Transfer on Curved Boundaries.....	24
1.2.4 Multiple-Relaxation-Time Lattice Boltzmann Model for the Axisymmetric Convection-Diffusion Equation.....	25
1.2.5 Thermal Analysis in a Porous Structure in a Solar Thermochemical System.....	26
2 HEAT TRANSFER BETWEEN COLLIDING SURFACES AND PARTICLES.....	28
2.1 Introduction.....	28
2.2 Formulation of the Collisional Heat Transfer Problem.....	30
2.2.1 Elastic Collision and Deformation.....	30
2.2.2 Governing Equations for Heat Transfer.....	32
2.2.3 Self-Similar Solution.....	35
2.2.4 Heat Transfer.....	36
2.3 Results and Discussion.....	37
2.3.1 Self-Similar Solution at Small Time.....	37
2.3.2 Behavior of the Singularity at $(r, z) = (R(t), 0)$	38
2.3.3 Asymptotic Limit at $Fo \rightarrow 0$	42
2.3.4 Numerical Results for Finite Fo	47
2.3.5 Particles of Different Materials.....	49
2.4 Summary and Conclusions.....	52
3 BOUNDARY CONDITIONS FOR THERMAL LATTICE BOLTZMANN EQUATION METHOD.....	64
3.1 Literature Review of Thermal Lattice Boltzmann Equation (TLBE) Models.....	64

3.2	Literature Review of Boundary Conditions in TLBE Simulations.....	66
3.3	Present Boundary Condition Treatments in TLBE Method	70
3.3.1	The Convection-Diffusion Equation	71
3.3.2	The D3Q7 and D2Q5 Thermal LBE models	72
3.3.3	Thermal Boundary Condition Treatments.....	77
3.3.3.1	Dirichlet boundary condition.....	79
3.3.3.2	Neumann boundary condition	82
3.4	Numerical Validation and Discussion.....	89
3.4.1	Two-D Steady-State Channel Flow	90
3.4.1.1	Dirichlet boundary condition.....	90
3.4.1.2	Neumann boundary condition	93
3.4.2	One-D Transient Conduction in an Inclined Semi-Infinite Solid	94
3.4.3	Two-D Steady-State Heat Conduction Inside a Circle.....	96
3.4.3.1	Dirichlet boundary condition.....	96
3.4.3.2	Neumann boundary condition	97
3.4.4	Two-D Transient Heat Conduction Inside a Circle.....	99
3.4.5	Three-D Steady-State Circular Pipe Flow.....	101
3.4.5.1	Dirichlet boundary condition.....	101
3.4.5.2	Neumann boundary condition	102
3.5	Summary and Conclusions.....	103
4	HEAT TRANSFER EVALUATION ON CURVED BOUNDARIES IN THERMAL LATTICE BOLTZMANN EQUATION METHOD.....	122
4.1	Introduction	122
4.2	Heat Transfer Evaluation	125
4.2.1	Boundary Heat Flux.....	125
4.2.2	Heat Transfer on Curved Boundaries.....	126
4.2.3	Temperature Gradient in the Interior Field.....	128
4.3	Numerical Results and Discussion.....	129
4.3.1	Two-D Steady-State Channel Flow	130
4.3.1.1	Channel flow with a Dirichlet boundary condition.....	131
4.3.1.2	Channel flow with a Neumann boundary condition	133
4.3.2	One-D Transient Conduction in an Inclined Semi-Infinite Solid	133
4.3.2.1	Dirichlet Boundary condition $f(t) = kt^{1/2}$	134
4.3.2.2	Dirichlet Boundary condition $f(t) = 1 - \exp(-\lambda t)$	134
4.3.3	Two-D Transient Heat Conduction Inside a Circle.....	135
4.3.4	Three-D Steady-State Circular Pipe Flow with a Dirichlet Condition	136
4.3.4	Two-D Steady-State Natural Convection in a Square Enclosure with a Circular Cylinder in the Center	137
4.4	Summary and Conclusions.....	141
5	MULTIPLE-RELAXATION-TIME LATTICE BOLTZMANN MODEL FOR THE AXISYMMETRIC CONVECTION DIFFUSION EQUATION.....	150
5.1	Introduction	150

5.2 Lattice Boltzmann Model for the Axisymmetric Convection-Diffusion Equations.....	156
5.3 Numerical Validation and Discussion.....	159
5.3.1 Steady convection-diffusion in an annulus	159
5.3.2 Steady convection-diffusion in a circular pipe.....	160
5.3.2.1 Dirichlet boundary condition on the wall.....	161
5.3.2.2 Neumann boundary condition on the wall	162
5.3.3 Steady heat conduction inside a sphere.....	163
5.3.3.1 Dirichlet boundary condition on the wall.....	164
5.3.3.2 Neumann boundary condition on the wall	165
5.3.4 Unsteady heat conduction in a circle.....	166
5.3.5 Steady natural convection in an annulus between two coaxial vertical cylinders.....	167
5.3.6 Swirling thermal flows in a vertical cylinder	169
5.4 Summary and Conclusions.....	172
6 ENERGY TRANSPORT IN A SOLAR THERMOCHEMICAL REACTOR FOR HYDROGEN PRODUCTION	185
6.1 Introduction	185
6.2 Horizontal Cavity-Receiver Solar Reactor.....	188
6.3 Heat Transfer Analysis.....	189
6.3.1 Radiative Heat Transfer.....	189
6.3.1.1 Radiation between the cavity wall and the absorbers	189
6.3.1.2 Radiation in the porous structure inside the absorbers	191
6.3.2 Convective Heat Transfer.....	192
6.3.3 Conductive Heat Transfer.....	192
6.3.4 Endothermic Chemical Reaction	192
6.4 TLBE Simulation of Heat Transfer in Absorbers	193
6.4.1 Scaling from the physical units to the LBE units.....	194
6.4.2 Rescaling for high-diffusion-coefficient CDE in TLBE.....	195
6.4.3 Computational Procedure for the Coupled Model.....	196
6.5 Simulation Results and Discussion	197
6.6 Summary and Conclusions.....	200
7 SUMMARY AND FUTURE WORKS.....	207
APPENDIX	
A VALIDITY OF THE SEMI-INFINITE MEDIA ASSUMPTION	210
B ASYMPTOTIC ANALYSIS OF SECOND-ORDER ACCURATE BOUNDARY SCHEMES	215
C EXTENSION OF ZHOU'S BGK AXISYMMETRIC LATTICE BOLTZMANN MODEL (ZHOU 2011) TO AN MRT LATTICE BOLTZMANN MODEL.....	222
LIST OF REFERENCES	226

BIOGRAPHICAL SKETCH..... 236

LIST OF TABLES

<u>Table</u>	<u>page</u>
2-1 Heat flux integral $q_w^*(t^*)$ based on the self-similar solution at small time ($t^* \ll 1$)	53
3-1 Accuracy of the TLBE simulations with Dirichlet/Neumann conditions	105
4-1 Surface-averaged Nusselt numbers at different grid resolution.....	142
4-2 Comparison of the present surface-averaged Nusselt numbers with previous results.....	142
5-1 Surface-averaged Nusselt numbers at different grid resolution.....	174
5-2 Comparison of the present surface-averaged Nusselt numbers with published results.....	174
6-1 Baseline simulation parameters for cavity aspect ratio $L_{cav, in} / D_{cav} = 0.69,$ 1.01, and 1.16 for Cases I, II and III, respectively.....	201
6-2 Solar-to-fuel efficiency calculations for Cases I, II and III.	201

LIST OF FIGURES

<u>Figure</u>	<u>page</u>
2-1 Variation of the contact area during collision.	54
2-2 Computational domain and boundary conditions at $z = 0$	54
2-3 Temperature contours on the surface of particle 1 based on the self-similar solutions at small time ($t^* \ll 1$).	55
2-4 Dimensionless heat flux across the contact area at small time ($t^* \ll 1$) based on self-similar solutions.	56
2-5 (a) Local solution of $(\theta - 0.5)/(w\rho^{1/2})$ around the singularity point at $(\xi, \eta) = (1, 0)$. (b) The value of w in the local solution of θ around the singularity point at $(\xi, \eta) = (1, 0)$	57
2-6 Local transient temperature profiles at $(\xi > 1, \eta = 0)$ when $Fo = 1.0$	58
2-7 Comparison of numerical results and analytical fit for $f_i(\eta)$ in Eq. (2-58).	58
2-8 Variation of the dimensionless heat flux integral $q_w^*(t^*)$ over the contact area at $Fo = 0$	59
2-9 Variation of the multiplier $A^* / \sqrt{t^*}$ in Eqs. (2-30b) and (2-31c).	59
2-10 Variations of the dimensionless heat flow rate $Q^*(t^*)$ at $Fo = 0$; the self-similar solution is $Q^*(t^*) = 0.2820948 A^* / \sqrt{t^*}$	60
2-11 Comparison of the dimensionless heat flux integral $q_w^*(t^*)$ at different Fourier numbers.	60
2-12 Heat flux $q^*(t^*, \xi)$ in the contact area at various times for $Fo = 1.0$	61
2-13 Temperature variations along ξ -direction ($\eta = 0$) at various times for $Fo = 1.0$	61
2-14 Heat transfer as a function of the impact Fourier number (particles of the same material).	62
2-15 Correction factor comparison between computation and the approximate expression at (a) $k_2/k_1=1.0$, (b) $k_2/k_1=0.1$ and (c) $k_2/k_1=10.0$	63
3-1 Discrete velocity set $\{\mathbf{e}_\alpha\}$ for the D3Q7 TLBE model.	106

3-2	Schematic depiction of the lattice link intersected by a boundary wall.....	106
3-3	Layout of the rectangular lattice and a curved boundary (solid circles: field nodes; solid squares: boundary nodes; open circles: exterior nodes).	106
3-4	Schematic representation of the lattice in a 2-D channel with an arbitrary Δ value.	107
3-5	(a) Lower stability bound of the adjustable parameter $c_{\sigma 1}$ versus $(\tau_D - 0.5)$, and (b) variations of $c_{\sigma 1}$ as a function the lattice fraction.	107
3-6	Temperature contours in a 2-D channel with a Dirichlet boundary condition using $\tau_D = 0.75$, $\Delta = 0.5$ and $H = 64$	108
3-7	Relative L-2 error norm E_2 versus the grid resolution, $1/H$, for the channel flow Dirichlet problem.	109
3-8	Relative L-2 error norm E_2 versus the boundary lattice fraction, Δ , for the channel flow Dirichlet problem at $N_y = 34$	110
3-9	Comparison of E_2 obtained using Scheme 2 with those using Ginzburg's schemes (Ginzburg 2005) for the channel flow Dirichlet problem.....	110
3-10	Wall heat flux error E_{2_qw} versus the grid resolution, $1/H$, for the channel flow Dirichlet problem. (a) $\Delta = 0.50, 0.25$, and 0.75 at $\tau_D = 0.75$, (b) $\Delta = 0.50, 0.01$, and 0.99 at $\tau_D = 0.75$	111
3-11	Interior gradient error E_{2_grad} versus the grid resolution, $1/H$, for the channel flow Dirichlet problem. (a) $\Delta = 0.50, 0.25$, and 0.75 at $\tau_D = 0.75$, (b) $\Delta = 0.50, 0.01$, and 0.99 at $\tau_D = 0.75$	111
3-12	Temperature contours in a 2-D channel with a Neumann boundary condition using $\tau_D = 0.75$, $\Delta = 0.5$ and $H = 64$	112
3-13	Relative L-2 error norm E_2 versus the grid resolution, $1/H$, for the channel flow Neumann problem with various Δ . (a) $\tau_D = 0.51$, (b) $\tau_D = 0.55$, and (c) $\tau_D = 0.75$	113
3-14	Wall temperature error E_{2_tw} versus the grid resolution, $1/H$, for the channel flow Neumann problem. (a) $\Delta = 0.50, 0.25$, and 0.75 at $\tau_D = 0.75$, (b) $\Delta = 0.50, 0.01$, and 0.99 at $\tau_D = 0.75$	114
3-15	Interior gradient error E_{2_grad} versus the grid resolution, $1/H$, for the channel flow Neumann problem.....	114
3-16	Layout of the lattice around the inclined semi-infinite solid.....	115

3-17	(a) Temperature variations with time at point P ; (b) temperature profiles in the y -direction going through P at $t = 500\delta t$	115
3-18	(a) Schematic layout of the lattice around a circle; (b) distribution of Δ values along the azimuthal angle φ at $r_0 = 30.5$	116
3-19	Relative L-2 norm error E_2 versus the grid resolution, $1/r_0$, for the steady-state heat conduction inside a circle with a Dirichlet condition (results based on Ginzburg's schemes (2005) are included).....	116
3-20	Wall heat flux error E_{2_qw} versus the grid resolution, $1/r_0$, for the steady-state heat conduction inside a circle with a Dirichlet condition (results based on Ginzburg's schemes (2005) are included).....	117
3-21	Interior gradient error E_{2_grad} versus the grid resolution, $1/r_0$, for the steady-state heat conduction inside a circle with a Dirichlet condition (results based on Ginzburg's schemes (2005) are included).....	117
3-22	Relative L-2 norm error E_2 versus the grid resolution, $1/r_0$, for the steady-state heat conduction inside a circle with a Neumann condition.....	118
3-23	Wall temperature error E_{2_tw} versus the grid resolution, $1/r_0$, for the steady-state heat conduction inside a circle with a Neumann condition.....	118
3-24	Interior gradient error E_{2_grad} versus the grid resolution, $1/r_0$, for the steady-state heat conduction inside a circle with a Neumann condition.....	119
3-25	Comparison of the error norm $E(t^*)$ defined in Eq. (3-71) for the transient heat conduction inside a circle using Schemes 1, 2 and 3 with $r_0 = 5.8$	119
3-26	Relative L-2 norm error E_2 versus the grid resolution, $1/r_0$, for the transient heat conduction inside a circle.....	120
3-27	Relative L-2 norm error E_2 versus the grid resolution, $1/r_0$, for the pipe flow with a Dirichlet condition.....	120
3-28	Wall heat flux error E_{2_qw} versus the grid resolution, $1/r_0$, for the pipe flow with a Dirichlet condition.	121
3-29	Relative L-2 norm error E_2 versus the grid resolution, $1/r_0$, for the pipe flow with a Neumann condition.	121
4-1	Illustration of the heat transfer evaluation on a curved boundary (closed circles: field nodes; closed squares: boundary nodes; open circles: exterior nodes).	143

4-2	Wall heat flux error E_{2_qw} versus the grid resolution, $1/H$, for the channel flow Dirichlet problem at (a) $\Delta = 0.50, 0.25,$ and $0.75,$ and (b) $\Delta = 0.50, 0.01,$ and $0.99.$	143
4-3	Wall heat flux error E_{2_qw} versus the lattice link fraction Δ at $Ny = 34$ for the channel flow Dirichlet problem.....	144
4-4	Wall heat flux error E_{2_qw} versus $(\tau_D - 0.5)$ at $Ny = 66$ for the channel flow Dirichlet problem.....	144
4-5	Interior gradient error E_{2_gx} (in x -direction) versus the grid resolution, $1/H$, for the channel flow Dirichlet problem at (a) $\Delta = 0.50, 0.25,$ and $0.75,$ and (b) $\Delta = 0.50, 0.01,$ and $0.99.$	145
4-6	Interior gradient error E_{2_gy} (in y -direction) versus the grid resolution, $1/H$, for the channel flow Dirichlet problem at (a) $\Delta = 0.50, 0.25,$ and $0.75,$ and (b) $\Delta = 0.50, 0.01,$ and $0.99.$	145
4-7	Interior gradient errors of (a) $E_{2_gx},$ and (b) $E_{2_gy},$ respectively, versus the grid resolution, $1/H$, for the channel flow Neumann problem.....	146
4-8	Variations of the heat transfer rate with time for the Dirichlet condition $T(l=0) = t^{1/2}$ at the end of an inclined semi-infinite solid (symbols: LBE results; lines: exact solutions).....	146
4-9	Variations of the heat transfer rate with time for the Dirichlet condition $T(l = 0) = 1 - \exp(-0.1t)$ at the end of an inclined semi-infinite solid (symbols: LBE results; lines: exact solutions).....	147
4-10	Variations of the error $E(t^*)$ defined in Eq. (4-16) with time at different grid resolution for the transient heat conduction inside a circle.	147
4-11	Heat transfer error, $E_2,$ defined in Eq. (4-17) versus the grid resolution, $1/r_0,$ for the transient heat conduction inside a circle.....	148
4-12	Heat transfer error $E_{2_q_w}$ versus the grid resolution, $1/r_0,$ for the circular pipe flow with a Dirichlet boundary condition.....	148
4-13	Schematic depiction of the computational domain ($r_0 = 0.2L$) and the Dirichlet thermal and velocity boundary conditions on the inner and outer walls.....	149
4-14	Isotherms in the field between the circular cylinder and the cavity walls at (a) $Ra = 10^3,$ (b) $Ra = 10^4,$ (c) $Ra = 10^5,$ and (d) $Ra = 10^6.$	149
4-15	Streamlines in the field between the circular cylinder and the cavity walls at (a) $Ra = 10^3,$ (b) $Ra = 10^4,$ (c) $Ra = 10^5,$ and (d) $Ra = 10^6.$	149

5-1	Discrete velocity set $\{\mathbf{e}_\alpha\}$ for the D2Q5 LB model. $\mathbf{e}_\alpha = (0, 0), (\pm 1, 0),$ and $(0, \pm 1)$	175
5-2	Relative L-2 error norm E_2 for the interior field of ϕ versus the grid resolution, $1/R_i$, for the 1-D annulus convection-diffusion problem.	175
5-3	Schematic of the square lattice in the r - z plane of a 3-D circular pipe.	176
5-4	Contours of ϕ in the r - z plane at $Nr = 42, Nz = 83,$ and $\Delta = 0.5$ for the steady convection-diffusion in a pipe with a Dirichlet boundary condition on the wall. .	176
5-5	Relative L-2 error norms versus the grid resolution, $1/R_0$, for the steady convection-diffusion in a pipe with a Dirichlet boundary condition.	177
5-6	Relative L-2 error norms versus the grid resolution, $1/R_0$, for the steady convection-diffusion in a pipe with a Neumann boundary condition.	178
5-7	Schematic representation of the computational domain and the lattice layout for the heat conduction inside a sphere.	179
5-8	Relative L-2 error norms E_2 and E_{2_qw} for the interior field of ϕ and the boundary flux, respectively, versus the grid resolution, $1/R_0$, for the steady heat conduction inside a sphere with a Dirichlet boundary condition.	179
5-9	Relative L-2 error norms E_2 and E_{2_tw} for the interior field and boundary values of ϕ , respectively, versus the grid resolution, $1/R_0$, for the steady heat conduction inside a sphere with a Neumann boundary condition.	180
5-10	Time-averaged error norm E_2 for the interior field of ϕ versus the grid resolution, $1/R_0$, for the unsteady heat conduction in a circle with a temporal Dirichlet boundary condition.	180
5-11	Schematic depiction of the computational domain ($R_o/R_i = 2.0,$ and $H/(R_o - R_i) = 2.0$) and the thermal boundary conditions on the walls all placed in the center of the lattice links ($\Delta = 0.5$).	181
5-12	Streamlines in the annulus between two coaxial vertical cylinders at (a) $Ra = 10^3,$ (b) $Ra = 10^4,$ and (c) $Ra = 10^5$	182
5-13	Isotherms in the annulus between two coaxial vertical cylinders at (a) $Ra = 10^3,$ (b) $Ra = 10^4,$ and (c) $Ra = 10^5$	182
5-14	Contours of the azimuthal velocity u_ϕ (a) and isotherms (b) of the confined swirling flow at $Re = 2000$ and $Ri = 0$	183
5-15	Contours of the azimuthal velocity u_ϕ (a) and isotherms (b) of the confined swirling flow at $Re = 2000$ and $Ri = 1.0$	183

5-16	Velocity components and temperature profiles along the vertical line at $r/R = 0.8$ for $Re = 2000$: (a) radial velocity u_r , (b) azimuthal velocity u_ϕ , (c) axial velocity u_z , and (d) temperature.....	184
6-1	Schematical depiction of the horizontal solar reactor configuration: (a) cross section view, and (b) front view.	202
6-2	(a) Variations of the average bed temperature (T_{bed}) with time, and (b) variations of T_{bed} and solar power input (\dot{Q}_{solar}) with time at $1200\text{ }^\circ\text{C} \leq T_{bed} \leq 1450\text{ }^\circ\text{C}$ for Cases I, II and III.	202
6-3	Incident heat flux distribution (in W/m^2) on the surface of Absorber 1 (see Fig. 6-1) for (a) Cases I, (b) Case II, and (c) Case III.	203
6-4	Net heat flux distribution (in W/m^2) on the surface of Absorber 1 for (a) Cases I, (b) Case II, and (c) Case III.	204
6-5	Temperature distribution (in K) on the surface of Absorber 1 for (a) Cases I, (b) Case II, and (c) Case III.	205
6-6	Comparison of temperature profiles (in K) along ($\theta = 0, z$) on the surface of Absorber 1 for the three cases simulated.	205
6-7	Interior temperature distribution on the central x-z plane of Absorber 1 for (a) Cases I, (b) Case II, and (c) Case III.	206
A-1	Isothermals on the surface of particle 1 at $Fo = 50$ when (a) $t^* = 0.50$, (b) $t^* = 0.75$, and (c) $t^* = 0.95$	214

LIST OF ABBREVIATIONS

CDE	convection-diffusion equation
CFD	computational fluid dynamics
LB	lattice Boltzmann
LBE	lattice Boltzmann equation
MCRT	Monte Carlo ray tracing
MRT	multiple-relaxation-time
SRT	single-relaxation-time
TDF	temperature distribution function
TLBE	thermal lattice Boltzmann equation

Abstract of Dissertation Presented to the Graduate School
of the University of Florida in Partial Fulfillment of the
Requirements for the Degree of Doctor of Philosophy

COMPUTATIONAL STUDY OF HEAT TRANSFER IN FLUID-SOLID FLOWS

By

Like Li

August 2013

Chair: Renwei Mei
Cochair: James F. Klausner
Major: Mechanical Engineering

Efficient and accurate heat transfer evaluation is essential to the study of thermal flows and energy exchange in fluid-solid systems. For fluid-solid flows with moving solid particles, heat transfer between the colliding particles is investigated computationally using a finite difference method and analytically using various asymptotic methods. An efficient heat transfer evaluation technique for any curved boundary has also been proposed and validated in this dissertation based on the thermal lattice Boltzmann equation (TLBE) method with an improved boundary condition treatment. Two specific topics are further studied with the proposed boundary schemes and heat transfer evaluation technique, including the development of a multiple-relaxation-time (MRT) lattice Boltzmann (LB) model for the axisymmetric convection-diffusion equation (CDE), and a radiation-conduction coupled model for the energy transport in a solar thermochemical reactor.

From the computationally determined heat transfer during the collision, a closed-form formula is developed to predict the heat transfer as a function of the impact Fourier

number, the thermal diffusivity ratio and the thermal conductivity ratio of the impacting particles.

To develop a general and efficient technique for evaluating the heat transfer on a curved boundary, the TLBE method is applied for its simple algorithm and capability to deal with complex geometries. An improved thermal boundary condition treatment is proposed based on the “bounce-back” and interpolation of the temperature distribution functions (TDFs) of the TLBE model.

The exact geometry on a boundary is preserved with the proposed boundary condition treatment so that the boundary heat fluxes in the discrete velocity directions of the TLBE model can be directly obtained from the TDFs at the neighboring lattice nodes. The total heat transfer on the boundary is simply a summation of all the discrete heat fluxes with a constant surface area.

As applications of the proposed boundary schemes and heat transfer evaluation technique in the TLBE method, 1) a quasi-two-dimensional (2-D) axisymmetric LB model with an MRT collision operator is proposed to simulate the general axisymmetric CDE in 3-D, and 2) a radiation-conduction coupled model is developed to simulate the energy transport in a solar reactor.

CHAPTER 1

INTRODUCTION TO HEAT TRANSFER IN FLUID-SOLID FLOWS

1.1 Background and Motivations

Transport phenomena including momentum, heat and mass exchange are routinely investigated in many engineering systems such as heat exchangers, heat pipes, electronic cooling devices, fluidized beds and chemical reactors. Efficient modeling tools are required for system design and optimization purposes (Faghri and Zhang 2006). There has also been growing interest in simulating the fluid flows and heat and mass transfer on the pore-scale in porous media, micro channels, and micro reactors (Sullivan et al. 2005, Manjhi et al. 2006, Verma et al. 2007, Verma et al. 2008, Kao et al. 2007, Garimella and Sobhan 2003, Kang et al. 2006, Kang et al. 2007, Wang et al. 2007, Chen et al. 2012, Maier and Bernard 2010) due to the growth of supercomputing power and the need to gain a fundamental understanding of the local transport processes. The present dissertation is concentrated on the computational study of heat transfer in fluid-solid systems.

Heat transfer between two impacting solids, such as particle-to-particle and particle-to-wall, initially at different temperatures is the first topic addressed. For most engineering applications, the collision period is very short and the contact area is much smaller than the characteristic length of the solids (Sun and Chen 1988, Li et al. 2012). Under the assumptions of semi-infinite media and no thermal resistance, the contact area is characterized by the Hertzian elastic theory. With a coordinate transformation employed the computational domain becomes fixed for this moving boundary problem and the heat transfer through the contact area is conveniently evaluated.

For heat transfer evaluation on an arbitrarily-shaped curved boundary, a general, efficient and accurate technique that preserves the local geometry is desirable. The thermal lattice Boltzmann equation (TLBE) method, which is a direct extension of the lattice Boltzmann equation (LBE) for fluid dynamics simulations, has proved to be a promising candidate considering the inherent benefits of the LBE method and the continuous development of effective TLBE models (Alexander et al. 1993, Chen et al. 1994, Shan 1997, He et al. 1998, Lallemand and Luo 2003, Guo et al. 2007, Shi and Guo 2009, Mezrhad et al. 2010, Yoshida and Nagaoka 2010).

The evolution of the microscopic temperature/energy distribution functions is simulated in the TLBE method and the macroscopic temperature is obtained from the moment of the temperature distribution functions (TDFs). Accurate and robust boundary conditions for the TDFs that conserve the macroscopic Dirichlet and Neumann conditions are essential to the integrity of the TLBE simulation and the overall heat transfer evaluation.

1.2 Objectives

The main objective of the present research is to investigate the thermal field and heat transfer in fluid-solid systems. To gain a fundamental understanding of the local thermal behavior, a computational study on the scale of the impact solid particles is conducted to analyze the heat transfer between colliding particles and surfaces initially at different temperatures, and a kinetic-based mesoscopic lattice Boltzmann equation (LBE) method is applied to investigate the heat transfer on the fluid-solid interface and the temperature distribution inside a porous structure in a solar thermochemical system. Specifically, the following topics are studied in detail.

1.2.1 Heat Transfer between Colliding Solid Particles

There have been continuous interest and effort in evaluating and predicting the transient heat transfer across the interface between two contacting solids initially at different surface temperatures (Heasley 1965, Barber 1989, Ammar et al. 1992, Li and Mason 2000, Kostoglou and Konstandopoulos 2002). This transient problem is encountered in frictional heating where surface temperatures are different (Heasley 1965), in thermal machine components whose surfaces are meeting and separating periodically, such as the exhaust valves of internal combustion engines (Howard and Sutton 1970), and in the heat exchange between impacting particles in fluidized beds, where the heat conducted during the deformation of the impacting bodies must be considered (Sun and Chen 1988, Kaviany 1988).

In this work we aim at obtaining an accurate closed-form expression to predict the heat transfer between two colliding particles as a function of the impact Fourier number, the thermal diffusivity ratio, and the thermal conductivity ratio of the particles (Li et al. 2012a).

1.2.2 Thermal Boundary Conditions on Curved Boundaries

The kinetic-based lattice Boltzmann equation (LBE) method has become an alternative and attractive numerical approach for fluid dynamics simulations because it is explicit in formulation, easy to implement and compatible with parallelization compared with solving the Navier-Stokes equations. It has been successfully applied in a variety of fluid flow problems (Qian et al. 1992, Chen and Doolen 1998, Succi 2001, Yu et al. 2003) and has been extended to complex flows, such as multi-phase and multi-component flows (Luo and Girimaji 2003, Zheng et al. 2006, Premnath and Abraham 2007, Asinari 2008, Aidun and Clausen 2010), turbulent flows (Lätt et al.

2006, Yu et al. 2006, Aidun and Clausen 2010), micro-flows (Guo et al. 2006, Aidun and Clausen 2010), and flows through porous media (Guo and Zhao 2002a, Pan et al. 2006). Because of the advantages of the LBE method, various thermal LBE (TLBE) models have been developed and successfully used for thermal transport problems (Alexander et al. 1993, Chen et al. 1994, Shan 1997, He et al. 1998, Lallemand and Luo 2003, Guo et al. 2007, Shi and Guo 2009, Mezrhad et al. 2010, Yoshida and Nagaoka 2010).

Accurate boundary condition treatment is essential for the overall integrity of the LBE simulations. For the fluid velocity field, the “bounce-back” scheme has been intensively studied (Ziegler 1993, Noble et al. 1995, Ginzbourg and d’Humières 1996, Chen et al. 1996, He et al. 1997, Zou and He 1997, Ginzburg and d’Humières 2003) and extended to curved boundaries (Filippova and Hänel 1998, Mei et al. 1999, Mei et al. 2000, Bouzidi et al. 2001, Guo et al. 2002). The standard bounce-back method is second-order accurate for no-slip wall boundaries when the distance from the wall to the nearest fluid node is half of the lattice unit spacing. For other hydrodynamic boundary conditions such as given density, pressure, slipping velocity or their derivatives, the bounce-back scheme can be modified with the flow properties at on the boundary included in the treatments (Ginzbourg and d’Humières 1996, Chen et al. 1996, He et al. 1997, Zou and He 1997, Filippova and Hänel 1998, Mei et al. 1999, Mei et al. 2000, Bouzidi et al. 2001, Guo et al. 2002, Ginzburg and d’Humières 2003). Spatial interpolation or extrapolation has also been incorporated to improve the degraded accuracy of the bounce-back scheme when the boundary is located in arbitrary position in the lattice cell (Chen et al. 1996, Filippova and Hänel 1998, Mei et al. 1999, Mei et al.

2000, Bouzidi et al. 2001, Guo et al. 2002). With appropriate modifications, some of the athermal boundary condition treatments have been extended to TLBE simulations as well. With different types of thermal boundary condition treatments available in the literature, we notice that discussions about the applicability and accuracy of these treatments in curved-boundary situations are rather limited.

The objectives of the present work are twofold. The first is to develop second-order accurate boundary condition treatments for both the Dirichlet and Neumann conditions on straight boundaries that can be placed at arbitrary locations in the lattice. The second is to extend the present boundary condition treatments to curved-boundary situations and to investigate the effect of curved-geometry on the accuracy of the present boundary condition treatments.

1.2.3 Heat Transfer on Curved Boundaries

With conventional computational fluid dynamics (CFD) techniques, heat transfer on the complex fluid-solid interface is frequently simulated with a multi-scale analysis in order to capture the local thermal behavior on the interface. Accurate integration is often required to determine the total heat transfer across the boundary.

The mesoscopic nature of the LBE method makes it very efficient in examining the local flow and momentum exchange at the fluid-solid interface. Mei et al. (2002) investigated two different methods for evaluating the fluid force on the fluid-solid boundary based on momentum exchange and stress integration, respectively, in the lattice Boltzmann equation. The momentum-exchange approach was found to be reliable, accurate and much easier to implement than the stress-integration approach for both two-dimensional and three-dimensional flows.

Following the “conservation” and “exchange” ideas for force evaluation in the LBE method (Mei et al. 2002), an energy-exchange approach for heat transfer evaluation on the fluid-solid interface in the TLBE is proposed in this work. The boundary heat flux in the discrete velocity directions of the TLBE model is directly obtained from the temperature distribution functions at the lattice nodes, rather than using any finite-difference schemes with the obtained temperature field. The heat fluxes in the discrete velocity directions can be integrated over the lattice surface area to obtain the heat transfer on the interface, thus avoiding the calculations of the normal heat flux on the boundary and the surface area approximations.

1.2.4 Multiple-Relaxation-Time Lattice Boltzmann Model for the Axisymmetric Convection-Diffusion Equation

Although 3-D LB models can be directly applied to simulate the axisymmetric CDE when the curved boundary condition is properly handled, quasi-2-D LB models, which require far less computational effort and bypass the curved boundary treatment for straight pipes, are attractive alternatives for solving the axisymmetric CDE as demonstrated by the LB models developed for axisymmetric athermal flows (Halliday et al. 2001, Lee et al. 2006, Reis and Phillips 2007, Reis and Phillips 2008, Zhou 2008, Chen et al. 2008, Huang and Lu 2009, Guo et al. 2009, Wang et al. 2010, Li et al. 2010, Zhou 2011) and thermal problems (Peng et al. 2003, Huang et al. 2007, Chen et al. 2009, Li et al. 2009, Zheng et al. 2010a, Zheng et al. 2010b). It is noted that all the existing LB models for axisymmetric thermal flows in (Chen et al. 2009, Li et al. 2009, Zheng et al. 2010a, Zheng et al. 2010b) used the BGK collision operator. A robust and straightforward MRT-LB model that can simulate the general axisymmetric CDE is

highly desired. Furthermore, we notice that the numerical validation regarding the order-of-accuracy of the axisymmetric thermal LB models has not been well established.

In this work, we propose an MRT-LB model for the general axisymmetric CDE for scalar transport such as temperature, mass concentration and azimuthal velocity component in rotational flows. When the CDE is coupled with the hydrodynamic equations, the radial-axial velocity field is solved using Zhou's axisymmetric LB model (Zhou et al. 2011) with the BGK collision model replaced by an MRT-based model.

1.2.5 Thermal Analysis in a Porous Structure in a Solar Thermochemical System

The energy transport in a solar thermochemical high-temperature system is numerically studied and the temperature distribution in the porous reacting bed inside the absorbers sitting inside a cavity-receiver is simulated. We apply the Monte Carlo ray-tracing technique to analyze the radiative transfer between the cavity wall and the absorber surfaces. The temperature field inside the absorbers is modeled with the TLBE method and the proposed thermal boundary condition treatments for curved boundaries; endothermic chemical reaction is treated as a heat sink based on the reaction rate. These two modules are explicitly coupled with the re-emission from the absorber surfaces included in the radiative transfer analysis. An optimal design of the cavity-reactor can be pursued by investigating the solar energy absorption efficiency and the temperature distribution inside the absorbers with different configurations.

The present dissertation is constructed as follows. Chapter 2 presents the heat transfer computation between colliding solid particles and surfaces with a closed-form formula for heat transfer prediction obtained in the end. Chapter 3 reviews the boundary conditions in TLBE method in the literature and improved boundary condition treatments are proposed for the Dirichlet, Neumann and mixed thermal boundary conditions. The

stability and accuracy of the proposed boundary schemes are validated with detailed numerical tests. Based on the improved boundary condition treatments in Chapter 3, an efficient and accurate heat transfer evaluation technique is proposed and numerical validated in Chapter 4. Chapter 5 presents an MRT-LB model for the axisymmetric CDE. Next in Chapter 6, a radiation-conduction coupled numerical model is developed for simulating the energy transport in a high-temperature solar thermochemical reactor based on a Monte-Carlo ray tracing radiation model and the TLBE conduction model. Chapter 7 summarizes the dissertation and discusses the related future works.

CHAPTER 2 HEAT TRANSFER BETWEEN COLLIDING SURFACES AND PARTICLES*

2.1 Introduction

Transient heat transfer across the interface between two contacting solids initially at different temperatures has been investigated in many previous works (Heasley 1965, Barber 1989, Ammar et al. 1992, Li and Mason 2000, Kostoglou and Konstandopoulos 2002). Although some approximate solutions for the transient heat flow (Heasley 1965) and an asymptotic solution for the short-time transient heat conduction (Barber 1989) have been presented, no analytical expression was provided in their work for predicting the amount of heat exchange between contacting bodies. Sun and Chen (1988) carried out a computational study using a finite difference method to solve the unsteady conduction equations in the region near the contact area of the colliding surfaces. Because both the contact area and the collision time are typically very small, the heat transfer media were assumed to be semi-infinite which greatly simplified the formulation of the problem and the subsequent computation. They gave a closed-form solution for the heat transfer in the limit of zero impact Fourier number (Fo , based on the maximum contact radius and the contact duration). Typical numerical results from the finite difference solution were presented graphically over a range of Fourier numbers, thermal diffusivity ratios, and conductivity ratios. Zhou et al. (2008) employed the finite element method to solve the heat conduction problem between colliding particles. The temperature distributions on the entire body of the colliding spheres were computed and the total amount of heat transfer during the impact was determined. A closed-form approximate expression for the heat transfer was developed based on their computed results for a special case when the colliding materials have the same thermal

* This work has been published in *ASME Journal of Heat Transfer* (Li et al. 2012).

conductivity. Close examination also indicates that the energy transfer computed by Zhou et al. (2008) is noticeably smaller than that by Sun and Chen (1988).

The main objective in the present research is to develop an accurate closed-form expression to predict the amount of heat transfer between two colliding particles with arbitrary impact Fourier number, thermal diffusivity ratio, and thermal conductivity ratio. Hertzian contact theory of elasticity (Timoshenko and Goodier 1970, Johnson 1987) is used to characterize the particle impact and associated deformations. The semi-infinite media assumption (Sun and Chen 1988) is also employed and the governing conduction equation is then transformed to a moving coordinate so that the computational domain remains fixed. Grid stretching in both the radial and axial directions is applied to resolve the high temperature gradient and singular regions. A self-similar solution of the temperature field during the initial contact period is obtained to provide an accurate initial condition for the simulation of the entire collision period and to gain an insight into the asymptotic state of the heat transfer. In addition, the singular behavior of the discontinuity at the edge of the contact area is analyzed based on a local analytical solution, which also offers an insight into the evolution of the temperature field in the whole spatial domain and the heat flux during the collision period. The asymptotic solutions for the thermal field and the transient heat flux over the contact area at small-time and large-time are obtained in the zero-Fourier number limit. The behavior of the transient heat flux and heat flow rate in the contact area is fully simulated and analyzed. Finally, a closed-form expression for predicting the heat exchange between impacting particles of various thermal properties is provided based on various asymptotic limits and computational results over a wide range of Fourier

numbers, thermal diffusivity ratios, and thermal conductivity ratios of the colliding materials.

2.2 Formulation of the Collisional Heat Transfer Problem

2.2.1 Elastic Collision and Deformation

When two spherical particles of masses m_1 and m_2 , radii R_1 and R_2 , elastic moduli E_1 and E_2 , and Poisson ratios ν_1 and ν_2 , impact with a normal relative velocity v_{12} , the contact area A is circular and its rate of change during the compression process can be expressed as below according to the Hertzian elastic theory (Timoshenko and Goodier 1970, Johnson 1987)

$$\frac{dA}{dt} = \left[(\pi v_{12} R_{12})^2 - \frac{4}{5\sqrt{\pi}} \frac{E_{12}}{m_{12}} A^{5/2} \right]^{1/2} \quad (2-1)$$

where

$$R_{12} = \frac{R_1 R_2}{R_1 + R_2} \quad (2-2)$$

$$E_{12} = \frac{4/3}{(1-\nu_1^2)/E_1 + (1-\nu_2^2)/E_2} \quad (2-3)$$

and

$$m_{12} = \frac{m_1 m_2}{m_1 + m_2} \quad (2-4)$$

If the second surface is flat, R_2 should be set to infinity; and if the second surface is the interior wall of a pipe, R_2 should take the negative value of the pipe radius.

The decompression is an inverse process of the compression. The maximum contact area A_c is obtained by setting the derivative in Eq. (2-1) to zero.

$$A_c \equiv \pi r_c^2 = \pi \left(\frac{5m_{12} R_{12}^2}{4E_{12}} \right)^{2/5} v_{12}^{4/5} \quad (2.5)$$

Equation (2-1) can also be integrated to yield a dimensionless relationship between the transient contact area and the collision time as

$$\tau = \int_0^{A^*} \frac{dx}{(1-x^{5/2})^{1/2}} \quad (2-6)$$

where

$$\tau \equiv \left(\frac{4E_{12}}{5m_{12}} \right)^{2/5} (R_{12} v_{12})^{1/5} t \quad (2-7)$$

and

$$A^* \equiv A / A_c \equiv R^2 / R_c^2 \quad (2-8)$$

In the compression process Eq. (2-6) is numerically integrated from $A^* = 0$ to $A^* = 1$ to yield a dimensionless time of $\tau_c = 1.4716376$. The total contact duration t_c is then found from Eq. (2-7) as

$$t_c = 2\tau_c \left(\frac{5m_{12}}{4E_{12}} \right)^{2/5} (R_{12} v_{12})^{-1/5} \quad (2-9)$$

Defining

$$\dot{t}^* = t/t_c = \tau/(2\tau_c) \quad (2-10)$$

the relationship between A^* and \dot{t}^* can be numerically obtained; the result is shown in Fig. 2-1.

To carry out asymptotic analyses for the heat flux in the contact area, the following are noted for $\dot{t}^* \rightarrow 0$

$$A^* = (2\tau_c)\dot{t}^* - \frac{1}{7}(2\tau_c)^{7/2}(\dot{t}^*)^{7/2} + \frac{1}{112}(2\tau_c)^6(\dot{t}^*)^6 + \dots \quad (2-11a)$$

$$\frac{t^*}{A^*} \frac{dA^*}{dt^*} = 1 + b_1(t^*)^{5/2} + b_2(t^*)^5 + \dots \quad (2-11b)$$

with
$$b_1 = -\frac{5}{14}(2r_c)^{5/2}, b_2 = -\frac{5}{784}(2r_c)^5 \quad (2-11c)$$

Equation (2-11a) also implies that

$$A^* \propto t^* \text{ and hence } R \propto (t^*)^{1/2} \text{ as } t^* \rightarrow 0 \quad (2-12)$$

2.2.2 Governing Equations for Heat Transfer

The transient heat conduction equation for the two colliding particles in the axisymmetric cylindrical coordinates (Fig. 2-2) is (Sun and Chen 1988, Zhou et al. 2008)

$$\frac{1}{\alpha_i} \frac{\partial T_i}{\partial t} = \frac{\partial^2 T_i}{\partial z^2} + \frac{1}{r} \frac{\partial}{\partial r} \left(r \frac{\partial T_i}{\partial r} \right) \quad (i = 1, 2) \quad (2-13)$$

The semi-infinite media assumption was used by Sun and Chen (1988). Its validity is closely examined in this study and the details are given in Appendix A. It is shown that this assumption is valid over a wide range of conditions and thus is used in the present work. Hence for a contact area with instantaneous contact radius $R(t)$, the boundary conditions are summarized as follows

$$\left. \begin{array}{l} T_1 = T_2, k_1 \frac{\partial T_1}{\partial z} = -k_2 \frac{\partial T_2}{\partial z}, \quad r \leq R(t) \\ \frac{\partial T_1}{\partial z} = 0, \quad \frac{\partial T_2}{\partial z} = 0, \quad r > R(t) \end{array} \right\} \text{ at } z = 0 \quad (2-14)$$

$$T_1 = T_{01} \text{ as } z \rightarrow \infty, \quad T_2 = T_{02} \text{ as } z \rightarrow -\infty \quad (2-15)$$

$$T_1 = T_{01} \text{ and } T_2 = T_{02} \text{ as } r \rightarrow \infty \quad (2-16)$$

$$\frac{\partial T_1}{\partial r} = \frac{\partial T_2}{\partial r} = 0 \text{ at } r = 0 \quad (2-17)$$

where k_1 and k_2 are the thermal conductivities of the two particles, T_{01} and T_{02} are the surface temperatures of the particles before contact ($T_{01} > T_{02}$).

The initial condition is assumed to be

$$T_1 = T_{01} \text{ and } T_2 = T_{02} \text{ at } t = 0 \quad (2-18)$$

The above formulation is the same as described in Sun and Chen's work (1988). It is important to note that the discontinuity of the boundary conditions in Eq. (2-14) occurs at $r = R(t)$, which changes with time.

Noting that the contact area varies with time during the entire collision period, a coordinate transformation is applied so that the computation can be more conveniently carried out in a well defined, fixed coordinate system. To this end, the following dimensionless variables are introduced

$$\eta = \frac{z}{\sqrt{\alpha_1 t}}, \quad \xi = \frac{r}{R(t)}, \quad \theta = \frac{T - T_{02}}{T_{01} - T_{02}} \quad (2-19)$$

The governing equations become

$$t^* \frac{\partial \theta_1}{\partial t^*} - R^* \frac{\xi}{2} \frac{\partial \theta_1}{\partial \xi} - \frac{\eta}{2} \frac{\partial \theta_1}{\partial \eta} = \frac{\partial^2 \theta_1}{\partial \eta^2} + Fo \frac{t^*}{A^*} \frac{1}{\xi} \frac{\partial}{\partial \xi} \left(\xi \frac{\partial \theta_1}{\partial \xi} \right) \quad (2-20a)$$

$$t^* \frac{\partial \theta_2}{\partial t^*} - R^* \frac{\xi}{2} \frac{\partial \theta_2}{\partial \xi} - \frac{\eta}{2} \frac{\partial \theta_2}{\partial \eta} = \alpha' \left[\frac{\partial^2 \theta_2}{\partial \eta^2} + Fo \frac{t^*}{A^*} \frac{1}{\xi} \frac{\partial}{\partial \xi} \left(\xi \frac{\partial \theta_2}{\partial \xi} \right) \right] \quad (2-20b)$$

where

$$R^* = \frac{2t}{R} \frac{dR}{dt} = \frac{t^*}{A^*} \frac{dA^*}{dt^*} \quad (2-21)$$

$$\alpha' = \alpha_2 / \alpha_1 \quad (2-22)$$

and the characteristic impact Fourier number is

$$Fo = \frac{\alpha_1 t_c}{R_c^2} \quad (2-23a)$$

Using Eqs. (2-5) and (2-9), the Fourier number can also be expressed in terms of the equivalent radius and the impacting velocity as

$$Fo = \frac{2\tau_c \alpha_1}{R_{12} V_{12}} = 2.9432752 \frac{\alpha_1}{R_{12} V_{12}} \quad (2-23b)$$

The boundary conditions given by Eq. (2-14) now become

$$\theta_1 = \theta_2, \quad \frac{\partial \theta_1}{\partial \eta} = -\frac{k_2}{k_1} \frac{\partial \theta_2}{\partial \eta} = -k' \frac{\partial \theta_2}{\partial \eta}, \quad \xi \leq 1 \text{ at } \eta = 0 \quad (2-24a)$$

$$\frac{\partial \theta_1}{\partial \eta} = 0, \quad \frac{\partial \theta_2}{\partial \eta} = 0, \quad \xi > 1 \text{ at } \eta = 0 \quad (2-24b)$$

It is important to note that the discontinuity in the boundary conditions in Eq. (2-14) now occurs at $\xi = 1$ which does not vary with time. The conditions given by Eqs. (2-15 – 2-17) can be similarly modified to:

$$\theta_1 = 1 \text{ and } \theta_2 = 0 \text{ as } \eta \rightarrow \pm\infty \quad (2-25)$$

$$\theta_1 = 1 \text{ and } \theta_2 = 0 \text{ as } \xi \rightarrow \infty \quad (2-26)$$

$$\frac{\partial \theta_1}{\partial \xi} = \frac{\partial \theta_2}{\partial \xi} = 0 \text{ at } \xi = 0 \quad (2-27)$$

In order to maintain sufficient resolution near the contact area (especially near the singularity at $\xi = 1$) and to obtain a computational domain large enough to avoid numerical interference of the far-field boundaries, grid stretching in both directions is employed.

Equation (2-20) is solved using the alternative direction iteration (ADI) scheme. A second-order upwind scheme is used for the first-order derivative terms in Eq. (2-20). This avoids the grid level oscillation which normally occurs in the presence of large advection when central difference is used. This also avoids heavy numerical damping when a first-order upwind is used. For finite Fo , near $t^* = 1$, it is found that the integral of the heat flux over the contact area increases rapidly due to the detachment of the

particles. This necessitates a gradual reduction of the time step to ensure accuracy of the solution.

2.2.3 Self-Similar Solution

While the initial condition for the temperature distribution given by Eq. (2-18) is theoretically correct at $t = 0$, it results in persistent oscillation of the temperature during the initial period when Eq. (2-18) is applied directly. Thus a self-similar solution for $t^* \ll 1$ is sought. As $t^* \rightarrow 0$, $t^* \partial \theta / \partial t^* \rightarrow 0$, from Eqs. (2-11) and (2-21) we also have $R^* \rightarrow 1$ and $t^*/A^* \rightarrow 1/(2\tau_c)$, thus the transient conduction problem has a self-similar steady solution in the transformed coordinate (ξ, η) in the small-time limit, then Eq. (2-20) becomes

$$-\frac{\xi}{2} \frac{\partial \theta_i}{\partial \xi} - \frac{\eta}{2} \frac{\partial \theta_i}{\partial \eta} = \frac{\alpha_i}{\alpha_1} \left[\frac{\partial^2 \theta_i}{\partial \eta^2} + \frac{Fo}{2\tau_c} \frac{1}{\xi} \frac{\partial}{\partial \xi} \left(\xi \frac{\partial \theta_i}{\partial \xi} \right) \right] \quad (i = 1, 2) \quad (2-28)$$

The boundary conditions for the self-similar solution are the same as given by Eqs. (2-24 – 2-27). The above equation can be further simplified when $\alpha' = k' = 1$. For example, only half of the domain needs to be solved and $\theta_1(\xi, 0) = \theta_2(\xi, 0) = 0.5$ can be enforced directly for $\xi \leq 1$ on the contact area. The converged solution obtained through an iterative procedure is used as an initial condition for solving Eq. (2-20) on the same grids.

Of particular interest is the limiting case of $Fo = 0$ with $\alpha' = k' = 1$. In this special case, the governing equation (2-28) for θ_1 becomes $-\frac{\xi}{2} \frac{\partial \theta_1}{\partial \xi} - \frac{\eta}{2} \frac{\partial \theta_1}{\partial \eta} = \frac{\partial^2 \theta_1}{\partial \eta^2}$. The solution for θ_1 at $\xi = 0$ is the standard error function: $\theta_1(\xi = 0, \eta) = (1 + \text{erf}(\eta/2))/2$. The solution for θ_1 at $\xi = 1$ is, however, singular. A transformation using $Y = \eta / \sqrt{1 - \xi}$ gives

$$\frac{\partial^2 \theta}{\partial Y^2} + \frac{\xi(1-\xi)}{2} \frac{\partial \theta}{\partial \xi} + \frac{(1-\xi/2)Y}{2} \frac{\partial \theta}{\partial Y} = 0. \text{ At } \xi = 1, \text{ this equation becomes } \frac{\partial^2 \theta}{\partial Y^2} + \frac{Y}{4} \frac{\partial \theta}{\partial Y} = 0;$$

the solution is another error function of $\frac{1}{2}[1 + \operatorname{erf}(\frac{Y}{2\sqrt{2}})]$. Thus near $\xi = 1$ the leading

order behavior for the temperature is $\theta_1 \sim \frac{1}{2}[1 + \operatorname{erf}(\frac{1}{2\sqrt{2}} \frac{\eta}{\sqrt{1-\xi}})]$. The derivative on the

interface for $Fo = 0$ near $\xi = 1$ is

$$\frac{\partial \theta_1(\xi \sim 1)}{\partial \eta} \Big|_{\eta=0} \sim \frac{1}{2\sqrt{2\pi}} \frac{1}{\sqrt{1-\xi}} \quad (2-29)$$

2.2.4 Heat Transfer

Denoting $q(t, r)$ as the instantaneous heat flux at the interface and $\dot{Q}(t)$ as the instantaneous heat flow rate across the contact area, we have

$$q(t, r) = -k_1 \frac{\partial T_1}{\partial z} \Big|_{z=0} = -\frac{k_1(T_{01} - T_{02})}{\sqrt{\alpha_1 t}} \frac{\partial \theta_1}{\partial \eta} \Big|_{\eta=0} \quad (2-30a)$$

$$\dot{Q}(t) = 2\pi \int_0^{R(t)} q(t, r) r dr = -\frac{2k_1(T_{01} - T_{02})A_c}{\sqrt{\alpha_1 t_c}} \frac{A^*}{\sqrt{t^*}} \int_0^1 \frac{\partial \theta_1}{\partial \eta} \Big|_{\eta=0} \xi d\xi \quad (2-30b)$$

From Eq. (2-30) we can further define the dimensionless heat flux $q^*(t^*, \xi)$, the

dimensionless heat flux integral $q_w^*(t^*)$, and the dimensionless heat flow rate $\dot{Q}^*(t^*)$ as

$$q^*(t^*, \xi) \equiv \frac{\partial \theta_1}{\partial \eta} \Big|_{\eta=0} \quad (2-31a)$$

$$q_w^*(t^*) \equiv \int_0^1 \frac{\partial \theta_1}{\partial \eta} \Big|_{\eta=0} \xi d\xi \quad (2-31b)$$

$$\dot{Q}^*(t^*) \equiv \frac{A^*}{\sqrt{t^*}} q_w^*(t^*) \quad (2-31c)$$

The total energy transfer during the impact is

$$e = \int_0^{t_c} \dot{Q}(t) dt \quad (2-32)$$

2.3 Results and Discussion

First, a grid-refinement study is carried out using the self-similar solutions as a surrogate. The results for the dimensionless heat flux integral $q_w^*(t^*)$ defined in Eq. (2-31b) at $t^* \rightarrow 0$ with different mesh sizes are compared in Table 2-1. The iterative solutions are considered to be converged when the maximum difference in the temperature field between two continuous iterations is less than 10^{-10} . Typically, 320x128 intervals in the ξ - and η -directions are chosen to obtain the temperature field, respectively, on each side of the contact. For the purpose of extracting the parameters associated with the singular behavior near $\xi = 1$ throughout this paper, grids much finer than 320x128 have been used to ensure the reliability of the numerical solutions. For finite Fo and finite t^* , a nominal $\Delta t^* = 1/800$ is used; at $t^* \rightarrow 1$, a linear decrease in Δt^* is used in order to capture the rapid rise in the heat flux near the detachment. For $Fo = 0$, $\Delta t^* = 1/800$, $1/1600$, and $1/3200$ were used in order to obtain an accurate value of the correction factor C_0 (see Eq. (2-61)). The infinity boundary in the η -direction is placed at $\eta_\infty = 15$. In the ξ -direction, the boundary location varies depending on the Fourier number. For $Fo = 0$, $\xi_\infty = 1$ is used and for $Fo > 1$, $\xi_\infty = 35$ is used.

2.3.1 Self-Similar Solution at Small Time

The self-similar solution of the temperature field serves as an excellent initial condition to obtain accurate and smoothly varying temperature fields. More importantly, it is found that the dimensionless heat flow rate $\dot{Q}^*(t^*)$ obtained from the self-similar solution remains very close to the time dependent solution for $t^* < 0.2$ (see Fig. 2-10 later). Thus a great deal of insight can be gained by examining the much simpler self-

similar solution first. Since in most of the practical situations heat transfer occurs between particles of the same material, only the results corresponding to $\alpha' = k' = 1$ will be presented here for brevity.

Figure 2-3 (a-d) shows the temperature contours for Fo ranging from 0.02 to 10 based on the self-similar solutions. Fig. 2-3(b) also includes a schematic of the grid distribution near the discontinuity. For $Fo = 0.02$ and $Fo = 0.1$, the contours are very similar, indicating the existence of an asymptotic limiting solution as $Fo \rightarrow 0$ which can be representative of the solution for $Fo \leq 0.1$ to the leading order. Fig. 2-3 (c-d) clearly shows that as Fo increases, the heat conduction in the r -direction becomes more and more significant as part of the total heat conduction.

From the self-similar solution, the dimensionless heat flux $q^*(t^*, \xi)$ in the contact area from $\xi = 0$ to $\xi = 1$ can be obtained and the results at different Fourier numbers are presented in Fig. 2-4. As Fo increases, there is a strong increase in $q^*(t^*, \xi)$ throughout the entire contact area. It is also clear that there exists a singularity for $q^*(t^*, \xi)$ at $\xi = 1$, as shown analytically by Eq. (2-29) for the case of $Fo = 0$. This singularity has a significant effect on the computation of the total heat flow rate across the contact area. The nature of this singularity for $Fo > 0$ is further investigated next.

2.3.2 Behavior of the Singularity at $(r, z) = (R(t), 0)$

Because of the discontinuity in the boundary conditions at $(\xi, \eta) = (1, 0)$, the solutions to θ are expected to be singular near $(\xi, \eta) = (1, 0)$ for Eq. (2-20) as well as for Eq. (2-28). In order to gain an insight, $\alpha' = k' = 1$ is considered for simplicity and thus only the temperature on the surface of particle 1 is simulated. Thus, the boundary condition at $\eta = 0$ becomes

$$\theta(\xi \leq 1) = 0.5 \text{ and } \frac{\partial \theta}{\partial \eta}(\xi > 1) = 0 \text{ at } \eta = 0 \quad (2-33)$$

To investigate the behavior of the singularity at $(\xi, \eta) = (1, 0)$, the following variables are introduced

$$\zeta = \frac{\xi - 1}{(Fo/2\tau_c)^{1/2}}, \sigma = \sqrt{\zeta^2 + \eta^2}, \psi = \tan^{-1}(\eta / \zeta) \quad (2-34)$$

With the boundary conditions in Eq. (2-33), the local solution to θ is expected to be

$$\theta \sim 0.5 + O(\sigma^n), \quad \frac{\partial \theta}{\partial \sigma} \sim O(\sigma^{n-1}) \quad (2-35)$$

One can also deduce that the dominant terms in Eq. (2-28), in the limit of $\sigma \rightarrow 0$ become

$$\frac{\partial^2 \theta}{\partial \sigma^2} + \frac{1}{\sigma^2} \frac{\partial^2 \theta}{\partial \psi^2} \sim 0 \quad (2-36)$$

The boundary involved in Eq. (2-33) for the local singular solution dictates that $n = 1/2$ in Eq. (2-35). Thus the solution to the Laplace's Eq. (2-36) subjected to Eq. (2-33) is

$$\theta = 0.5 + w\sigma^{1/2}\cos(\psi/2) \quad (2-37)$$

Hence the leading order solution to θ near $\sigma = 0$ is

$$\theta = 0.5 + w \left[\frac{(\xi - 1)^2}{Fo/2\tau_c} + \eta^2 \right]^{1/4} \cos \left[\frac{1}{2} \tan^{-1} \frac{\eta(Fo/2\tau_c)^{1/2}}{\xi - 1} \right] \quad (2-38)$$

where w is a constant that depends on Fo and needs to be determined by matching the local solution to the finite difference solution in the outer region for different values of Fo .

It is observed from the local solution, Eq. (2-38), that

$$\frac{\partial \theta(\xi, 0)}{\partial \eta} \propto \frac{w (Fo / 2\tau_c)^{1/4}}{2 \sqrt{1-\xi}} \quad \text{for } \xi < 1 \quad (2-39)$$

thus there is an integrable square-root type of singularity in the heat flux, $q^*(t^*, \xi)$, near $\xi = 1$ (or $r = R(t)$) in the contact region for all values of Fo , as shown in Fig. 2-4. Although the foregoing analysis is presented for particles of the same material ($\alpha' = k' = 1$), and for small time, the nature of the singularity is the same for particles of different materials and for the entire duration of collision as well.

Figure 2-5 (a) shows the variations of $(\theta - 0.5)/(w\rho^{1/2})$ given by Eq. (2-38) from $\varphi = 0$ to π (notice (σ, φ) is another coordinate system related to (σ, ψ) with $\rho \equiv \sqrt{(\xi - 1)^2 + \eta^2}$ and $\varphi = \tan^{-1}(\eta / (\xi - 1))$) at $Fo = 0.02, 1.0, \text{ and } 10.0$ together with the finite difference results obtained from the self-similar solution. The values of w in Eq. (2-38) are determined by fitting the analytical solution to the numerical solution near the singularity. Excellent agreement between the analytical and numerical solutions can be observed for the variation in the azimuthal direction. Although not shown here, similar agreement is observed for the variation of θ in the ξ -direction at $\eta = 0$ for a wide range of Fo values. This ensures the validity of the local solution given by Eq. (2-38). For very small Fo , there is a rapid decrease of θ as φ increases and passes $\pi/2$. This is entirely consistent with the temperature contour in Fig. 2-3(a) near $\xi = 1$ and $\eta = 0$. From $\xi > 1$ to $\xi < 1$, for a given local radius ρ , there is a large drop in θ in the tangential direction because of the discontinuity in the boundary conditions in Eq. (2-33).

Comparing Eq. (2-29) with Eq. (2-39) near $\xi = 1$, it can be deduced that $w \sim (2\tau_c / Fo)^{1/4} / \sqrt{2\pi} = 0.52254 / Fo^{1/4}$ as $Fo \rightarrow 0$. Fig. 2-5 (b) shows the variation of the w value with Fo in the local singularity from the self-similar solution. As $Fo \rightarrow 0$, the data in

Fig. 2-5 (b) agrees very well with the prediction $w \sim 0.52254 / Fo^{1/4}$. As Fo becomes larger, the stronger diffusion together with the advection in the ξ -direction causes a much stronger heat flow in the ξ -direction toward the contact point. Hence w increases with increasing Fo and for $Fo > 5$, the numerical result can be fit with $w \sim 0.62 + 0.05772Fo^{1/2}$ very well.

For larger value of t^* ($0 < t^* < 1$), self-similarity no longer exists. The dominant terms in the governing equation (2-20) for particles with the same material near the discontinuity point becomes

$$\frac{\partial^2 \theta}{\partial \eta^2} + Fo \frac{t^*}{A^*} \frac{1}{\xi} \frac{\partial}{\partial \xi} \left(\xi \frac{\partial \theta}{\partial \xi} \right) = 0 \quad (2-40)$$

The transient local solution can be obtained through similar procedure as

$$\theta \sim 0.5 + w \left[\frac{(\xi - 1)^2}{Fo \cdot t^* / A^*} + \eta^2 \right]^{1/4} \cos \left[\frac{1}{2} \tan^{-1} \frac{\eta (Fo \cdot t^* / A^*)^{1/2}}{\xi - 1} \right] \quad (2-41)$$

It should be noted that the constant w in Eq. (2-41) now varies not only with the Fourier number but also with time during the collision and should be determined by matching the local solution to the time-varying outer-region finite difference solution.

Figure 2-6 shows the temperature variations along the ξ -axis ($\eta = 0$) near $\xi = 1$ when $Fo = 1$, at $t^* = 0.40, 0.60, 0.70, 0.80, 0.90$, and 0.95 from the finite difference and local analytical solutions. The values of w used in the local solution are: 0.645, 0.545, 0.480, 0.430, 0.370 and 0.330 respectively, which are determined again from the numerical solutions for the temperature field near the singularity point. The transient behavior of the temperature field is largely the same for $t^* < 0.25$ as given by the self-similar solution. In the region close to the discontinuity ($\xi = 1$), the computed results from finite difference solution agree well with the analytical solutions given by Eq. (2-

41). The decrease in w as t^* increases suggests that while the nature of the singularity remains the same, the strength of the singularity continues to weaken during the decompression process. It is noted that the increasing diffusion in the ξ -direction (see the second terms on the right hand side of Eq. (2-20)) tends to smear the discontinuity and decrease effectively the strength of the singularity. The increasing larger advection in the positive ξ -direction given by the second terms on the left hand side of Eq. (2-20) for $t^* > 0.5$ represents the sweeping from the cold region ($\xi < 1$) with $\theta = 0.5$ to the warmer region ($\xi > 1$) and reducing effectively the temperature values after the contact point. This is in general true for all other values of Fo . The insight gained from the local solution for the thermal field is essential to the understanding on the behavior of the global thermal field.

2.3.3 Asymptotic Limit at $Fo \rightarrow 0$

In the present study, the numerical result at very small Fo indicates that when $\alpha' = k' = 1$, $q_w^* \sim 1/(2\sqrt{\pi})$ is obtained from the self-similar solution (see Fig. 2-4). Thus the asymptotic limit (as $Fo \rightarrow 0$) for the heat transfer is pursued by solving Eq. (2-20) while setting $Fo = 0$. Because of the loss of the diffusion term in the ξ -direction in Eq. (2-20) when $Fo = 0$, the solution must be separated into two stages depending on the sign of R^* .

When $R^* > 0$, inspection of Eqs. (2-20) and (2-24) quickly yields

$$\theta_1 = 1, \theta_2 = 0, \text{ for } \xi \geq 1; \quad (2-42)$$

$$t^* \frac{\partial \theta_i}{\partial t^*} - R^* \frac{\xi}{2} \frac{\partial \theta_i}{\partial \xi} - \frac{\eta}{2} \frac{\partial \theta_i}{\partial \eta} = \frac{\alpha_i}{\alpha_1} \frac{\partial^2 \theta_i}{\partial \eta^2} \quad (i = 1, 2), \text{ for } \xi \leq 1. \quad (2-43)$$

It is clear that in the absence of the $\partial^2\theta_i / \partial\xi^2$ term, Eq. (2-43) is parabolic in the ξ -direction. The boundary condition by Eq. (2-27) must be abandoned for $R^* > 0$, thus the only boundary condition in the ξ -direction should be

$$\theta_1 = 1 \text{ and } \theta_2 = 0 \text{ at } \xi = 1 \quad (2-44)$$

At each time step, the temperature $\theta_i(t^*, \xi, \eta)$ for $\xi < 1$ can be obtained numerically by marching from $\xi = 1$ to $\xi = 0$.

On the other hand, when $R^* < 0$ ($t^* > 1/2$), Eq. (2-27) should be applied as the only boundary condition in the ξ -direction and the solution is obtained by marching from $\xi = 0$.

While the foregoing procedure leads to correct numerical solution for the $Fo = 0$ case, further insight in the asymptotic limits can be gained by considering a perturbation solution for the temperature distribution.

At small time $t^* \ll 1$ the temperature can be sought in the form of

$$\theta_i(t^*, \xi, \eta) = \theta_{i,0}(\xi, \eta) + \theta_{i,1}(\xi, \eta)(t^*)^{2.5} + \theta_{i,2}(\xi, \eta)(t^*)^5 + \dots \quad (2-45)$$

The powers of t^* are determined based on the expansion of $A^*(t^*)$ given by (2-11b).

Substitution of Eq. (2-45) into Eq. (2-43) leads to a set of steady-state parabolic equations for $\theta_{1,0}$, $\theta_{1,1}$ and $\theta_{1,2}$ which can be solved numerically using a finite difference method. These solutions in turn give the heat flux integral in the contact zone as

$$q_w^*(t^*) = \int_0^1 \left. \frac{\partial\theta_1}{\partial\eta} \right|_{\eta=0} \xi d\xi \approx \int_0^1 \left(\left. \frac{\partial\theta_{1,0}}{\partial\eta} \right|_0 + (t^*)^{2.5} \left. \frac{\partial\theta_{1,1}}{\partial\eta} \right|_0 + (t^*)^5 \left. \frac{\partial\theta_{1,2}}{\partial\eta} \right|_0 \right) \xi d\xi, \quad t^* \ll 1 \quad (2-46)$$

The result is

$$q_w^*(t^*) \sim 0.2820948 - 0.430065(t^*)^{2.5} - 0.236343(t^*)^5, \quad t^* \ll 1 \quad (2-47)$$

Similarly, as $t^* \rightarrow 1$ at the large-time stage, one can deduce from Eq. (2-11) that

$$R^* = \frac{t^* dA^*}{A^* dt^*} \sim -\frac{t^* [1 + b_1(1-t^*)^{5/2} + b_2(1-t^*)^5 + \dots]}{1-t^*} \rightarrow \infty, \text{ the solution for the large-time}$$

behavior of the temperature near the detachment point can thus be sought in the form of

$$\theta_i(t^*, \xi, \eta) = \theta_{i,0}(\xi, \eta) + \beta_1(t^*)\theta_{i,1}(\xi, \eta) + \beta_2(t^*)\theta_{i,2}(\xi, \eta) + \dots, \quad t^* \rightarrow 1 \quad (2-48)$$

where the leading term $\theta_{i,0}(\xi, \eta)$ must be of $O(1)$ due to the finite boundary conditions while β_1 and β_2 are the gauge functions for the next two higher-order terms with $\beta_2(t^*) \ll \beta_1(t^*) \ll 1$. Substitution of the above expansion into Eq. (2-43) gives

$$[1 - (1-t^*)](\beta_1' \theta_{i,1} + \beta_2' \theta_{i,2} + \dots) + \left[\frac{1}{1-t^*} - 1 + b_1(1-t^*)^{3/2} + \dots \right] \frac{\xi}{2} \left[\frac{\partial \theta_{i,0}}{\partial \xi} + \beta_1 \frac{\partial \theta_{i,1}}{\partial \xi} + \beta_2 \frac{\partial \theta_{i,2}}{\partial \xi} + \dots \right] - \frac{\eta}{2} \left[\frac{\partial \theta_{i,0}}{\partial \eta} + \beta_1 \frac{\partial \theta_{i,1}}{\partial \eta} + \beta_2 \frac{\partial \theta_{i,2}}{\partial \eta} + \dots \right] = \frac{\alpha_i}{\alpha_1} \left[\frac{\partial^2 \theta_{i,0}}{\partial \eta^2} + \beta_1 \frac{\partial^2 \theta_{i,1}}{\partial \eta^2} + \beta_2 \frac{\partial^2 \theta_{i,2}}{\partial \eta^2} + \dots \right] \quad (i = 1, 2) \quad (2-49)$$

the largest term in the above is of $O(1/(1-t^*))$. The balance of the equation to $O(1/(1-t^*))$ requires that

$$\frac{\partial \theta_{i,0}}{\partial \xi} = 0 \quad (i = 1, 2) \quad (2-50)$$

Equation (2-50) simply states that $\theta_{i,0}$ is a function of η only. Since $R^* < 0$ for $t^* > 1/2$, $\theta_{i,0}(\eta)$ can be determined at $\xi = 0$. Setting $\xi = 0$ in Eq. (2-43) for $\theta_{i,0}(\eta)$ gives

$$-\frac{\eta}{2} \frac{\partial \theta_{i,0}}{\partial \eta} = \frac{\alpha_i}{\alpha_1} \frac{\partial^2 \theta_{i,0}}{\partial \eta^2} \quad (i = 1, 2) \quad (2-51)$$

The solution to the above can be expressed in terms of the error functions. For particles of the same material ($\alpha' = k' = 1$) we will have

$$\theta_{1,0}(\xi, \eta) = (1 + \text{erf}(\eta/2)) / 2 \quad (2-52)$$

The second largest term in Eq. (2-49) is of $O(1)$ and the balance of the equation to $O(1)$ gives

$$\beta_1 \theta_{i,1} + \frac{\beta_1}{1-t^*} \frac{\xi}{2} \frac{\partial \theta_{i,1}}{\partial \xi} - \frac{\eta}{2} \frac{\partial \theta_{i,0}}{\partial \eta} = \frac{\alpha_i}{\alpha_1} \frac{\partial^2 \theta_{i,0}}{\partial \eta^2} \quad (i = 1, 2) \quad (2-53)$$

which requires $\beta_1 = 1 - t^*$ (the continuation of the same procedure would yield $\beta_2 = (1 - t^*)^2$). Then Eq. (2-53) becomes

$$-\theta_{i,1} + \frac{\xi}{2} \frac{\partial \theta_{i,1}}{\partial \xi} = \frac{\eta}{2} \frac{\partial \theta_{i,0}}{\partial \eta} + \frac{\alpha_i}{\alpha_1} \frac{\partial^2 \theta_{i,0}}{\partial \eta^2} \quad (i = 1, 2) \quad (2-54)$$

Based on Eq. (2-51) the above can be further simplified to

$$-\theta_{i,1} + \frac{\xi}{2} \frac{\partial \theta_{i,1}}{\partial \xi} = 0 \quad (i = 1, 2) \quad (2-55)$$

so that

$$\theta_{i,1} = \xi^2 f_i(\eta) \quad (i = 1, 2) \quad (2-56)$$

With the numerical solutions to Eq. (2-43) and the expansion (2-48), $f_i(\eta)$ can be numerically estimated from

$$f_i(\eta) \sim [\theta_i(t^*, \xi, \eta) - \theta_{i,0}(\xi, \eta)] / [(1 - t^*) \xi^2] \quad (2-57)$$

Figure 2-7 shows $f_i(\eta)$ for $\alpha' = k' = 1$ at $t^* = 0.99$ with $\xi = 0.2, 0.4, 0.6$ and 0.8 . The numerical results collapse very well into a single curve. Furthermore, the data can be fit almost exactly using

$$f_i(\eta) \approx \frac{1}{4\sqrt{\pi}} \eta \exp\left(-\frac{\eta^2}{4}\right) \quad (2-58)$$

so that the second term in Eq. (2-48) can be approximated as

$$\theta_{i,1}(\xi, \eta) \approx \frac{\xi^2}{4\sqrt{\pi}} \eta \exp\left(-\frac{\eta^2}{4}\right) \text{ for } \alpha' = k' = 1 \quad (2-59)$$

Thus the large-time behavior of the heat flux integral for $\alpha' = k' = 1$ can be approximated as

$$q_w^*(t^* \rightarrow 1) = \int_0^1 \frac{\partial \theta_1}{\partial \eta} \Big|_{\eta=0} \xi d\xi \sim \frac{-t^* + 5}{16\sqrt{\pi}} \quad (2-60)$$

Figure 2-8 compares the computationally obtained $q_w^*(t^*)$ with the perturbation solutions given by Eqs. (2-47) and (2-60) for particles of the same material at $Fo = 0$. Excellent agreement in the limits can be observed.

To compute the heat flow rate, the heat flux integral is multiplied by the time-varying term $A^* / \sqrt{t^*}$ as shown in Eq. (2-31c). Fig. 2-9 shows the variation of the multiplier of $A^* / \sqrt{t^*}$ and Fig. 2-10 shows the heat flow rate $\dot{Q}^*(t^*)$ during the entire collision period for particles of the same material at $Fo = 0$. The rapid rise of $\dot{Q}^*(t^*)$ during the initial contact is associated with the thin thermal diffusion layer on the order of $(t^*)^{-1/2}$ and the contact area on the order of t^* as indicated by Eq. (2-12). For comparison, the result of $\dot{Q}^*(t^*)$ obtained from the self-similar solution is also included in Fig. 2-10.

Integrating $\dot{Q}^*(t^*)$ over the entire collisional period gives the energy transfer at $Fo \rightarrow 0$

$$e_0 = \frac{C_0(T_{01} - T_{02})A_c t_c^{1/2}}{(\rho_1 c_1 k_1)^{-1/2} + (\rho_2 c_2 k_2)^{-1/2}} \quad (2-61)$$

where the subscript "0" for e_0 indicates that this is the energy transfer for the zero-Fourier number case. For particles of the same material, which will be used to normalize the energy transfer under general conditions, extensive computation with high grid

resolution yields $C_0 = 0.87093$. This is in exact agreement with the earlier result of $C_0 = 0.87$ given by Sun and Chen (1988) based on their asymptotic analysis for $Fo = 0$.

2.3.4 Numerical Results for Finite Fo

To understand the effect of the characteristic Fourier number on the heat conduction, the dimensionless heat flux integral $q_w^*(t^*)$ in the contact area is examined using the full numerical solution to Eq. (2-20). Figure 2-11 shows the variations of q_w^* with time at different Fo values. When $Fo \leq 0.1$, the transient heat flux integral is close to that of $Fo = 0$. However, for $Fo \geq 1.0$, a rapid rise in the heat flux integral is observed at the late stage, and its peak value occurs at the end of the collision when the diffusion in the r -direction becomes dominant. Thus the heat flux $q^*(t^*, \xi)$ throughout the contact area as well as the temperature variations along the ξ -axis ($\eta = 0$) at various times are examined. Figs 2-12 and 2-13 show $q^*(t^*, \xi)$ and $\theta(t^*, \xi > 1)$, respectively at $Fo = 1$. As shown in Fig. 2-12, as t^* increases the overall heat flux $q^*(t^*, \xi)$ increases. Towards the end of the collision, $q^*(t^*, \xi)$ increase more rapidly in the central region of the contact. In the meantime, the strength of the singularity at $\xi = 1$ becomes weaker as the distribution along ξ becomes less steep as $t^* \rightarrow 1$. In Fig. 2-13 for $\theta(1 < \xi < 30)$ at different times, the strength of the singularity continues to decrease as $\theta(\xi)$ spreads out further which is

caused by the increasing diffusion in the ξ -direction, $Fo \frac{t^* - 1}{A} \frac{\partial}{\partial \xi} (\xi \frac{\partial \theta_1}{\partial \xi})$, and the

increasing advection from the cold contact region, $-R^* \frac{\xi}{2} \frac{\partial \theta_i}{\partial \xi}$, as discussed at the end of

Section 2.3.2. In fact, Fig. 2-13 is a large scale view of Fig. 2-6; together they show that the large scale temperature distribution in Fig. 2-13 is actually a consequence of the

local singular temperature distribution near $\xi = 1$. As $t^* \rightarrow 1$, $t^* / A^* \rightarrow \infty$ so that the diffusion of the heat flow in the presence of the singularity in the ξ -direction becomes extremely effective; this causes a rapid rise of $q^*(t^*, \xi)$ as $t^* \rightarrow 1$ in the central portion of the contact area as shown in Fig. 2-12.

In order to develop a general expression for the heat transfer during the collision, the thermal fields for a large range of Fourier numbers are computed and the heat transferred, e , is normalized by e_0 in Eq. (2-61) as

$$C \equiv e/e_0 = \text{func}(Fo, \alpha', k') \quad (2-62)$$

Asymptotic analysis of the results for $\alpha' = k' = 1$ indicates that there are two limits for the correction factor C as a function of Fo :

$$C(Fo, \alpha' = 1, k' = 1) = 1 + 1.07646Fo, \text{ when } Fo \ll 1 \quad (2-63a)$$

$$C(Fo, \alpha' = 1, k' = 1) = 0.605039 + 1.08748Fo^{1/2}, \text{ when } Fo \gg 1 \quad (2-63b)$$

Combining the above, the following formula for C is obtained

$$\begin{aligned} C(Fo, \alpha' = 1, k' = 1) &\equiv g(Fo) \\ &\approx 0.605039 + [0.155994 + (1.182618 - 0.332298e^{-2Fo})Fo]^{1/2} \end{aligned} \quad (2-64)$$

Figure 2-14 compares the computed $e/e_0 = g(Fo)$ versus the approximation given by Eq. (2-64). Excellent agreement is observed. The computational results obtained by Sun and Chen (1988) and Zhou et al. (2008) are also included in Fig. 2-14. The result of Sun and Chen (1988) is very close to the present work for $Fo \leq 10$, which indicates that the finite difference solutions by Sun and Chen (1988) are highly accurate despite the low resolution used in their work. At high Fourier numbers, the heat exchange based on a finite element method by Zhou et al. (2008) is much smaller than the present result and that in Sun and Chen's (1988) work.

2.3.5 Particles of Different Materials

When particles of different materials collide, besides the Fourier number, the heat transfer will be affected by two additional dimensionless parameters—the thermal diffusivity ratio α' and the thermal conductivity ratio k' as observed in Eqs. (2-20b) and (2-24a), respectively. The asymptotic limit for e_0 given by Eq. (2-61) will still be used to normalize e under general conditions.

It is first noted that when two particles have the same value of thermal diffusivity ($\alpha' = 1$), the governing equations for the two particles are identical:

$$t^* \frac{\partial \theta_i}{\partial t^*} - R^* \frac{\xi}{2} \frac{\partial \theta_i}{\partial \xi} - \frac{\eta}{2} \frac{\partial \theta_i}{\partial \eta} = \frac{\partial^2 \theta_i}{\partial \eta^2} + Fo \frac{t^*}{A^*} \frac{1}{\xi} \frac{\partial}{\partial \xi} \left(\xi \frac{\partial \theta_i}{\partial \xi} \right) \quad (i = 1, 2) \quad (2-65)$$

when $\alpha' = 1$, it is convenient to introduce a conductivity-weighted average temperature $\omega(t^*, \xi, \eta)$ that satisfies Eq. (2-65)

$$\omega(t^*, \xi, \eta) = (k_1 \theta_1 + k_2 \theta_2) / (k_1 + k_2) \quad (2-66)$$

The relevant boundary conditions at $\eta = 0$ and $\eta \rightarrow \infty$, are

$$\frac{\partial \omega}{\partial \eta} \Big|_{\eta=0} = 0 \quad (2-67)$$

$$\omega(t^*, \xi, \eta \rightarrow \infty) = k_1 / (k_1 + k_2) \quad (2-68)$$

At $t^* = 0$, the initial condition is

$$\omega(0, \xi, \eta) = k_1 / (k_1 + k_2) \quad (2-69)$$

Thus by inspection, the solution to ω must be

$$\omega(t^*, \xi, \eta) = k_1 / (k_1 + k_2) \quad (2-70)$$

That is

$$k_1 \theta_1(t^*, \xi, \eta) + k_2 \theta_2(t^*, \xi, \eta) = k_1 \quad (2-71)$$

Combing Eq. (2-71) with $\theta_1(t^*, \xi, 0) = \theta_2(t^*, \xi, 0)$ in the contact area, it is revealed that

$$\theta_1(\dot{t}, \xi, 0) = \theta_2(\dot{t}, \xi, 0) = k_1/(k_1+k_2) \quad (2-72)$$

Equation (2-72) shows that at $\alpha' = 1$ the temperature in the contact area is constant when the conductivity ratio $k' = k_2 / k_1$ is fixed; a similar phenomenon was also presented by Heasley (1965), where they derived that the steady temperature at the edge of the contact spot is constant. Here we have obtained in Eq. (2-72) a more general conclusion that the temperature throughout the contact area at anytime is constant, which was also numerically verified for all Fo and k' cases in our study.

Furthermore, the temperature difference between $\eta = 0$ and $\eta \rightarrow \infty$ for particle 1 is $k_2/(k_1+k_2)$, which drives the wall heat flux at $\eta = 0$. Thus the heat flux integral $q_w^*(\dot{t}^*)$ and the heat transfer follows

$$q_w^*(\dot{t}^*) \propto k_1 k_2 / (k_1 + k_2) \quad (2-73)$$

$$e_0 \propto k_1 k_2 / (k_1 + k_2), \text{ and } e \propto k_1 k_2 / (k_1 + k_2) \quad (2-74)$$

Hence $C = e/e_0$ is independent of k' when $\alpha' = 1$ and Eq. (2-64) is also valid for arbitrary values of k' when $\alpha' = 1$. This fact is directly verified in the present computational study for the entire range of Fourier numbers (from 0 to 50) and this observation is critical to deduce the form postulated in Eq. (2-77) later on for $\alpha' > 1$. It is noticed that this fact was not represented in the “closed-form” formula provided by Zhou et al. (2008), which is only applicable to the special case of $k' = 1$.

For $\alpha' \neq 1$, it is convenient to introduce a relative correction factor λ based on the results from $\alpha' = k' = 1$ as

$$\lambda(Fo, \alpha', k') \equiv C(Fo, \alpha', k') / C(Fo, 1, 1) = C(Fo, \alpha', k') / g(Fo) \quad (2-75)$$

where $g(Fo)$ is given by Eq. (2-64). An accurate approximation for λ allows one to obtain $C = e/e_0$ from Eq. (2-75).

For $\alpha' > 1$, in the limit of very large Fo , the computational results show that λ has the following asymptotic behavior

$$\lambda(\infty, \alpha', k') = C(\infty, \alpha', k') / C(\infty, 1, 1) \sim k' / (1 + k') + \sqrt{\alpha'} / (1 + k') \quad (2-76)$$

It should be noticed that the $Fo \rightarrow \infty$ indicated in Eq. (2-76) is bounded by the upper limit as restricted by the semi-infinite media assumption (see Appendix A). In our simulations, the asymptotic behavior of Eq. (2-76) is obtained at $Fo = 50$.

For finite Fo , the relative correction factor λ can be approximated as

$$\lambda = f(Fo, \alpha', k') = 1 + \frac{\beta(\sqrt{\alpha'} - 1)}{1 + k'} + \gamma \frac{4k'}{(1 + k')^2} \quad (\alpha' > 1) \quad (2-77)$$

with

$$\beta = \frac{0.95Fo}{0.95Fo + 0.50Fo^{1/2} + 0.12} \quad (2-78)$$

$$\gamma = [1 - e^{-10(\log \alpha')^2}] \frac{0.0777}{0.7666Fo^{-1/3} + Fo^{1/2}} \quad (2-79)$$

Since switching the definition of the subscripts of the particles does not affect the amount of heat transfer, there exists a symmetric relation for $\alpha' < 1$

$$C(Fo, \alpha', k') = C(\alpha'Fo, 1/\alpha', 1/k') \quad (2-80)$$

Thus the correction factor for $\alpha' < 1$ can be simply written as

$$C(Fo, \alpha' < 1, k') = f(\alpha'Fo, 1/\alpha', 1/k')g(\alpha'Fo) \quad (2-81)$$

where f is given by Eq. (2-77).

Figure 2-15 shows the correction factor C from the finite difference method and the above approximate expressions for k' and α' ranging from 0.1 to 10.0. Good

agreement suggests that the approximate formula developed in this study based on numerical computations and asymptotic analyses is accurate. It can be used as a practical tool to predict the heat transfer between two colliding particles or between particles and surfaces.

2.4 Summary and Conclusions

Heat conduction between two colliding particles of various materials is computationally and analytically investigated over a large range of Fourier numbers with high-quality resolution. The singular nature of the thermal field and heat flux at the edge of the contact area is elucidated through analytical solutions. A self-similar solution for the thermal field during the initial period of contact is developed. It serves as an accurate initial condition for the heat transfer simulation during the entire collisional period. A two-dimensional asymptotic analysis is presented for the thermal field and heat flux in the contact area in the small Fourier number limit to facilitate the understanding of collisional heat transfer. A closed-form expression is developed for the heat transfer prediction as a function of the Fourier number, the thermal diffusivity ratio and the thermal conductivity ratio of the impacting particles.

Table 2-1. Heat flux integral $q_w^*(t^*)$ based on the self-similar solution at small time
 ($t^* \ll 1$)

	320×128	640×256	1280×512
$Fo = 0.1$	0.300430	0.300085	0.299867
$Fo = 1.0$	0.396332	0.396192	0.395993
$Fo = 10.0$	0.772609	0.775793	0.777692

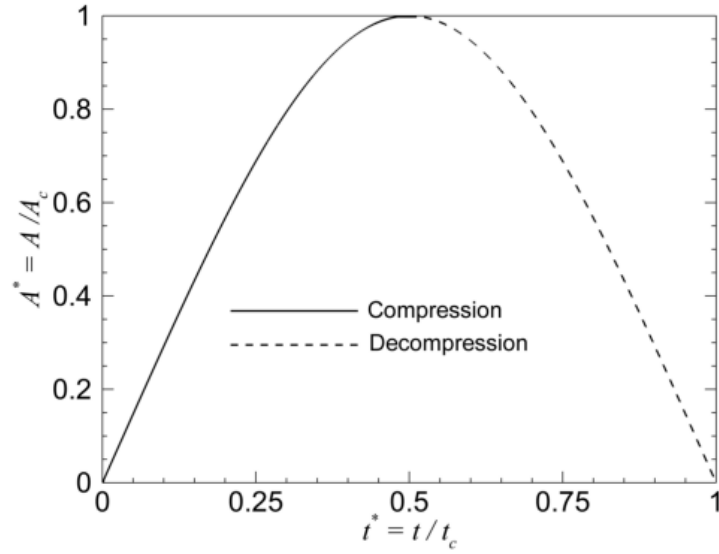


Figure 2-1. Variation of the contact area during collision.

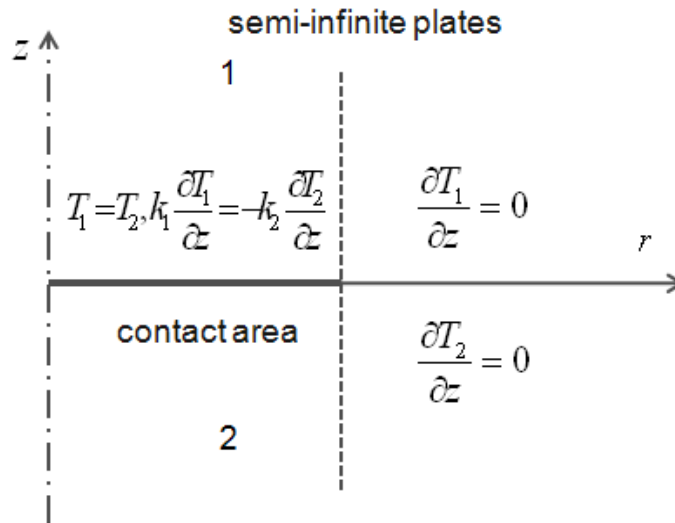


Figure 2-2. Computational domain and boundary conditions at $z = 0$.

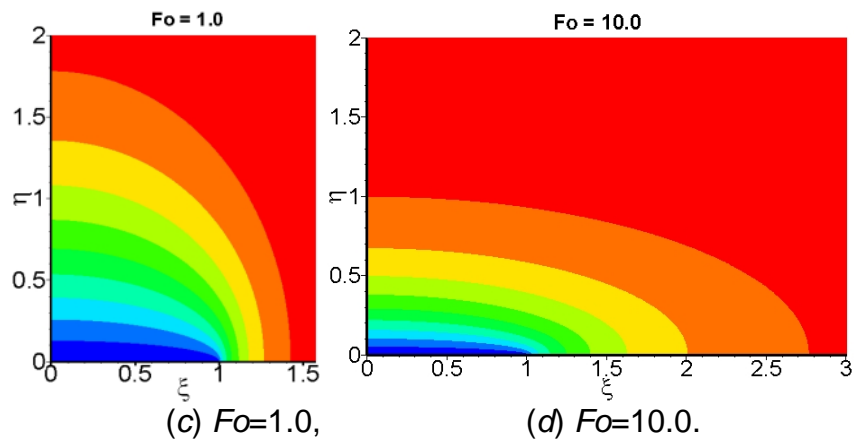
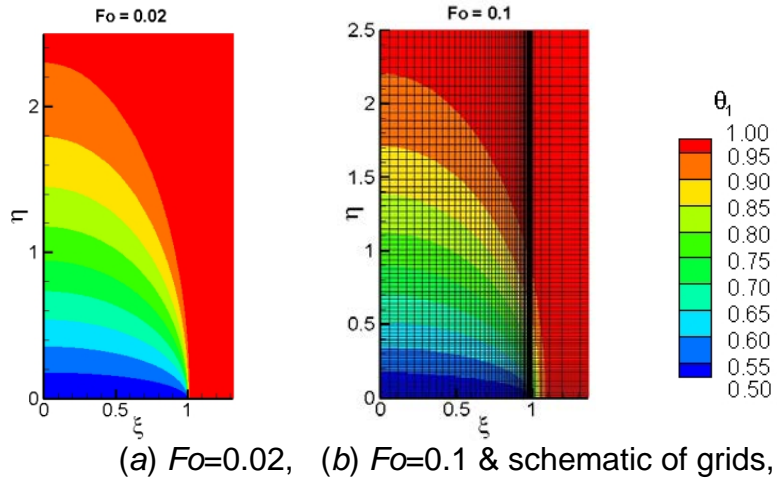


Figure 2-3. Temperature contours on the surface of particle 1 based on the self-similar solutions at small time ($t^* \ll 1$) at (a) $Fo=0.02$, (b) $Fo=0.1$, (c) $Fo=1.0$ and (d) $Fo=10.0$.

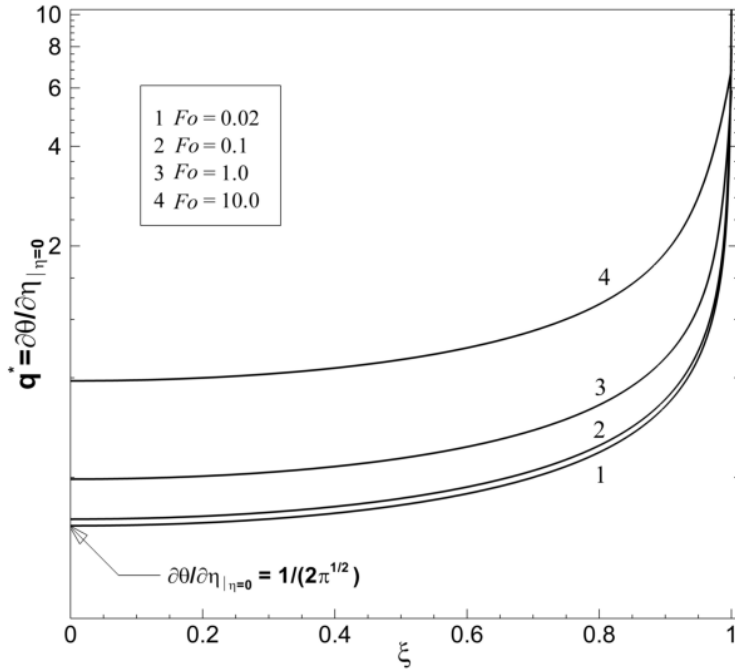
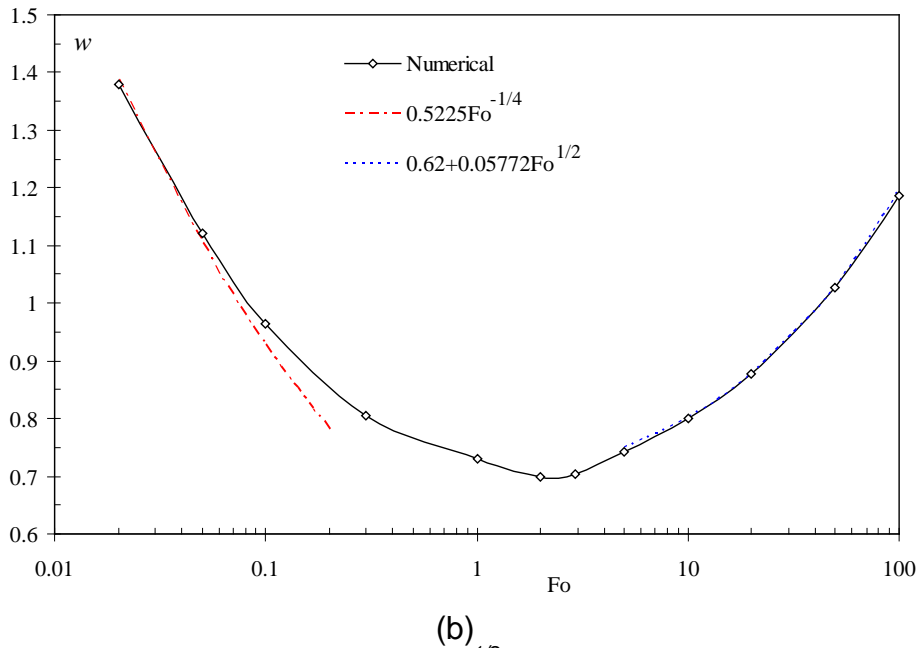
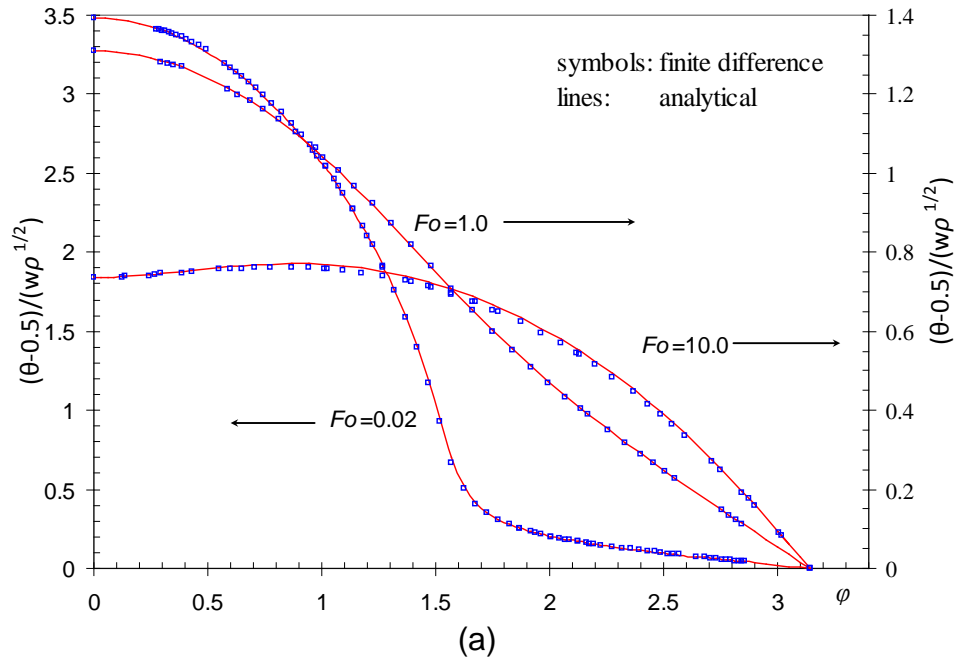


Figure 2-4. Dimensionless heat flux across the contact area at small time ($t^* \ll 1$) based on self-similar solutions.



(b)
 Figure 2-5. (a) Local solution of $(\theta - 0.5)/(w\rho^{1/2})$ around the singularity point at $(\xi, \eta) = (1, 0)$. (b) The value of w in the local solution of θ around the singularity point at $(\xi, \eta) = (1, 0)$.

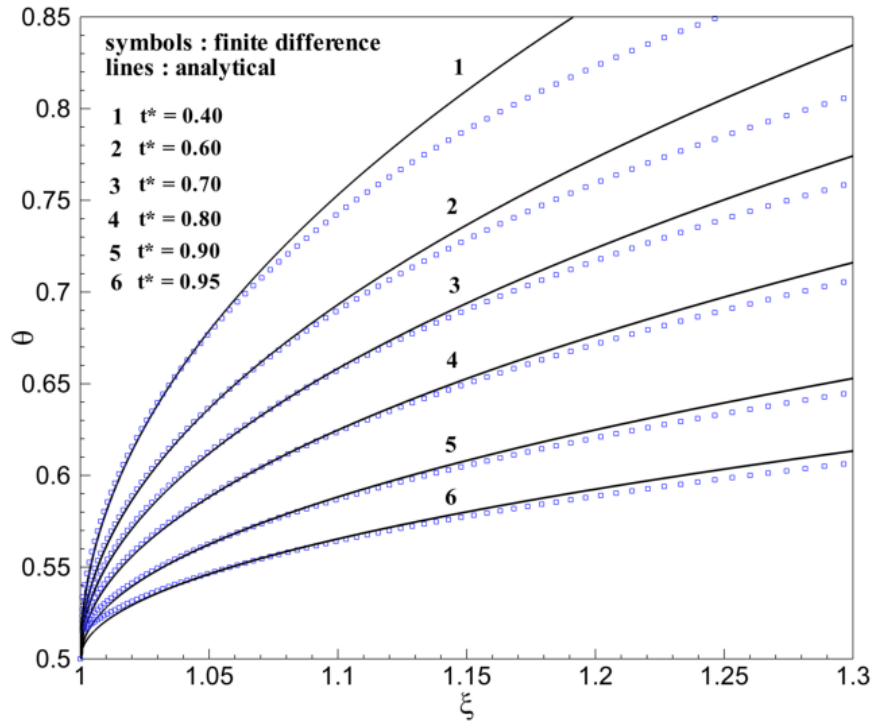


Figure 2-6. Local transient temperature profiles at ($\xi > 1, \eta = 0$) when $Fo = 1.0$.

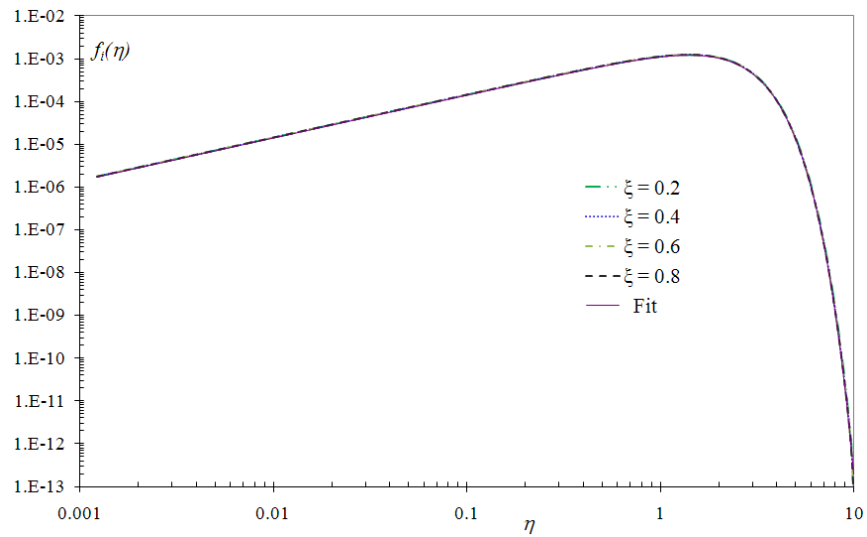


Figure 2-7. Comparison of numerical results and analytical fit for $f_i(\eta)$ in Eq. (2-58).

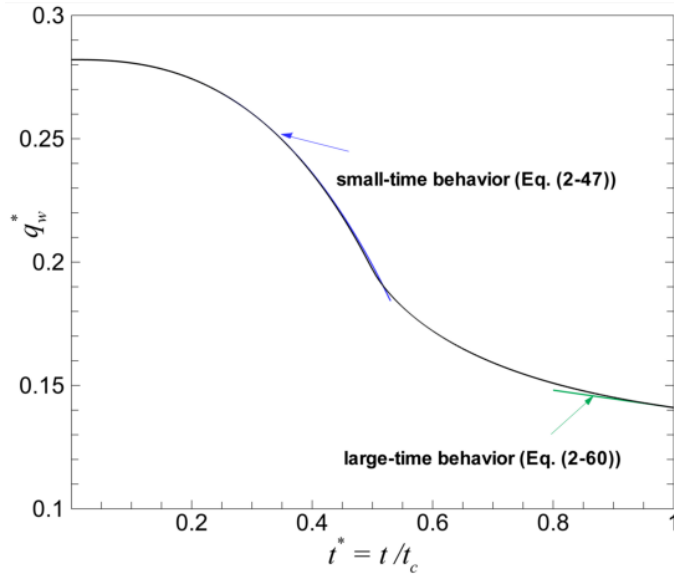


Figure 2-8. Variation of the dimensionless heat flux integral $q_w^*(t^*)$ over the contact area at $Fo = 0$.

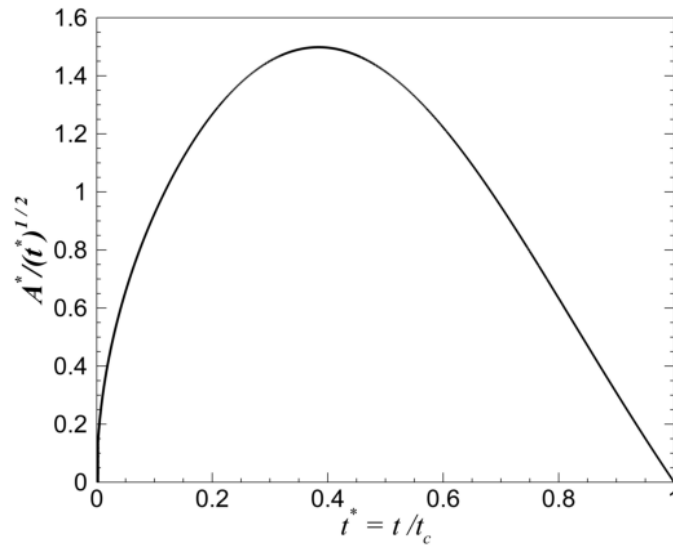


Figure 2-9. Variation of the multiplier $A^* / \sqrt{t^*}$ in Eqs. (2-30b) and (2-31c).

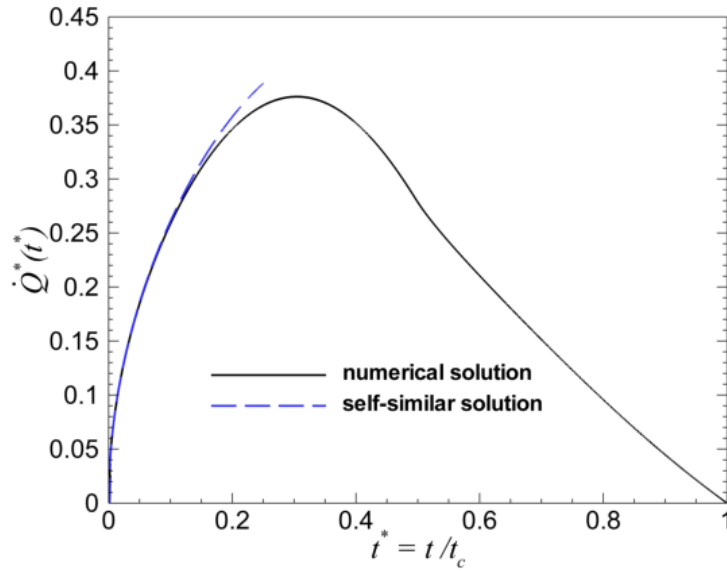


Figure 2-10. Variations of the dimensionless heat flow rate $Q^*(t^*)$ at $Fo = 0$; the self-similar solution is $Q^*(t^*) = 0.2820948 A^* / \sqrt{t^*}$.

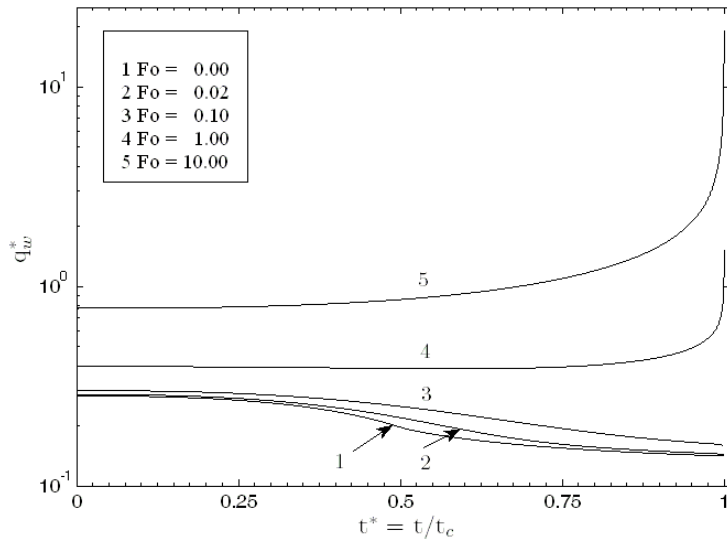


Figure 2-11. Comparison of the dimensionless heat flux integral $q_w^*(t^*)$ at different Fourier numbers.

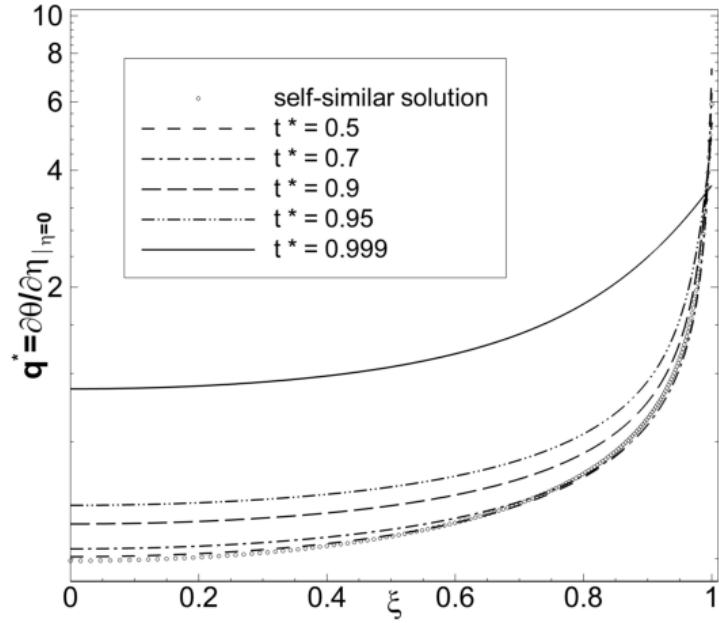


Figure 2-12. Heat flux $q^*(t^*, \xi)$ in the contact area at various times for $Fo = 1.0$.

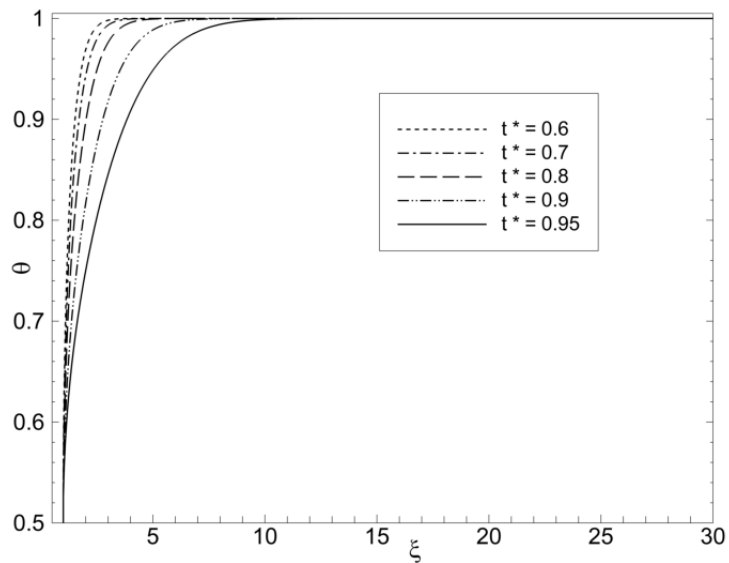


Figure 2-13. Temperature variations along ξ -direction ($\eta = 0$) at various times for $Fo = 1.0$.

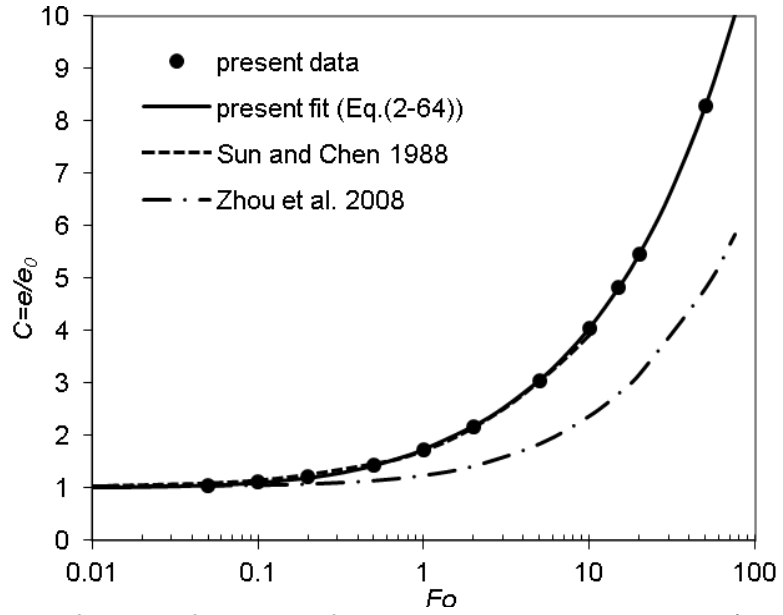


Figure 2-14. Heat transfer as a function of the impact Fourier number (particles of the same material).

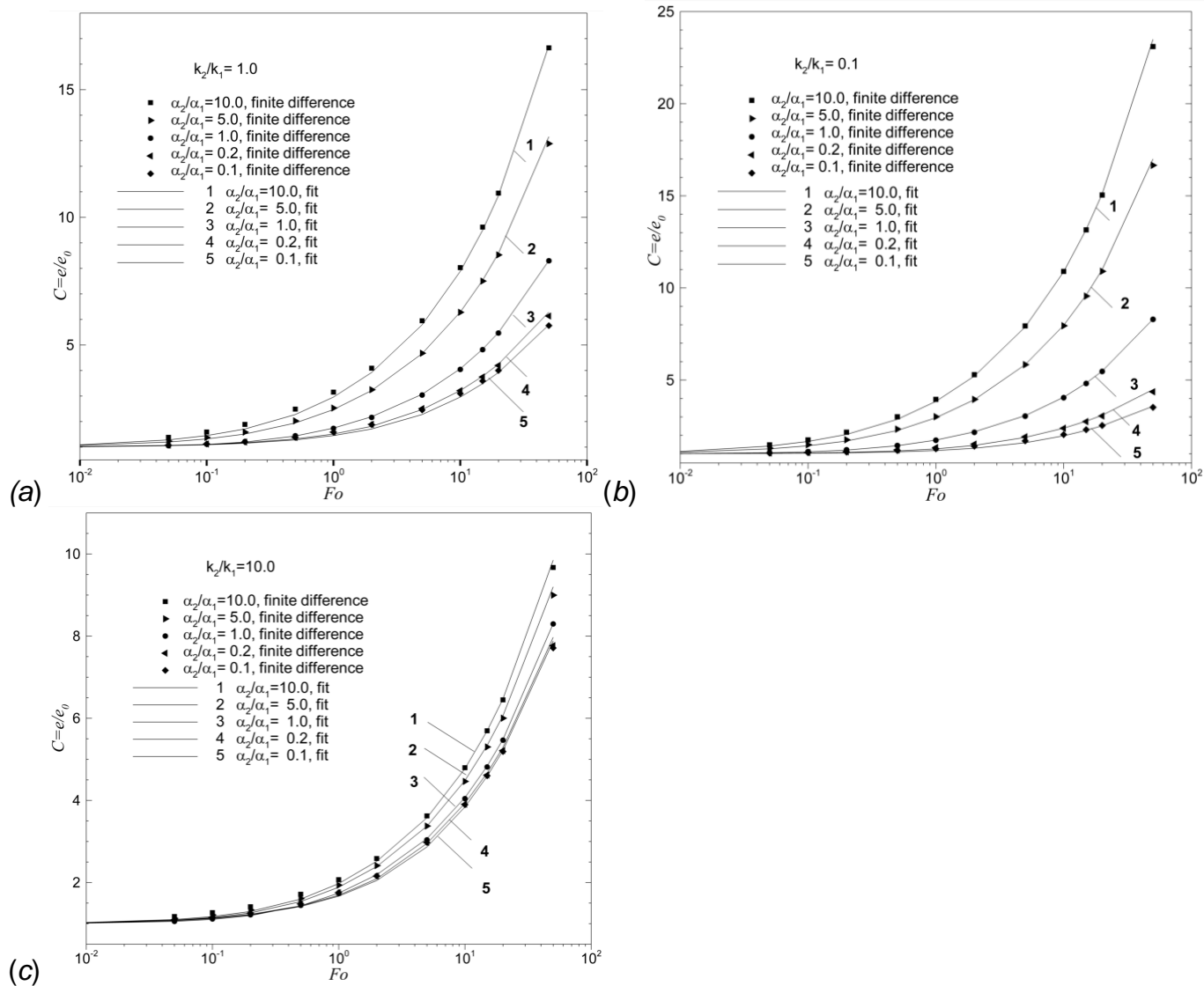


Figure 2-15. Correction factor comparison between computation and the approximate expression at (a) $k_2/k_1=1.0$, (b) $k_2/k_1=0.1$ and (c) $k_2/k_1=10.0$.

CHAPTER 3 BOUNDARY CONDITIONS FOR THERMAL LATTICE BOLTZMANN EQUATION METHOD*

3.1 Literature Review of Thermal Lattice Boltzmann Equation (TLBE) Models

The LBE method simulates the particle interactions on a discrete phase space with a specific set of discrete velocities, and the particle dynamics is represented by the particle distribution functions (also called particle density distribution function or particle velocity distribution function). The velocity distribution functions of the particles are governed by the lattice Boltzmann equation, from which the macroscopic Navier-Stokes equations can be recovered. Particle collision in the LBE method is approximated by a relaxation process toward the equilibrium state of the particle distributions. There are basically two collision models for the LBE methods: the first and most commonly used single-relaxation-time (SRT), or the Bhatnagar-Gross-Krook (BGK) model (Qian et al. 1992, Chen et al. 1992) based on the work of Bhatnagar et al. (1954); and the multiple-relaxation-time (MRT), also known as the moment model (d'Humières 1992, Lallemand and Luo 2000, d'Humières et al. 2002). The MRT-LBE model overcomes some obvious defects of the BGK model such as fixed Prandtl number and fixed ratio between the kinematic and bulk viscosities (d'Humières et al. 2002) and shows better numerical stability (Lallemand and Luo 2000) and reduced numerical dispersion (Yu et al. 2003).

Because of the advantages of the LBE method, there have been continuous interest and effort in developing thermal LBE (TLBE) models for thermal transport problems (Alexander et al. 1993, Chen et al. 1994, Shan 1997, He et al. 1998, Lallemand and Luo 2003, Guo et al. 2007, Shi and Guo 2009, Mezrhad et al. 2010, Yoshida and Nagaoka 2010). In general, the TLBE models fall into four categories: the

* This work has been published in *Journal of Computational Physics* (Li et al. 2013a)

passive scalar approach, the multispeed approach, the hybrid approach, and the double-population distribution function (DDF) approach.

In the passive-scalar-based TLBE model, the macroscopic temperature is considered as a passive scalar that is advected by the velocity field and satisfies the convection-diffusion equation (Shan 1997). The main shortcoming of this model is that the temperature field is driven by the flow velocity, while the temperature does not affect the flow field. The multispeed approach is a direct extension of the athermal LBE model so that only the velocity distribution function is used. In order to obtain the macroscopic temperature, additional discrete speeds and higher-order velocity expansion for the Maxwell-Boltzmann equilibrium distribution are required in this model (Chen et al. 1994). In the hybrid approach, the mass and momentum conservation equations are solved with the athermal LBE model, whereas the advection-diffusion equation for the temperature is solved separately by using the finite-difference method or other conventional numerical techniques (Lallemand and Luo 2003). The DDF approach utilizes two different distribution functions, one for the velocity field and the other one for the temperature or energy distribution. With this approach, the interaction between the flow fields (density and velocity) and the temperature field can be properly accounted for. Based on the methods of defining the temperature distribution functions, the DDF approach can be further classified into two groups. The first derives the temperature distribution function from the continuous Boltzmann equation as that in the athermal LBE model. Thus these two sets of distribution functions are explicitly coupled in the thermal LBE. For example, He et al. (1998) used an internal-energy-based distribution function and Guo et al. (2007) used a total-energy-based distribution function to

simulate the thermal flows. In the other group for the DDF approach, however, the temperature distribution function is defined with the objective of recovering the macroscopic convection-diffusion equation (CDE), in which the other terms of the energy equation such as pressure work and heat dissipation are conveniently treated as source terms. With this approach the macroscopic velocities, rather than the velocity distribution functions, are included in the evolution equation of the temperature distribution functions. Thus no explicit coupling between the velocity- and temperature-distribution functions is needed. To this end, Shi and Guo (2009) proposed a thermal LBE model for nonlinear CDE simulations, in which the equilibria of the temperature distribution functions are defined to recover the correct CDE. Recognizing the advantages of the MRT model over the BGK model, Mezrhab et al. (2010) and Yoshida and Nagaoka (2010) proposed their MRT-TLBE models for the CDE. To recover the CDE, the equilibria of the thermal moments are specified in Mezrhab et al.'s model while the thermal equilibrium distribution functions are specified in Yoshida and Nagaoka's model. A detailed derivation of the macroscopic CDE from the MRT-TLBE model can be found in Yoshida and Nagaoka's work (2010). The present work also uses the MRT-LBE model by Yoshida and Nagaoka.

3.2 Literature Review of Boundary Conditions in TLBE Simulations

Accurate boundary condition treatment is essential for the overall integrity of the LBE simulations. For the fluid velocity field, the "bounce-back" scheme has been intensively studied (Ziegler 1993, Noble et al. 1995, Ginzbourg and d'Humières 1996, Chen et al. 1996, He et al. 1997, Zou and He 1997, Ginzburg and d'Humières 2003) and extended to handle curved boundaries (Filippova and Hänel 1998, Mei et al. 1999, Mei et al. 2000, Bouzidi et al. 2001, Guo et al. 2002). The standard bounce-back

method is second-order accurate for no-slip wall boundaries when the distance from the wall to the nearest fluid node is half of the lattice unit spacing. For other hydrodynamic boundary conditions such as given density, pressure, slipping velocity or their derivatives, the bounce-back scheme can be modified with the flow properties at on the boundary included in the treatments (Ginzbourg and d'Humières 1996, Chen et al. 1996, He et al. 1997, Zou and He 1997, Filippova and Hänel 1998, Mei et al. 1999, Mei et al. 2000, Bouzidi et al. 2001, Guo et al. 2002, Ginzburg and d'Humières 2003). Spatial interpolation or extrapolation has also been incorporated to improve the degraded accuracy of the bounce-back scheme when the boundary is located in arbitrary position in the lattice cell (Chen et al. 1996, Filippova and Hänel 1998, Mei et al. 1999, Mei et al. 2000, Bouzidi et al. 2001, Guo et al. 2002).

With appropriate modifications, some of the athermal boundary condition treatments have been extended to TLBE simulations as well. He et al. (1998) extended the bounce-back rule of the non-equilibrium distributions proposed by Zou and He (1997) to impose thermal boundary conditions. This non-equilibrium extrapolation approach was also applied by Tang et al. (2005), Huang et al. (2006) and Jeong et al. (2010). Liu et al. (2010), however, used correction functions for the unknown energy distributions based on local known energy distributions, which is an extension of their hydrodynamic boundary condition treatment (Ho et al. 2009). It is noticed that those thermal boundary condition treatments in Refs. (Tang et al. 2005, Huang et al. 2006, Jeong et al. 2010, Liu et al. 2010) were directly proposed for Dirichlet boundary condition and the Neumann (flux) condition was transformed into Dirichlet condition by various finite-difference schemes. This transformation will become inconvenient when

mixed thermal boundary conditions are encountered. As a consequence, the requirement of a direct boundary condition treatment for the Neumann condition becomes natural. D’Orazio et al. (2003) used a “counter-slip” approach to handle thermal boundary conditions, where a counter-slip thermal energy density is introduced to represent the given temperature or heat flux condition on the boundary. Kuo and Chen (2009) proposed a non-equilibrium “mirror-reflection” scheme to implement both the isothermal and adiabatic thermal boundary conditions. Ginzburg (2005) extended the “multi-reflection” approach (Ginzburg and d’Humières 2003) to model both Dirichlet and Neumann boundary conditions. The recent 2-D MRT-TLBE model (Mezrhab et al. 2010) implemented the bounce-back scheme to handle Dirichlet boundary conditions where they provided an explicit formula to determine the unknown populations based on the distributions at the neighboring fluid nodes and the temperature on the boundary. And a simple “mirroring” treatment was used for the adiabatic condition. In the MRT-TLBE model by Yoshida and Nagaoka (2010) for both 2-D and 3-D cases, boundary condition treatments for both the Dirichlet and the Neumann conditions were provided for the “halfway” case where the physical boundary is placed in the center of the lattice cell.

Although thermal boundary condition treatment is an important issue, the discussions about the applicability and accuracy of these treatments in curved-boundary situations in the literature are rather limited. Huang et al. (2006) extended the non-equilibrium approach to deal with curved boundary condition, where the equilibrium part of the unknown population is evaluated according to the Dirichlet condition and linear extrapolation is used for the non-equilibrium component; for Neumann condition, they

also transferred it into Dirichlet condition with a finite difference scheme and a simple projection rule was used to convert the normal boundary flux into the heat fluxes in the discrete velocity directions of the TLBE model. Second-order accuracy of the temperature field was observed for Dirichlet condition on the curved boundary while no examples were provided regarding their heat flux conversion and the accuracy of the transferred Neumann condition treatment in their work. For curved boundaries with Neumann conditions, Yoshida and Nagaoka (2010) realized that the “halfway” thermal bounce-back scheme leads to considerable disagreement between their simulation and analytical solutions. Thus they presented a modified treatment with the intersection area accounted to alleviate the discrepancy. Noticeable improvement was achieved in their numerical example but the accuracy was not investigated in detail. In the “multi-reflection” approach for arbitrarily shaped surfaces, Ginzburg (2005) decomposed the equilibrium populations into the symmetric and anti-symmetric components. The symmetric part was tuned to build second-order and “third-order” accurate Dirichlet boundary conditions and the anti-symmetric part was used for Neumann conditions. It was also pointed out that the Neumann condition with zero tangential heat flux yielded second-order accuracy while only linear convergence was achieved when non-zero tangential heat flux exists (Ginzburg 2005). It is also noted that the heat flux in one of the discrete velocity directions is required in (Ginzburg 2005) in order to remove the tangential flux constraint and to obtain linear convergence. In principle, however, only the derivative in the normal direction is specified in Neumann problems. Ginzburg (2005) did not provide a means to evaluate the heat fluxes in the discrete lattice velocity directions based on the normal derivative on the curved boundary.

3.3 Present Boundary Condition Treatments in TLBE Method

The objectives of the present work are twofold. The first one is to develop second-order accurate boundary condition treatments for both the Dirichlet and Neumann conditions on straight boundaries that can be placed at arbitrary locations in the lattice. The second is to extend the present boundary condition treatments into curved-boundary situations and to investigate the effect of curved-geometry on the accuracy of the present boundary condition treatments.

The present boundary condition treatments are independent of the specific TLBE model and the collision operator; thus for illustration purposes, we formulate the problem using Yoshida and Nagaoka's MRT-TLBE model (Yoshida and Nagaoka 2010). For the Dirichlet condition, there is an adjustable parameter in the treatment with second-order accuracy. Three particular choices are discussed and their performances are examined. For the Neumann problem, the second-order accurate boundary condition is unique. When the present boundary treatments are extended to handle inclined or curved boundary walls, the Dirichlet condition can be directly implemented. For Neumann problems on curved boundaries the given heat flux condition in the normal direction alone cannot be used to determine the fluxes in the discrete velocity directions in the TLBE model. Only for the special case where the tangential temperature gradient does not contribute to the fluxes in the discrete directions, i.e., the tangential gradient is known to be zero or the boundary is perpendicular to one of the discrete velocity directions, can a simple formula for the distribution function be obtained with second order accuracy based on the normal derivative. For general cases the boundary heat fluxes in the discrete velocity directions must be coupled with the unknown temperature value on the boundary which can be independently evaluated on

each lattice velocity direction. An expression for the heat flux determination in the discrete velocity directions is derived from the solution of the coupled equations. The accuracy of the proposed boundary condition treatments is examined using a series of numerical tests for which analytical solutions are available. The test cases include: i) 2-D steady-state channel flow with a constant and uniform velocity and a sinusoidal wall temperature or heat flux boundary condition; ii) 1-D transient heat conduction in an inclined semi-infinite solid with a constant normal heat flux at the end; iii) 2-D steady-state heat conduction inside a circle with a sinusoidal wall temperature or heat flux boundary condition; iv) 2-D transient heat conduction inside a circle with a transient wall temperature boundary condition; and v) 3-D steady-state circular pipe flow with a constant and uniform velocity and a sinusoidal wall temperature or heat flux boundary condition. Because of the irregularity of the lattice fractions cut by the curved boundary, second-order accuracy for the temperature field is realized for Dirichlet problems, but only first-order accuracy can be obtained for Neumann problems on curved boundaries.

3.3.1 The Convection-Diffusion Equation

Following Yoshida and Nagaoka's formulation (Yoshida and Nagaoka 2010), the standard convection-diffusion equation (CDE) can be written as

$$\frac{\partial \phi}{\partial t} + \frac{\partial}{\partial x_j} (v_j \phi) = \frac{\partial}{\partial x_i} (D_{ij} \frac{\partial \phi}{\partial x_j}) + G, \quad (3-1)$$

where ϕ is a scalar variable that can be either temperature in thermal simulations or mass concentration in mass transfer problems, v_j is the velocity component in the x_j direction, D_{ij} is the diffusion coefficient, and G represents the source term.

The Dirichlet boundary condition is

$$\phi = \Phi_d, \quad (3-2)$$

and for the Neumann boundary condition involving normal derivatives, it is in general written as

$$-n_i D_{ij} \frac{\partial \phi}{\partial x_j} + n_j v_j \phi = \Phi_n, \quad (3-3)$$

where Φ_d and Φ_n are given functions of time and space on the boundary, n_i and n_j denote the i - and j -components of the unit normal vector pointing inward to the domain.

3.3.2 The D3Q7 and D2Q5 Thermal LBE models

The discrete phase space in the TLBE model is defined by a regular lattice in D dimensions together with a set of discrete velocities $\{\mathbf{e}_\alpha | \alpha = 0, 1, \dots, m\}$. Analogous to the athermal MRT-LBE model, Yoshida and Nagaoka (2010) proposed a D3Q7 thermal LBE model (Fig. 3-1) with an MRT collision operator for the CDE, in which they have carried out an asymptotic analysis based on diffusive scaling to show that the TLBE model is first- and second-order accurate in time and space, respectively. This MRT-TLBE model is also used in the present work.

The TLBE governs the set of temperature distribution functions $\{g_\alpha(\mathbf{x}, t) | \alpha = 0, 1, \dots, m\}$, from which the leading-order solution of the macroscopic temperature is

obtained with $\phi = \sum_{\alpha=0}^m g_\alpha$. In the D3Q7 TLBE model, the discrete velocity set is defined

as

$$\mathbf{e}_\alpha = \begin{cases} (0,0,0), & (\alpha = 0), \\ (\pm 1,0,0), (0,\pm 1,0), (0,0,\pm 1), & (\alpha = 1,2,3,4,5,6), \end{cases} \quad (3-4)$$

The evolution of the TLBE can be written as

$$g_\alpha(\mathbf{x} + \mathbf{e}_\alpha \delta t, t + \delta t) - g_\alpha(\mathbf{x}, t) = L g_\alpha(\mathbf{x}, t) + \omega_\alpha G \delta t, \quad (3-5)$$

where δt is the time step, ω_α is the weight coefficient defined to satisfy the CDE in Eq. (3-1), and L is the collision operator.

In the SRT-BGK model, the collision operator is represented by

$$Lg_\alpha(\mathbf{x}, t) = -\frac{1}{\tau} (g_\alpha(\mathbf{x}, t) - g_\alpha^{\text{eq}}(\mathbf{x}, t)), \quad (3-6)$$

where τ is a coefficient that represents the relaxation time relative to the time step. In the BGK thermal model by Yoshida and Nagaoka (2010), the following equilibrium distribution functions are proposed to recover the CDE:

$$g_\alpha^{\text{eq}} = (\omega_\alpha + \frac{\delta t v_j}{\delta x \varepsilon} e_{\alpha j} \omega_\alpha) \phi, \quad (3-7)$$

where δx is the grid spacing in the lattice. The weight coefficients are set to be

$$\omega_\alpha = \begin{cases} 1/4, & (\alpha = 0), \\ 1/8, & (\alpha = 1, 2, 3, 4, 5, 6), \end{cases} \quad (3-8)$$

and the constant $\varepsilon = 1/4$ for the 3-D model.

In the MRT model (Yoshida and Nagaoka 2010), the collision operator is given by

$$L\mathbf{g}(\mathbf{x}, t) = M^{-1}SMQ\mathbf{g}(\mathbf{x}, t). \quad (3-9)$$

Thus the evolution of the TLBE becomes

$$g_\alpha(\mathbf{x} + \mathbf{e}_\alpha \delta t, t + \delta t) - g_\alpha(\mathbf{x}, t) = [M^{-1}SMQ\mathbf{g}(\mathbf{x}, t)]_\alpha + \omega_\alpha G \delta t, \quad (3-10)$$

and the matrix Q is explicitly given as below based on Eq. (3-7)

$$Q = [(\omega_0, \omega_1, \dots, \omega_6)^T + \frac{\delta t v_j}{\delta x \varepsilon} (e_{0j} \omega_0, e_{1j} \omega_1, \dots, e_{6j} \omega_6)^T] (1, 1, 1, 1, 1, 1, 1) - I_{7 \times 7}, \quad (3-11)$$

with $I_{7 \times 7}$ being the 7×7 identity matrix. The transformation matrix M for the D3Q7 TLBE model was given as (Yoshida and Nagaoka 2010)

$$M = \begin{bmatrix} 1 & 1 & 1 & 1 & 1 & 1 & 1 \\ 0 & 1 & -1 & 0 & 0 & 0 & 0 \\ 0 & 0 & 0 & 1 & -1 & 0 & 0 \\ 0 & 0 & 0 & 0 & 0 & 1 & -1 \\ 6 & -1 & -1 & -1 & -1 & -1 & -1 \\ 0 & 2 & 2 & -1 & -1 & -1 & -1 \\ 0 & 0 & 0 & 1 & 1 & -1 & -1 \end{bmatrix}, \quad (3-12)$$

and the relaxation matrix S is

$$S^{-1} = \begin{bmatrix} \tau_0 & 0 & 0 & 0 & 0 & 0 & 0 \\ 0 & \tau_{xx} & \tau_{xy} & \tau_{xz} & 0 & 0 & 0 \\ 0 & \tau_{xy} & \tau_{yy} & \tau_{yz} & 0 & 0 & 0 \\ 0 & \tau_{xz} & \tau_{yz} & \tau_{zz} & 0 & 0 & 0 \\ 0 & 0 & 0 & 0 & \tau_4 & 0 & 0 \\ 0 & 0 & 0 & 0 & 0 & \tau_5 & 0 \\ 0 & 0 & 0 & 0 & 0 & 0 & \tau_6 \end{bmatrix}. \quad (3-13)$$

As pointed out by Yoshida and Nagaoka (2010), the off-diagonal components in the relaxation matrix can take non-zero values to account for anisotropic diffusion. The relaxation coefficients are related to the diffusion coefficient matrix as

$$\tau_{ij} = \frac{1}{2} \delta_{ij} + \frac{\delta t}{\varepsilon (\delta x)^2} D_{ij}, \quad (3-14)$$

in order to recover the solution of the CDE to the leading-order. In the above, δ_{ij} is the Kronecker's delta.

As in the athermal MRT-LBE model, the equilibria of the conserved “hydrodynamic” moments and the non-conserved “kinetic” moments, are explicitly defined (d’Humières et al. 2002). The equilibria of the conserved “thermal” moments and the non-conserved “kinetic” moments $\{m_\alpha^{eq} \mid \alpha = 0, 1, \dots, m\}$ in the MRT-TLBE model can also be explicitly specified, as demonstrated in the D2Q5 model (Mezrhab et

al. 2010). In the following we show that the D3Q7 TLBE model (Yoshida and Nagaoka 2010) can be equivalently formulated with the equilibrium moments explicitly defined.

The thermal LBE is rewritten as

$$g_\alpha(\mathbf{x} + \mathbf{e}_\alpha \delta t, t + \delta t) - g_\alpha(\mathbf{x}, t) = - [M^{-1}S(\mathbf{m}(\mathbf{x}, t) - \mathbf{m}^{\text{eq}}(\mathbf{x}, t))]_\alpha + \omega_\alpha G \delta t, \quad (3-15)$$

where the transformation matrix M and the relaxation matrix S are the same as that in Eqs. (3-12) and (3-13), respectively; the thermal moments $\mathbf{m}(\mathbf{x}, t)$ are related to the distribution functions $\mathbf{g}(\mathbf{x}, t)$ by

$$\mathbf{m} = M\mathbf{g}, \quad (3-16)$$

and the equilibria of the moments are defined as

$$\mathbf{m}^{\text{eq}} = (m_0^{\text{eq}}, m_1^{\text{eq}}, m_2^{\text{eq}}, m_3^{\text{eq}}, m_4^{\text{eq}}, m_5^{\text{eq}}, m_6^{\text{eq}})^T = (0, uT, vT, wT, aT, 0, 0)^T, \quad (3-17)$$

where u, v, w are the velocity components and a is a constant related to the coefficients ω_α by

$$a = (7\omega_0 - 1) = 3/4. \quad (3-18)$$

Now the conservation of the first moment results in the macroscopic temperature

$$m_0 = T = \sum_{\alpha=0}^6 g_\alpha. \quad (3-19)$$

Comparing Eq. (3-15) with Eq. (3-10), we can relate these two equivalent forms of evolution by

$$\mathbf{m}(\mathbf{x}, t) - \mathbf{m}^{\text{eq}}(\mathbf{x}, t) = -MQ\mathbf{g}(\mathbf{x}, t). \quad (3-20)$$

Similarly, keeping only the first five discrete velocity components from Fig. 3-1 for the D2Q5 TLBE model yields the following from Eq. (3-8)

$$\mathbf{e}_\alpha = \begin{cases} (0, 0), & (\alpha = 0), \\ (\pm 1, 0), (0, \pm 1), & (\alpha = 1, 2, 3, 4), \end{cases} \quad (3-21)$$

and the transformation from the distribution functions g_α to the thermal moments m_α now becomes

$$\mathbf{m} = \begin{bmatrix} m_0 \\ m_1 \\ m_2 \\ m_3 \\ m_4 \end{bmatrix} = \begin{bmatrix} 1 & 1 & 1 & 1 & 1 \\ 0 & 1 & -1 & 0 & 0 \\ 0 & 0 & 0 & 1 & -1 \\ 4 & -1 & -1 & -1 & -1 \\ 0 & 1 & 1 & -1 & -1 \end{bmatrix} \begin{bmatrix} g_0 \\ g_1 \\ g_2 \\ g_3 \\ g_4 \end{bmatrix} = \mathbf{M}\mathbf{g}. \quad (3-22)$$

The corresponding equilibria of the moments are defined as

$$\mathbf{m}^{\text{eq}} = (m_0^{\text{eq}}, m_1^{\text{eq}}, m_2^{\text{eq}}, m_3^{\text{eq}}, m_4^{\text{eq}})^T = (0, uT, vT, aT, 0)^T. \quad (3-23)$$

In the D2Q5 model, the weight coefficients are chosen to be

$$\omega_\alpha = \begin{cases} 1/3, & (\alpha = 0), \\ 1/6, & (\alpha = 1, 2, 3, 4), \end{cases} \quad (3-24)$$

and the constant a in Eq. (3-23) is determined by

$$a = (5\omega_0 - 1) = 2/3. \quad (3-25)$$

The relaxation matrix \mathbf{S} for the D2Q5 model now becomes

$$\mathbf{S}^{-1} = \begin{bmatrix} \tau_0 & 0 & 0 & 0 & 0 \\ 0 & \tau_{xx} & \tau_{xy} & 0 & 0 \\ 0 & \tau_{xy} & \tau_{yy} & 0 & 0 \\ 0 & 0 & 0 & \tau_3 & 0 \\ 0 & 0 & 0 & 0 & \tau_4 \end{bmatrix}, \quad (3-26)$$

and the conservation of the first moment results in the macroscopic temperature

$$m_0 = T = \sum_{\alpha=0}^4 g_\alpha. \quad (3-27)$$

For efficient computation, the TLBE is solved in two steps:

collision step

$$\hat{g}_\alpha(\mathbf{x}, t) = g_\alpha(\mathbf{x}, t) - [\mathbf{M}^{-1}\mathbf{S}(\mathbf{m}(\mathbf{x}, t) - \mathbf{m}^{\text{eq}}(\mathbf{x}, t))]_\alpha + \omega_\alpha G\delta t, \quad \text{and} \quad (3-28)$$

streaming step

$$g_{\alpha}(\mathbf{x} + \mathbf{e}_{\alpha}\delta t, t + \delta t) = \hat{g}_{\alpha}(\mathbf{x}, t), \quad (3-29)$$

where \hat{g}_{α} represents the post-collision state.

3.3.3 Thermal Boundary Condition Treatments

The lattice cut by the boundary wall with arbitrary intersection distance is illustrated in Fig. 3-2. In the present work, the lattice spacing is set to be unity ($\delta x = \delta y = 1$) and the fraction of the intersected link in the field to be solved is denoted by $\Delta = \|\mathbf{x}_f - \mathbf{x}_w\| / \|\mathbf{x}_f - \mathbf{x}_e\|$. Boundary condition treatment for the TLBE simulation is required during the streaming step when unknown populations from the undefined exterior nodes (\mathbf{x}_e in Fig. 3-2) to the “field” nodes (\mathbf{x}_f) are encountered. It should be noted that the CDE can also be used to govern the energy equation in the solid phase by setting the velocity to zero; thus the TLBE method can be extended to simulate the thermal field in the solid phase. Hence we replace the conventional “fluid” node with the more general “field” node notation in the computational domain.

The standard momentum “bounce-back” scheme is derived for the case where the distance from the boundary wall to the nearest field lattice node in the computational domain is equal to half of the lattice spacing. The basic idea of the momentum bounce-back can be applied to derive the thermal boundary conditions in TLBE. Considering the special case of $\Delta = 0.5$, Yoshida and Nagaoka (2010) proposed the following treatments for the Dirichlet and Neumann boundary conditions for walls perpendicular to one of the lattice velocity directions in the D3Q7 model. An asymptotic analysis was also given in their work to show that second-order accuracy is obtained for both conditions (Yoshida and Nagaoka 2010).

Dirichlet condition:

$$g_{\bar{\alpha}}(\mathbf{x}_f, t + \delta t) = -\hat{g}_{\alpha}(\mathbf{x}_f, t) + \varepsilon \Phi_d, \quad (3-30)$$

Neumann condition:

$$g_{\bar{\alpha}}(\mathbf{x}_f, t + \delta t) = \hat{g}_{\alpha}(\mathbf{x}_f, t) + (\delta t / \delta x) \Phi_n, \quad (3-31)$$

where \mathbf{n} is parallel to $\mathbf{e}_{\bar{\alpha}}$ and \mathbf{e}_{α} . If \mathbf{n} is not parallel to $\mathbf{e}_{\bar{\alpha}}$, one would need to replace Φ_n in Eq. (3-31) with $\Phi_{n\bar{\alpha}}$ which in turn involves the unknown heat flux in the tangential direction normal to $\mathbf{e}_{\bar{\alpha}}$.

It is important to have second-order accurate boundary conditions for the Dirichlet and Neumann problems for arbitrary Δ values. Based on the bounce-back idea on the boundary and spatial interpolation, one can develop various boundary schemes with different number of neighboring field nodes and their populations in different discrete directions. The schemes in Eqs. (3-30) and (3-31) above use only one post-collision value $\hat{g}_{\alpha}(\mathbf{x}_f, t)$ at the node adjacent to the boundary in the \mathbf{e}_{α} direction; thus it is considered as a “localized scheme”. The “multi-reflection” schemes (Ginzburg 2005) utilize five post-collision neighboring values involving three field nodes, and thus up to “third-order” accurate boundary condition schemes were derived for the Dirichlet condition. In this work we show that second-order accuracy for both the Dirichlet and Neumann boundary conditions can be achieved by using only three post-collision neighboring values, $\hat{g}_{\alpha}(\mathbf{x}_f, t)$, $\hat{g}_{\alpha}(\mathbf{x}_{ff}, t)$, and $\hat{g}_{\bar{\alpha}}(\mathbf{x}_f, t)$ for each unknown population $\hat{g}_{\bar{\alpha}}(\mathbf{x}_f, t + \delta t)$. Furthermore, we compare the present second-order Dirichlet boundary condition treatment with the “third-order” scheme (Ginzburg 2005) by examining the errors of the temperature fields, the boundary and interior heat fluxes with numerical examples and

observe that: i) both show quadratic convergence since the TLBE model is second-order accurate in the interior space; ii) the “third-order” scheme yields close, quantitatively even higher for some cases, numerical errors comparing with the present treatment under the same conditions; iii) both give very similar performance for curved-boundary simulations such as quadratic convergence of the temperature field and linear convergence of the heat flux on the boundary; thus the degradation of the accuracy due to the curved-boundary cannot be mitigated by increasing the order-of-accuracy on the boundary by using more lattice nodes and populations in the field. The construction of the present boundary condition treatment is given next in detail.

3.3.3.1 Dirichlet boundary condition

As shown in Fig. 3-2, the present treatment for the Dirichlet boundary condition is given by

$$g_{\bar{\alpha}}(\mathbf{x}_f, t + \delta t) = c_{d1} \hat{g}_{\alpha}(\mathbf{x}_f, t) + c_{d2} \hat{g}_{\alpha}(\mathbf{x}_{ff}, t) + c_{d3} \hat{g}_{\bar{\alpha}}(\mathbf{x}_f, t) + c_{d4} \varepsilon \Phi_d, \quad (3-32)$$

where c_{d1} , c_{d2} , c_{d3} , and c_{d4} are coefficients related to the specific Δ value. To maintain second-order accuracy, the following relations are required, leaving c_{d1} adjustable (see Eq. (B-19) in Appendix B)

$$\begin{cases} c_{d2} = -\frac{2\Delta c_{d1} + 1}{2\Delta + 1} \\ c_{d3} = \frac{c_{d1} + 2\Delta}{2\Delta + 1} \\ c_{d4} = \frac{-c_{d1} + 1}{2\Delta + 1} \\ c_{d1} \neq 1 \end{cases} . \quad (3-33)$$

Furthermore, in order to minimize numerical instability one may require

$$|c_{di}| \leq 1, \quad (i = 1, 2, \text{ and } 3), \quad (3-34a)$$

so that the following constraint may be desired

$$-1 \leq c_{d1} < 1. \quad (3-34b)$$

A stability study with a numerical example in Sec. 3.4.1 shows that (3-34b) would always guarantee numerical stability for reasonable parameters used. It is also shown that while the upper bound for the numerical stability region is indeed $c_{d1} = 1$, the lower bound can be extended from -1 to certain values depending on the relaxation coefficient τ_{ij} and the lattice fraction Δ .

Note that further effort can be devoted to construct more constraints on the parameter c_{d1} by using more distributions on extra lattice nodes in the interpolation, such as the local third-order Dirichlet schemes provided in (Ginzburg 2005). However, considering the LBE is second-order accurate in the interior lattice nodes, we aim at only obtaining a second-order boundary treatment scheme in this work. Furthermore, the choice of the relaxation coefficients τ_{ij} will affect the error terms in the TLBE solution. A comprehensive study on the effects of the relaxation coefficients and optimization of the parameters in Eq. (3-32) is thus beyond the scope of this work. To demonstrate the applicability and the second-order accuracy of the present boundary condition treatment, we provide the following three particular choices for the Dirichlet condition treatment.

Scheme 1:

$$g_{\bar{\alpha}}(\mathbf{x}_f, t + \delta t) = \begin{cases} (-2\Delta)\hat{g}_{\alpha}(\mathbf{x}_f, t) + (2\Delta - 1)\hat{g}_{\alpha}(\mathbf{x}_{\bar{f}}, t) + \varepsilon\Phi_d, & (\Delta \leq 0.5) \\ \left(-\frac{1}{2\Delta}\right)\hat{g}_{\alpha}(\mathbf{x}_f, t) + \left(1 - \frac{1}{2\Delta}\right)\hat{g}_{\bar{\alpha}}(\mathbf{x}_f, t) + \left(\frac{1}{2\Delta}\right)\varepsilon\Phi_d, & (\Delta > 0.5) \end{cases}, \quad (3-35a)$$

Scheme 2:

$$g_{\bar{\alpha}}(\mathbf{x}_f, t + \delta t) = 2(\Delta - 1)\hat{g}_{\alpha}(\mathbf{x}_f, t) - \frac{(2\Delta - 1)^2}{2\Delta + 1}\hat{g}_{\alpha}(\mathbf{x}_{ff}, t) + 2\left(\frac{2\Delta - 1}{2\Delta + 1}\right)\hat{g}_{\bar{\alpha}}(\mathbf{x}_f, t) + \left(\frac{3 - 2\Delta}{2\Delta + 1}\right)\varepsilon\Phi_d, \text{ and} \quad (3-35b)$$

Scheme 3:

$$g_{\bar{\alpha}}(\mathbf{x}_f, t + \delta t) = -\hat{g}_{\alpha}(\mathbf{x}_f, t) + \frac{2\Delta - 1}{2\Delta + 1}\hat{g}_{\alpha}(\mathbf{x}_{ff}, t) + \frac{2\Delta - 1}{2\Delta + 1}\hat{g}_{\bar{\alpha}}(\mathbf{x}_f, t) + \frac{2}{2\Delta + 1}\varepsilon\Phi_d. \quad (3-35c)$$

The three schemes in Eq. (3-35) all have second-order accuracy in space and they reduce to the ordinary bounce-back scheme in Eq. (3-30) when $\Delta = 0.5$. They are all computationally stable. One may also observe that Scheme 1 is very similar to the hydrodynamic boundary condition treatment (Bouzidi et al. 2001) which is based on the bounce-back rule and linear interpolation. The present analysis and the derivation in Appendix B can also offer some insights into the understanding of the various interpolation schemes for velocity boundary conditions as those in (Ginzburg and d’Humières 2003, Chen et al. 1996, Filippova and Hänel 1998, Mei et al. 1999, Mei et al. 2000, and Bouzidi et al. 2001). We notice that, however, a rigorous second-order accurate scheme for the Dirichlet velocity boundary condition cannot be similarly formulated, even though for some special cases such as pressure-driven channel flows second-order accuracy of the velocity field can be obtained for arbitrary Δ with the coefficients carefully chosen based on interpolation. The reason is that in athermal LBE simulations, in principle, the leading-order and first-order moments of the velocity distribution functions must be able to recover the mass and momentum equations, respectively, which necessitates more constraints on the velocity distribution functions. Some of the relationships for the temperature distribution functions in TLBE do not have

their corresponding forms for the velocity distribution functions in athermal LBE simulations.

Ginzburg showed that with five populations incorporated, a “third-order” Dirichlet condition treatment can be constructed with one adjustable coefficient. With the present notation, the “one-parameter family of third-order conditions” (Ginzburg 2005) becomes

$$\begin{aligned}
g_{\bar{\alpha}}(\mathbf{x}_f, t + \delta t) = & \frac{1}{\kappa + 1} \left[\left(\frac{1}{2} - \Delta - \frac{1}{2} \Delta^2 + \kappa \right) \hat{g}_{\alpha}(\mathbf{x}_f, t) + \left(-\frac{3}{2} + \frac{3}{2} \Delta + \Delta^2 - 2\kappa \right) \hat{g}_{\alpha}(\mathbf{x}_{ff}, t) \right. \\
& + \left(\frac{1}{2} - \frac{1}{2} \Delta - \frac{1}{2} \Delta^2 + \kappa \right) \hat{g}_{\alpha}(\mathbf{x}_{ff}, t) + \left(1 - \frac{1}{2} \Delta + 2\kappa \right) \hat{g}_{\bar{\alpha}}(\mathbf{x}_f, t) \\
& \left. + \left(-\frac{1}{2} + \frac{1}{2} \Delta - \kappa \right) \hat{g}_{\bar{\alpha}}(\mathbf{x}_{ff}, t) + \frac{1}{2} \varepsilon \Phi_d \right], \quad (3-36)
\end{aligned}$$

where $\mathbf{x}_{fff} = \mathbf{x}_{ff} + \mathbf{e}_{\bar{\alpha}} \delta t = \mathbf{x}_f + 2 \mathbf{e}_{\bar{\alpha}} \delta t$ and κ is an adjustable coefficient. Two particular solutions were provided in Ginzburg’s work by choosing $\kappa = 0$ and $\kappa = (-1 + 2\Delta + \Delta^2) / 2$ in Eq. (3-36). In addition, the particular second-order Dirichlet condition applied in (Ginzburg 2005) used the same three populations as in the present treatment and can be obtained with $c_{d1} = (1/2 - \Delta)$ in Eq. (3-34), which yields

$$g_{\bar{\alpha}}(\mathbf{x}_f, t + \delta t) = \left(\frac{1}{2} - \Delta \right) \hat{g}_{\alpha}(\mathbf{x}_f, t) + (\Delta - 1) \hat{g}_{\alpha}(\mathbf{x}_{ff}, t) + \frac{1}{2} \hat{g}_{\bar{\alpha}}(\mathbf{x}_f, t) + \frac{1}{2} \varepsilon \Phi_d. \quad (3-37)$$

3.3.3.2 Neumann boundary condition

In order to develop an appropriate boundary condition for a curved wall with an arbitrary Δ and arbitrary orientation, we first consider the case when the wall normal is aligned with $\mathbf{e}_{\bar{\alpha}}$ and \mathbf{e}_{α} as in Eq. (3-31). Hence, the boundary condition for $g_{\bar{\alpha}}(\mathbf{x}_f, t + \delta t)$ can be represented as

$$g_{\bar{\alpha}}(\mathbf{x}_f, t + \delta t) = c_{n1} \hat{g}_{\alpha}(\mathbf{x}_f, t) + c_{n2} \hat{g}_{\alpha}(\mathbf{x}_{ff}, t) + c_{n3} \hat{g}_{\bar{\alpha}}(\mathbf{x}_f, t) + c_{n4} (\delta t / \delta x) \Phi_{n\bar{\alpha}}, \quad (3-38)$$

where c_{n1} , c_{n2} , c_{n3} , and c_{n4} are coefficients related to Δ , and $\Phi_{n\bar{\alpha}} = \Phi_n$.

Different from the adjustability of the treatment for the Dirichlet condition, the second-order accurate scheme for the Neumann boundary condition is determined by (see Eq. (B-28) in Appendix B)

$$\begin{cases} c_{n1} = 1 \\ c_{n2} = -\frac{2\Delta - 1}{2\Delta + 1} \\ c_{n3} = \frac{2\Delta - 1}{2\Delta + 1} \\ c_{n4} = \frac{2}{2\Delta + 1} \end{cases} \quad (3-39)$$

Thus Eq. (3-38) can be explicitly expressed as

$$g_{\bar{\alpha}}(\mathbf{x}_f, t + \delta t) = \hat{g}_{\alpha}(\mathbf{x}_f, t) - \frac{2\Delta - 1}{2\Delta + 1} \hat{g}_{\alpha}(\mathbf{x}_{ff}, t) + \frac{2\Delta - 1}{2\Delta + 1} \hat{g}_{\bar{\alpha}}(\mathbf{x}_f, t) + \frac{2}{2\Delta + 1} \frac{\delta t}{\delta x} \Phi_{n\bar{\alpha}} \quad (3-40)$$

Equation (3-40) reduces to the ordinary bounce-back scheme in Eq. (3-31) when $\Delta = 0.5$ and its coefficients satisfy the stability requirement $|c_{ni}| \leq 1$ ($i = 1, 2, \text{ and } 3$).

Remark 1: The present Dirichlet and Neumann boundary condition treatments given by Eqs. (3-32) and (3-38) with their coefficients determined by Eqs. (3-33) and (3-39), respectively, are derived for straight boundary surfaces with arbitrary Δ values and with their normal direction parallel to the discrete velocity direction $\mathbf{e}_{\bar{\alpha}}$. For curved boundaries, Eq. (3-32) can be directly extended for Dirichlet problems and Eq. (3-38) constitutes an excellent starting point for general Neumann problems.

Remark 2: Eq. (3-38) is also valid for Dirichlet problems, and Eq. (3-32) is also applicable to Neumann problems. Thus the combination of Eqs. (3-32) and (3-38) gives a means to evaluate heat flux on the wall along $\mathbf{e}_{\bar{\alpha}}$ direction for Dirichlet problems and to evaluate the wall temperature at the cuts for Neumann problems. With the

coefficients given by Eqs. (3-33) and (3-39), the following expressions can be obtained on the wall intersected by the lattice vector $\mathbf{e}_{\bar{\alpha}}$

$$\Phi_{n\bar{\alpha}} = \frac{1-c_{d1}}{2} \frac{\delta x}{\delta t} \left[-(2\Delta + 1)\hat{g}_{\alpha}(\mathbf{x}_f, t) + (2\Delta - \frac{2}{1-c_{d1}})\hat{g}_{\alpha}(\mathbf{x}_{ff}, t) + (\frac{2}{1-c_{d1}} - 1)\hat{g}_{\bar{\alpha}}(\mathbf{x}_f, t) + \varepsilon\Phi_d \right], \quad (3-41a)$$

or

$$\Phi_d = \frac{1}{\varepsilon} \left[(2\Delta + 1)\hat{g}_{\alpha}(\mathbf{x}_f, t) + (\frac{2}{1-c_{d1}} - 2\Delta)\hat{g}_{\alpha}(\mathbf{x}_{ff}, t) + (1 - \frac{2}{1-c_{d1}})\hat{g}_{\bar{\alpha}}(\mathbf{x}_f, t) + \frac{2}{1-c_{d1}} \frac{\delta t}{\delta x} \Phi_{n\bar{\alpha}} \right], \quad (3-41b)$$

where c_{d1} is the aforementioned adjustable variable in Eq. (3-32) and its values based on the three different choices in Eq. (3-35) will be examined subsequently.

Remark 3: The temperature gradient within the interior of the field can be evaluated using the formula (Yoshida and Nagaoka 2010)

$$\tau_{ij} \frac{\partial \phi}{\partial x_j} = \frac{v_i \delta t}{\varepsilon (\delta x)^2} \phi - \frac{1}{\varepsilon \delta x} \sum_{\alpha=0}^m \mathbf{e}_{\alpha i} g_{\alpha}. \quad (3-42)$$

This allows for an assessment of the error propagation in terms of heat flux into the field due to the boundary condition treatment.

Remark 4: For Neumann problems with curved boundaries, the heat flux $\Phi_{n\bar{\alpha}}$ in the discrete velocity direction must be obtained based on the given Φ_n in the absence of explicit knowledge on the tangential derivative, Φ_t , along the wall for curved boundaries (see Fig. 3-3). A practical strategy for the numerical determination of $\Phi_{n\bar{\alpha}}$ is discussed next.

Consider a curved boundary wall intersected by the lattice as shown in Fig. 3-3. The wall cuts the horizontal lattice link along the $\mathbf{e}_{\bar{\alpha}}$ direction between \mathbf{x}_e and \mathbf{x}_f at \mathbf{x}_w , and the heat flux along the link direction ($\mathbf{e}_{\bar{\alpha}}$) from exterior to interior, $\Phi_{n\bar{\alpha}}$, is to be derived. The angles between $\mathbf{e}_{\bar{\alpha}}$ and the wall tangent and normal are $\theta_{t\bar{\alpha}}$ and $\theta_{n\bar{\alpha}}$ respectively. Along $\mathbf{e}_{\bar{\alpha}}$, the two neighboring field lattice nodes are \mathbf{x}_f and \mathbf{x}_{ff} . Along the direction perpendicular to $\mathbf{e}_{\bar{\alpha}}$, we designate $\mathbf{x}'_f = \mathbf{x}_w$ and $\mathbf{x}'_{ff} = \mathbf{x}_w + \mathbf{e}_{\bar{\beta}} \delta t$ in which $\mathbf{e}_{\bar{\beta}}$ is the lattice vector from exterior to the interior along the direction perpendicular to $\mathbf{e}_{\bar{\alpha}}$.

The projection of the boundary fluxes gives $\Phi_{n\bar{\alpha}} = \Phi_n \cos \theta_{n\bar{\alpha}} + \Phi_t \cos \theta_{t\bar{\alpha}}$. In general, Φ_t is needed in the calculation of $\Phi_{n\bar{\alpha}}$, unless $\cos \theta_{t\bar{\alpha}} = 0$ (i.e. the wall is perpendicular to $\mathbf{e}_{\bar{\alpha}}$) or $\Phi_t = 0$ is implicitly known in very special cases. However, well-posedness of the mathematical problem for CDE does not even allow the specification of Φ_t in addition to Φ_n on the same boundary. Thus the Neumann boundary condition, or the more general mixed boundary condition in the form of

$$\sigma_1 \frac{\partial \phi}{\partial n} + \sigma_2 \phi = \sigma_3, \quad (\sigma_1 \neq 0) \quad (3-43)$$

involving the normal derivative on the boundary requires a fundamentally different approach than the Dirichlet problem. By rearranging Eq. (3-43), the boundary heat flux in the normal direction can be written as

$$\Phi_n = -D_t \frac{\partial \phi}{\partial n} = -D_t \left(\frac{\sigma_3}{\sigma_1} - \frac{\sigma_2}{\sigma_1} \phi \right) = -D_t \left(\frac{\sigma_3}{\sigma_1} - \frac{\sigma_2}{\sigma_1} \Phi_d \right). \quad (3-44)$$

The standard Neumann condition is recovered by setting $\sigma_2 = 0$ in the above.

For brevity, only the D2Q5 TLBE model in 2-D is considered here as the extension to 3-D is straightforward. As in Fig. 3-3 the normal heat flux can be expressed as

$$\Phi_{n\bar{\alpha}} \cos \theta_{n\bar{\alpha}} + \Phi_{n\bar{\beta}} \cos \theta_{n\bar{\beta}} = \Phi_n, \quad (3-45)$$

where $\theta_{n\bar{\beta}}$ is the angle between $\mathbf{e}_{\bar{\beta}}$ and the normal \mathbf{n} . Additionally, we can eliminate $g_{\bar{\alpha}}(\mathbf{x}_f, t + \delta t)$ by combining Eqs. (3-32) and (3-38) to obtain a relation between Φ_d and the heat flux $\Phi_{n\bar{\alpha}}$ in the discrete velocity direction $\mathbf{e}_{\bar{\alpha}}$ on the boundary (see Eq. 3-41b),

$$c_{d4} \varepsilon \Phi_d = (c_{n1} - c_{d1}) \hat{g}_{\alpha}(\mathbf{x}_f, t) + (c_{n2} - c_{d2}) \hat{g}_{\alpha}(\mathbf{x}_{ff}, t) + (c_{n3} - c_{d3}) \hat{g}_{\bar{\alpha}}(\mathbf{x}_f, t) + c_{n4} (\delta t / \delta x) \Phi_{n\bar{\alpha}}. \quad (3-46a)$$

It is important to recognize that a similar relation can be derived between Φ_d and the heat flux $\Phi_{n\bar{\beta}}$ in the $\mathbf{e}_{\bar{\beta}}$ direction as well. That is

$$c'_{d4} \varepsilon \Phi_d = (c'_{n1} - c'_{d1}) \hat{g}'_{\beta}(\mathbf{x}'_f, t) + (c'_{n2} - c'_{d2}) \hat{g}'_{\beta}(\mathbf{x}'_{ff}, t) + (c'_{n3} - c'_{d3}) \hat{g}'_{\bar{\beta}}(\mathbf{x}'_f, t) + c'_{n4} (\delta t / \delta x) \Phi_{n\bar{\beta}}, \quad (3-46b)$$

where c'_{di} , c'_{ni} are the coefficients corresponding to c_{di} , c_{ni} ($i = 1, 2, 3, 4$) defined in Eqs. (3-33) and (3-39), respectively, with the fraction $\Delta_{\bar{\beta}} = 0$ in the $\mathbf{e}_{\bar{\beta}}$ direction. The distribution functions $\hat{g}'_{\beta}(\mathbf{x}'_f, t)$, $\hat{g}'_{\beta}(\mathbf{x}'_{ff}, t)$, and $\hat{g}'_{\bar{\beta}}(\mathbf{x}'_f, t)$ at \mathbf{x}'_f and \mathbf{x}'_{ff} can be obtained using a quadratic interpolation or extrapolation of the distributions at the closest interior lattice nodes. Further elimination of Φ_d from Eqs. (3-46 a-b) results in the following relation between $\Phi_{n\bar{\alpha}}$ and $\Phi_{n\bar{\beta}}$,

$$\frac{1}{c_{d4}} [(c_{n1} - c_{d1}) \hat{g}_{\alpha}(\mathbf{x}_f, t) + (c_{n2} - c_{d2}) \hat{g}_{\alpha}(\mathbf{x}_{ff}, t) + (c_{n3} - c_{d3}) \hat{g}_{\bar{\alpha}}(\mathbf{x}_f, t) + c_{n4} (\delta t / \delta x) \Phi_{n\bar{\alpha}}]$$

$$= \frac{1}{c_{d4}} [(c_{n1}' - c_{d1}') \hat{g}_{\beta}(\mathbf{x}'_f, t) + (c_{n2}' - c_{d2}') \hat{g}_{\beta}(\mathbf{x}'_{\#}, t) + (c_{n3}' - c_{d3}') \hat{g}_{\beta}(\mathbf{x}'_f, t) + c_{n4}' (\delta t / \delta x) \Phi_{n\bar{\beta}}]. \quad (3-47)$$

Finally, combining Eqs. (3-45) and (3-47) leads to the desired expression for $\Phi_{n\bar{\alpha}}$ in terms of the normal heat flux and the post-collision distributions in the neighboring lattice nodes,

$$\begin{aligned} \Phi_{n\bar{\alpha}} = & \left\{ \frac{1}{c_{d4}} [(c_{n1}' - c_{d1}') \hat{g}_{\beta}(\mathbf{x}'_f, t) + (c_{n2}' - c_{d2}') \hat{g}_{\beta}(\mathbf{x}'_{\#}, t) + (c_{n3}' - c_{d3}') \hat{g}_{\beta}(\mathbf{x}'_f, t)] \sin \theta_{n\bar{\alpha}} \right. \\ & - \frac{1}{c_{d4}} [(c_{n1}' - c_{d1}') \hat{g}_{\alpha}(\mathbf{x}'_f, t) + (c_{n2}' - c_{d2}') \hat{g}_{\alpha}(\mathbf{x}'_{\#}, t) + (c_{n3}' - c_{d3}') \hat{g}_{\alpha}(\mathbf{x}'_f, t)] \sin \theta_{n\bar{\alpha}} \\ & \left. + \frac{c_{n4}'}{c_{d4}} \frac{\delta t}{\delta x} \Phi_n \right\} / \left[\frac{c_{n4}'}{c_{d4}} \frac{\delta t}{\delta x} \sin \theta_{n\bar{\alpha}} + \frac{c_{n4}'}{c_{d4}} \frac{\delta t}{\delta x} \cos \theta_{n\bar{\alpha}} \right]. \quad (3-48) \end{aligned}$$

Equation (3-48) can be directly applied to Neumann problems on curved boundaries.

For the special case where $\Phi_t = 0$ or $\cos \theta_{\bar{\alpha}} = 0$, a simpler formula can be used to relate $\Phi_{n\bar{\alpha}}$ to Φ_n

$$\Phi_{n\bar{\alpha}} = \Phi_n \cos \theta_{n\bar{\alpha}}. \quad (3-49)$$

The above is equivalent to that used by Huang et al. (2006), but it should not be used in general.

For mixed boundary conditions, Φ_n is not specified. Instead, Φ_n is related to Φ_d through Eqs. (3-44) and (3-46). Substitution of Eq. (3-46a) into Eq. (3-44) yields

$$\Phi_n = -D_t \frac{\sigma_3}{\sigma_1} + D_t \frac{\sigma_2}{\sigma_1 c_{d4} \varepsilon} [(c_{n1}' - c_{d1}') \hat{g}_{\alpha}(\mathbf{x}'_f, t) + (c_{n2}' - c_{d2}') \hat{g}_{\alpha}(\mathbf{x}'_{\#}, t) + (c_{n3}' - c_{d3}') \hat{g}_{\alpha}(\mathbf{x}'_f, t) + c_{n4}' \frac{\delta t}{\delta x} \Phi_{n\bar{\alpha}}]. \quad (3-50)$$

Combining Eqs. (3-48) and (3-50) gives

$$\begin{aligned}
\Phi_{n\bar{\alpha}} = & \left\{ \frac{1}{c_{d4}} [(c_{n1}' - c_{d1}') \hat{g}_{\beta}(\mathbf{x}_f, t) + (c_{n2}' - c_{d2}') \hat{g}_{\beta}(\mathbf{x}_{ff}, t) + (c_{n3}' - c_{d3}') \hat{g}_{\beta}(\mathbf{x}_f, t)] \sin \theta_{n\bar{\alpha}} \right. \\
& - \frac{1}{c_{d4}} [(c_{n1}' - c_{d1}') \hat{g}_{\alpha}(\mathbf{x}_f, t) + (c_{n2}' - c_{d2}') \hat{g}_{\alpha}(\mathbf{x}_{ff}, t) + (c_{n3}' - c_{d3}') \hat{g}_{\alpha}(\mathbf{x}_f, t)] \sin \theta_{n\bar{\alpha}} \\
& + D_t \frac{c_{n4}'}{c_{d4}} \frac{\delta t}{\delta x} \frac{\sigma_2}{\sigma_1 c_{d4} \varepsilon} [(c_{n1}' - c_{d1}') \hat{g}_{\alpha}(\mathbf{x}_f, t) + (c_{n2}' - c_{d2}') \hat{g}_{\alpha}(\mathbf{x}_{ff}, t) + (c_{n3}' - c_{d3}') \hat{g}_{\alpha}(\mathbf{x}_f, t)] \\
& \left. - D_t \frac{c_{n4}'}{c_{d4}} \frac{\delta t}{\delta x} \frac{\sigma_3}{\sigma_1} \right\} / \left[\frac{c_{n4}'}{c_{d4}} \frac{\delta t}{\delta x} \sin \theta_{n\bar{\alpha}} + \frac{c_{n4}'}{c_{d4}} \frac{\delta t}{\delta x} \cos \theta_{n\bar{\alpha}} - \frac{c_{n4}'}{c_{d4}} \left(\frac{\delta t}{\delta x} \right)^2 D_t \frac{c_{n4} \sigma_2}{c_{d4} \varepsilon \sigma_1} \right]. \quad (3-51)
\end{aligned}$$

Once $\Phi_{n\bar{\alpha}}$ is obtained the boundary condition treatment in Eq. (3-40) can be used to complete the streaming step. It is noted that $\Phi_{n\bar{\beta}}$ is not needed in Eq. (3-40) as \mathbf{x}_w in Fig. 3-3 is located on the link along the $\mathbf{e}_{\bar{\alpha}}$ direction. The same procedure can be applied to derive $\Phi_{n\bar{\beta}}$ when \mathbf{x}_w is located on the link along the $\mathbf{e}_{\bar{\beta}}$ direction. For more general cases such as those lattice models that are more complicated than D3Q7 (for 3-D) or D2Q5 (for 2-D), and when a lattice velocity vector $\mathbf{e}_{\bar{\alpha}}$ is not in the axial x -, y - or z -direction, the same procedure can be used to compute the axial heat fluxes Φ_{nx} , Φ_{ny} and Φ_{nz} in a coupled manner first. The non-axial heat flux $\Phi_{n\bar{\alpha}}$ can be subsequently obtained using Φ_{nx} , Φ_{ny} and Φ_{nz} . This method of determining $\Phi_{n\bar{\alpha}}$ for Neumann or mixed boundary condition is hereinafter referred to as Cartesian decomposition method.

The accuracy of the present boundary condition treatments will be examined through a series of numerical tests in the next section, and the asymptotic analysis is given in Appendix B. When the node \mathbf{x}_{ff} is outside the field, we recommend using the localized schemes by Yoshida and Nagaoka (2010).

3.4 Numerical Validation and Discussion

To verify the applicability and accuracy of the present thermal boundary condition treatments, we have conducted several numerical tests involving both 2-D and 3-D geometries. Both convection and diffusion are considered in the first example, where the Dirichlet and Neumann boundary conditions are separately applied and investigated. The second example shows how to convert the Neumann condition in the normal direction of an inclined wall into the heat fluxes in the discrete velocity directions when there is no tangential flux. From the third example through the fifth example, curved geometries are considered. Steady-state and transient boundary conditions are given in the third and fourth problems; while the fifth test is for the simulation of steady-state convection and diffusion inside a circular (3-D) pipe.

In this study, only isotropic diffusion is considered, i.e., $D_{ij} = D_t \delta_{ij}$; thus the off-diagonal components in the relaxation matrix are set to be zeros, and the constraint for the diagonal coefficients is maintained so that Eq. (3-14) can be rewritten as

$$\tau_{ij} = \tau_D \delta_{ij} = \left(\frac{1}{2} + \frac{\delta t}{\varepsilon (\delta x)^2} D_t \right) \delta_{ij}. \quad (3-52)$$

The positivity of the diffusion coefficient D_t requires that $\tau_D > 1/2$. A typical value of $\tau_D = 0.75$ is used in each of the numerical examples to demonstrate the accuracy of the present boundary condition treatments. Although no detailed stability analysis is performed for the proposed Dirichlet and Neumann boundary schemes, we have numerically checked their stability by using τ_D values close to $1/2$, for which numerical instability is most likely to occur. For brevity, the results for $\tau_D = 0.55$ and $\tau_D = 0.51$ are presented for some cases. The relaxation coefficient τ_0 for the conserved quantity ϕ has no effect on the numerical solution, and the remaining adjustable coefficients do not

contribute to the leading-order solution of the CDE since they only affect the higher-order error terms of the LBE solutions; thus $\tau_0 = 0$, and $\tau_p = 1$ ($p = 4, 5, 6$ in 3-D and $p = 3, 4$ in 2-D) are used in the rest of this work.

3.4.1 Two-D Steady-State Channel Flow

First we consider a plug flow of velocity U in a 2-D channel of constant height, H (Fig. 3-4). Each wall is placed at a distance of $(\Delta\delta y)$ from the first interior lattice in the y -direction. The CDE for the temperature inside the channel is

$$U \frac{\partial T}{\partial x} = D_t \left(\frac{\partial^2 T}{\partial x^2} + \frac{\partial^2 T}{\partial y^2} \right), \quad (3-53)$$

This thermal flow problem is characterized by the Péclet number $Pe = HU/D_t$; and $Pe = 20$ is used in this study. Periodic boundary conditions are imposed in the x -direction so that $f(x+L) = f(x)$ for both the temperature T and distribution functions g_a . Both Dirichlet and Neumann thermal boundary conditions on the wall are considered.

3.4.1.1 Dirichlet boundary condition

On the wall at $y = 0$ and $y = H$,

$$T(x, y = 0) = T(x, y = H) = \cos(kx), \quad \text{with } k = 2\pi / L. \quad (3-54)$$

An analytical solution for the thermal field can be obtained. When expressed with complex variables, the exact solution is

$$T_{\text{ex}}(x, y) = \text{Real} \left[e^{ikx} \frac{e^{\lambda y} + e^{\lambda(H-y)}}{e^{\lambda H} + 1} \right], \quad (3-55)$$

where “*Real*” means taking the real part of a complex variable and $\lambda = k \sqrt{1 + \frac{iU}{D_t k}}$.

Before evaluating the accuracy of the present Dirichlet schemes, the numerical stability is investigated first for this problem. The work of (Mei et al. 1999) indicates that

the numerical instability associated with boundary condition treatments in using the LBE method is more pronounced in channel flows than in curved geometries. Hence guidance on numerical instability from solving the thermal problem in the channel flow will be useful. Fig. 3-5 (a) shows the lower stability bound for the adjustable coefficient c_{d1} at $Pe = 20$ and $Ny = 34$ (Ny denotes the number of lattice nodes in y-direction). Very close results for the lower bound are obtained also for $(Pe, Ny) = (20, 130)$, $(100, 34)$ and $(100, 130)$. The upper bound for c_{d1} is 1.0 for all cases, noting that $c_{d1} \neq 1$ as required in Eq. (3-33). An asymptotic lower bound of c_{d1} is noticed for each Δ value tested as τ_D approaches 0.5 in Fig. 3-5 (a). On the other hand, when τ_D increases, the lower bound drops, resulting in a broader stable region while the overall relative error of the temperature field increases (see Figs. 3-7 and 3-8 below). Fig. 3-5 (b) shows the dependence of c_{d1} on Δ in the range of $0 \leq \Delta \leq 1$ for the three schemes in relation to the lower stability bound $\tau_D = 0.50001$ and the upper stability bound. Clearly, all three schemes are well within the stable region.

As an illustration, Fig. 3-6 shows the temperature contours obtained using $\tau_D = 0.75$, $\Delta = 0.5$ and $H = 64$. To assess the accuracy of the LBE solution of the temperature T_{LBE} the following relative L-2 error norm is defined:

$$E_2 = \left(\sum_{x,y} (T_{LBE} - T_{ex})^2 / \sum_{x,y} T_{ex}^2 \right)^{1/2}. \quad (3-56)$$

Figure 3-7 (a-f) shows the log-log plots of E_2 versus the dimensionless grid resolution, $1/H$, over a complete range of Δ for the three schemes given in Eq. (3-35 a-c). Three relaxation coefficient values $\tau_D = 0.51$, 0.55 and 0.75 are used. Second order accuracy is observed for all cases. At $\tau_D = 0.51$, all three schemes give very close results as

shown in Fig. 3-7 (a, b). As τ_D increases, the differences among the three schemes become more noticeable and Scheme 2 gives smallest relative error for each case as shown in Fig. 3-7 (c-f). The variations of E_2 in the range of Δ from 0 to 1 are shown in Fig. 3-8 with $Ny = 34$. It is noticed that with $\tau_D = 0.75$, all the three schemes have minimum error at $\Delta = 0.5$, where the standard thermal bounce-back scheme is applied. When τ_D increases to 1.0, the relative error also increases for each scheme when $\Delta \leq 0.5$; while for $\Delta > 0.5$, the error behavior becomes more complicated. The results in Figs. 3-7 and 3-8 clearly verify the existence of the adjustable parameter c_{d1} in using the TLBE method for CDE subjected to Dirichlet boundary conditions; and the proposed Dirichlet schemes are stable and of second-order accurate for $\tau_D > 0.5$.

For comparison purposes, the results obtained using the “third-order” and second-order schemes (Ginzburg 2005) for $\Delta = 0.25, 0.50$, and 0.75 are compared with that from Scheme 2 in Fig. 3-9 (a, b), where the “Ginzburg 3rd-order # 1” and “Ginzburg 3rd-order # 2” represent the two particular schemes whose coefficients are constructed with $\kappa = 0$ and $\kappa = (-1 + 2\Delta + \Delta^2)/2$ in Eq. (3-36), respectively, and the coefficients for the second-order scheme are given in Eq. (3-37). Fig. 3-9 demonstrates that the “third-order” Dirichlet schemes (Ginzburg 2005) also lead to second-order convergence since the TLBE method is second-order accurate in the interior. In addition, Scheme 2 gives smaller error than the local “third-order” schemes in (Ginzburg 2005) for each Δ value tested in Fig. 3-9 (a, b). compared with those obtained using Ginzburg’s schemes.

To gain further insight into the impact of the boundary condition treatment on the accuracy of the TLBE solution, we compute the boundary heat flux and interior temperature gradient using the formulas given by Eqs. (3-41a) and (3-42), respectively.

The relative L-2 norm errors are computed using the respective derivatives obtained from the analytical solutions given by Eq. (3-55),

$$E_{2_qw} = \left[\sum_{\text{boundary nodes}} \left[\left(\frac{\partial T}{\partial y} \right)_{\text{LBE}} - \left(\frac{\partial T}{\partial y} \right)_{\text{ex}} \right]^2 / \sum_{\text{boundary nodes}} \left(\frac{\partial T}{\partial y} \right)_{\text{ex}}^2 \right]^{1/2}, \quad (3-57)$$

$$E_{2_grad} = \left[\sum_{\text{interior nodes}} \left[\left(\frac{\partial T}{\partial y} \right)_{\text{LBE}} - \left(\frac{\partial T}{\partial y} \right)_{\text{ex}} \right]^2 / \sum_{\text{interior nodes}} \left(\frac{\partial T}{\partial y} \right)_{\text{ex}}^2 \right]^{1/2}. \quad (3-58)$$

The results of E_{2_qw} for the wall heat flux and E_{2_grad} for the interior temperature gradient at $\tau_D = 0.75$ are shown in Figs. 3-10 and 3-11, respectively.

It is clear that the numerical solutions for boundary heat flux and interior temperature gradient are of second-order accuracy for Dirichlet problems for straight walls perpendicular to one of the lattice vectors. Scheme 2 gives slightly smaller error than the other two.

3.4.1.2 Neumann boundary condition

For the Neumann problem, the normal heat flux on the wall is given as

$$q_w = -D_t \frac{\partial T}{\partial y} \Big|_{y=H} = -D_t \cos(kx) / H. \quad (3-59)$$

The exact solution for the temperature is

$$T_{\text{ex}}(x, y) = \text{Real} \left[e^{ikx} \frac{e^{\lambda y} + e^{\lambda(H-y)}}{\lambda H (e^{\lambda H} - 1)} \right]. \quad (3-60)$$

Again, the numerical solution of the temperature field at $\tau_D = 0.75$, $\Delta = 0.5$ and $H = 64$ is shown in Fig. 3-12 as an example; in addition to the interior temperature and temperature gradient error norms defined in Eqs. (3-56, 3-58), the relative L-2 error norm for the boundary temperature is defined as

$$E_{2_tw} = \left[\frac{\sum_{\text{boundary nodes}} (T_{\text{LBE}} - T_{\text{ex}})^2}{\sum_{\text{boundary nodes}} T_{\text{ex}}^2} \right]^{1/2}. \quad (3-61)$$

Figures 3-13 (a-c) show E_2 (Eq. (3-56)) versus $1/H$ for Δ ranging from 0.01 to 0.99 and $\tau_D = 0.51, 0.55$ and 0.75 at $Pe = 20$, and Figs. 3-14 and 3-15 show E_{2_tw} and E_{2_grad} , respectively, for $\tau_D = 0.75$. The results confirm that the present Neumann condition scheme is stable, and second-order accuracy is achieved for the temperature field, boundary temperature, and interior heat flux when the straight-wall is perpendicular to one of the lattice vectors. Extreme cases including $\tau_D = 0.501, 0.5001, 0.50001$ and $\Delta = 0.001, 0.999, 0.0001, 0.9999$ at $Ny = 34$ have also been examined. The computations using present Neumann boundary scheme are all stable and give good numerical results for all cases.

3.4.2 One-D Transient Conduction in an Inclined Semi-Infinite Solid

In order to demonstrate the applicability of the present Neumann boundary condition treatment to inclined walls, we consider the transient heat conduction of a constant heat flux into an inclined semi-infinite solid as shown in Fig. 3-16. For a given wall inclination angle θ with respect to the y -axis, the specific fractions of Δ_x and Δ_y are calculated for each field point adjacent to the boundary. Note there is still no tangential variation in this case; the Neumann boundary condition with nonzero tangential gradient will be investigated in Sec. 3.4.3.

The initial temperature is zero in the field (solid), and the constant heat flux condition is imposed as

$$q_w = -D_t \frac{\partial T}{\partial n} \Big|_{l=0} = \frac{\sqrt{D_t \pi}}{2}. \quad (3-62)$$

Hence the transient temperature along the solid is solved to be

$$T_{\text{ex}}(t, l) = t^{1/2} \left[e^{-l^2/4D_t t} - \frac{l\sqrt{\pi}}{2\sqrt{D_t t}} \text{erfc}\left(\frac{l}{2\sqrt{D_t t}}\right) \right], \quad (3-63)$$

where l is the distance in the normal direction and “erfc” is the complementary error function. The temperature on the wall is $f(t) = T(t, l = 0) = t^{1/2}$.

With no temperature variation along the tangential direction, the boundary heat fluxes in the discrete velocity directions can be directly calculated using Eq. (3-49),

$$q_2 = q_w \cos \theta = \frac{\sqrt{D_t \pi}}{2} \cos \theta \quad (3-64a)$$

and

$$q_3 = q_w \sin \theta = \frac{\sqrt{D_t \pi}}{2} \sin \theta. \quad (3-64b)$$

Figure 3-17 (a) shows the variations of the temperature with time at point P in Fig. 3-16 for inclination angles $\theta = \tan^{-1}(1.0)$, $\tan^{-1}(1.2)$, $\tan^{-1}(1.5)$, and $\tan^{-1}(2.0)$. For each inclination angle, the temperature profile along the vertical line going through point P at $t = 500\delta t$ is compared with the exact solution in Fig. 3-17 (b), where the distances in the y coordinate have been projected into that in the normal direction of the physical boundary.

Very good agreement between the simulation and the analytical solution is noticed in Figs. 3-17 (a) and (b). These results verify that Eq. (3-49) is correct when the tangential temperature gradient on the boundary is zero. This test also serves as a good example to show that the present Neumann boundary condition treatment can be readily implemented for a boundary that is intersected by the rectangular lattice with arbitrary link fractions, i.e., irregularly spaced Δ values, which is also the subject of the next example.

3.4.3 Two-D Steady-State Heat Conduction Inside a Circle

Figure 3-18 (a) shows the schematic layout of the lattice covering the entire surface and the interior of a circle of radius r_0 . The specific Δ_x or Δ_y value of each boundary cut must be calculated first. It should be noted that the Δ values are irregularly distributed along the azimuthal direction; as an example, the distribution of Δ values, including both Δ_x and Δ_y , as a function of the azimuthal angle φ of the boundary nodes at $r_0 = 30.5$ is depicted in Fig. 3-18 (b).

3.4.3.1 Dirichlet boundary condition

First we consider the steady-state Dirichlet boundary condition

$$T(r = r_0) = f(\varphi) = \cos(n\varphi) ; n = \text{integer.} \quad (3-65)$$

The exact solution for the temperature field is

$$T_{\text{ex}}(r, \varphi) = (r/r_0)^n \cos(n\varphi). \quad (3-66)$$

Figure 3-19 shows the relative L-2 norm error E_2 defined in Eq. (3-56) for all the interior nodes versus the grid resolution, $1/r_0$, on the log-log scale with $n = 4$ used in Eq. (3-65). The present Schemes 1, 2 and 3 are based on Eq. (3-35 a-c), respectively, and the second-order and “third-order” schemes from (Ginzburg 2005) are used for comparison (those schemes are rewritten in Eqs. (3-36, 3-37)). Second-order accuracy for the temperature field is observed in Fig. 3-19 for each scheme examined. It is seen that Scheme 2 gives better accuracy comparing with the other two given by Eq. (3-35).

The results for the error norm $E_{2_q\bar{w}}$ of the boundary heat flux $\Phi_{n\bar{a}}$ according to Eq. (3-41a) are shown in Fig. 3-20, where on average only first-order convergence is observed. It should be noted that in Fig. 3-20 the results of Ginzburg’s third- and second-order schemes are obtained by combining Eqs. (3-36) and (3-37) with our

second-order Neumann scheme in Eq. (3-40), respectively, and following the same procedure as that for Eq. (3-41a). Fig. 3-21 gives the results of the error norm of the interior temperature gradient E_{2_grad} defined in Eq. (58). Realizing Scheme 2 has better accuracy than the other two given by Eq. (35) in the previous examples only the results using Scheme 2 are presented in Figs. 3-20 and 3-21. The “finite-difference” case represents a quadratic finite-difference scheme based on the numerical values of the temperature field at the lattice nodes and the given wall temperature.

One valuable insight to be gained from Figs. 3-20 and 3-21 is that for the boundary heat flux and interior temperature gradient in Eqs. (3-41a) and (3-42), respectively, these various Dirichlet schemes all yield linear convergence for the boundary heat flux, and the error norm of the interior temperature gradient E_{2_grad} is proportional to $(1/r_0)^{1.5}$, both of which are lower than the second-order convergence as shown in Figs. 3-10 and 3-11, respectively for straight boundaries. The degradation of the convergence rates for the derivative related physical quantities is due to the curved boundary at which the intersected link fractions (Δ values) are irregularly distributed (see Fig. 3-18 (b)). On the whole, the present Dirichlet condition treatment on a curved boundary is able to produce second-order accurate temperature field and first-order boundary heat flux, and the interior temperature gradient converges to the exact solution with a “superlinear” order close to 1.5. This conclusion also offers an insight into the accuracy of the Neumann boundary condition treatment in curved-boundary situations, which will be discussed next.

3.4.3.2 Neumann boundary condition

Now consider the following Neumann (flux) condition applied on the boundary

$$q_w = -D_t \frac{\partial T}{\partial r} \Big|_{r_0} = -nD_t \cos(n\varphi) / r_0. \quad (3-67)$$

The solution of the temperature field is the same as that in Eq. (3-66) and the case of $n = 4$ is used.

To account for the contribution to $\Phi_{n\bar{\alpha}}$ from the tangential temperature gradient, Eq. (3-48) is used. After $\Phi_{n\bar{\alpha}}$ is obtained numerically, Eq. (3-40) is implemented to complete the streaming step for Neumann problems. The error norms E_2 , E_{2_tw} and E_{2_grad} of the interior temperature field, the boundary temperature, and the interior temperature gradient as defined in Eqs. (3-56, 3-61, and 3-58) versus the grid resolution, $1/r_0$, are shown in Figs. 3-22 – 3-24, respectively, where the present “coupled schemes 1, 2 and 3” represent the different coefficient sets c_{di} and c'_{di} in Eq. (3-46) determined by the three schemes in Eqs. (3-35 a-c), respectively.

From the analytical solution for the temperature field, Eq. (3-66), the exact boundary heat flux $\Phi_{n\bar{\alpha}}$ in the discrete velocity direction can be obtained with projection of the normal and tangential heat fluxes into the x - or y -coordinate. For comparison, the results of the three types of error norms E_2 , E_{2_tw} and E_{2_grad} based on this exact boundary flux are also presented in Figs. 3-22 – 3-24, respectively.

First of all, we notice that with the “exact boundary flux” $\Phi_{n\bar{\alpha}}$ applied, the use of Eq. (3-40) for the evaluation of the distribution function leads to second-order accuracy for all the three quantities, i.e., the interior and boundary temperatures and the interior temperature gradients. However, only first-order accuracy is obtained for both the interior and boundary temperatures for all the three “coupled” schemes. The average decrease of the error norms in Figs. 3-22 and 3-23 is proportional to the grid resolution,

$1/r_0$, on the log-log scale and considerable oscillations are observed even at high grid resolution. The interior temperature gradient as shown in Fig. 3-24 still converges with a “superlinear” order around 1.5, which is similar to the result of E_{2_grad} in Fig. 3-21 with a Dirichlet condition. Compared with the second-order convergence in the case of the exact boundary flux, the degradation of the order-of-accuracy in the coupled schemes is due to the heat flux approximation of $\Phi_{n\bar{a}}$ for irregularly distributed Δ values along the curved boundary. Recalling in Fig. 3-20 only a linear convergence of the boundary heat flux is obtained for the Dirichlet problem, and the heat flux formula Eq. (3-41a, or 3-46a) is used in deriving the ultimate heat flux approximation in Eq. (3-48), it is believed that some second-order error terms $O(\delta_x^2)$, which are related to the local Δ values, are introduced in the heat flux approximation. Those second-order errors cannot be always cancelled out due to the “random” distribution of Δ values (Fig. 3-18 (b)), resulting in averaged linear convergence and persistent oscillations even at high resolution as shown in Figs. 3-22 and 3-23. Based on the “multi-reflection” approach, Ginzburg (2005) also found that only linear convergence can be achieved for the Neumann condition on the curved boundary when tangential temperature gradient exists.

The orders of accuracy for the Dirichlet and Neumann conditions on straight and curved boundaries for the temperature and its derivative related quantities are summarized in Table 1 for 2-D steady thermal problems.

3.4.4 Two-D Transient Heat Conduction Inside a Circle

In this case, a transient boundary condition is applied on the curved boundary to examine the temporal accuracy of the present boundary condition treatment for time-dependent problems. The geometry is the same as that in Fig. 3-18 (a).

The temperature is uniform in the azimuthal direction and the transient Dirichlet boundary condition reads

$$T(t, r = r_0) = f(t) = \sin(\omega t), \quad (3-68)$$

where ω is the frequency of the imposed thermal boundary condition. This transient problem is characterized by the Stokes number S_t defined as

$$S_t^2 = \frac{r_0^2 \omega}{2\pi D_t}. \quad (3-69)$$

The analytical solution for this 2-D problem can be found as (Hahn and Ozisik 2012)

$$\begin{aligned} T_{\text{ex}}(r, t) &= f(t) - \frac{2}{r_0} \sum_{n=1}^{\infty} \frac{J_0(\beta_n r)}{\beta_n J_1(\beta_n r_0)} [f(0)e^{-D_t \beta_n^2 t} + \int_0^t e^{-D_t \beta_n^2 (t-\tau)} df(\tau)] \\ &= \sin(\omega t) - \frac{2}{r_0} \sum_{n=1}^{\infty} \frac{\omega J_0(\beta_n r)}{\beta_n J_1(\beta_n r_0)} \left[\frac{D_t \beta_n^2 \cos(\omega t) + \omega \sin(\omega t) - D_t \beta_n^2 e^{-D_t \beta_n^2 t}}{(D_t \beta_n^2)^2 + \omega^2} \right], \end{aligned} \quad (3-70)$$

where $J_i(\beta r)$ ($i = 0, 1$) is the solution to the Bessel's function of the first kind of order i , and β_n is determined by $J_0(\beta_n r_0) = 0$.

For error assessment purposes for the this transient problem we define two error norms

$$E(t^*) = \left[\frac{1}{N_x N_y} \sum_{x,y} (T_{\text{LBE}} - T_{\text{ex}})^2 \right]^{1/2}, \quad (3-71)$$

$$E_2 = \left[\frac{\omega}{2\pi} \int_0^{2\pi/\omega} \frac{1}{N_x N_y} \sum_{x,y} (T_{\text{LBE}} - T_{\text{ex}})^2 dt \right]^{1/2} = \left[\int_0^1 \frac{1}{N_x N_y} \sum_{x,y} (T_{\text{LBE}} - T_{\text{ex}})^2 dt^* \right]^{1/2}, \quad (3-72)$$

where $t^* = \omega t / 2\pi$ and the product of $(N_x N_y)$ accounts for the total number of the lattice nodes inside the circle.

To eliminate the effect of initial transient, the computation is performed for a sufficiently long period of time ($t^* > 1$). The Stokes number St is set to be unity in all

simulations. The results of $E(t^*)$ defined in Eq. (3-71) at $\tau_D = 0.51$ and 0.75 are presented in Fig. 3-25 using the three schemes in Eqs. (3-35 a-c). The grid resolution here is relatively poor as $r_0 = 5.8$. The average error E_2 defined in Eq. (3-72) is evaluated over one single period after the dynamic steady state is reached. The results of E_2 with different resolution are shown in Fig. 3-26 as a function of $1/r_0$ for $\tau_D = 0.75$. The decrease of the error norm E_2 is proportional to $(1/r_0)^2$ on the log-log scale for each of the three schemes. It can also be observed in Fig. 3-26 that Schemes 2 and 3 have very close errors and they are more accurate than Scheme 1 in general. When $\tau_D = 0.51$ is used, the three schemes give almost identical results for E_2 and the magnitude is very close to that in Fig. 3-26 for $\tau_D = 0.75$ thus they are not shown here for brevity. Overall, Scheme 2 appears to give smaller error than the other two schemes given by Eq. (35).

It is thus confirmed that the present Dirichlet boundary condition treatment can be applied in transient problems with curved-geometry, and second-order accuracy is preserved for the temperature field.

3.4.5 Three-D Steady-State Circular Pipe Flow

To test the TLBE model and the boundary condition treatments in 3-D cases, the convection and diffusion inside a circular pipe are considered in this example. The temperature is assumed to be uniform in the azimuthal direction in order to obtain analytical solutions.

3.4.5.1 Dirichlet boundary condition

The plug flow with constant velocity U in the axial z -direction is assumed. The periodic boundary condition in the z -direction is applied as

$$T(r, z = L) = T(r, z = 0), \quad (3-73)$$

and the Dirichlet boundary condition is imposed as

$$T(r = r_0, z) = \cos(kz), \text{ with } k = 2\pi / L. \quad (3-74)$$

Following the same procedure for 2-D channel flow with Dirichlet boundary conditions in Sec. 3.4.1.1, the analytical solution for the temperature field is solved to be

$$T_{\text{ex}}(r, z) = \text{Real} \left[e^{ikz} \frac{I_0(\lambda r)}{I_0(\lambda r_0)} \right] \quad (3-75)$$

where $I_0(\lambda r)$ is the modified Bessel's function of the first kind of order 0 and

$$\lambda = k \sqrt{1 + \frac{iU}{D_t k}}.$$

The relative error norms E_2 and E_{2_qw} are extended from 2-D to 3-D cases

$$E_2 = \left[\sum_{r,\theta,z} (T_{\text{LBE}} - T_{\text{ex}})^2 / \sum_{r,\theta,z} T_{\text{ex}}^2 \right]^{1/2}, \quad (3-76)$$

$$E_{2_qw} = \left[\sum_{r=r_0,\theta,z} \left(\left(\frac{\partial T}{\partial r} \right)_{\text{LBE}} - \left(\frac{\partial T}{\partial r} \right)_{\text{ex}} \right)^2 / \sum_{r=r_0,\theta,z} \left(\frac{\partial T}{\partial r} \right)_{\text{ex}}^2 \right]^{1/2}. \quad (3-77)$$

Figures 3-27 and 3-28 show the results of E_2 and E_{2_qw} for this 3-D case, respectively, versus the grid resolution, $1/r_0$, with the three schemes given in Eqs. (3-35 a-c) implemented. The characteristic Péclet number is $Pe = (2r_0)U/D_t = 20$ and the relaxation coefficient is $\tau_D = 0.75$.

Similar to the 2-D example in Sec. 3.4.1.1, this 3-D example with Dirichlet condition on the curved boundary gives quadratic convergence of the temperature field and only a linear convergence of the boundary heat flux. The second-order accuracy of the present Dirichlet boundary condition treatment for the temperature field is therefore verified for 3-D thermal flows with curved geometry.

3.4.5.2 Neumann boundary condition

For the Neumann problem, the heat flux is given as

$$q_w = -D_t \frac{\partial T}{\partial r} \Big|_{r=r_0} = -D_t \cos(kz) / r_0, \quad (3-78)$$

and the other conditions are the same as in Sec. 3.4.5.1. The analytical solution for the temperature field is

$$T_{\text{ex}}(r, z) = \text{Real} \left[e^{ikz} \frac{I_0(\lambda r)}{\lambda r_0 I_1(\lambda r_0)} \right], \quad (3-79)$$

where $I_1(\lambda r)$ is the modified Bessel's function of the first kind of order 1. There is no azimuthal temperature gradient along the curved boundary; the non-zero tangential gradient is on the z-direction, which is aligned with \mathbf{e}_5 and \mathbf{e}_6 of the lattice velocity vectors. Thus the exact flux conversion formula in Eq. (3-49) can be directly applied.

The error norm E_2 defined in Eq. (3-76) is again examined for the Neumann problem and the results using $\tau_D = 0.51, 0.55$ and 0.75 are shown in Fig. 3-29.

For each of the τ_D values tested, the present Neumann boundary condition treatment leads to a stable computation. The decrease of the relative error E_2 is proportional to $(1/r_0)^2$ on the log-log scale. The temperature field obtained is thus second-order accurate. Comparing with the linear convergence of the temperature field in Sec. 3.4.3.2, it is confirmed that with zero temperature gradient along the curved boundary, second-order accuracy of the temperature field can be achieved with the present Neumann boundary condition treatment for 2-D and 3-D problems.

3.5 Summary and Conclusions

Thermal boundary condition treatments based on the “bounce-back” scheme and spatial interpolation are presented for both the Dirichlet and Neumann conditions. When second-order accuracy is pursued, there is an adjustable parameter for the Dirichlet problem, while the Neumann condition treatment is unique. Three particular schemes

for the Dirichlet condition treatment are presented and their stability and accuracy are examined. All three Dirichlet schemes are stable and Scheme 2 gives smaller error in most cases investigated.

When extended to curved boundaries, the present Dirichlet condition treatment can be applied directly and it leads to second-order accuracy of the temperature field and first-order accuracy of the boundary heat flux. In contrast the proposed Neumann condition treatment requires the determination of heat fluxes in the discrete velocity directions of the TLBE model. A general formula to convert the normal heat flux into the fluxes in the discrete velocity directions is derived. Different from the Dirichlet problem, only first-order accuracy is obtained for the temperature field with Neumann conditions due to the combined effect of the curved boundary and the heat flux conversion. For the special case with no tangential variation of temperature along the curved boundary, the heat flux conversion becomes exact and second-order accuracy of the temperature field can be obtained.

Table 3-1. Accuracy of the TLBE simulations with Dirichlet/Neumann conditions

	Dirichlet condition		Neumann condition		
	parallel straight boundary [†]	curved boundary	parallel straight boundary [†]	curved boundary [§]	curved boundary [¶]
Interior temperature field	2nd-order	2nd-order	2nd-order	2nd-order	1st-order
Boundary heat flux	2nd-order	1st-order	–	–	–
Boundary temperature	–	–	2nd-order	2nd-order	1st-order
Interior temperature gradient	2nd-order	“superlinear” order ~ 1.5	2nd-order	2nd-order	“superlinear” order ~ 1.5

[†] the boundary normal is parallel with a lattice vector;

[§] exact boundary flux;

[¶] coupled schemes.

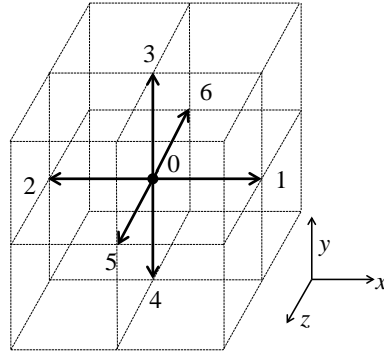


Figure 3-1. Discrete velocity set $\{\mathbf{e}_\alpha\}$ for the D3Q7 TLBE model.

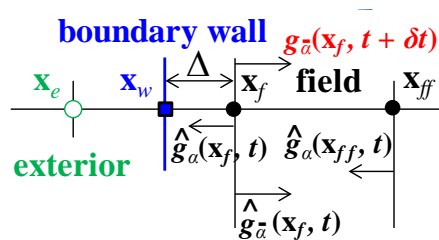


Figure 3-2. Schematic depiction of the lattice link intersected by a boundary wall.

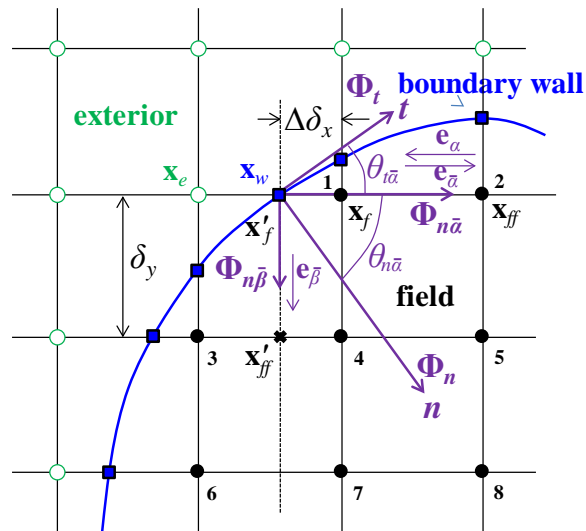


Figure 3-3. Layout of the rectangular lattice and a curved boundary (solid circles: field nodes; solid squares: boundary nodes; open circles: exterior nodes).

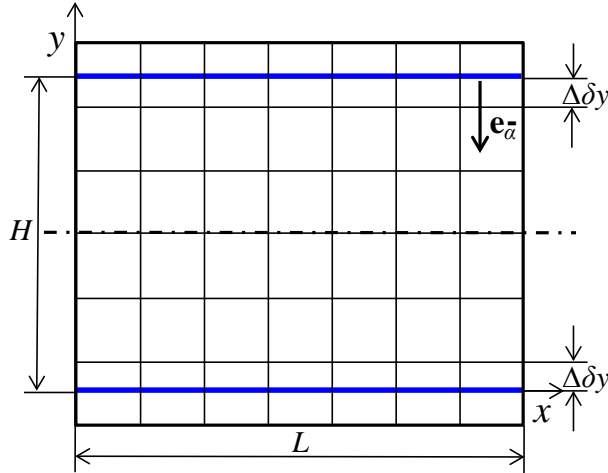


Figure 3-4. Schematic representation of the lattice in a 2-D channel with an arbitrary Δ value.

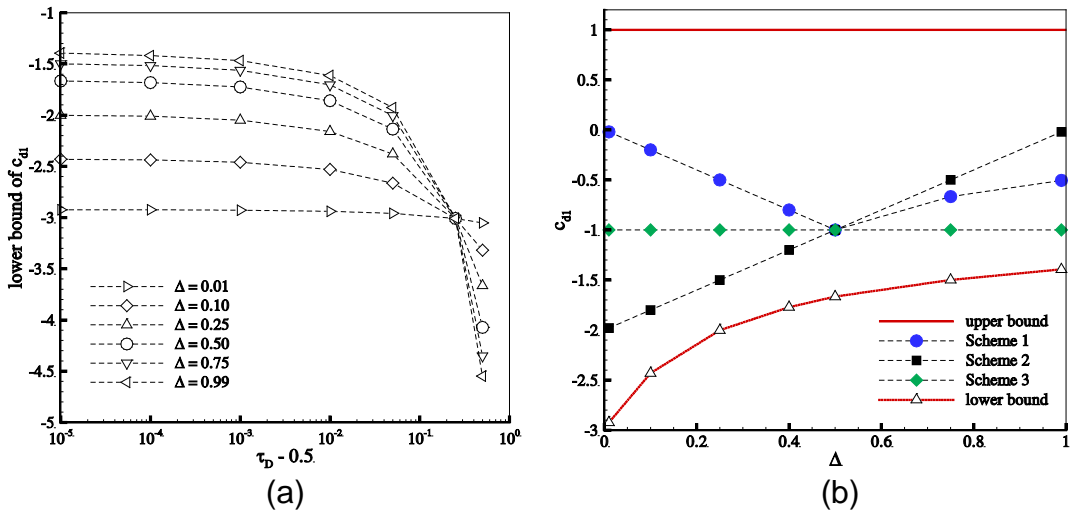


Figure 3-5. (a) Lower stability bound of the adjustable parameter c_{d1} versus $(\tau_D - 0.5)$, and (b) variations of c_{d1} as a function the lattice fraction, Δ , for the present Dirichlet schemes at $\tau_D = 0.50001$ for the channel flow Dirichlet problem (the lower and upper stability bounds are included).

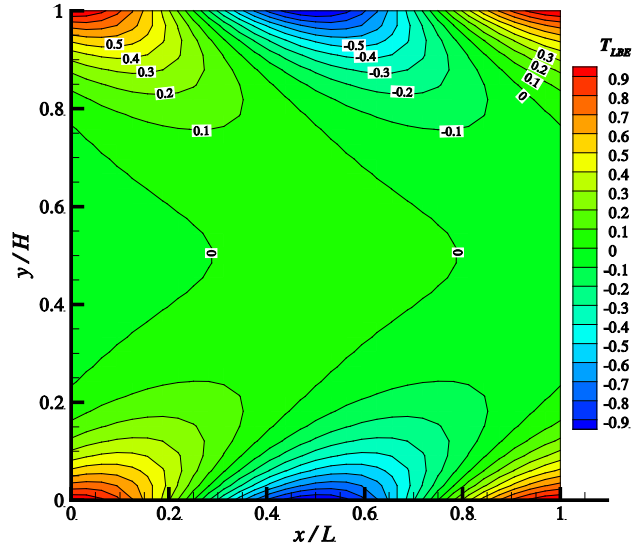


Figure 3-6. Temperature contours in a 2-D channel with a Dirichlet boundary condition using $\tau_D = 0.75$, $\Delta = 0.5$ and $H = 64$. All three schemes reduce to the “bounce-back” condition.

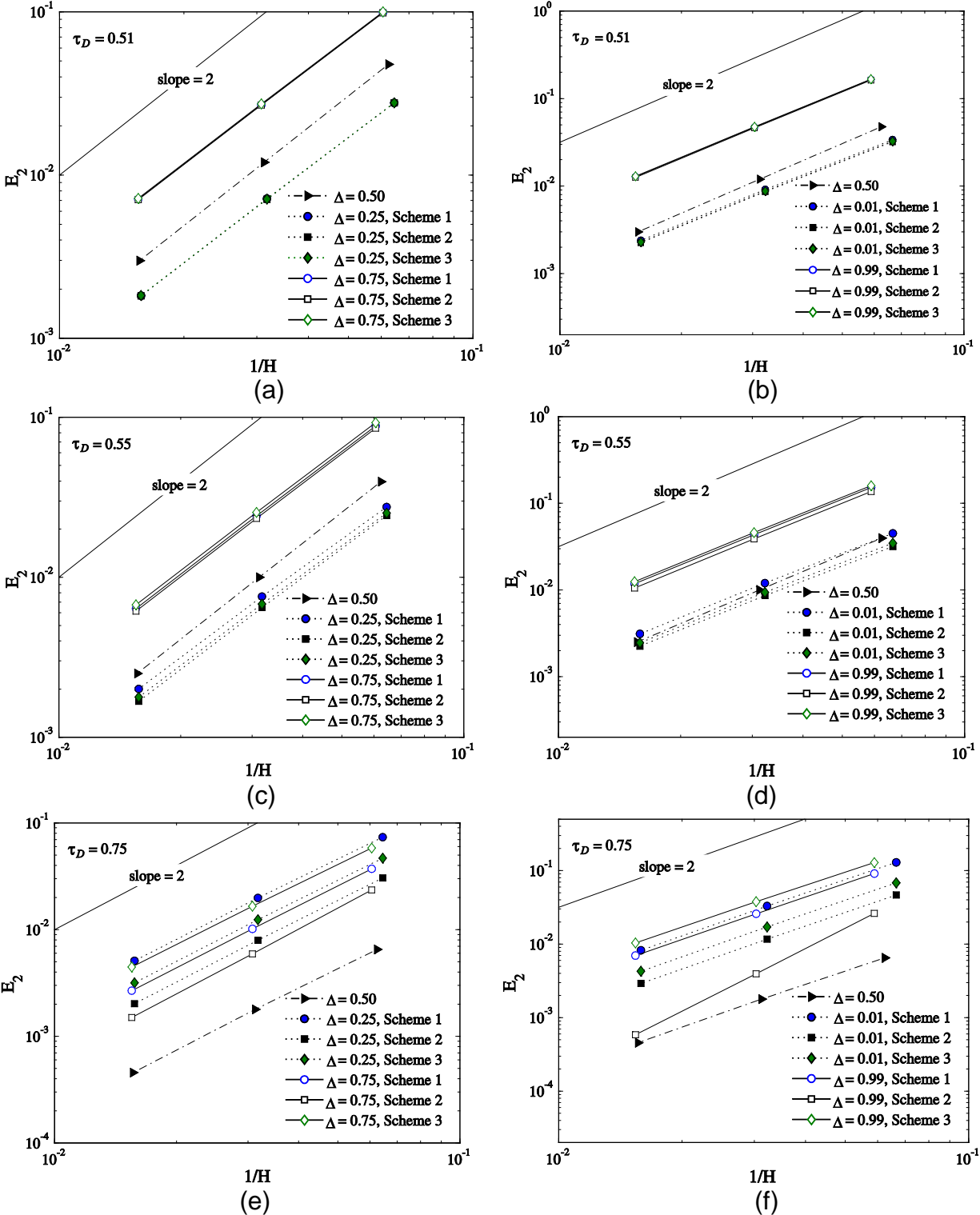


Figure 3-7. Relative L-2 error norm E_2 versus the grid resolution, $1/H$, for the channel flow Dirichlet problem.

(a) $\Delta = 0.50, 0.25$, and 0.75 at $\tau_D = 0.51$, (b) $\Delta = 0.50, 0.01$, and 0.99 at $\tau_D = 0.51$,
(c) $\Delta = 0.50, 0.25$, and 0.75 at $\tau_D = 0.55$, (d) $\Delta = 0.50, 0.01$, and 0.99 at $\tau_D = 0.55$,
(e) $\Delta = 0.50, 0.25$, and 0.75 at $\tau_D = 0.75$, (f) $\Delta = 0.50, 0.01$, and 0.99 at $\tau_D = 0.75$.

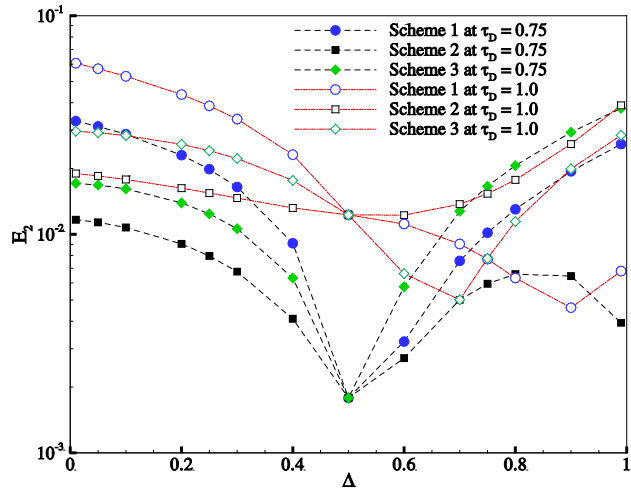


Figure 3-8. Relative L-2 error norm E_2 versus the boundary lattice fraction, Δ , for the channel flow Dirichlet problem at $N_y = 34$.

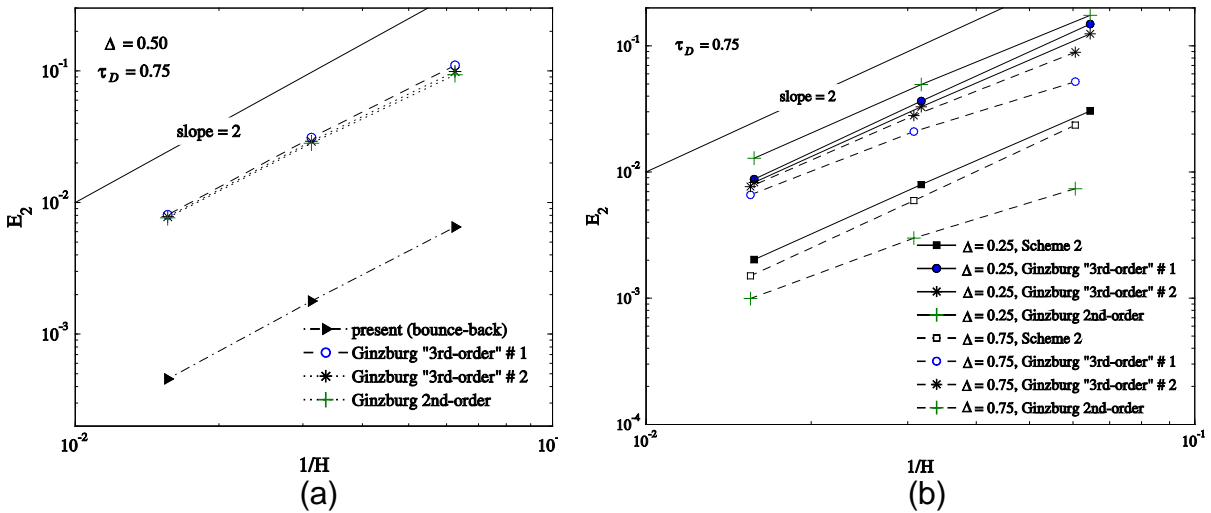


Figure 3-9. Comparison of E_2 obtained using Scheme 2 with those using Ginzburg's schemes (Ginzburg 2005) for the channel flow Dirichlet problem at $\tau_D = 0.75$. (a) $\Delta = 0.50$ (all three schemes reduce to the "bounce-back" scheme), (b) $\Delta = 0.25$ and 0.75 .

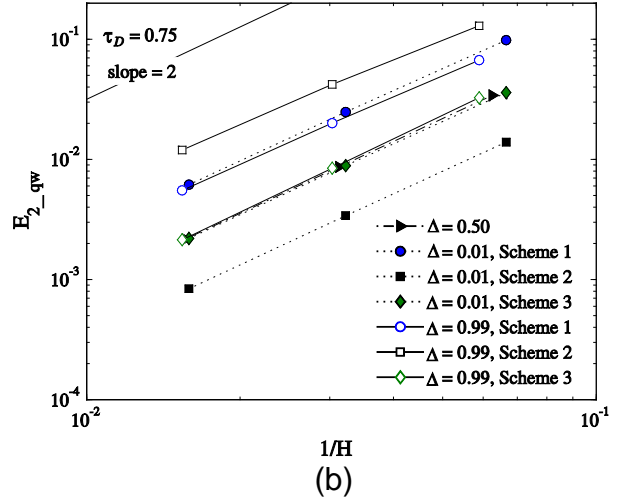
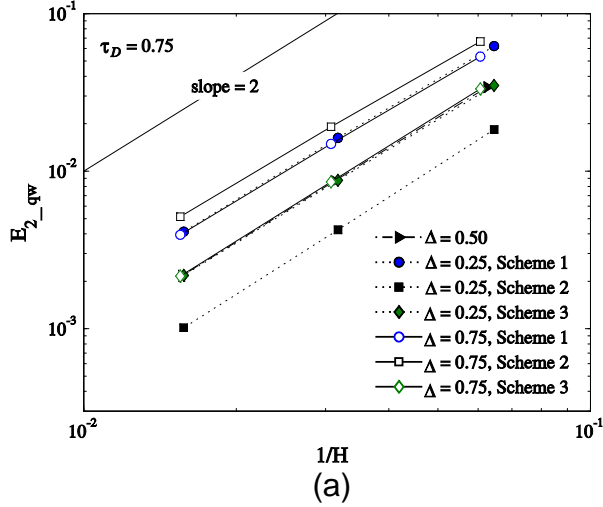


Figure 3-10. Wall heat flux error $E_{2,qw}$ versus the grid resolution, $1/H$, for the channel flow Dirichlet problem. (a) $\Delta = 0.50, 0.25$, and 0.75 at $\tau_D = 0.75$, (b) $\Delta = 0.50, 0.01$, and 0.99 at $\tau_D = 0.75$.

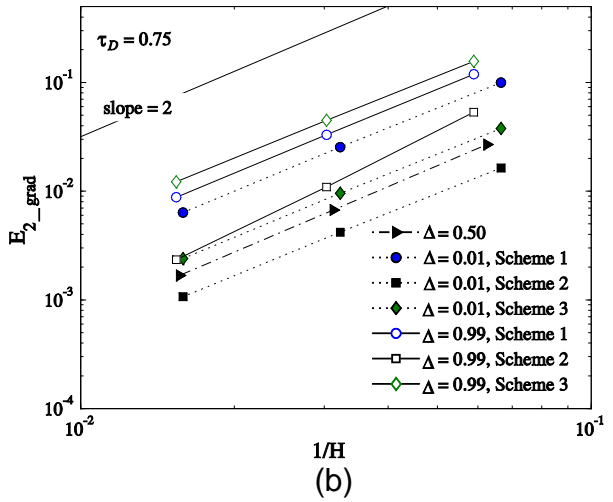
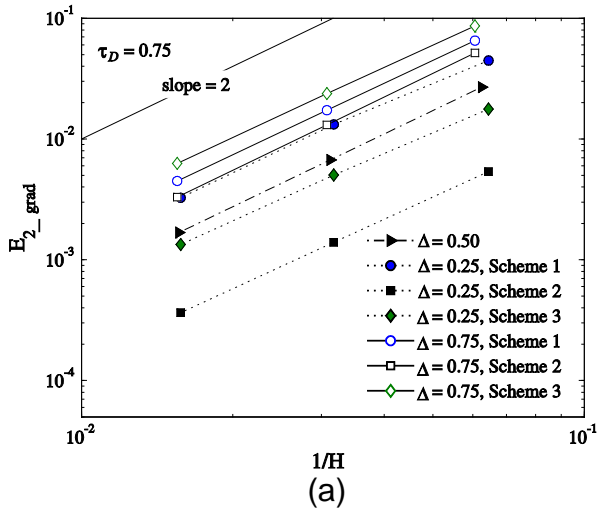


Figure 3-11. Interior gradient error $E_{2,grad}$ versus the grid resolution, $1/H$, for the channel flow Dirichlet problem. (a) $\Delta = 0.50, 0.25$, and 0.75 at $\tau_D = 0.75$, (b) $\Delta = 0.50, 0.01$, and 0.99 at $\tau_D = 0.75$.

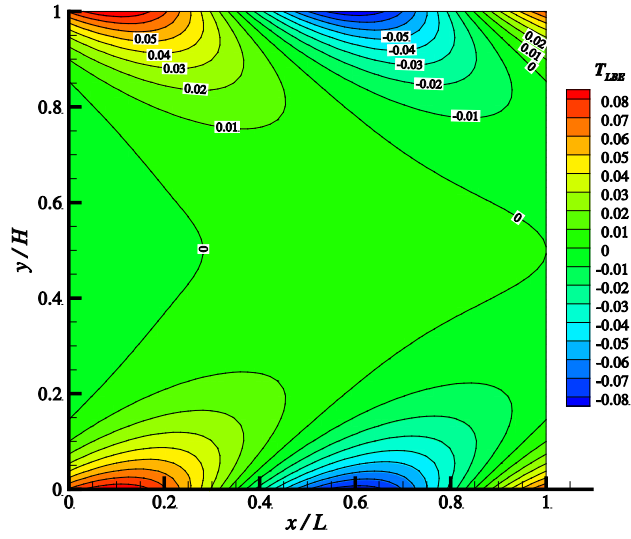


Figure 3-12. Temperature contours in a 2-D channel with a Neumann boundary condition using $\tau_D = 0.75$, $\Delta = 0.5$ and $H = 64$.

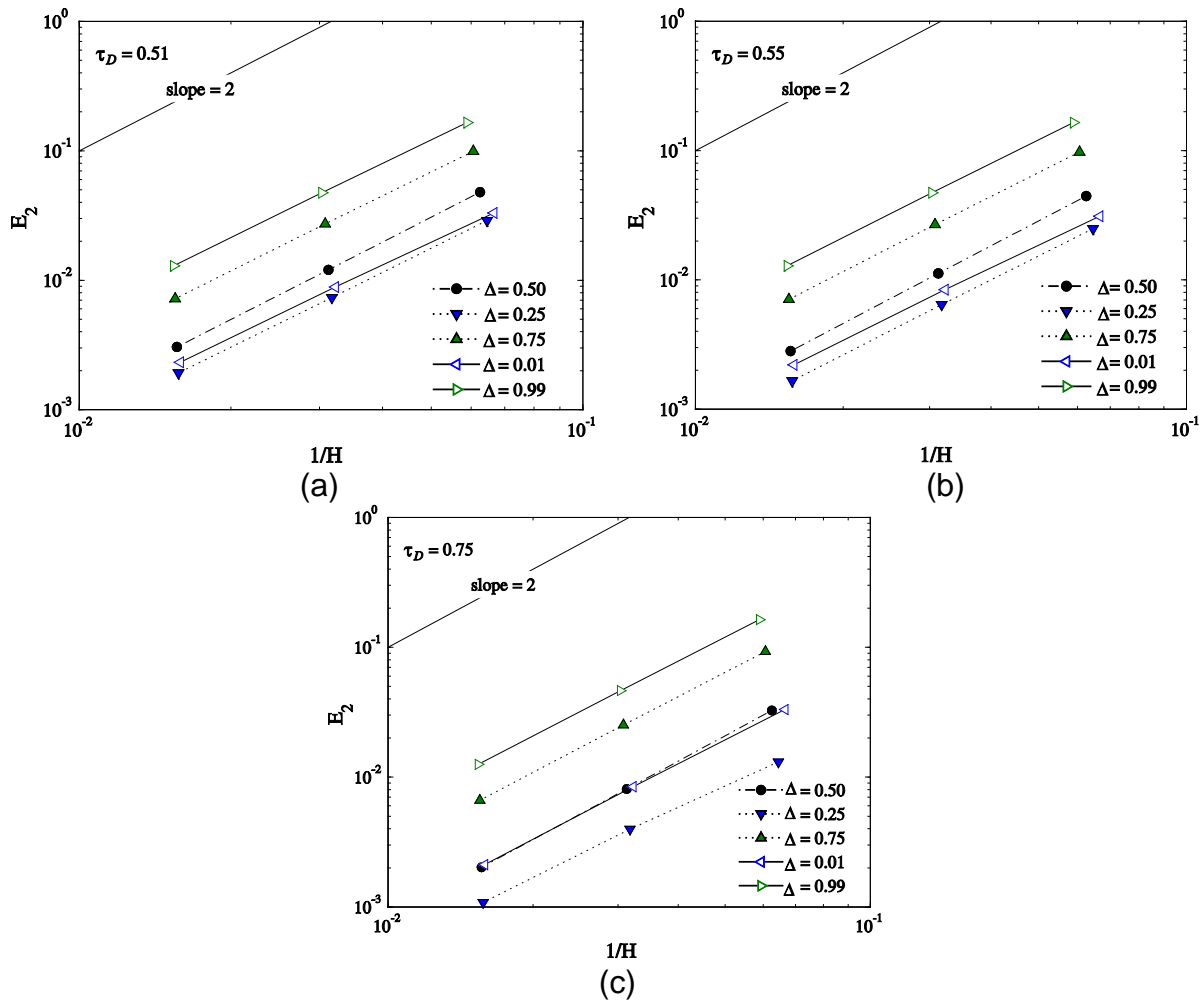


Figure 3-13. Relative L-2 error norm E_2 versus the grid resolution, $1/H$, for the channel flow Neumann problem with various Δ . (a) $\tau_D = 0.51$, (b) $\tau_D = 0.55$, and (c) $\tau_D = 0.75$.

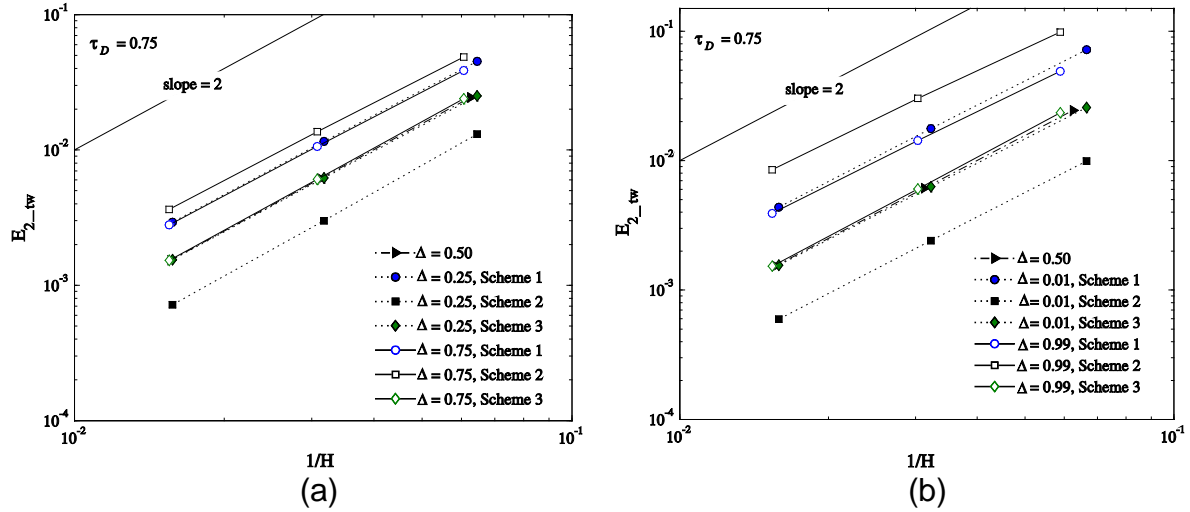


Figure 3-14. Wall temperature error $E_{2,tw}$ versus the grid resolution, $1/H$, for the channel flow Neumann problem. (a) $\Delta = 0.50, 0.25$, and 0.75 at $\tau_D = 0.75$, (b) $\Delta = 0.50, 0.01$, and 0.99 at $\tau_D = 0.75$.

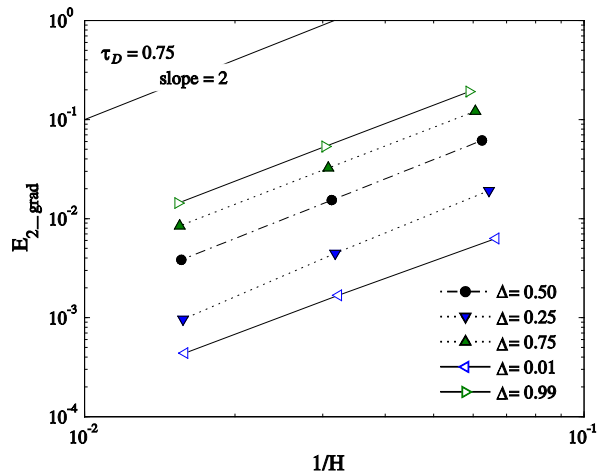


Figure 3-15. Interior gradient error $E_{2,grad}$ versus the grid resolution, $1/H$, for the channel flow Neumann problem.

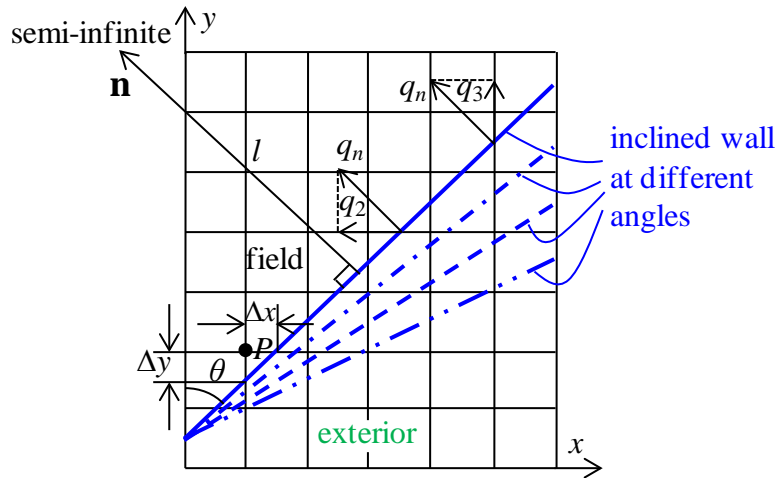


Figure 3-16. Layout of the lattice around the inclined semi-infinite solid.

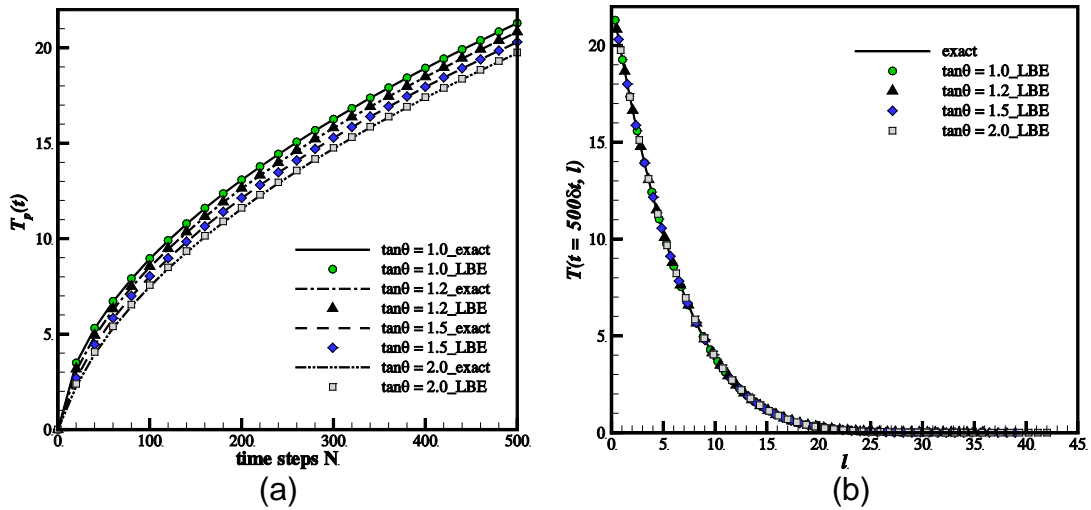


Figure 3-17. (a) Temperature variations with time at point P ; (b) temperature profiles in the y -direction going through P at $t = 500\delta t$.

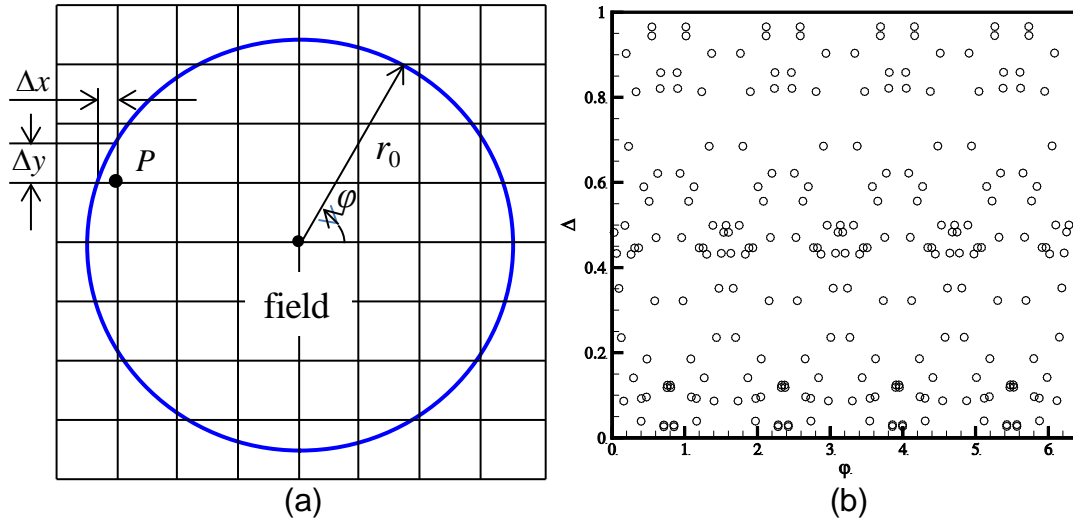


Figure 3-18. (a) Schematic layout of the lattice around a circle; (b) distribution of Δ values along the azimuthal angle φ at $r_0 = 30.5$.

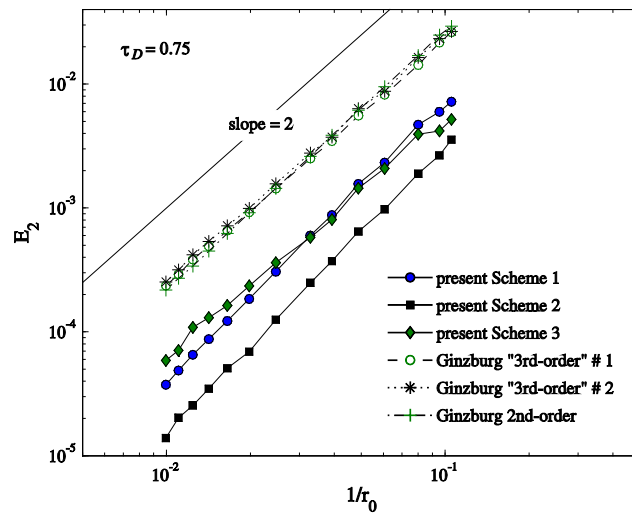


Figure 3-19. Relative L-2 norm error E_2 versus the grid resolution, $1/r_0$, for the steady-state heat conduction inside a circle with a Dirichlet condition (results based on Ginzburg's schemes (2005) are included).

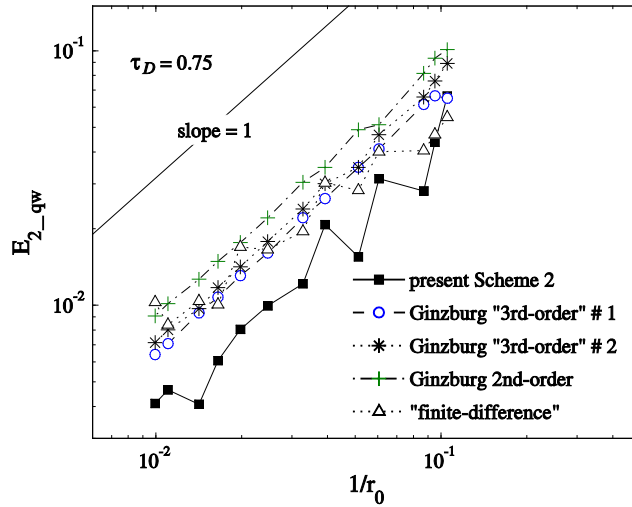


Figure 3-20. Wall heat flux error $E_{2,qw}$ versus the grid resolution, $1/r_0$, for the steady-state heat conduction inside a circle with a Dirichlet condition (results based on Ginzburg's schemes (2005) are included).

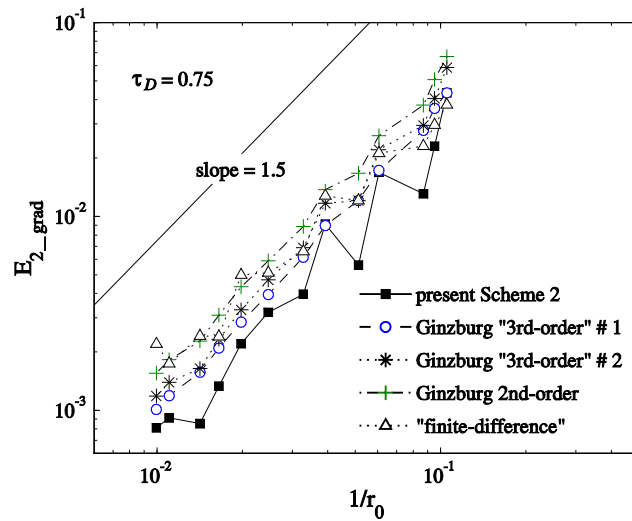


Figure 3-21. Interior gradient error $E_{2,grad}$ versus the grid resolution, $1/r_0$, for the steady-state heat conduction inside a circle with a Dirichlet condition (results based on Ginzburg's schemes (2005) are included).

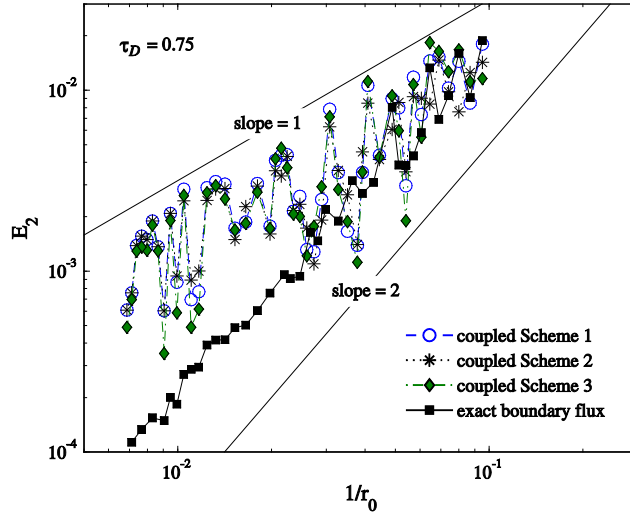


Figure 3-22. Relative L-2 norm error E_2 versus the grid resolution, $1/r_0$, for the steady-state heat conduction inside a circle with a Neumann condition.

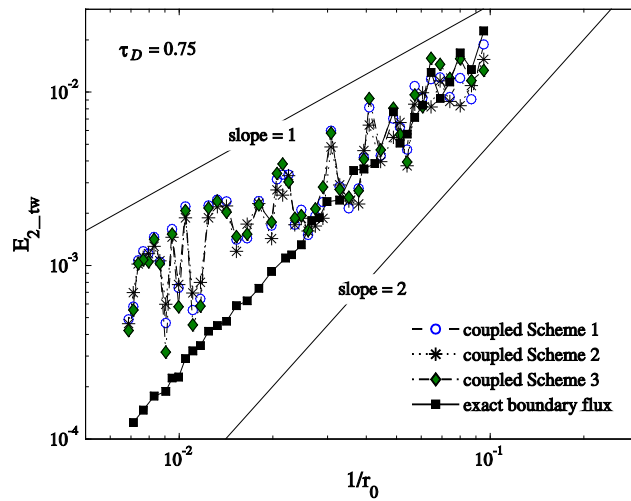


Figure 3-23. Wall temperature error E_{2_tw} versus the grid resolution, $1/r_0$, for the steady-state heat conduction inside a circle with a Neumann condition.

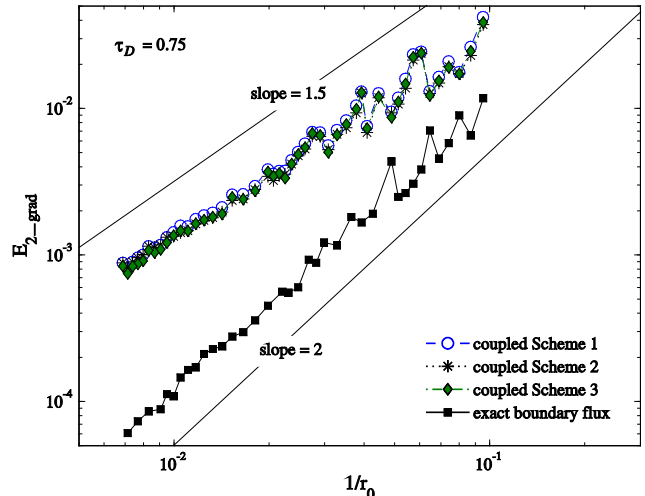


Figure 3-24. Interior gradient error $E_{2,grad}$ versus the grid resolution, $1/r_0$, for the steady-state heat conduction inside a circle with a Neumann condition.

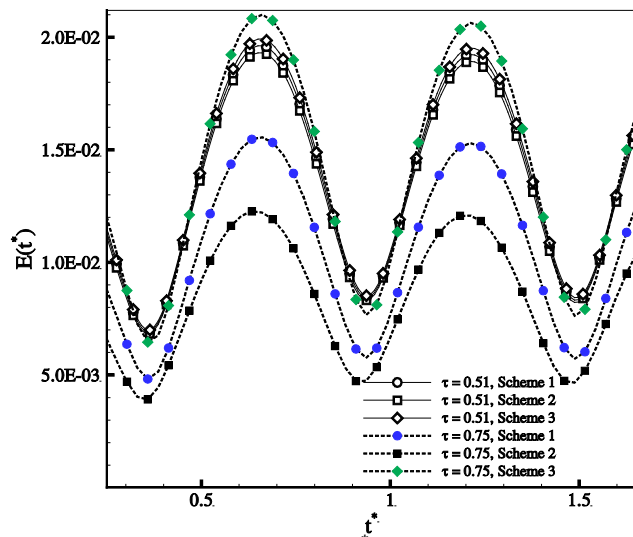


Figure 3-25. Comparison of the error norm $E(t)$ defined in Eq. (3-71) for the transient heat conduction inside a circle using Schemes 1, 2 and 3 with $r_0 = 5.8$.

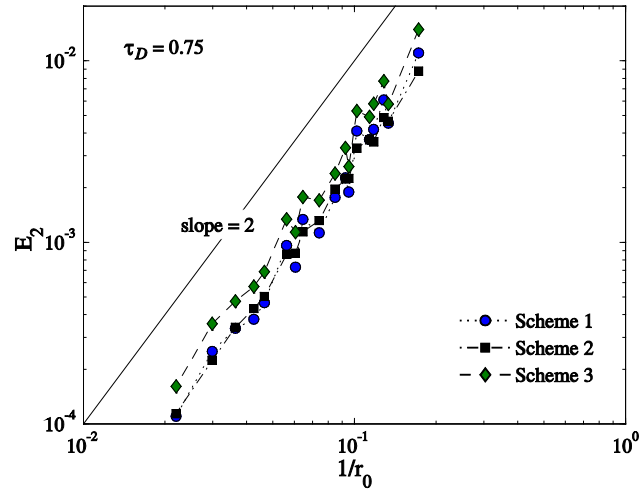


Figure 3-26. Relative L-2 norm error E_2 versus the grid resolution, $1/r_0$, for the transient heat conduction inside a circle.

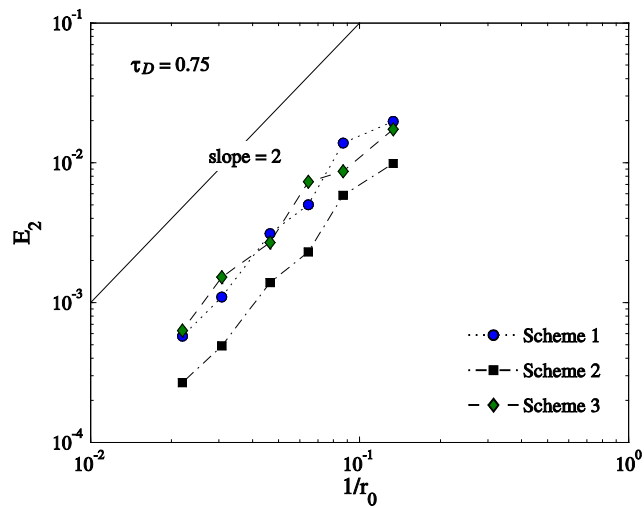


Figure 3-27. Relative L-2 norm error E_2 versus the grid resolution, $1/r_0$, for the pipe flow with a Dirichlet condition.

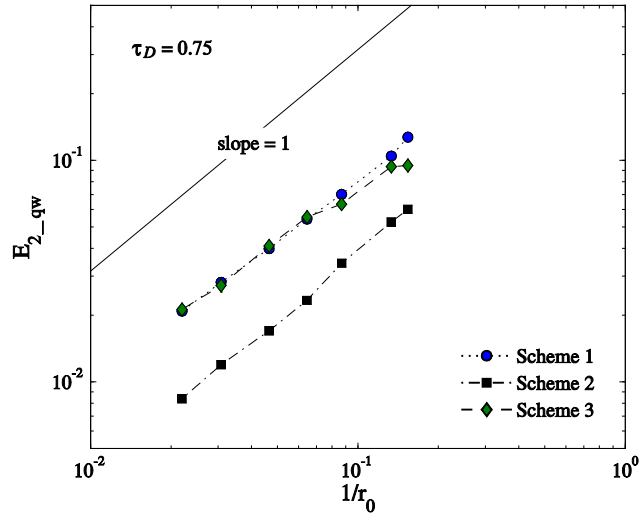


Figure 3-28. Wall heat flux error $E_{2,qw}$ versus the grid resolution, $1/r_0$, for the pipe flow with a Dirichlet condition.

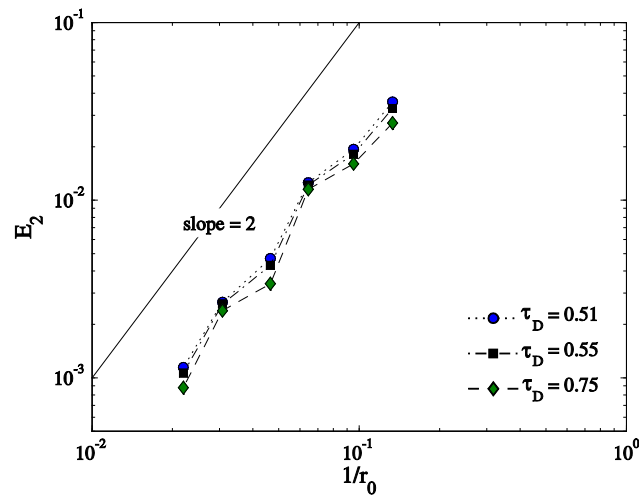


Figure 3-29. Relative L-2 norm error E_2 versus the grid resolution, $1/r_0$, for the pipe flow with a Neumann condition.

CHAPTER 4 HEAT TRANSFER EVALUATION ON CURVED BOUNDARIES IN THERMAL LATTICE BOLTZMANN EQUATION METHOD*

4.1 Introduction

Accurate and efficient evaluation of hydrodynamic forces and heat and mass transfer on boundaries and interfaces involving curved geometry is critical to the growth of the lattice Boltzmann equation (LBE) method for modeling and analyzing transport phenomena.

For momentum transfer on curved boundaries, an accurate force evaluation is crucial, and there are basically two different approaches to determine the fluid dynamic forces in the LBE method: the momentum-exchange approach (Ladd 1994, Behrend 1995, Mei et al. 2002, Yin et al. 2012) and the surface stress integration approach (Mei et al. 2002, He and Doolen 1997, Filippova and Hänel 1998). Mei et al. (2002) compared these two different methods with numerical tests and concluded that the momentum-exchange approach is reliable, accurate and much easier to implement than the stress-integration approach for both two- and three-dimensional flows.

Following the momentum-exchange idea for force evaluation in the LBE method in (Ladd 1994, Mei et al. 2002), an energy-exchange approach for total heat transfer evaluation on curved boundaries in the TLBE method is proposed in this work. At the present time, most of the existing TLBE simulations focus on the temperature field, while the heat transfer on the boundaries and fluid-solid interfaces, especially those with curved geometries, has not been systematically studied. It is the main objective of the present study to establish an accurate and efficient numerical approach to determine the boundary heat transfer based on the TLBE temperature distribution functions

* This work has been accepted for publication in *ASME Journal of Heat Transfer* (Li et al. 2013b).

instead of approximating the heat transfer from the solved temperature field using finite-difference schemes. In this manner, the heat transfer simulation is conducted on the same level as that of the temperature distribution functions, and thus the mesoscopic nature of the LBE method is preserved in the heat transfer evaluation.

To formulate the problem, the TLBE model with a multiple-relaxation-time (MRT) collision operator for the convection-diffusion equation (CDE) proposed by Yoshida and Nagaoka (2010) is used in the present work. This approach has proved useful due to its second-order accuracy in space and convenience for implementation compared with those TLBE models (Chen et al. 1994, He et al. 1998, Guo et al. 2007) that were derived from the continuous Boltzmann equation. The thermal boundary condition treatment in Chapter 3 is implemented as it preserves the exact geometry on the boundary, and has second-order accuracy for both the Dirichlet and Neumann conditions on straight walls and at least first-order accuracy on curved boundaries (Li et al. 2013a). In the present heat transfer evaluation method, the boundary heat fluxes in the discrete lattice velocity directions of the TLBE model are directly obtained from the temperature distribution functions at the lattice nodes and the temperature values on the boundary, rather than using any finite-difference schemes based on the solution for the temperature field. From the conservation of energy, integration of the discrete heat fluxes with effective surface areas gives the energy exchange on the boundary, thus bypassing the need for determining the boundary heat flux in the normal direction. In addition, due to the uniform lattice spacing in the TLBE model, the effective surface area for each of the discrete heat fluxes is uniform and constant. The surface area approximation in the heat flux integration, which is laborious in general and impractical

in complex geometries such as porous structures, is thus avoided. These two major benefits make the present heat transfer evaluation very efficient in curved-boundary simulations. It is worth noting that the present heat transfer evaluation method can be simply extended to mass transfer computations on curved boundaries as the general CDE also governs the species mass concentration. The Dirichlet, Neumann and mixed thermal boundary conditions can be simply replaced with corresponding concentration boundary conditions.

A series of numerical test cases are presented to validate the proposed heat transfer evaluation scheme, including (i) 2-dimensional (2-D) steady-state plug flow in a channel with a constant axial velocity and a sinusoidal wall temperature distribution, (ii) 1-D transient heat conduction in an inclined semi-infinite solid, (iii) 2-D transient heat conduction inside a circle with a temporal sinusoidal wall temperature variation, (iv) 3-D steady-state thermal flow in a circular pipe with a constant axial velocity and a sinusoidal wall temperature variation along the flow direction, and (v) 2-D steady-state natural convection in a square enclosure with a circular cylinder located at the center. For cases (i) through (iv) analytical solutions are available and the convergence of numerical results shows that the proposed heat transfer evaluation scheme is second-order accurate for straight boundaries perpendicular to one of the discrete lattice velocity vectors, while for curved boundaries only first-order accuracy of the heat transfer can be obtained due to the irregularly distributed lattice fractions cut by the curved boundary. For case (v), the surface-averaged Nusselt numbers computed using the proposed technique for heat transfer evaluation on curved boundaries agree well with published numerical results in the literature.

4.2 Heat Transfer Evaluation

The D3Q7 and D2Q5 TLBE models by Yoshida and Nagaoka (2010) and the thermal boundary condition treatment by Li et al. (2013a) are implemented in the present boundary heat transfer evaluation. The details for the TLBE models and thermal boundary condition treatment are presented in Sections 3.3.2 and 3.3.3 of Chapter 3.

4.2.1 Boundary Heat Flux

The present heat transfer evaluation is based on the integration of the boundary heat flux $\Phi_{n\bar{\alpha}}$ in the discrete velocity direction $\mathbf{e}_{\bar{\alpha}}$ with constant effective surface area in the TLBE model instead of integrating the normal heat flux Φ_n . As discussed in Remark 2 of Section 3.3.3, the boundary heat flux $\Phi_{n\bar{\alpha}}$ can be conveniently obtained by combining the Dirichlet and Neumann treatments in Eqs. (3-32) and (3-38) to yield

$$\Phi_{n\bar{\alpha}} = \frac{1-c_{d1}}{2} \frac{\delta x}{\delta t} \left[-(2\Delta + 1)\hat{g}_{\alpha}(x_f, t) + (2\Delta - \frac{2}{1-c_{d1}})\hat{g}_{\alpha}(x_{\#}, t) + (\frac{2}{1-c_{d1}} - 1)\hat{g}_{\bar{\alpha}}(x_f, t) + \varepsilon\Phi_d \right], \quad (4-1)$$

where c_{d1} is the adjustable variable discussed in Eq. (3-32) (see also Eq. (3-41a) for the notations).

For mixed boundary conditions, Φ_n is not explicitly known; thus Eq. (4-1) for $\Phi_{n\bar{\alpha}}$ cannot be used. Instead, the Cartesian decomposition method discussed in Section 3.3 should be employed to compute $\Phi_{n\bar{\alpha}}$. The computed values of $\Phi_{n\bar{\alpha}}$ at all the boundary intersections along all the relevant lattice vector directions then form the basis for heat transfer evaluation on the boundary surface.

4.2.2 Heat Transfer on Curved Boundaries

Intuitively, heat transfer on a boundary can be computed following a three-step procedure for given Dirichlet or mixed boundary conditions in the TLBE method. First, the heat flux $\Phi_{n\bar{\alpha}}$ in the discrete lattice velocity direction is obtained along the boundary. Then the relationship between $\Phi_{n\bar{\alpha}}$ and Φ_n can be applied to obtain the normal heat flux, Φ_n , on the boundary. Integration of the normal heat flux along the boundary wall gives the heat transfer rate

$$\dot{Q}_w = \int_{\Omega} q_n dA = \int_{\Omega} \Phi_n dA, \quad (4-2)$$

where dA is the local surface area.

There are two main difficulties associated with the heat transfer rate integration in Eq. (15), especially for that on curved boundaries. First, the heat flux conversion from $\Phi_{n\bar{\alpha}}$ to Φ_n is laborious in general. Second, the integration of the normal heat flux requires a local surface area approximation of the actual boundary. When the boundary nodes, i.e., the intersection locations on the boundary by the lattice, are not uniformly distributed (see Fig. 4-1), the effective surface area approximation for the normal heat flux would require a great amount of effort for curved boundaries and might be impractical for irregular-geometries such as thermal simulations in porous media. To avoid the boundary heat flux conversion and surface area approximation, we propose the following heat transfer evaluation technique based on the idea of energy exchange.

Following the principle of energy conservation, the integration of the normal heat flux at a boundary, which accounts for the energy transferred into the field, must be equal to the integration of the heat flux in the discrete velocity directions of the TLBE model with effective surface areas. For each of the boundary nodes such as \mathbf{x}_w in Fig.

4-1 there is a discrete boundary heat flux, $\Phi_{n\bar{\alpha}}$, or $\Phi_{n\bar{\beta}}$, that needs to be determined in TLBE simulations, according to whether the boundary is cut by the link along the discrete velocity vector, $\mathbf{e}_{\bar{\alpha}}$, or $\mathbf{e}_{\bar{\beta}}$, respectively. When the boundary is intersected exactly at a lattice node, i.e., $\Delta = 0$ or $\Delta = 1$, both $\Phi_{n\bar{\alpha}}$ and $\Phi_{n\bar{\beta}}$ need to be determined at the same boundary node. Because the lattice nodes are distributed in the Cartesian coordinates with uniform lattice spacing in the standard TLBE models, the effective surface areas for $\Phi_{n\bar{\alpha}}$ and $\Phi_{n\bar{\beta}}$ are $(\delta y \times \delta z)$ and $(\delta x \times \delta z)$, respectively, with δz the lattice spacing in the direction perpendicular to the plane. When $\delta x = \delta y = \delta z = 1$, the effective surface area is unity for all the discrete heat fluxes, and thus the heat transfer on the boundary is simply a summation of all the discrete heat fluxes multiplied by the unit effective surface area.

For efficient computation, two scalar arrays, $w(i, j)$ and $w_b(i, j)$ are introduced, where i and j are the indices of the lattice nodes in a 2-D problem. The extension to 3-D problems is straightforward. We choose $w(i, j) = 1$ for all the field nodes \mathbf{x}_f , and $w(i, j) = 0$ for all the exterior nodes \mathbf{x}_e . The array $w_b(i, j)$ is set to zero everywhere except for those field nodes that satisfy $\mathbf{x}_f + \mathbf{e}_{\bar{\alpha}} \delta t = \mathbf{x}_e$ (see Fig. 4-1), where a value of 1 is assigned. By summing the boundary heat fluxes from all discrete velocity directions into the field nodes with $w_b(i, j) = 1$, the heat transfer across the boundary into the field over one time step δt is

$$\dot{Q}_w = \sum_{w_b=1} \sum_{\bar{\alpha} \neq 0} \left[\Phi_{n\bar{\alpha}} (\delta x)^2 \right] \times \left[1 - w(\mathbf{x}_f + \mathbf{e}_{\bar{\alpha}} \delta t) \right]. \quad (4-3)$$

It is noticed that the fraction $\Delta = \|\mathbf{x}_f - \mathbf{x}_w\| / \|\mathbf{x}_f - \mathbf{x}_e\|$ is not explicitly included in Eq. (4-3), but it is implicitly taken into account in the determination of $\Phi_{n\bar{\alpha}}$ in the boundary

condition treatment. Thus it is expected that the heat transfer evaluated from Eq. (4-3) will converge with the same order-of-accuracy as that of the corresponding boundary condition treatment. This will be verified in the Section 4.3 with numerical tests.

4.2.3 Temperature Gradient in the Interior Field

In athermal LBE simulations, Mei et al. (2002) gave a formula for deviatoric stress evaluation as

$$\sigma_{ij} = \left(1 - \frac{1}{2T}\right) \sum_{\alpha} f_{\alpha}^{(\text{neq})}(\mathbf{x}, t) \left(e_{\alpha i} e_{\alpha j} - \frac{1}{D} \mathbf{e}_{\alpha} \cdot \mathbf{e}_{\alpha} \delta_{ij} \right), \quad (4-4)$$

where $f_{\alpha}^{(\text{neq})}$ is the nonequilibrium component of the velocity distribution function $f(\mathbf{x}, \boldsymbol{\xi}_{\alpha}, t)$, $e_{\alpha i}$ and $e_{\alpha j}$ are the Cartesian components of the discrete velocity vector \mathbf{e}_{α} and D is the spatial dimensions.

Similarly, with the definition of the nonequilibrium part of the temperature distribution function $g_{\alpha}^{(\text{neq})} = g_{\alpha} - g_{\alpha}^{(\text{eq})}$, the following formula for the temperature gradient inside the field can be derived

$$-D_{ij} \frac{\partial \phi}{\partial x_j} = \left(\frac{\delta x}{\delta t} \right) \sum_{\alpha=1}^m e_{\alpha i} g_{\alpha}^{(\text{neq})} - \frac{\delta_{ij}}{2\tau_{ij}} \left(\frac{\delta x}{\delta t} \right) \sum_{\alpha=1}^m e_{\alpha j} g_{\alpha}^{(\text{neq})}. \quad (4-5)$$

The physical basis for the shear stress or temperature gradient in terms of respective $f_{\alpha}^{(\text{neq})}$ or $g_{\alpha}^{(\text{neq})}$ is that only the nonequilibrium components of the distribution functions contribute to the velocity or temperature gradient evaluations.

Yoshida and Nagaoka (2010) also provided a formula for the temperature gradient approximation in terms of the total temperature distribution g_{α} as

$$\tau_{ij} \frac{\partial \phi}{\partial x_j} = \frac{\delta t v_i}{\varepsilon (\delta x)^2} \phi - \frac{1}{\varepsilon \delta x} \sum_{\alpha=0}^m e_{\alpha i} g_{\alpha}. \quad (4-6)$$

The formula in Eq. (4-6) was also used in Chapter 3. Recalling the relationship between τ_{ij} and D_{ij} in Eq. (3-14), Eq. (4-6) can be rewritten as

$$-D_{ij} \frac{\partial \phi}{\partial x_j} = \left(\frac{\delta x}{\delta t} \right) \left[\sum_{\alpha=0}^m e_{\alpha i} g_{\alpha} - \frac{\delta t}{\delta x} v_i \phi \right] - \frac{\delta_{ij}}{2\tau_{ij}} \left(\frac{\delta x}{\delta t} \right) \left[\sum_{\alpha=0}^m e_{\alpha j} g_{\alpha} - \frac{\delta t}{\delta x} v_j \phi \right]. \quad (4-7)$$

With the definition of $g_{\alpha}^{(eq)}$ in Eq. (3-7), $\sum_{\alpha=0}^m e_{\alpha i, j} g_{\alpha}^{(eq)} = \frac{\delta t}{\delta x} v_{i, j} \phi$ can be derived and Eq. (4-7)

becomes the same as Eq. (4-5). Thus the present interior temperature gradient evaluation (4-5) is equivalent to that proposed by Yoshida and Nagaoka (2010) in Eq. (4-6).

4.3 Numerical Results and Discussion

A series of numerical tests are conducted to validate the applicability and accuracy of the proposed heat transfer evaluation method. The first test is for thermal flows in a 2-D channel with straight walls. The boundary walls in this test are placed in arbitrary locations between the lattice nodes so that the effect of the Δ value on the heat transfer evaluation is fully investigated. Interior temperature gradient evaluation is also examined in this test. The second test is for the transient heat conduction in an inclined semi-infinite solid intersected by the lattice with irregular Δ distributions. Curved boundaries are considered in the third to fifth tests. A transient Dirichlet condition is imposed on the surface of a circle in the third test, and thermal convection diffusion in a 3-D circular pipe is studied in the fourth test. Analytical solutions are available for tests (i) to (iv), and thus the accuracy of the present heat transfer evaluation can be fully assessed. The fifth test involves the natural convection simulation in a square enclosure with a circular cylinder placed in the center and is intended to demonstrate the

applicability of the proposed heat transfer evaluation method when the TLBE model is coupled with an athermal LBE model for the velocity field.

For simplicity, thermal diffusion is assumed to be isotropic in all cases, and thus the off-diagonal components in the relaxation matrix are zeros and the diagonal elements are related to the diffusion coefficient D_t as

$$\tau_D = \frac{1}{2} + \frac{\delta t}{\varepsilon(\delta x)^2} D_t. \quad (4-8)$$

A typical value of $\tau_D = 0.75$ is used in each case; the other relaxation coefficients are $\tau_P = 1$ ($p = 0, 4, 5, 6$ in 3-D and $p = 0, 3, 4$ in 2-D) since they do not contribute to the leading-order solution of the CDE. More details about the numerical stability and accuracy of the temperature field computations for those examples have been presented in Chapter 3.

4.3.1 Two-D Steady-State Channel Flow

First we consider the 2-D steady-state plug flow as discussed in Section 3.4.1. The boundary walls are straight and perpendicular to the discrete velocity vector $\mathbf{e}_{\bar{\alpha}}$ (see Fig. 3-4), thus the boundary heat flux in the discrete velocity direction is equal to the normal heat flux, i.e., $\Phi_{n\bar{\alpha}} = \Phi_n$ and the surface area is exact. Hence we only need to examine the heat flux on the boundaries for heat transfer evaluation with Dirichlet conditions. In addition, the interior temperature gradients in both x - and y - directions are separately examined when Dirichlet and Neumann boundary conditions are respectively imposed. It is worth mentioning that the present heat transfer evaluation method in Eq. (4-3) can be directly applied to determine the heat transfer over any portion of a complete boundary wall. Hence even though the overall heat transfer on the boundary walls from $x = 0$ to $x = L$ in this test is zero due to the sinusoidal boundary conditions

applied to obtain analytical solutions, the accuracy assessment of the boundary heat flux on the whole boundary is representative for the heat transfer evaluation on any portion of the boundary wall and for any other boundary conditions applied as well. The following results are presented at the Péclet number, $Pe = HU/D_t = 50$.

4.3.1.1 Channel flow with a Dirichlet boundary condition

The Dirichlet problem in Section 3.4.1.1 is further studied to evaluate the heat transfer evaluation. With the analytical solution of the temperature field available in Eq. (3-55), the exact boundary heat fluxes on the walls and the interior temperature gradients in both directions can be calculated and the following L-2 error norms are computed to assess the accuracy of the LBE solutions

$$E_{2_qw} = \left\{ \sum_{\text{boundary nodes}} [(\Phi_{n\bar{a}})_{\text{LBE}} - (\Phi_{n\bar{a}})_{\text{ex}}]^2 / \sum_{\text{boundary nodes}} (\Phi_{n\bar{a}})_{\text{ex}}^2 \right\}^{1/2}, \quad (4-9)$$

$$E_{2_gx} = \left\{ \sum_{\text{interior nodes}} \left[\left(\frac{\partial T}{\partial x} \right)_{\text{LBE}} - \left(\frac{\partial T}{\partial x} \right)_{\text{ex}} \right]^2 / \sum_{\text{interior nodes}} \left(\frac{\partial T}{\partial x} \right)_{\text{ex}}^2 \right\}^{1/2}, \quad (4-10)$$

$$E_{2_gy} = \left\{ \sum_{\text{interior nodes}} \left[\left(\frac{\partial T}{\partial y} \right)_{\text{LBE}} - \left(\frac{\partial T}{\partial y} \right)_{\text{ex}} \right]^2 / \sum_{\text{interior nodes}} \left(\frac{\partial T}{\partial y} \right)_{\text{ex}}^2 \right\}^{1/2}. \quad (4-11)$$

The results of E_{2_qw} versus the grid resolution, $1/H$, at different Δ values are shown in Figs. 4-2 (a, b). The Schemes 1, 2 and 3 throughout the simulation results in this work correspond to the three different choices of the adjustable coefficient c_{d1} that are specified in Eqs. (3-35 a-c) and used in Eqs. (3-32) and (4-1), respectively, for the Dirichlet condition implementation and boundary heat flux evaluation. Clearly, quadratic convergence is observed for all cases, demonstrating the second-order accuracy for the boundary heat flux and thus the overall heat transfer evaluation. Fig. 4-3 shows the

error norm E_{2_qw} as a function of the link fraction Δ for the three schemes at $Ny = 34$ (Ny denotes the number of lattice nodes in y -direction in Fig. 3-4). For both $\tau_D = 0.75$ and 1.0 , it is observed that the variations of the error norm E_{2_qw} are very small for Scheme 3 in the whole range of $0 \leq \Delta \leq 1$. For $0 \leq \Delta \leq 1/2$, Scheme 2 gives the smallest errors and Scheme 1 gives the largest of the three. For the other half range of $1/2 \leq \Delta \leq 1$, however, Scheme 2 shows larger errors than the other two. It is thus more favorable to place the boundary at the locations of $\Delta \leq 1/2$ and applying Scheme 2 to obtain better accuracy of the heat transfer. For curved boundaries, the Δ values are irregularly distributed thus the three schemes are expected to have similar overall performance. The computational results of the entire temperature field in Section 3.4.1.1 showed that Scheme 2 gave smaller errors than Schemes 1 and 3 in most cases studied thus Scheme 2 is also recommended in the proposed heat transfer evaluation schemes.

Furthermore, the dependence of E_{2_qw} on the relaxation parameter τ_D is illustrated in Fig. 4-4, where $Ny = 66$ is used and the results are presented with respect to $(\tau_D - 0.5)$ since the positivity of the diffusion coefficient and numerical stability require that $\tau_D > 1/2$ (Yoshida and Nagaoka 2010, Li et al. 2013a). All three schemes approach an asymptotic minimum E_{2_qw} when $\tau_D \rightarrow 1/2$. It is noted that smaller τ_D values correspond to smaller time steps; thus more time steps are required in general to reach steady state. On the other hand, the error norms increase almost linearly with τ_D for $\tau_D > 0.60$ as observed in Fig. 4-4. For accurate computations it is thus preferable to choose $\tau_D < 1.0$.

The interior temperature gradients in both x - and y - directions are evaluated with the formula in Eq. (4-5) and their error norms E_{2_gx} and E_{2_gy} defined in Eqs. (4-10) and

(4-11), versus the grid resolution, $1/H$, at different Δ values are shown in Figs. 4-5 and 4-6, respectively, with the three Dirichlet schemes in Eqs. (3-35 a-c) used. Second-order accuracy is obtained for each case in Figs. 4-5 and 4-6 and Scheme 2 shows better performance than the other two for most cases studied.

4.3.1.2 Channel flow with a Neumann boundary condition

The Neumann problem in Section 3.4.1.2 is again used here to study the interior temperature gradient errors E_{2_gx} and E_{2_gy} defined in (4-10) and (4-11), respectively. Figs. 4-7 (a, b) show the results of E_{2_gx} and E_{2_gy} versus $1/H$ for Δ ranging from 0.01 to 0.99. Again, second-order accuracy is obtained.

It is thus concluded that the proposed boundary heat transfer and interior temperature gradient evaluation methods are second-order accurate on straight boundaries perpendicular to one of the lattice vectors.

4.3.2 One-D Transient Conduction in an Inclined Semi-Infinite Solid

The layout of the lattice around a semi-infinite solid with different inclination angles is shown in Fig. 3-16. The width of the solid end is W and identical boundary conditions are given along the solid end for this one-D conduction problem.

With zero initial temperature and Dirichlet condition $T(l=0) = f(t)$ at the end, the transient temperature is solved to be

$$T_{\text{ex}}(t, l) = \frac{2}{\sqrt{\pi}} \int_{\frac{l}{2\sqrt{D_t t}}}^{\infty} f\left(t - \frac{l^2}{4D_t \mu^2}\right) e^{-\mu^2} d\mu, \quad (4-12)$$

where l is the distance in the normal direction of the solid end, and the heat transfer rate at the boundary is

$$\dot{Q}_w = Wq_n = -WD_t(\partial T_{\text{ex}} / \partial n)|_{l=0}. \quad (4-13)$$

Two transient boundary conditions for $f(t)$ are considered in this section. The three Dirichlet schemes in Eqs. (3-35 a-c) give very similar numerical solutions; thus only the results from Scheme 2 are presented for brevity.

4.3.2.1 Dirichlet Boundary condition $f(t) = kt^{1/2}$

This temperature boundary condition with k being a constant corresponds to a constant heat flux on the solid end (Hahn and Ozisik, 2012)

$$q_n = -D_t \frac{\partial T_{\text{ex}}}{\partial n} \Big|_{l=0} = \frac{k}{2} \sqrt{\pi D_t} . \quad (4-14)$$

In the TLBE simulations, the boundary heat fluxes $\Phi_{n\bar{a}}$ in the discrete velocity directions obtained from Eq. (4-1) are summed up along the boundary to yield the heat transfer rate \dot{Q}_w as in Eq. (4-3). The numerical results of \dot{Q}_w are compared with exact solutions in Fig. 4-8 for different inclination angles $\theta = \tan^{-1}(1.0)$, $\tan^{-1}(1.2)$, $\tan^{-1}(1.5)$, and $\tan^{-1}(2.0)$ with $k = 1$. Because of the initial temperature discontinuity at $t = 0$ on the boundary, there exists oscillation in the numerical results of \dot{Q}_w at small time in Fig. 4-8 for each case tested. After 10 time steps, the numerical results agree very well with exact solutions. To further verify the heat transfer evaluation in this test, another Dirichlet boundary condition resulting in time-varying heat transfer is considered in the following.

4.3.2.2 Dirichlet Boundary condition $f(t) = 1 - \exp(-\lambda t)$

When an exponentially decaying boundary condition $f(t) = 1 - \exp(-\lambda t)$ is applied, the heat flux on the boundary becomes (Hahn and Ozisik, 2012)

$$q_n = -D_t \frac{\partial T_{\text{ex}}}{\partial n} \Big|_{l=0} = -\sqrt{D_t} \frac{\Gamma(1)}{\Gamma(1/2)} t^{-1/2} + \sqrt{D_t / \pi} t^{-1/2} [1 - \text{erfi}(\sqrt{\lambda t}) e^{-\lambda t} \sqrt{\pi \lambda t}] , \quad (4-15)$$

where Γ is the Gamma function and “erfi” is the imaginary error function.

The results of the heat transfer rate $\dot{Q}_w(t)$ obtained from Eq. (4-3) are compared with the exact solutions in Fig. 4-9 for different inclination angles at $\lambda = 0.1$. Again, limited oscillations of the simulated \dot{Q}_w values are observed at small time ($N < 10$) in Fig. 4-9 due to the discontinuity of the initial condition. After that very good agreement between the numerical and exact solutions is noticed in Fig. 4-9 for all cases tested.

This test demonstrates that when the straight boundary is not perpendicular to the discrete velocity vectors of the TLBE model and intersected by the square lattice with irregular Δ values, the proposed heat transfer evaluation scheme, Eq. (4-3), is still able to provide accurate results.

4.3.3 Two-D Transient Heat Conduction Inside a Circle

Following the example in Section 3.4.4, we consider here the transient sinusoidal boundary condition applied on the curved boundary of a circle with radius r_0 . The analytical solution for this 2-D problem is given by Eq. (3-70), assuming no temperature variation in the azimuthal direction.

Two error norms are defined to assess the present heat transfer evaluation

$$E(t^*) = |\dot{Q}_{w_LBE}(t^*) - \dot{Q}_{w_ex}(t^*)| / r_0, \quad \text{and} \quad (4-16)$$

$$E_2 = \frac{\omega}{2\pi} \frac{1}{r_0} \int_0^{2\pi/\omega} |\dot{Q}_{w_LBE}(t^*) - \dot{Q}_{w_ex}(t^*)| dt = \frac{1}{r_0} \int_0^1 |\dot{Q}_{w_LBE}(t^*) - \dot{Q}_{w_ex}(t^*)| dt^*, \quad (4-17)$$

where $t^* = \omega t / 2\pi$. To eliminate the effect of the initial variations on the average error E_2 defined in Eq. (4-17), the computation is performed for a sufficiently long period of time ($t^* > 1$). The variations of $E(t^*)$ in Eq. (4-16) at different grid resolution, $1/r_0$, are plotted in Fig. 4-10 when the coefficient c_{d1} determined from Scheme 2 in Eq. (3-35b) is used in Eq. (4-1). After the dynamic steady state is reached the average error E_2 is computed

and the results are shown in Fig. 4-11 for each of the three schemes implemented. The Stokes number St is set to be unity in all of the present simulations.

On average, the decrease of the error norm E_2 in Fig. 4-11 is linearly proportional to the grid resolution, $1/r_0$, as shown on the log-log scale for each of the three schemes implemented. The results demonstrate that the present heat transfer evaluation is first-order accurate for curved-boundary situations. Compared with the quadratic convergence of the boundary heat flux and heat transfer for the 2-D channel flow with straight walls, the degradation of the convergence order in this test is due to the first-order accurate heat flux approximation on the curved boundary. It has been verified with numerical tests in Chapter 3 that the boundary heat flux obtained from Eq. (4-1) in TLBE simulations is first-order accurate for Dirichlet conditions on curved boundaries because of the irregularly distributed lattice fractions intersected by the curved boundary, even though the temperature field obtained from the TLBE results is second-order accurate. Thus it is concluded that the proposed heat transfer evaluation method has the same first-order accuracy as the heat flux computation on curved boundaries. It is noticed that in this test the boundary heat flux in the normal direction and the surface area on the curved boundary are not required in the determination of the overall heat transfer. It is thus believed that the proposed heat transfer evaluation method is very efficient in curved-boundary situations such as thermal flows in porous media.

4.3.4 Three-D Steady-State Circular Pipe Flow with a Dirichlet Condition

This example simulates the thermal convection and diffusion inside a 3-D circular pipe for which the temperature field has been studied in Section 3.4.5.1 for boundary condition implementation analysis. Applying the same sinusoidal Dirichlet boundary condition the analytical solution for the temperature field is given in Eq. (3-75). The heat

transfer rate at the curved surface of the circular pipe based on Eq. (4-3) is computed and the following error norm is defined to assess the present heat transfer evaluation

$$E_{2_{\dot{q}_w}} = \left(\frac{\sum_z (\dot{Q}_{w_LBE} - \dot{Q}_{w_ex})^2}{\sum_z \dot{Q}_{w_ex}^2} \right)^{1/2} \quad (4-18)$$

Note that the boundary heat transfer in Eq. (4-18) is evaluated at each location along the axial z-direction since the overall heat transfer over the entire surface of the circular pipe is zero. Figure 4-12 shows the results of $E_{2_{\dot{q}_w}}$ versus the grid resolution, $1/r_0$, with the three boundary schemes given in Eqs. (3-35 a-c) implemented. The characteristic Péclet number is $Pe = (2r_0)U/D_t = 50$ in all simulations.

Linear convergence for the heat transfer is observed in Fig. 4-12 for all three schemes; and Scheme 2 gives smaller errors than the other two. The first-order accuracy of the present heat transfer evaluation method is thus verified for 3-D thermal flows with curved boundaries.

4.3.4 Two-D Steady-State Natural Convection in a Square Enclosure with a Circular Cylinder in the Center

Natural convection between an outer square enclosure with length L and an inner circular cylinder of radius r_0 has been investigated in a number of previous studies (Shu and Zhu 2002, Peng et al. 2003, Kim et al. 2008, Jeong et al. 2010, Moukalled and Acharya 1996). The present study considers the basic configuration that the cylinder is located in the center of the square enclosure with $r_0 = 0.2L$ and all the boundary walls are stationary. The straight walls of the enclosure are maintained at a constant low temperature of T_c , whereas the inner circular wall is at a constant high temperature T_h (see Fig. 4-13). The fluid properties are assumed to be constant except that the density

in the buoyancy term is based on the Boussinesq approximation. The Prandtl number is set to be 0.71, corresponding to that of air, and the Rayleigh number, Ra , varies in the range of $10^3 - 10^6$ in present simulations.

To simulate the velocity field, the 2-D MRT-LBE model by Lallemand and Luo (2000) is applied. The outer straight walls are placed in the center of the lattice links ($\Delta = 0.5$ in both direction as shown in Fig. 4-13) so that the standard bounce-back condition is used. For the inner circular boundary, the second-order accurate no-slip velocity condition treatment by Mei et al. (1999) is implemented. The LBE model for the velocity field and the TLBE model for the temperature field are coupled in the simulation. The convergence is considered to be obtained when the relative error between 50 successive lattice time steps is less than 10^{-8} for both the velocity and temperature fields.

Figures 4-14 and 4-15 show the isotherms and streamlines, respectively, at $Ra = 10^3, 10^4, 10^5$ and 10^6 (the lattice grids 309×309 are used for all cases). The present results agree well qualitatively with those reported in (Shu and Zhu 2002, Peng et al. 2003, Kim et al. 2008, Jeong et al. 2010, Moukalled and Acharya 1996).

To quantify the accuracy of the present simulation results, the surface-averaged Nusselt numbers on both the inner circular wall and the outer straight walls are examined. At steady state, the local heat transfer rate on the boundary walls of the inner cylinder and the outer enclosure can be obtained from

$$q = h(T_h - T_c) = -k_f \left. \frac{\partial T}{\partial n} \right|_{\text{wall}}, \quad (4-19)$$

where h is the local heat transfer coefficient, k_f is the thermal conductivity of the fluid, and n is the normal of the boundary walls pointing outward of the enclosure. From Eq. (4-19) one can determine h as

$$h = -k_f \frac{1}{\Delta T} \frac{\partial T}{\partial n} \Big|_{\text{wall}} = -k_f \frac{\partial \theta}{\partial n} \Big|_{\text{wall}}, \quad (4-20)$$

where $\Delta T = T_h - T_c$, and θ is the dimensionless temperature $\theta = (T - T_c) / \Delta T$. The average Nusselt numbers over the inner and outer boundaries are then defined as

$$\overline{Nu}_i = \frac{\overline{h}_i S_i}{k_f} = - \frac{\overline{\partial \theta}}{\partial n} \Big|_i S_i, \text{ and } \overline{Nu}_o = \frac{\overline{h}_o S_o}{k_f} = - \frac{\overline{\partial \theta}}{\partial n} \Big|_o S_o. \quad (4-21)$$

Here S_i denotes half of the circumferential length of the inner circle, and S_o is half of the total length of the outer straight walls due to symmetry. At steady state, the average Nusselt numbers \overline{Nu}_i and \overline{Nu}_o should be equal to each other.

Based on the present heat transfer evaluation method, the heat transfer on the inner circular surface is obtained by integrating the boundary heat flux $\Phi_{n\bar{a}}$ in the discrete velocity directions of the TLBE model with unit effective surface area. Thus the average Nusselt number \overline{Nu}_i on the inner surface in Eq. (4-21) is obtained from

$$\overline{Nu}_i = - \frac{\overline{\partial \theta}}{\partial n} \Big|_i S_i = \frac{1}{k_f} \left(\overline{\Phi}_n \Big|_i S_i \right) = \frac{1}{2k_f} \sum_{\bar{a}} \Phi_{n\bar{a}} \Big|_i (\delta x)^2 = \frac{1}{2k_f} (\dot{Q}_w)_i, \quad (4-22a)$$

where $\Phi_{n\bar{a}} \Big|_i$ is determined using Eq. (4-1), and $(\dot{Q}_w)_i$ is the total heat transfer rate on the entire circular boundary that is computed using Eq. (4-3). For the outer straight boundaries perpendicular to the discrete velocity vectors in x - or y -direction, the normal heat flux is the same as the corresponding heat flux in the discrete velocity direction,

i.e., $\Phi_n = \Phi_{n\bar{\alpha}}$, and the surface area is exact as the outer boundaries are placed in the center of the lattice links. Thus the average Nusselt number \overline{Nu}_o on the outer surface is

$$\overline{Nu}_o = -\frac{\partial\theta}{\partial n}\bigg|_o S_o = \frac{1}{k_f}(\overline{\Phi}_n|_o S_o) = \frac{1}{2k_f} \sum_{\bar{\alpha}} \Phi_{n\bar{\alpha}}|_o (\delta x)^2 = \frac{1}{2k_f}(\dot{Q}_w)_o. \quad (4-22b)$$

It should be noted $\Phi_{n\bar{\alpha}}|_o$ in the above is determined using Eq. (4-1) with $\Delta = 0.5$, and

$(\dot{Q}_w)_o$ is the heat flow rate on the entire outer surface.

A grid-refinement study is carried out first, and the average Nusselt numbers \overline{Nu}_i and \overline{Nu}_o obtained from Eqs. (4-22a) and (4-22b), respectively, are presented in Table 4-1 at different lattice grid sizes. The results can be considered well converged at the mesh size 359×359 . Table 4-2 compares the present converged results with the average Nusselt number \overline{Nu}_i evaluated on the inner surface in (Shu and Zhu 2002, Peng et al. 2003, Kim et al. 2008, Jeong et al. 2010, Moukalled and Acharya 1996). The specific methods applied in those references are also listed at the bottom of Table 4-2. The present results in Tables 4-1 and 4-2 are obtained using Scheme 2 for both the boundary implementation and the heat flux evaluation. The present results for \overline{Nu}_i and \overline{Nu}_o in Tables 4-1 and 4-2 are very close to each other for all Ra values simulated, indicating that the present heat transfer evaluation method on curved boundaries is accurate compared with that obtained from straight boundaries. In addition, the present results are in good agreement with previous numerical results reported in (Shu and Zhu 2002, Peng et al. 2003, Kim et al. 2008, Jeong et al. 2010, Moukalled and Acharya

1996). It is thus verified that the present heat transfer evaluation method is accurate and efficient in thermal-hydrodynamic coupling simulations involving curved geometry.

4.4 Summary and Conclusions

An efficient and accurate approach for evaluating local and overall heat transfer rates on curved boundaries is proposed in the thermal lattice Boltzmann equation method. The boundary heat flux in the discrete velocity directions is obtained with the temperature distribution functions at the lattice nodes close to the boundary and the given Dirichlet or mixed boundary condition. As the lattice spacing is uniform in the Cartesian coordinate system, the effective surface area for any of the discrete heat fluxes on the boundary is constant. Based on energy conservation, the integration of the heat fluxes in the discrete velocity directions with constant effective surface area leads to the total heat transfer rate. There are two major benefits for the proposed heat transfer evaluation: no requirement for the normal heat flux determination and no surface area approximation. Thus the proposed heat transfer evaluation method is very efficient and convenient to implement compared with other methods that approximate the boundary heat transfer based on the simulated temperature field. Numerical tests have demonstrated that the heat transfer evaluation method is second-order accurate for straight walls perpendicular to one of the discrete lattice velocity vectors and first-order accurate for curved boundaries.

Table 4-1. Surface-averaged Nusselt numbers at different grid resolution.

lattice grids	Average Nusselt numbers $\overline{Nu}_i, \overline{Nu}_o$			
	$Ra = 10^3$	$Ra = 10^4$	$Ra = 10^5$	$Ra = 10^6$
159×159	3.170, 3.168	3.229, 3.226	4.932, 4.924	9.313, 9.306
209×209	3.170, 3.167	3.229, 3.225	4.925, 4.918	9.121, 9.117
259×259	3.170, 3.167	3.228, 3.225	4.921, 4.915	9.041, 9.037
309×309	3.169, 3.167	3.227, 3.226	4.917, 4.913	8.997, 8.992
359×359	3.169, 3.167	3.227, 3.226	4.916, 4.912	8.971, 8.966

Table 4-2. Comparison of the present surface-averaged Nusselt numbers with previous results.

Ra	Average Nusselt number \overline{Nu}						
	Present \overline{Nu}_i	Present \overline{Nu}_o	Shu & Zhu ⁺	Peng et al. [◇]	Kim et al. [§]	Jeong et al. [♀]	Moukalled & Acharya [¶]
10^3	3.169	3.167	-	-	3.396	3.399	-
10^4	3.227	3.226	3.24	3.24	3.414	3.412	3.331
10^5	4.916	4.912	4.86	4.84	5.138	5.176	5.08
10^6	8.971	8.966	8.90	8.75	9.39	9.171	9.374

⁺ Differential quadrature method with vorticity-stream function formulation (Shu and Zhu 2002);

[◇] Taylor-series-expansion and least-squares-based lattice Boltzmann method (Peng et al. 2003);

[§] Immersed-boundary finite volume method (Kim et al. 2008);

[♀] Immersed-boundary thermal lattice Boltzmann method (Jeong et al. 2010);

[¶] Finite volume method (Moukalled and Acharya 1996).

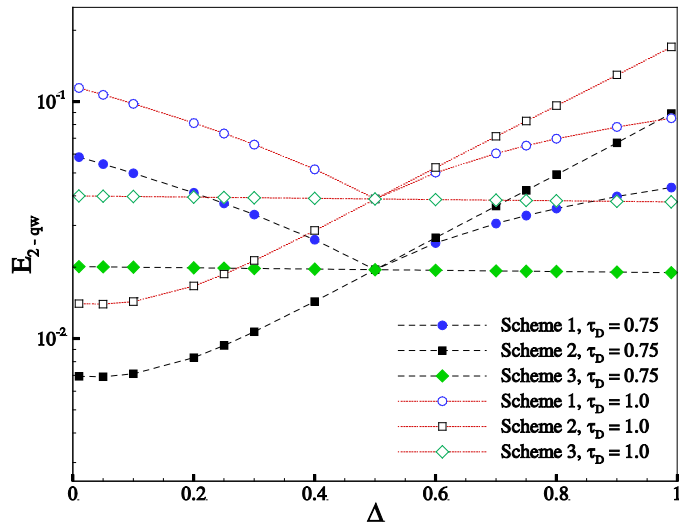


Figure 4-3. Wall heat flux error $E_{2,qw}$ versus the lattice link fraction Δ at $N_y = 34$ for the channel flow Dirichlet problem.

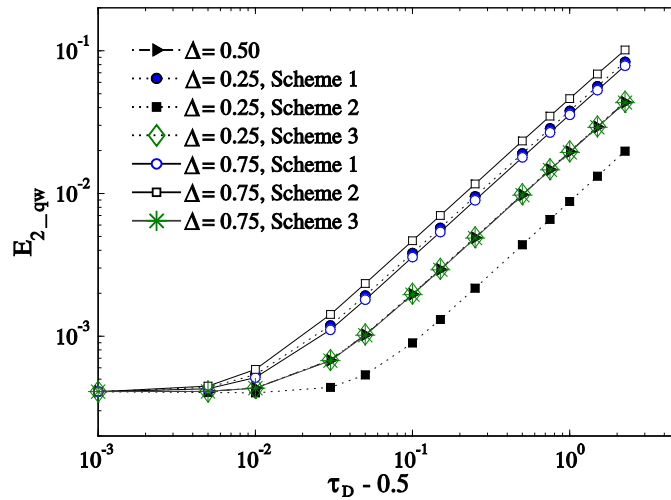


Figure 4-4. Wall heat flux error $E_{2,qw}$ versus $(\tau_D - 0.5)$ at $N_y = 66$ for the channel flow Dirichlet problem.

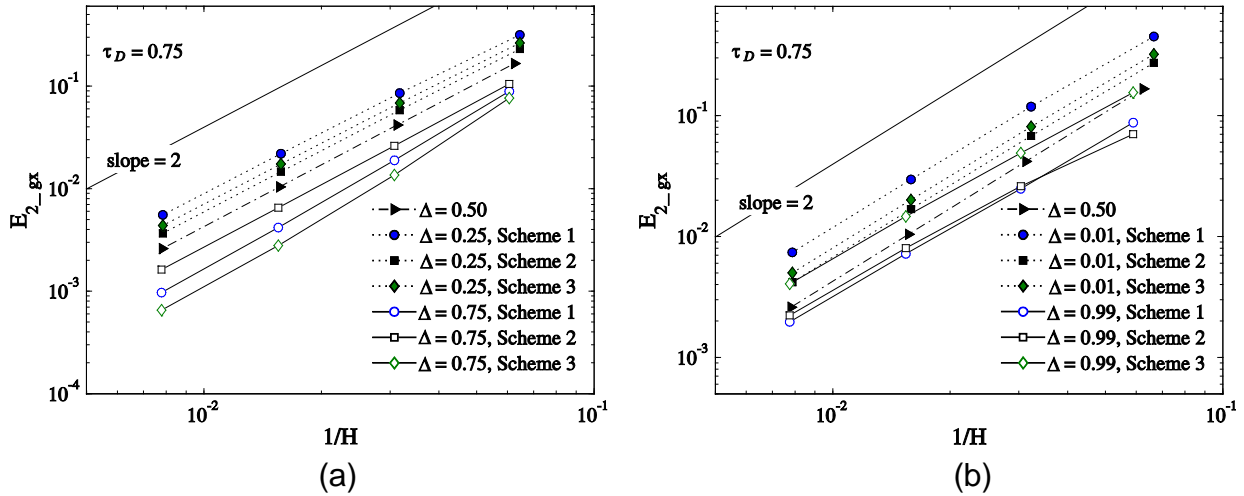


Figure 4-5. Interior gradient error E_{2_gx} (in x-direction) versus the grid resolution, $1/H$, for the channel flow Dirichlet problem at (a) $\Delta = 0.50, 0.25$, and 0.75 , and (b) $\Delta = 0.50, 0.01$, and 0.99 .

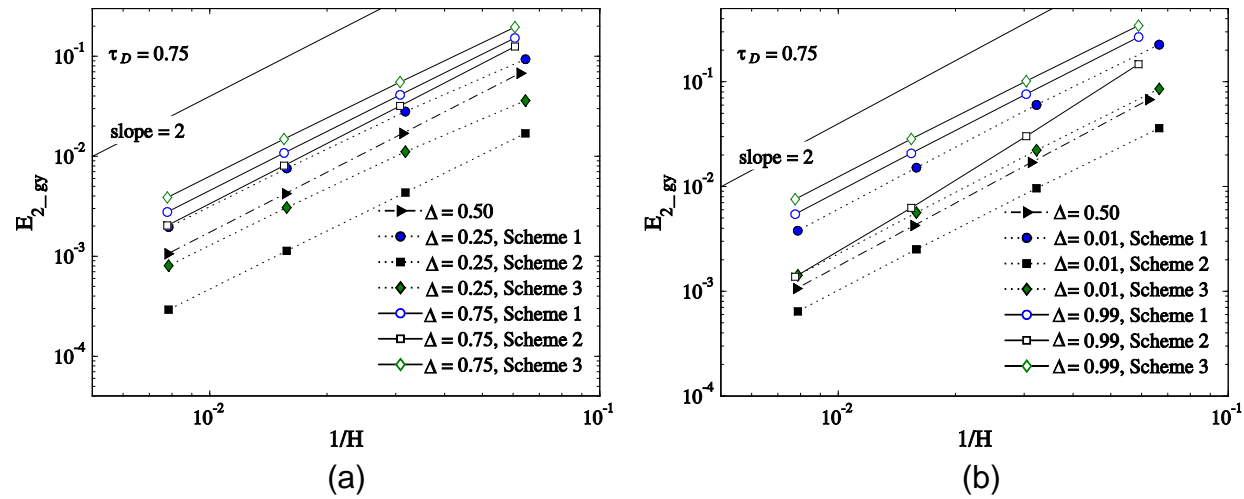


Figure 4-6. Interior gradient error E_{2_gy} (in y-direction) versus the grid resolution, $1/H$, for the channel flow Dirichlet problem at (a) $\Delta = 0.50, 0.25$, and 0.75 , and (b) $\Delta = 0.50, 0.01$, and 0.99 .

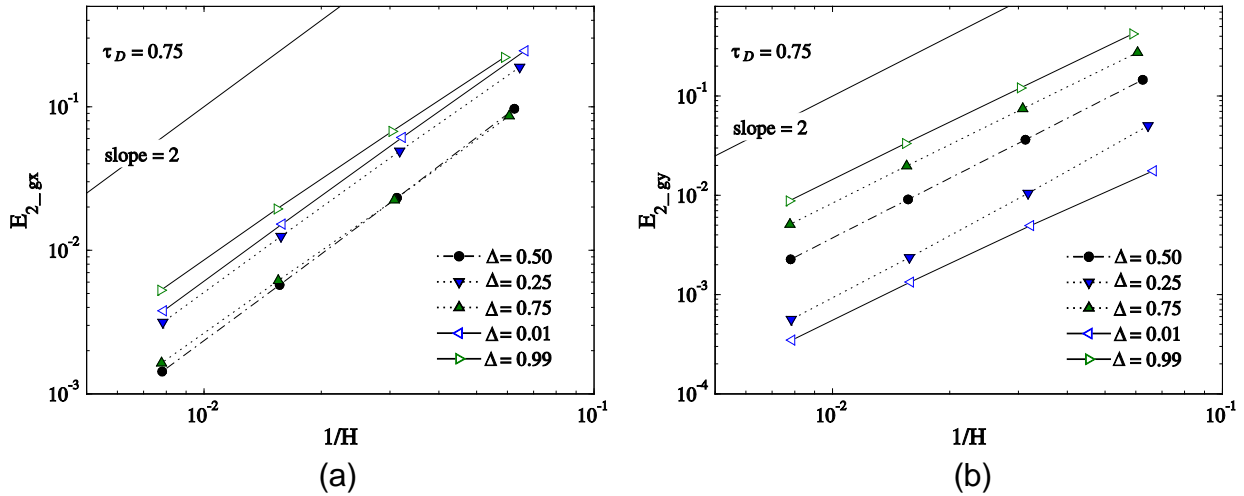


Figure 4-7. Interior gradient errors of (a) E_{2_gx} , and (b) E_{2_gy} , respectively, versus the grid resolution, $1/H$, for the channel flow Neumann problem.

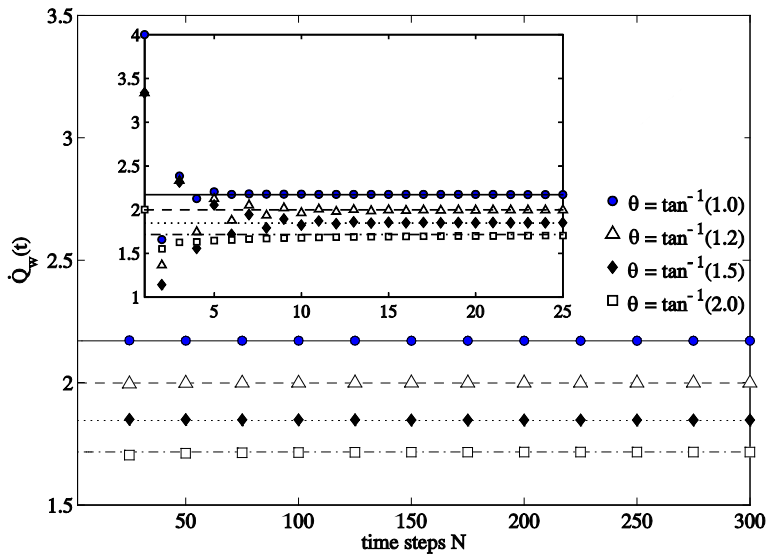


Figure 4-8. Variations of the heat transfer rate with time for the Dirichlet condition $T(l=0) = t^{1/2}$ at the end of an inclined semi-infinite solid (symbols: LBE results; lines: exact solutions).

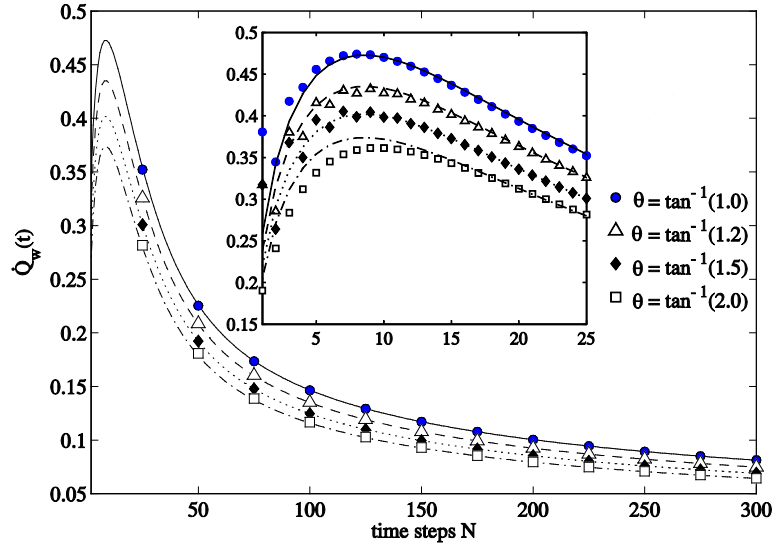


Figure 4-9. Variations of the heat transfer rate with time for the Dirichlet condition $T(l = 0) = 1 - \exp(-0.1t)$ at the end of an inclined semi-infinite solid (symbols: LBE results; lines: exact solutions).

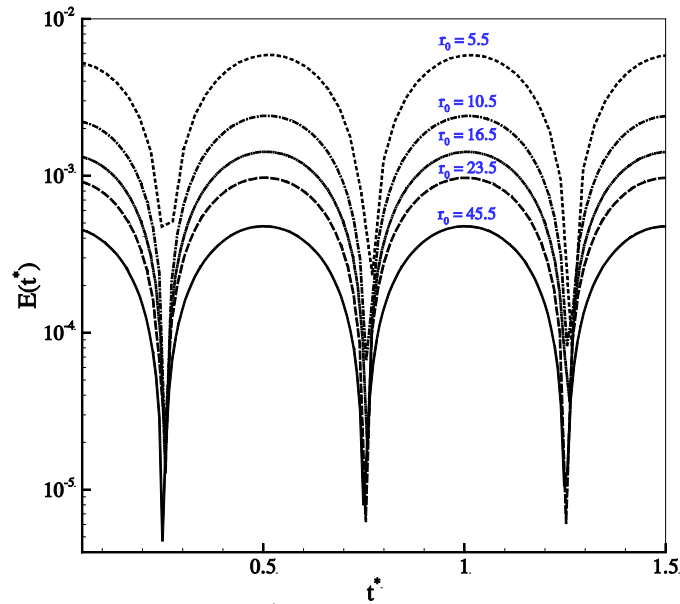


Figure 4-10. Variations of the error $E(t^*)$ defined in Eq. (4-16) with time at different grid resolution for the transient heat conduction inside a circle.

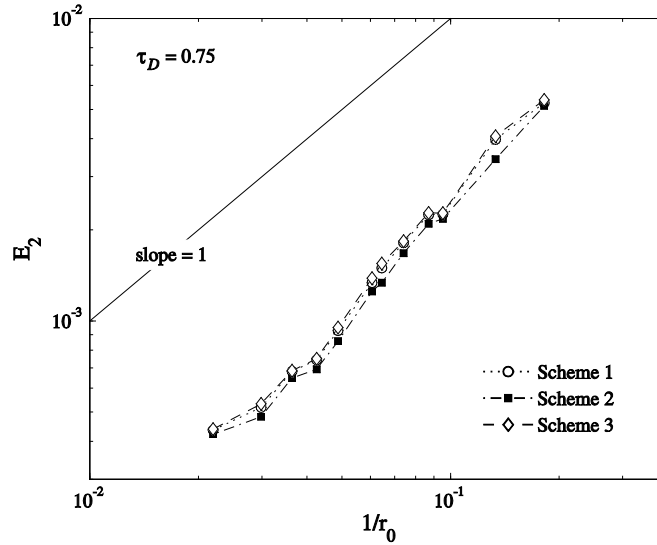


Figure 4-11. Heat transfer error, E_2 , defined in Eq. (4-17) versus the grid resolution, $1/r_0$, for the transient heat conduction inside a circle.

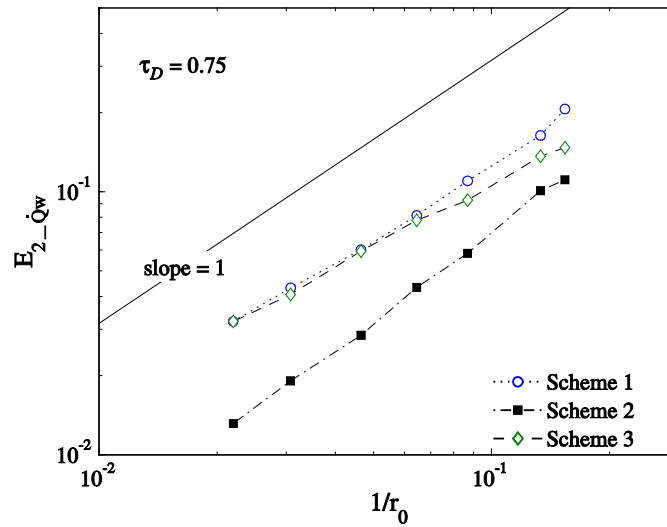


Figure 4-12. Heat transfer error $E_{2-\dot{Q}_w}$ versus the grid resolution, $1/r_0$, for the circular pipe flow with a Dirichlet boundary condition.

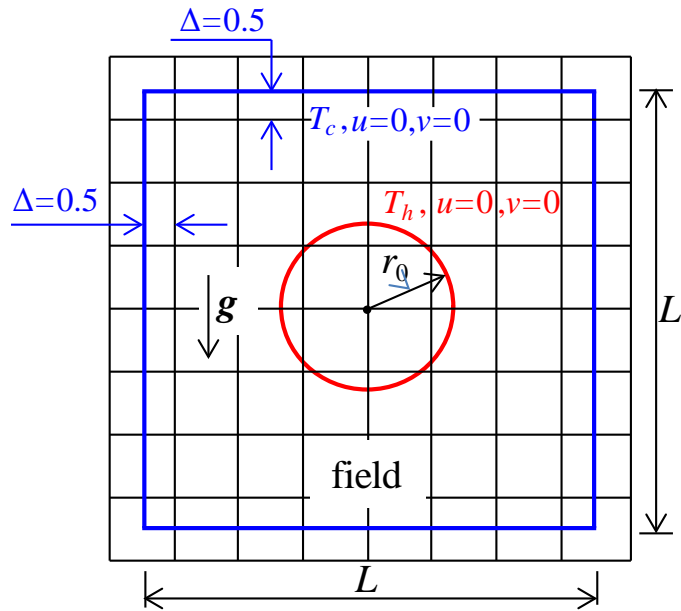


Figure 4-13. Schematic depiction of the computational domain ($r_0 = 0.2L$) and the Dirichlet thermal and velocity boundary conditions on the inner and outer walls.

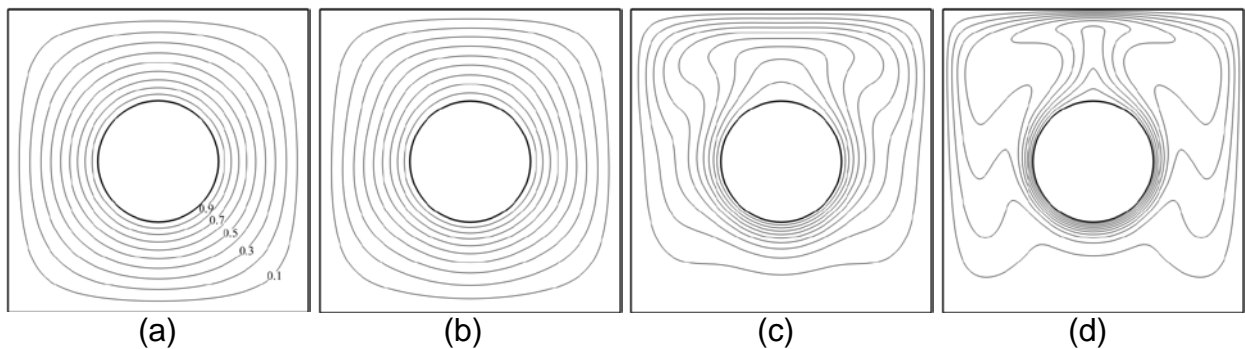


Figure 4-14. Isotherms in the field between the circular cylinder and the cavity walls at (a) $Ra = 10^3$, (b) $Ra = 10^4$, (c) $Ra = 10^5$, and (d) $Ra = 10^6$.

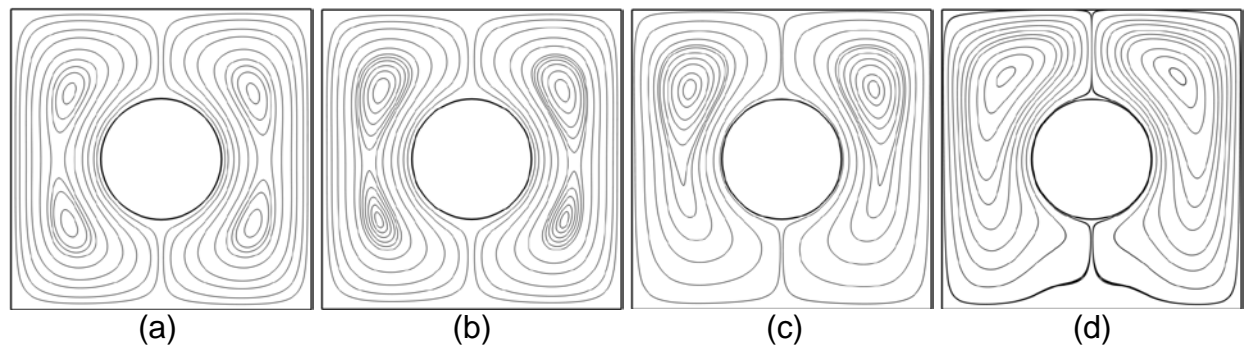


Figure 4-15. Streamlines in the field between the circular cylinder and the cavity walls at (a) $Ra = 10^3$, (b) $Ra = 10^4$, (c) $Ra = 10^5$, and (d) $Ra = 10^6$.

CHAPTER 5
MULTIPLE-RELAXATION-TIME LATTICE BOLTZMANN MODEL FOR THE
AXISYMMETRIC CONVECTION DIFFUSION EQUATION*

5.1 Introduction

Heat and mass convection-diffusion in axisymmetric systems such as circular cylinders and annular cavities formed by coaxial cylinders are widely encountered in engineering practices. Examples of applications include heat exchangers, desalination systems, solar energy collectors, electronic cooling devices and chemical reactors. Fluid flows and heat and mass transfer in cylindrical systems are essentially three-dimensional (3-D) problems, while under axisymmetric conditions they can be reduced to quasi-2-D problems, which greatly reduces the computational effort.

The lattice Boltzmann equation (LBE) method has become an effective numerical method for the convection-diffusion equation (CDE) (Flekky 1993, van der Sman and Ernst 2000, Servan-Camas and Tsai 2008, Shi and Guo 2009, Yoshida and Nagaoka 2010, Ginzburg et al. 2010, Ginzburg 2013, Li et al. 2013a, Li et al. 2013b). Especially, the multiple-relaxation-time (MRT) lattice Boltzmann (LB) model (Yoshida and Nagaoka 2010, Li et al. 2013a, Li et al. 2013b) is robust and retains the second-order accuracy for curved boundaries. Although 3-D LB models can be directly applied to simulate the axisymmetric CDE when the curved boundary condition is properly handled, quasi-2-D LB models, which require far less computational effort and bypass the curved boundary treatment for straight pipes, are attractive alternatives for solving the axisymmetric CDE as demonstrated by the LB models developed for axisymmetric athermal flows (Halliday et al. 2001, Lee et al. 2006, Reis and Phillips 2007, Reis and Phillips 2008, Zhou 2008, Chen et al. 2008, Huang and Lu 2009, Guo et al. 2009, Wang et al. 2010, Li et al. 2010,

* This work has been submitted to *International Journal of Heat and Mass Transfer* (Li et al. 2013c).

Zhou 2011) and thermal problems (Peng et al. 2003, Huang et al. 2007, Chen et al. 2009, Li et al. 2009, Zheng et al. 2010a, Zheng et al. 2010b).

The standard LB models break the computation into a collision step and a streaming step. In order for axisymmetric LB models to work using the existing LB models developed in 2-D Cartesian coordinate systems in terms of the standard collision-streaming procedure, either the governing equations for momentum and energy transport in the cylindrical coordinate system are represented in a pseudo-Cartesian coordinate system, or the effect of axisymmetry is modeled at the particle distribution function level (Guo et al. 2009, Wang et al. 2010, Zheng et al. 2010a, Zheng et al. 2010b).

The first approach results in additional terms, including the velocity and temperature gradients, in the transformed governing equations, and they can be treated as additional source terms in the respective macroscopic transport equations. This treatment is straightforward since it is carried out at the macroscopic level. For example, the typical axisymmetric CDE is

$$\frac{\partial \phi}{\partial t} + \frac{\partial}{r \partial r} (r u_r \phi) + \frac{\partial}{\partial z} (u_z \phi) = \frac{\partial}{r \partial r} \left(r D_{rr} \frac{\partial \phi}{\partial r} \right) + \frac{\partial}{\partial z} \left(D_{zz} \frac{\partial \phi}{\partial z} \right) + G, \quad (5-1)$$

where G is the typical source term representing possibly the effects of viscous dissipation, pressure work, volumetric heating, heat released or mass created from chemical reaction for the energy or species transport equation. In Eq. (5-1), u_r and u_z are the velocity components in the radial r - and axial z -directions, respectively, D_{rr} and D_{zz} are the diagonal diffusion coefficients of the diffusion tensor D_{ij} . It can be rewritten as

$$\frac{\partial \phi}{\partial t} + \frac{\partial}{\partial r}(u_r \phi) + \frac{\partial}{\partial z}(u_z \phi) = \frac{\partial}{\partial r} \left(D_{rr} \frac{\partial \phi}{\partial r} \right) + \frac{\partial}{\partial z} \left(D_{zz} \frac{\partial \phi}{\partial z} \right) + S_{a1} + S_{a2} + G,$$

$$\text{with } S_{a1} \equiv -\frac{u_r \phi}{r}, S_{a2} \equiv \frac{D_{rr}}{r} \frac{\partial \phi}{\partial r}. \quad (5-2)$$

Equation (5-2) becomes an ordinary CDE in the pseudo-Cartesian coordinate system (r, z) with three source terms, S_{a1} , S_{a2} , and G , of different origins.

In the second approach, new LB evolution equations for the particle distribution functions must be carefully constructed so that the correct macroscopic transport, Eq. (5-1), can be recovered through the Chapman-Enskog expansion for the new evolution equation. When MRT-LB models such as the standard ones in (Lallemand and Luo 2000, Yoshida and Nagaoka 2010) are desired, such modification at the microscopic level for the evolution equations of the distribution functions may involve redefining the transformation matrix and the equilibrium distribution functions. The first approach is thus preferred if the gradients can be efficiently obtained from the distribution functions instead of using finite-difference schemes.

A review of the various LB models for axisymmetric fluid momentum equations can be found in the recent work of Zhou (2011), which also introduced an improved axisymmetric LB model based on his original version in (Zhou 2008). The main advantages of Zhou's revised model compared with the other axisymmetric LB models are as follows: (i) the source terms represent the same additional terms in the transformed governing equations and no extra source terms are needed in the evolution equation, (ii) it preserves the original computational procedure for both the distribution functions and the macroscopic variables including density and velocities as those in the conventional LBE method, and (iii) no velocity gradients are required. It is well known

that the MRT-LB models (Lallemand and Luo 2000, Yu et al. 2003) have better numerical stability and accuracy than BGK-LB models, i.e., the single-relaxation-time (SRT) collision models based on the work of Bhatnagar, Gross and Krook (1954). Thus when the fluid momentum equations are involved, an MRT version of Zhou's axisymmetric LB model (Zhou 2011) is used in the present work.

Several axisymmetric thermal LB models, which simulate the axisymmetric CDE for temperature, have also been proposed in the literature (Peng et al. 2003, Huang et al. 2007, Chen et al. 2009, Li et al. 2009, Zheng et al. 2010a, Zheng et al. 2010b). Peng et al. (2003) and Huang et al. (2007) proposed hybrid approaches in which the fluid velocities in the radial and axial directions are simulated using the athermal axisymmetric LB model by Halliday et al. (2001), while the azimuthal velocity and the temperature field are solved using finite-difference schemes. Chen et al. (2009) proposed an LB model for axisymmetric buoyancy-driven thermal flows in which the vorticity-stream-function formulation was used for the velocity field so that the governing equations for vorticity and temperature became CDEs with source terms. The vorticity and temperature gradients in the source terms were obtained from finite-difference calculations. In addition, a Poisson equation for the stream function must be solved during each time step in (Chen et al. 2009). To avoid the finite-difference computation of the temperature gradient, i.e., Sa_2 in Eq. (2), in LB models, Li et al. (2009) proposed an implicit evolution equation for the distribution functions to recover the axisymmetric energy equation. Additional body forces can also be modeled by including a forcing term in this model. The implicitness is then eliminated by introducing a new distribution function, which includes not only the original distribution function but also the source

term. As a result, the modified evolution equation is more difficult to implement than that in standard LB models; Furthermore, the temperature calculation in (Li et al. 2009) requires the radial velocity component and thus it deviates from the standard calculation of macroscopic variables in the LBE method. Zheng et al. (2010a) extended their athermal axisymmetric LB model (Guo et al. 2009) to simulate thermal flows by including a D2Q4 LB model for the temperature field. The radial coordinate and the temperature distribution functions were lumped together and the source term in the evolution equation of the temperature distribution functions was properly constructed so that the scalar source term, S_{a1} , and the gradient term, S_{a2} given in Eq. (5-2), do not show up explicitly in the thermal LB model. It was realized that, however, due to its special construction of the source term, the extension of Zheng et al.'s model (2010a) to include additional source terms, such as viscous dissipation and pressure work, is not straightforward. To overcome this limitation, Zheng et al. (2010b) also proposed a coupled LB model for axisymmetric thermal flows with viscous dissipation and pressure work starting from the continuous axisymmetric Boltzmann equation. It is noticed that the velocity distribution functions are explicitly coupled in the evolution equation of the energy distribution functions in (Zheng et al. 2010b).

It is emphasized that all the existing LB models for axisymmetric thermal flows in (Chen et al. 2009, Li et al. 2009, Zheng et al. 2010a, Zheng et al. 2010b) used the BGK collision operator. A robust and straightforward MRT-LB model that can simulate the general axisymmetric CDE is highly desired. Furthermore, we notice that the numerical validation regarding the order-of-accuracy of the axisymmetric thermal LB models has not been well established.

In this work, we propose an MRT-LB model for the general axisymmetric CDE for scalar transport such as temperature, mass concentration and azimuthal velocity component in rotational flows. When the CDE is coupled with the hydrodynamic equations, the radial-axial velocity field is solved using Zhou's axisymmetric LB model (Zhou et al. 2011) with the BGK collision model replaced by an MRT-based model. The axisymmetric CDE in the cylindrical coordinate system is transformed to an ordinary CDE in the Cartesian coordinate system, and the extra terms due to the coordinate transformation are considered as additional sources. The scalar source term, S_{a1} in Eq. (5-2), is obtained from the summation of the distribution functions, and the gradient term, S_{a2} in Eq. (5-2), is calculated from the non-equilibrium parts of the distribution functions; thus no finite-difference calculations are required. The transformed CDE in the Cartesian coordinate system is then simulated with the D2Q5 MRT-LB model proposed in (Yoshida and Nagaoka 2010). Compared with the existing LB models for axisymmetric thermal flows in (Chen et al. 2009, Li et al. 2009, Zheng et al. 2010a, Zheng et al. 2010b), the proposed model for the axisymmetric CDE has the following features: (i) the macroscopic variable and its gradient terms in the CDE, such as S_{a1} and S_{a2} in Eq. (5-2), are naturally treated as additional source terms, and they are obtained from the distribution functions; thus no special treatment for the LB evolution equation or the equilibrium distribution functions is required; (ii) it is easier to implement when compared with Li et al.'s model (2009) and the standard calculation of the macroscopic variables is preserved; (iii) the forms of the source terms can be very general and they can be directly included in the present model, (iv) viscous dissipation and pressure work can be conveniently treated as source terms in the present model;

thus the explicit coupling of the velocity distribution function in the evolution equation for the energy distribution function in (Zheng 2010b) is avoided, and (iv) rather than using BGK collision operators as in (Chen et al. 2009, Li et al. 2009, Zheng et al. 2010a, Zheng et al. 2010b), an MRT collision operator is applied to the present model.

To validate the applicability and accuracy of the proposed LB model for the axisymmetric CDE, several numerical tests are conducted in this study. Analytical solutions are available for the first four tests, and the results show that the proposed model possesses second-order accuracy. The axisymmetric LB model for the radial-axial velocity field by Zhou (2011) and the present LB model for the temperature CDE are coupled in the fifth and sixth tests, where natural convection in an annulus between two coaxial vertical cylinders and confined swirling flows in a vertical cylindrical container are studied, respectively. The numerical results from these two tests are compared with published data, and good agreement is obtained for each case.

The rest of this chapter is organized as follows. In Sec. 5.2, the D2Q5 MRT-LB model for the axisymmetric CDE is proposed; in which the treatment of the macroscopic scalar variable and its gradient in the source terms in the transformed CDE is provided. Numerical validation with six tests is presented in Sec. 5.3, and Sec. 5.4 concludes the chapter.

5.2 Lattice Boltzmann Model for the Axisymmetric Convection-Diffusion Equations

The treatment of the additional terms, S_{a1} , and S_{a2} , in Eq. (5-2) due to the polar-to-Cartesian coordinate transformation as additional source terms is straightforward in the LBE method. While it is preferable to obtain these macroscopic quantities, especially the gradient term S_{a2} , from the microscopic distribution functions rather than

using finite-difference schemes on the solved macroscopic field since the standard collision-streaming procedure is carried out on the distribution function level.

As discussed in Sec. 4.2.3, Yoshida and Nagaoka (2010) gave a formula in their MRT-LB model to obtain the scalar gradient based on the distribution functions. The accuracy of the gradient formula was examined and verified in Chapter 2 with numerous computational examples. In Sec. 4.2.3, an evaluation formula for the gradient based on the moment of the local non-equilibrium components of the distribution functions is also proposed and it is verified that these two formulas are essentially equivalent. The non-equilibrium approach in Sec. 4.2.3 for the scalar gradient evaluation will be used in this chapter.

In the LBE method, the LBE governs the evolution of the scalar distribution function, $g(\mathbf{x}, \boldsymbol{\xi}, t)$, which is defined in the discrete phase space $(\mathbf{x}, \boldsymbol{\xi})$ and time t , where $\mathbf{x} = r\mathbf{e}_r + z\mathbf{e}_z$ is the spatial vector and $\boldsymbol{\xi}$ is the particle velocity usually discretized to a small set of discrete velocities $\{\boldsymbol{\xi}_\alpha | \alpha = 1, 2, \dots, m\}$. With the objective to recover the CDE (5-2), we propose the following evolution equation for the distribution functions

$$g_\alpha(\mathbf{x} + \mathbf{e}_\alpha \delta t, t + \delta t) - g_\alpha(\mathbf{x}, t) = (\mathbf{L}g)_\alpha + \omega_\alpha (S_{a1} + S_{a2} + G) \delta t. \quad (5-3)$$

where $g_\alpha(\mathbf{x}, t) \equiv g(\mathbf{x}, \boldsymbol{\xi}, t)$, \mathbf{e}_α is the α th discrete velocity vector (the discrete velocity set $\{\mathbf{e}_\alpha\}$ for the two-dimensional five-velocity (D2Q5) LB model is shown in Fig. 5-1), δt is the time step, \mathbf{L} is the standard collision operator, and ω_α is the weight coefficient. The leading order solution of the CDE is obtained from

$$\phi = \sum_{\alpha=0}^m g_\alpha, \quad (5-4)$$

and the additional source terms are obtained from the distribution functions as

$$S_{a1} \equiv -\frac{u_r}{r} \phi = -\frac{u_r}{r} \sum_{\alpha=0}^m g_{\alpha} = -\frac{u_r}{r} \sum_{\alpha=0}^m g_{\alpha}^{(\text{eq})}, \quad (5-5)$$

$$S_{a2} \equiv \frac{D_{rr}}{r} \frac{\partial \phi}{\partial r} = -\frac{1}{r} \left(1 - \frac{1}{2\tau_{rr}}\right) \frac{\delta x}{\delta t} \sum_{\alpha=1}^m e_{ar} g_{\alpha}^{(\text{neq})} = -\frac{1}{r} \left(1 - \frac{1}{2\tau_{rr}}\right) \frac{\delta x}{\delta t} \sum_{\alpha=1}^m e_{ar} [g_{\alpha} - g_{\alpha}^{(\text{eq})}], \quad (5-6)$$

where $g_{\alpha}^{(\text{eq})}$ (see definition in Eq. (3-7)) and $g_{\alpha}^{(\text{neq})}$ are the equilibrium and non-equilibrium components of the distribution function g_{α} , respectively, with

$g_{\alpha}^{(\text{neq})} = g_{\alpha} - g_{\alpha}^{(\text{eq})}$, τ_{rr} is a relaxation coefficient (see Eq. (3-26)) and e_{ar} is the projection of the discrete velocity \mathbf{e}_{α} in the radial direction. The derivation and numerical validation of the gradient evaluation in Eq. (5-6) in terms of $g_{\alpha}^{(\text{neq})}$ can be found in Sec. 4.2.3.

The D2Q5 LB model with a MRT collision operator (Yoshida and Nagaoka 2010) is employed to simulate the LBE (5-3). The two-step procedure is summarized as

collision step:

$$\hat{g}_{\alpha}(\mathbf{x}, t) = g_{\alpha}(\mathbf{x}, t) - \left[\mathbf{M}^{-1} \mathbf{S} (\mathbf{m}(\mathbf{x}, t) - \mathbf{m}^{(\text{eq})}(\mathbf{x}, t)) \right]_{\alpha} + \omega_{\alpha} (S_{a1} + S_{a2} + \mathbf{G}) \delta t, \text{ and } (5-7)$$

streaming step:

$$g_{\alpha}(\mathbf{x} + \mathbf{e}_{\alpha} \delta t, t + \delta t) = \hat{g}_{\alpha}(\mathbf{x}, t), \quad (5-8)$$

where \hat{g}_{α} is again the post-collision distribution function. The details of the transformation matrix and the multiple relaxation coefficients are given in Sec. 3.3.2.

When the CDE (2) is coupled with the momentum transport equation, the axisymmetric LB model by Zhou (2011) is applied for the radial-axial velocity field and the BGK collision operator is extended to an MRT version for consistency. The extension of Zhou's BGK model (2011) to the MRT model is given in Appendix C.

5.3 Numerical Validation and Discussion

To validate the accuracy of the proposed LB model for the axisymmetric CDE, we present six numerical tests in this section. The velocity field is specified in each of the first four tests and the analytical solutions for ϕ are available. The accuracy and convergence order of the numerical solutions are thus investigated in detail. The fifth and sixth tests consider axisymmetric thermo-hydrodynamic problems, where the radial-axial velocity fields are simulated with an MRT version of the athermal LB model by Zhou (2011), and the presently proposed LB model is applied for the thermal field as well as the azimuthal velocity field in the sixth test. These two LB models are coupled to reach the steady states and the numerical results are compared with published results.

5.3.1 Steady convection-diffusion in an annulus

In this example, we consider the axisymmetric convection-diffusion in an infinitely long annulus defined in $R_i \leq r \leq R_o$, where the variations in both the azimuthal and axial directions are neglected. With a constant volumetric flow rate Q supplied on the inner surface, the radial velocity in the annulus is $u_r = Q/r$. The convection-diffusion inside the annulus is characterized by the Péclet number, $Pe = u_{R_i} R_i / D_r = Q / D_r$. For given Dirichlet conditions $\phi(r = R_{i,o}) = \phi_{i,o}$, the exact solution for ϕ inside the annulus is

$$\phi_{\text{ex}}(R_i \leq r \leq R_o, z) = \frac{\phi_i (R_o^{Pe} - r^{Pe}) + \phi_o (r^{Pe} - R_i^{Pe})}{R_o^{Pe} - R_i^{Pe}}. \quad (5-9)$$

With no axial variation only five lattice nodes are used in the z-direction, and periodic boundary conditions are applied at the ends. Each of the inner and outer boundaries is placed at the center of the lattice link ($\Delta = 0.5$) so that the standard

Dirichlet “bounce-back” scheme, which is recovered by all three schemes in Eqs. (3-35 a-c), is implemented.

To assess the accuracy of the proposed LB model, the following relative L-2 error norm is defined in the annulus

$$E_2 = \left\{ \sum_{r,z} [(\phi)_{\text{LBE}} - (\phi)_{\text{ex}}]^2 / \sum_{r,z} (\phi)_{\text{ex}}^2 \right\}^{1/2}. \quad (5-10)$$

Figure 5-2 shows the error norm, E_2 , versus the grid resolution, $1/R_i$, at $Pe = 10, 20, 50$ and 100 , $R_o = 2R_i$, $\tau_{rr} = \tau_D = 0.75$, $\phi_i = 0.5$, and $\phi_o = 1.0$. The error norm E_2 increases as Pe becomes larger; and second-order convergence is noticed for each Pe number tested. Hence the present axisymmetric LB model is second-order accurate.

5.3.2 Steady convection-diffusion in a circular pipe

Following the circular pipe test in Sections 3.4.5 and 4.3.4, the fluid flow inside the circular pipe is assumed to be a plug flow with constant axial velocity U and zero radial velocity. The axisymmetric CDE at steady state is thus simplified to

$$U \frac{\partial \phi}{\partial z} = \frac{\partial}{\partial r} \left(D_{rr} \frac{\partial \phi}{\partial r} \right) + \frac{\partial}{\partial z} \left(D_{zz} \frac{\partial \phi}{\partial z} \right) + \frac{D_{rr}}{r} \frac{\partial \phi}{\partial r}. \quad (5-11)$$

The last term on the right side of Eq. (5-11) is treated as a source term in the present model as in Eq. (5-6). Only isotropic diffusion is considered for simplicity so that $D_{rr} = D_{zz} = D$ and the Péclet number is $Pe = (2R_o)U/D$. The computational domain and the square lattice in the r - z plane are schematically shown in Fig. 5-3. A periodic boundary condition in the z -direction is imposed so that $f(x + L) = f(x)$ is valid for both ϕ and the distribution function g_α . The centerline, $r = 0$, is always located half-way between the lattice nodes with $\Delta = 0.5$; and the Neumann condition $\partial \phi / \partial r|_{r=0} = 0$ is imposed due to axisymmetry. Dirichlet and Neumann boundary conditions on the surface of $r = R_o$ will

be studied separately in this section. For the Dirichlet condition on the boundary with specific Δ values, Scheme 2 in Eq. (3-35b) is implemented as it showed smaller relative errors than the other two schemes in Eqs. (3-35a) and (3-35c) for most cases studied in Chapter 3. The Péclet number $Pe = 20$ and the relaxation coefficient $\tau_D = 0.75$ are used in all simulations.

This problem has been studied in Chapters 3 and 4 where the D3Q7 LB model was used in the 3-D domain and curved boundary condition treatments were required to preserve the exact geometry of the circular pipe. In the present work, in contrast, as the 2-D axisymmetric LB model is used, the effect of the curved boundary can be eliminated.

5.3.2.1 Dirichlet boundary condition on the wall

A sinusoidal Dirichlet boundary condition is imposed on the boundary walls and the analytical solution for ϕ is given in Eq. (3-75).

For illustrative purposes, Fig. 5-4 shows the contours of ϕ in the r - z plane from the numerical simulation using $Nr = 42$, $Nz = 83$ (Nr and Nz denote the numbers of lattice nodes in the r - and z -directions, respectively) and $\Delta = 0.5$ for the pipe wall. To assess the accuracy of the present LB model, the error norm E_2 defined in Eq. (5-10) is computed. In addition, with the analytical solution in Eq. (3-75), the exact solutions for the boundary wall flux, the interior gradients $\partial\phi/\partial r$ and $\partial\phi/\partial z$ in both directions can be obtained. The numerical boundary flux is obtained from the technique proposed in Chapter 3 in the LBE method (see Eq. (3-41a)) with

$$\Phi_{n\bar{a}} = \left(\frac{1 - c_{d1}}{2} \right) \frac{\delta x}{\delta t} \left[-(2\Delta + 1)\hat{g}_a(\mathbf{x}_f, t) + \left(2\Delta - \frac{2}{1 - c_{d1}} \right) \hat{g}_a(\mathbf{x}_{ff}, t) + \left(\frac{2}{1 - c_{d1}} - 1 \right) \hat{g}_{\bar{a}}(\mathbf{x}_f, t) + \varepsilon_D \Phi_d \right],$$

and the interior gradient is evaluated using the idea shown in Eq. (5-6). The following error norms are further defined to assess their numerical accuracy

$$E_{2_qw} = \left\{ \sum_{r=R_0} \left[\left(\frac{\partial \phi}{\partial r} \right)_{\text{LBE}} - \left(\frac{\partial \phi}{\partial r} \right)_{\text{ex}} \right]^2 / \sum_{r=R_0} \left(\frac{\partial \phi}{\partial r} \right)_{\text{ex}}^2 \right\}^{1/2}, \quad (5-12)$$

$$E_{2_gr} = \left\{ \sum_{\text{interior nodes}} \left[\left(\frac{\partial \phi}{\partial r} \right)_{\text{LBE}} - \left(\frac{\partial \phi}{\partial r} \right)_{\text{ex}} \right]^2 / \sum_{\text{interior nodes}} \left(\frac{\partial \phi}{\partial r} \right)_{\text{ex}}^2 \right\}^{1/2}, \quad (5-13)$$

$$E_{2_gz} = \left\{ \sum_{\text{interior nodes}} \left[\left(\frac{\partial \phi}{\partial z} \right)_{\text{LBE}} - \left(\frac{\partial \phi}{\partial z} \right)_{\text{ex}} \right]^2 / \sum_{\text{interior nodes}} \left(\frac{\partial \phi}{\partial z} \right)_{\text{ex}}^2 \right\}^{1/2}. \quad (5-14)$$

The results of E_2 , E_{2_qw} , E_{2_gr} and E_{2_gz} , defined in Eqs. (5-10, 5-12 – 5-14) versus the grid resolution, $1/R_0$, at different Δ values are shown in Figs. 5-5 (a-d), respectively. For each case in Fig. 5-5, second-order convergence is observed. It should be noted that only first-order convergence was obtained for the boundary flux and boundary heat transfer in Figs. 3-28 and 4-12 in Sections 3.4.5.1 and 4.3.4, respectively, due to the curved boundary effect when the D3Q7 LB model was used. In the present axisymmetric case, the curved boundary effect is eliminated and thus second-order accuracy is preserved for the interior distribution of ϕ , the boundary flux, and the interior gradients in both directions.

5.3.2.2 Neumann boundary condition on the wall

When the sinusoidal Dirichlet condition in 5.3.2.1 is replaced with a sinusoidal Neumann condition, the analytical solution for ϕ can also be solved and it is given in Eq. (3-79).

The contours of ϕ in this case are very similar to that with a Dirichlet wall boundary condition except for the magnitude; thus the contours are not shown for brevity.

According to Eq. (3-41b), the boundary values of ϕ are computed based on the distribution functions at the adjacent lattice nodes and the boundary flux information,

$$\Phi_d = \frac{1}{\varepsilon_D} \left[(2\Delta + 1)\hat{g}_\alpha(\mathbf{x}_f, t) + \left(\frac{2}{1-c_{d1}} - 2\Delta \right) \hat{g}_\alpha(\mathbf{x}_{ff}, t) + \left(1 - \frac{2}{1-c_{d1}} \right) \hat{g}_{\bar{\alpha}}(\mathbf{x}_f, t) + \left(\frac{2}{1-c_{d1}} \right) \frac{\delta t}{\delta x} \Phi_{n\bar{\alpha}} \right].$$

The following L-2 error norm is further defined to assess the LB results

$$E_{2_tw} = \left\{ \sum_{r=R_0} [\phi_{LBE} - \phi_{ex}]^2 / \sum_{r=R_0} \phi_{ex}^2 \right\}^{1/2}. \quad (5-15)$$

Figures 5-6 (a-d) show the error norms E_2 , E_{2_tw} , E_{2_gr} and E_{2_gr} defined in Eqs. (5-10, 5-15, 5-13 and 5-14), respectively, versus the grid resolution, $1/R_0$, at different Δ values. Second-order accuracy is obtained for all cases in Fig. 5-6. The proposed LB model for the axisymmetric CDE with Neumann boundary conditions is also verified to be second-order accurate.

5.3.3 Steady heat conduction inside a sphere

When there is no temperature variation in the azimuthal direction, the heat conduction inside a sphere is axisymmetric and it can be represented in the radial-axial cylindrical coordinate system. Thus the axisymmetric LB model can be applied to simulate the heat conduction in a sphere. The computational domain and the lattice layout are schematically shown in Fig. 5-7. The curved geometry of the sphere is preserved by calculating the intersected link fractions (Δx and Δy) for those field lattice nodes, such as point P in Fig. 5-7, adjacent to the boundary. After the local Δ value

along the lattice velocity direction $\mathbf{e}_{\bar{\alpha}}$ is obtained for each boundary node, the Dirichlet and Neumann boundary condition treatments in Eqs. (3-32) and (3-38) are implemented, respectively.

5.3.3.1 Dirichlet boundary condition on the wall

A Dirichlet boundary condition of a Legendre polynomial $P_n(\mu = \cos\theta)$ on the sphere surface, $r = R_0$, is considered and the analytical solution for the interior temperature ϕ is (Hahn and Ozisik 2012)

$$\phi_{\text{ex}}(r, \mu) = (r / R_0)^n P_n(\mu). \quad (5-16)$$

A representative case of $P_4(\mu) = (35\mu^4 - 30\mu^2 + 3) / 8$ is studied in this work. The axis of the sphere is placed in the center of the lattice link (see Fig. 5-7) so that the symmetry condition, $\partial\phi/\partial r|_{r=0} = 0$, which is a Neumann boundary condition, is used in all simulations.

Figure 5-8 shows the error norms of the interior temperature field and the boundary heat flux E_2 and E_{2_qw} defined in Eqs. (5-10) and (5-12), respectively, versus the grid resolution $1/R_0$, with the Dirichlet Schemes 1-3 in Eqs. (3-35 a-c) implemented. It should be noted that the boundary heat flux in this test is evaluated along the discrete lattice velocity directions using the formula proposed in Eq. (3-41a). For those boundary nodes intersected by the lattice vectors along z-direction, $\partial\phi/\partial r|_{r=R_0}$ in Eq. (5-12) is replaced by $\partial\phi/\partial z|_{r=R_0}$. For each case, quadratic and linear convergence orders are noticed in Fig. 5-9 for E_2 and E_{2_qw} , respectively, which are consistent with the results in Figs. 3-27 and 3-28 for curved boundaries. Second-order accuracy of the temperature field is thus preserved with the present axisymmetric LB model, and the first-order

accurate boundary heat flux is due to the irregularly distributed link fractions in both the radial and axial directions caused by the curved boundary (Li et al. 2013a, 2013b).

5.3.3.2 Neumann boundary condition on the wall

When a Neumann flux condition $\Phi_n = -D\partial\phi/\partial r|_{r=R_0} = -DnP_n(\mu)/R_0$ is imposed on the sphere surface the analytical solution for ϕ is the same as that in Eq. (5-16) and $n = 4$ is again studied. To implement the Neumann condition treatment in Eq. (3-38), the boundary flux $\Phi_{n\bar{\alpha}}$ in each lattice velocity direction is required. The Cartesian decomposition method discussed in Chapter 3 to obtain $\Phi_{n\bar{\alpha}}$ based on the normal flux Φ_n on a curved boundary is used in the present case. The L-2 norms E_2 and E_{2_tw} defined in Eqs. (5-10) and (5-14), respectively, are computed for this test and their convergence is shown in Fig. 5-9, where on average a first-order convergence is obtained for both E_2 and E_{2_tw} . As demonstrated earlier in Fig. 5-8 for Dirichlet problems with curved boundaries, the evaluation of the boundary flux $\Phi_{n\bar{\alpha}}$ is only first-order accurate even with a second-order accurate temperature field obtained. The same formula for evaluating the boundary flux $\Phi_{n\bar{\alpha}}$ is directly used in the Cartesian decomposition method for Neumann problems, thus some first-order error terms are introduced in the boundary condition treatment.

The numerical tests in this section serve as an excellent example to show that even with a second-order LB model implemented, the overall accuracy of the LB solutions is directly affected by the relevant boundary condition treatment.

5.3.4 Unsteady heat conduction in a circle

For unsteady heat conduction inside a circle, the governing equation simplifies to

$$\frac{\partial \phi}{\partial t} = \frac{\partial}{\partial r} \left(D_{rr} \frac{\partial \phi}{\partial r} \right) + \frac{D_{rr}}{r} \frac{\partial \phi}{\partial r}. \text{ A sinusoidal boundary condition } \phi(t, r = R_0) = f(t) = \sin(\omega t) \text{ is}$$

specified and the analytical solution for ϕ can be found in Eq. (3-70).

This axisymmetric heat conduction problem has been studied in Section 3.4.4 to assess the thermal boundary condition treatment and in Section 4.3.3 for heat transfer evaluation on curved boundaries, respectively. In both studies the computational domain is in the 2-D circular plane. In this work, as the axisymmetric LB model is used, the computational domain is on the r - z plane and only a few lattice grids ($N_z = 5$ in the results shown below) are used in the z -direction since the variations are only in the r -direction. Both $r = 0$ and $r = R_0$ are located halfway between the lattice nodes ($\Delta = 0.5$). Following Section 3.4.4, the time-averaged error norm for ϕ in the interior of the domain on the r - z plane is defined as

$$E_2 = \left[\frac{\omega}{2\pi} \int_0^{2\pi/\omega} \frac{1}{N_r N_z} \sum_{r,z} (\phi_{\text{LBE}} - \phi_{\text{ex}})^2 dt \right]^{1/2}. \quad (5-17)$$

The results of E_2 defined in Eq. (5-17) versus the grid resolution, $1/R_0$, at different relaxation coefficients of τ_D are shown in Fig. 5-10. Second-order convergence is observed for each case in Fig. 5-10. This demonstrates that the proposed LB model can be effectively applied to simulate time-dependent axisymmetric convection diffusion problems and the second-order accuracy is preserved.

5.3.5 Steady natural convection in an annulus between two coaxial vertical cylinders

In the previous tests, the velocity fields are specified. With the objective to show that the proposed LB model for the axisymmetric CDE of ϕ can be effectively coupled with the athermal LB models for axisymmetric hydrodynamic equations, we consider in this test the natural convection in an annulus formed by two coaxial vertical cylinders. The velocity field is solved using an MRT version of Zhou's athermal axisymmetric LB model (Zhou 2011) and the temperature field is simulated with the present LB model at each time step. The two models are iterated to reach their steady states.

The computational domain, the thermal boundary conditions, and the schematic layout of the square lattice are sketched in Fig. 5-11. Both the radius ratio R_o/R_i and the aspect ratio $H/(R_o - R_i)$ are equal to 2.0 in the present simulations. The vertical cylinder surfaces are maintained at constant temperatures T_i and T_o , respectively with $T_i > T_o$, while the top and bottom walls are insulated. Invoking the Boussinesq approximation, the fluid properties in the annulus are assumed to be constant, except for the density in the buoyancy term in the momentum equation. The Prandtl number is fixed at $Pr = 0.7$, and the characteristic Rayleigh number is defined as $Ra = g\beta(T_i - T_o)(R_o - R_i)^3/\alpha\nu$, where g is the gravitational acceleration, β is the thermal-expansion coefficient, α is the thermal diffusivity and ν is the kinematic viscosity of the fluid.

The effect of the temperature distribution on the velocity field is taken into account by adding a body force term $\rho a_z = -\rho g\beta(T - T_m)$ in the momentum equation, where $T_m = (T_i + T_o)/2$ is the average temperature. It should also be noted that the present coupling between the athermal and thermal LB models is only on the macroscopic level, and the direct coupling of the distribution functions for the velocity

and temperature is eliminated. This makes the implementation of the LBE models more straightforward and convenient. The convergence is checked by monitoring the variations of the velocity and temperature values at some representative nodes, and the relative differences between successive iterations are at least less than 10^{-8} for both the velocity and temperature fields.

The streamlines and isotherms at steady states are shown in Figs. 5-12 and 5-13, respectively, for $Ra = 10^3$, 10^4 and 10^5 with $Nr \times Nz = 202 \times 402$. The present results agree well with those reported in (Li et al. 2009, de Vahl Davis and Thomas 1969, Kumar and Kalam 1991, Venkatachalappa et al. 2001). To quantify the numerical results, the following surface-averaged Nusselt numbers on the cylinder walls are defined and compared with the published results in (Li et al. 2009) and (Venkatachalappa et al. 2001)

$$Nu_i = -\frac{R_i}{H(T_i - T_o)} \int_0^H \frac{\partial T}{\partial r} \Big|_i dz, \text{ and } Nu_o = -\frac{R_o}{H(T_i - T_o)} \int_0^H \frac{\partial T}{\partial r} \Big|_o dz. \quad (5-18)$$

It is worth mentioning that in this work the boundary temperature gradients in Eq. (5-18) are evaluated on the basis of the temperature distribution functions as proposed in Section 4.2.3 rather than using any finite-difference schemes on the temperature field. And the overall heat transfer on the walls is obtained using the technique proposed in Chapter 4. Both the heat flux and heat transfer evaluations are second-order accurate as verified in Chapters 3 and 4 for straight boundaries.

A grid-refinement study is first carried out and the Nusselt numbers Nu_i and Nu_o defined in Eq. (5-18) obtained from different mesh sizes are listed in Table 5-1. The numerical results for Nu_i and Nu_o evaluated on the inner and outer surfaces are almost identical to each other for all cases, demonstrating the excellent conservation property

of the LBE scheme. It is emphasized that such high consistency between Nu_i and Nu_o can only be obtained after the numerical solutions are fully converged. In the present test, all the boundaries are placed in the center of the lattice links ($\Delta = 0.5$), thus the second-order accuracy is preserved for the LBE method in the interior, for the “bounce-back” hydrodynamic and thermal boundary conditions and the heat transfer evaluation on the straight boundaries. Hence more accurate results can be obtained using the Richardson extrapolation of the raw second-order results before they are rounded in Table 5-1. In the present case, $Nu_{\text{extrapolated}} = (\gamma^n Nu_{\text{fine}} - Nu_{\text{coarse}}) / (\gamma^n - 1)$ where $\gamma = (Nr - 2)_{\text{fine}} / (Nr - 2)_{\text{coarse}}$ is the grid resolution ratio, and $n = 2$ is the order of convergence of the LBE solutions. Table 5-2 compares the extrapolated Nusselt number with the published data in (Li et al. 2009) and (Venkatachalappa et al. 2001). Both the results for Nu_i and Nu_o are presented in (Li et al. 2009), and the results from (Venkatachalappa et al. 2001) are the average Nusselt numbers on the two cylinder surfaces, i.e., $Nu = (Nu_i + Nu_o)/2$. The present results in Table 5-2 are in good agreement with those from (Li et al. 2009) and (Venkatachalappa et al. 2001), demonstrating that the present LB model can be effectively coupled with the athermal axisymmetric LB models and the interaction between the velocity field and the thermal field is accurately captured.

5.3.6 Swirling thermal flows in a vertical cylinder

Confined axisymmetric flows driven by a rotational velocity is considered in this test to further demonstrate the utility of the present LB model when it is coupled with the axisymmetric LB model for the velocity field. The fluid inside the cylindrical container is assumed to be incompressible and the Boussinesq assumption is valid for the present

flow. The top disc rotates at a constant angular speed Ω , and the rest of the solid boundaries are stationary. The top and bottom discs are maintained at constant temperatures, T_h and T_c , respectively ($T_h > T_c$), while the side walls are insulated. The swirling flows are characterized by the Reynolds number Re , and the Richardson number Ri , defined as

$$Re = R^2\Omega/\nu, \text{ and } Ri = g\beta\Delta Th^3/(R\Omega^2), \quad (5-19)$$

where R is the radius of the cylinder, $\Delta T = T_h - T_c$, and h is the aspect ratio of the height to the radius of the cylinder, $h = H/R$.

The flow pattern and heat transfer of the swirling flows in the range of $10^2 \leq Re \leq 3 \times 10^3$ and $0 \leq Ri \leq 1.0$ at fixed Prandtl number $Pr = 1.0$ and cylinder aspect ratio $h = 1.0$ were investigated in detail by Iwatsu (2004) using the vorticity-stream function formulation. Zheng et al. (2010a) also simulated the same swirling flow problem and compared their results at $Re = 2000$, and $Ri = 0$ and 1.0 with that in (Iwatsu 2004) to validate their axisymmetric thermal LB model.

In the present simulations, the radial and axial velocity components u_r and u_z are solved using Zhou's axisymmetric LB model (Zhou 2011) with an MRT collision operator (see Appendix C). While it is noted that the governing equation for the azimuthal velocity, u_ϕ , is also a CDE (Zhou 2011, Graebel 2001)

$$\frac{\partial u_\phi}{\partial t} + \frac{\partial}{\partial r}(u_r u_\phi) + \frac{\partial}{\partial z}(u_z u_\phi) = \nu \left(\frac{\partial^2 u_\phi}{\partial r^2} + \frac{\partial^2 u_\phi}{\partial z^2} \right) - \left(\frac{2u_r}{r} + \frac{\nu}{r^2} \right) u_\phi + \frac{\nu}{r} \frac{\partial u_\phi}{\partial r}, \quad (5-20)$$

where ν is the kinematic viscosity of the fluid. Eq. (5-20) is very similar to Eq. (5-1) when u_ϕ is considered as a scalar variable. The source terms S_{a1} and S_{a2} in Eq. (5-2)

can be modified as $S_{a1} = -\left(\frac{2u_r}{r} + \frac{\nu}{r^2}\right)u_\phi$ and $S_{a2} = \frac{\nu}{r} \frac{\partial u_\phi}{\partial r}$, to account for the scalar

variable and its gradient terms in Eq. (5-20), respectively. Thus the azimuthal velocity component in rotational flows can also be solved using the present LB model for axisymmetric CDEs. In this study, Zhou's LB model (2011) for the radial and axial velocities and the present LB model for the azimuthal velocity and the temperature are coupled at each time step to reach the steady states. The following results are obtained with mesh sizes of 150×150 for $(Re, Ri) = (2000, 0)$, and 200×200 for $(Re, Ri) = (2000, 1.0)$ after a grid-refinement study.

The contours of the azimuthal velocity component u_ϕ and the isotherms are shown in Figs. 5-14 and 5-15 for the extreme values of $Ri = 0$ and 1.0 , respectively, at $Re = 2000$. The swirling flows driven by the rotating top disc are clearly seen, and thin boundary layers are observed near the top disc in the contours of u_ϕ . At $Ri = 1.0$, the effect of the buoyancy force becomes significant and the isotherms in Fig. 5-15 (b) become more horizontal than that for $Ri = 0$, especially in the half region near the bottom. It is also noticed that the magnitude of u_ϕ is very small and thus not shown in the lower portion of the cylinder at $Ri = 1.0$ in Fig. 5-15 (a). The present flow pattern and isotherm distributions are very similar to those reported in (Zheng et al. 2010a, Iwatsu 2004). To further quantify and validate the present results, the profiles of the velocity components and the temperature at $r/R = 0.8$ are compared with those from (Iwatsu 2004) in Figs. 5-16 (a-d). It should be noted that all the velocity components are normalized by $R\Omega$ and the dimensionless temperature is $\bar{T} = (T - T_m)/(T_h - T_c)$ with $T_m = (T_h + T_c)/2$. Good agreement is obtained for each case in Fig. 5-16. The rapid changes of the velocity and temperature profiles across the boundary layers are fully captured in the present simulations. The present LB model can thus be applied to axisymmetric

rotational flows where both the temperature and azimuthal velocity fields can be simulated with the proposed LB model for the axisymmetric CDEs.

5.4 Summary and Conclusions

A robust multi-relaxation-time (MRT) lattice Boltzmann model for the axisymmetric convection-diffusion equation (CDE) is proposed. The axisymmetric CDE is transformed to a standard CDE in the Cartesian coordinate system and the additional terms due to the coordinate transformation are treated as source terms at the macroscopic level. The scalar gradient in the source terms is formulated using the local moment of the non-equilibrium components of the distribution functions without the need for finite-difference type of calculations.

When the CDE for the scalar variable ϕ is coupled with the hydrodynamic equations, the radial-axial velocity field is solved with an MRT version of the athermal axisymmetric LB model (Zhou 2011). The macroscopic velocity components, instead of the velocity distribution functions, are coupled in the evolution equation of the distribution functions for ϕ . In this manner, there is no explicit coupling between the two sets of distribution functions, making the present model much easier to implement and more robust.

The second-order accuracy of the proposed LB model is validated with a series of numerical tests. The effect of the curved boundary on the convergence order of the LB solutions is also investigated and verified. The agreement between the present LB results and published numerical computations in the literature for the natural convection problem and the confined swirling flows also demonstrates that the present model can

be effectively coupled with athermal LB models to yield accurate results for axisymmetric thermo-hydrodynamic problems.

Table 5-1. Surface-averaged Nusselt numbers at different grid resolution.

mesh	Average Nusselt numbers Nu_i , Nu_o		
	$Ra = 10^3$	$Ra = 10^4$	$Ra = 10^5$
102×202	1.69200, 1.69200	3.21673, 3.21673	5.83096, 5.83095
127×252	1.69206, 1.69206	3.21607, 3.21607	5.81486, 5.81486
152×302	1.69210, 1.69210	3.21572, 3.21572	5.80636, 5.80636
202×402	1.69213, 1.69213	3.21531, 3.21531	5.79802, 5.79802

Table 5-2. Comparison of the present surface-averaged Nusselt numbers with published results.

Ra	Average Nusselt number Nu			
	Present (extrapolated)	Li et al. 2009 Nu_i (101×201)	Li et al. 2009 Nu_o	Venkatachalappa et al. 2001 (41×81)
10^3	1.6922	-	-	-
10^4	3.2148	3.216	3.218	3.1629
10^5	5.7873	5.782	5.787	5.8818

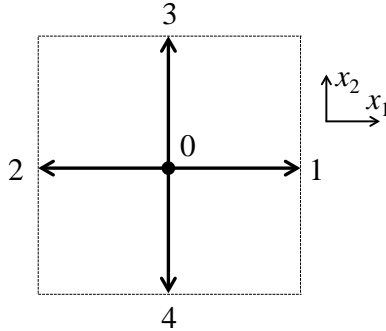


Figure 5-1. Discrete velocity set $\{\mathbf{e}_\alpha\}$ for the D2Q5 LB model. $\mathbf{e}_\alpha = (0, 0)$, $(\pm 1, 0)$, and $(0, \pm 1)$.

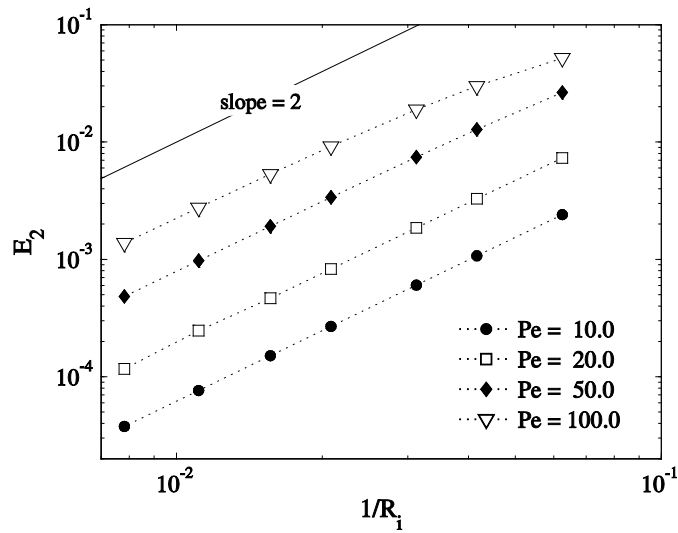


Figure 5-2. Relative L-2 error norm E_2 for the interior field of ϕ versus the grid resolution, $1/R_i$, for the 1-D annulus convection-diffusion problem.

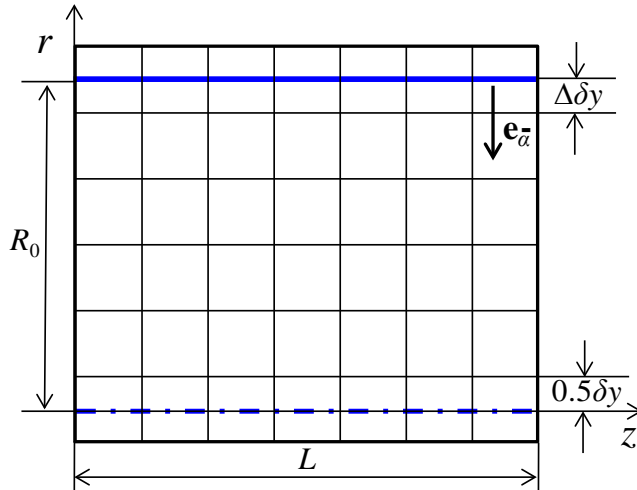


Figure 5-3. Schematic of the square lattice in the r - z plane of a 3-D circular pipe. The axis of the pipe, $r = 0$, is fixed at the center of the link with $\Delta = 0.5$, while the pipe surface, $r = R_0$, is placed at an arbitrary location in the link with $0 \leq \Delta \leq 1$.

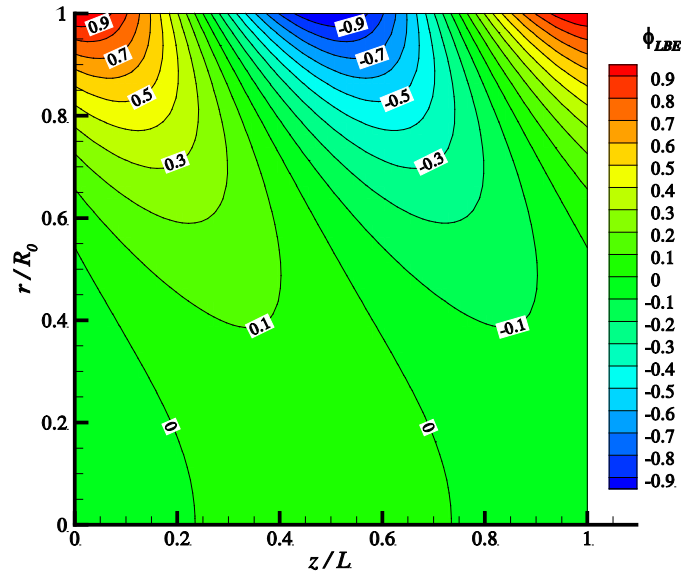


Figure 5-4. Contours of ϕ in the r - z plane at $Nr = 42$, $Nz = 83$, and $\Delta = 0.5$ for the steady convection-diffusion in a pipe with a Dirichlet boundary condition on the wall.

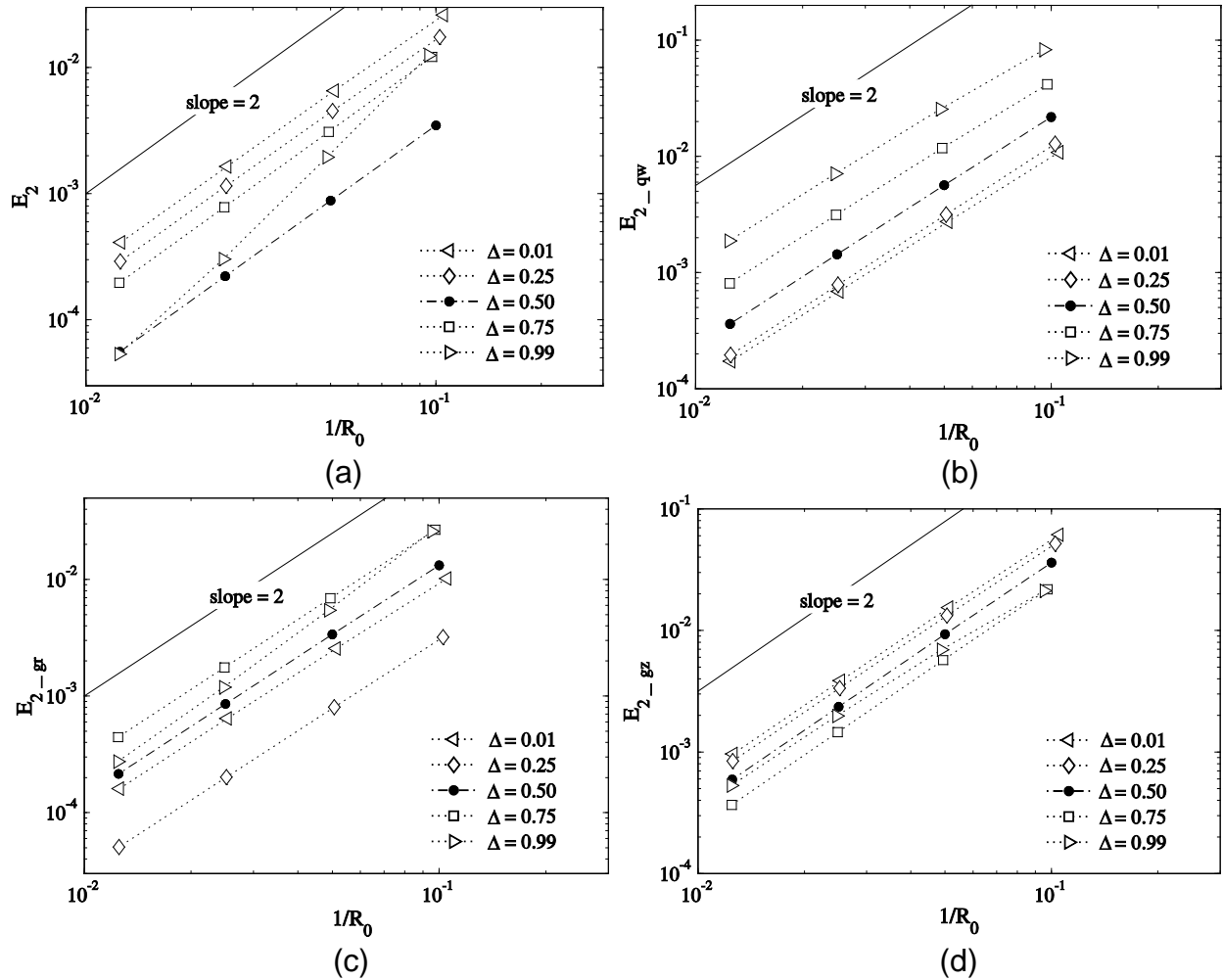


Figure 5-5. Relative L-2 error norms versus the grid resolution, $1/R_0$, for the steady convection-diffusion in a pipe with a Dirichlet boundary condition on the wall: (a) E_2 for the interior field of ϕ , (b) E_{2-qw} for the boundary flux, (c) E_{2-gr} for the interior radial gradient $\partial\phi/\partial r$, and (d) E_{2-gz} for the interior axial gradient $\partial\phi/\partial z$.

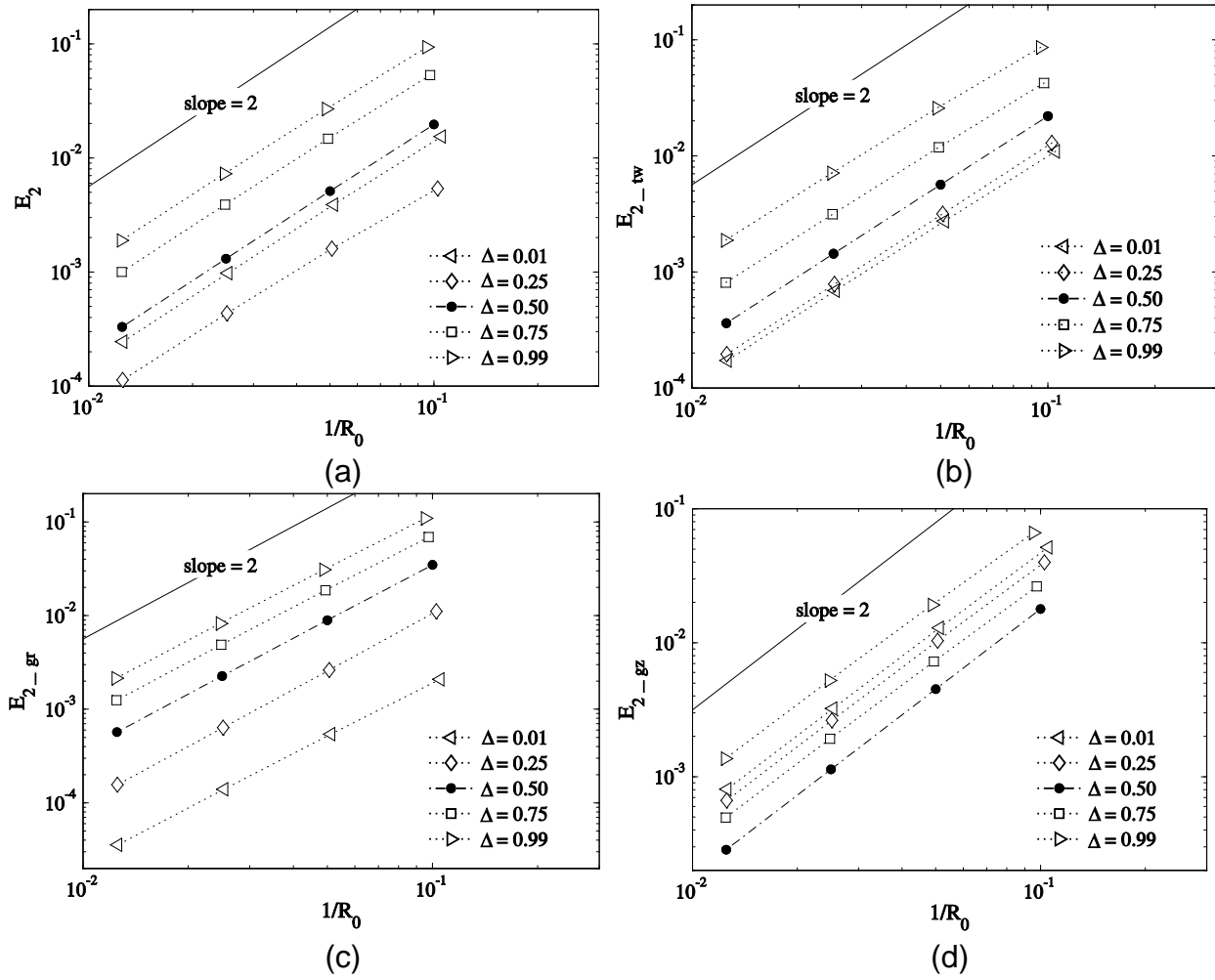


Figure 5-6. Relative L-2 error norms versus the grid resolution, $1/R_0$, for the steady convection-diffusion in a pipe with a Neumann boundary condition on the wall: (a) E_2 for the interior field of ϕ , (b) E_{2_tw} for the boundary values of ϕ , (c) E_{2_gr} for the interior radial gradient $\partial\phi/\partial r$, and (d) E_{2_gz} for the interior axial gradient $\partial\phi/\partial z$.

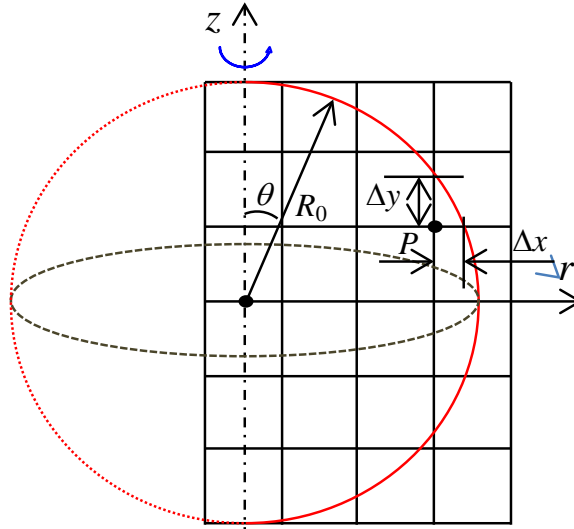


Figure 5-7. Schematic representation of the computational domain and the lattice layout for the heat conduction inside a sphere.

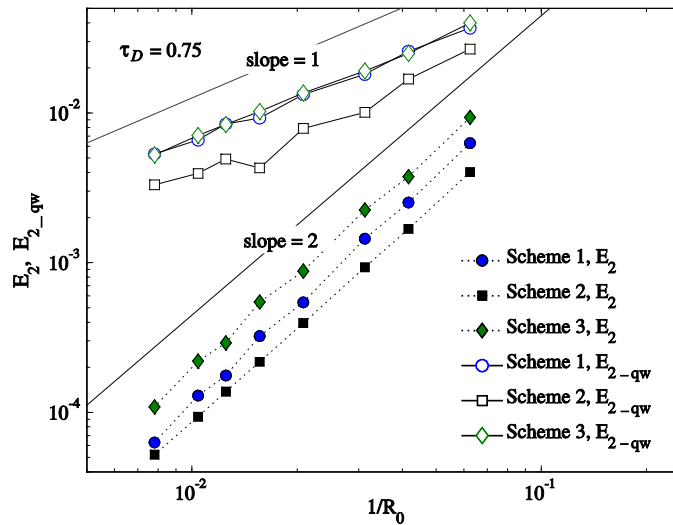


Figure 5-8. Relative L-2 error norms E_2 and E_{2_qw} for the interior field of ϕ and the boundary flux, respectively, versus the grid resolution, $1/R_0$, for the steady heat conduction inside a sphere with a Dirichlet boundary condition.

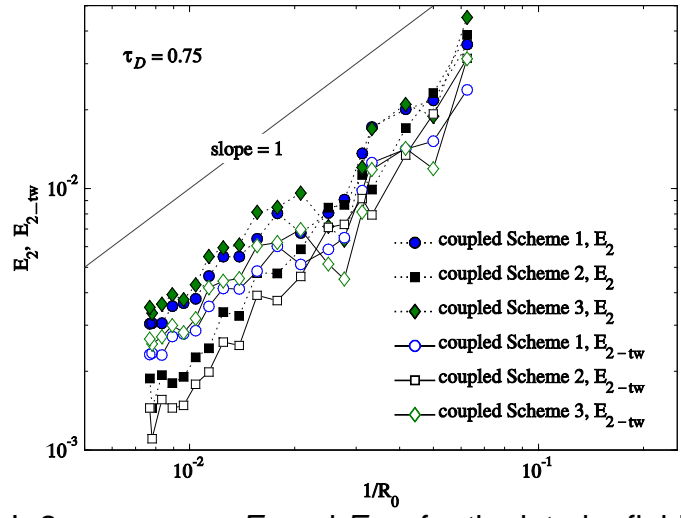


Figure 5-9. Relative L-2 error norms E_2 and E_{2-tw} for the interior field and boundary values of ϕ , respectively, versus the grid resolution, $1/R_0$, for the steady heat conduction inside a sphere with a Neumann boundary condition.

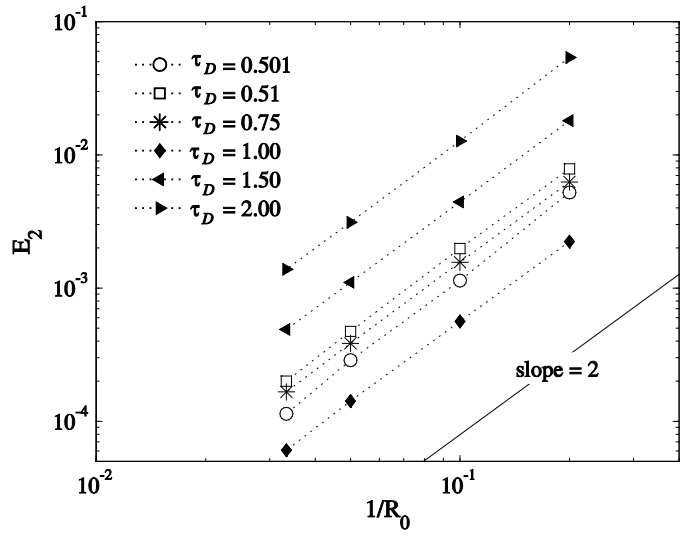


Figure 5-10. Time-averaged error norm E_2 for the interior field of ϕ versus the grid resolution, $1/R_0$, for the unsteady heat conduction in a circle with a temporal Dirichlet boundary condition.

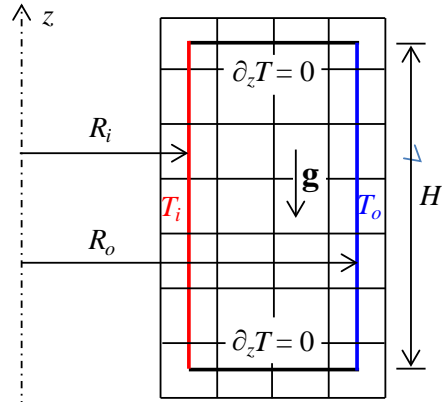


Figure 5-11. Schematic depiction of the computational domain ($R_o/R_i = 2.0$, and $H/(R_o - R_i) = 2.0$) and the thermal boundary conditions on the walls all placed in the center of the lattice links ($\Delta = 0.5$).

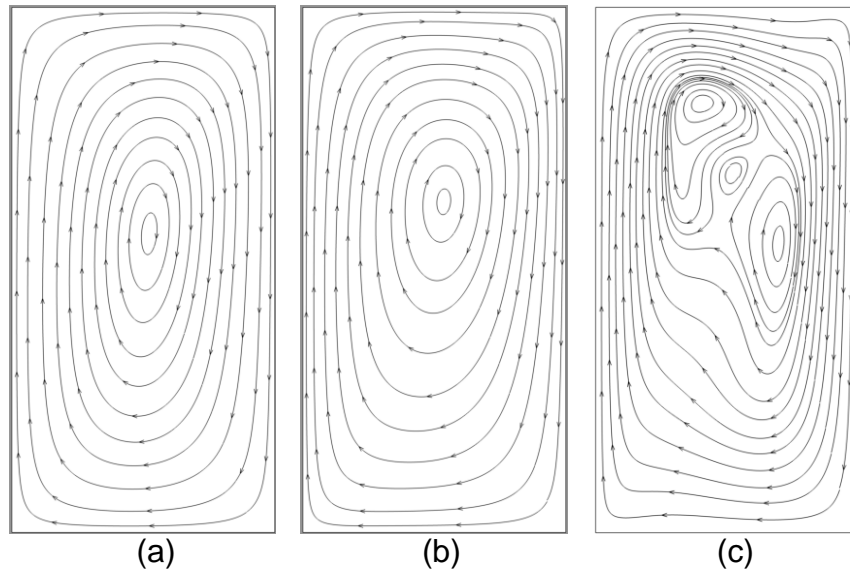


Figure 5-12. Streamlines in the annulus between two coaxial vertical cylinders at (a) $Ra = 10^3$, (b) $Ra = 10^4$, and (c) $Ra = 10^5$.

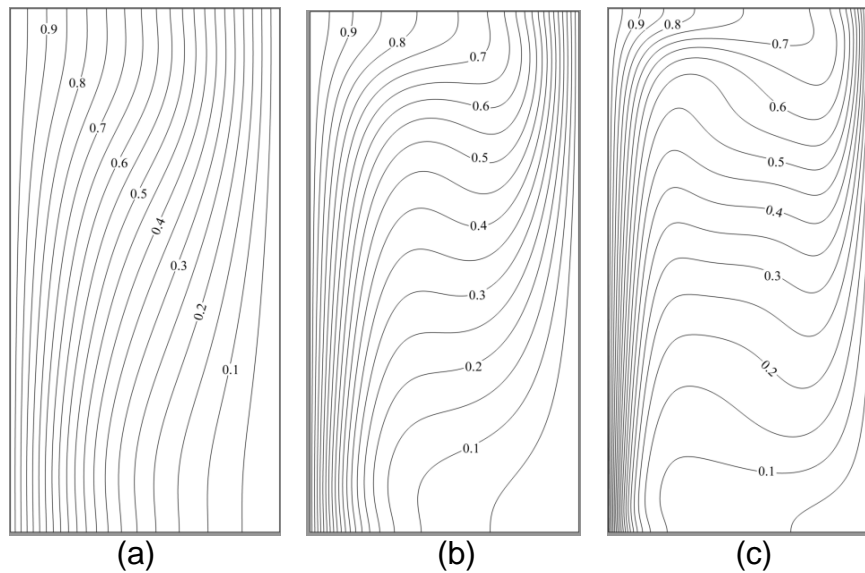


Figure 5-13. Isotherms in the annulus between two coaxial vertical cylinders at (a) $Ra = 10^3$, (b) $Ra = 10^4$, and (c) $Ra = 10^5$.

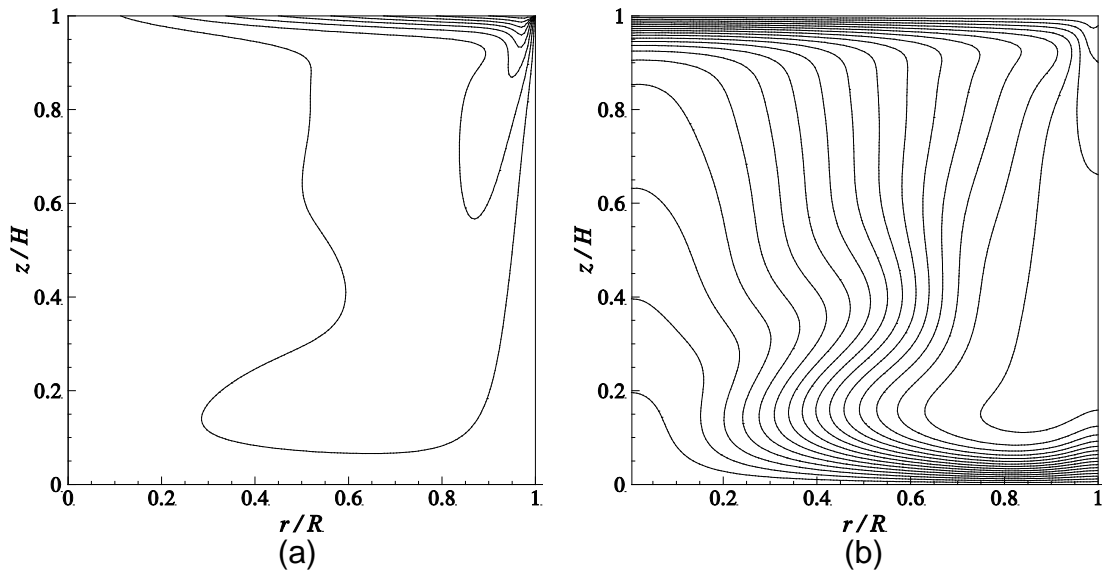


Figure 5-14. Contours of the azimuthal velocity u_ϕ (a) and isotherms (b) of the confined swirling flow at $Re = 2000$ and $Ri = 0$.

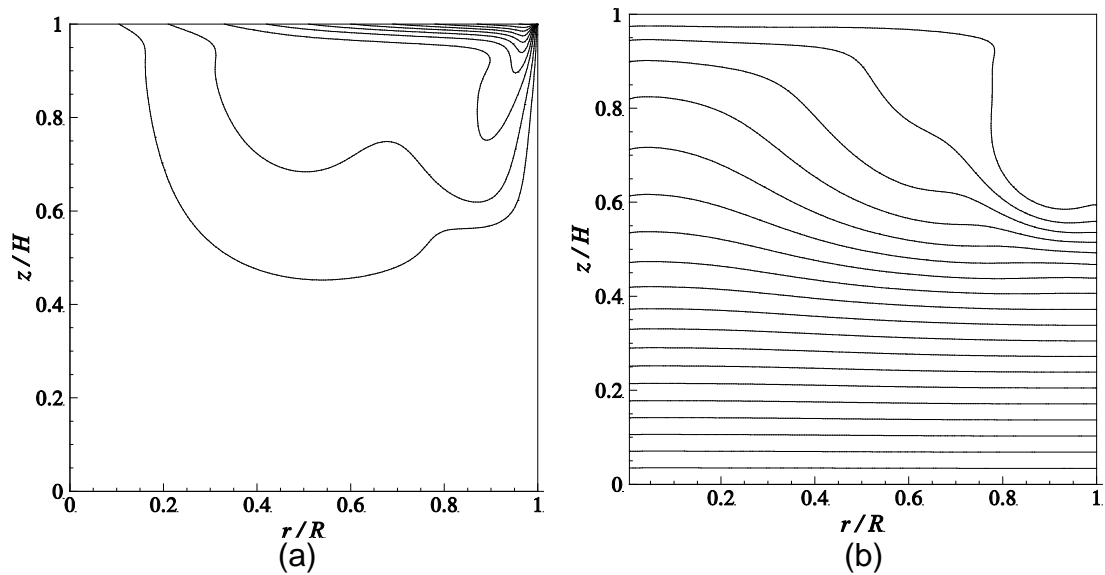


Figure 5-15. Contours of the azimuthal velocity u_ϕ (a) and isotherms (b) of the confined swirling flow at $Re = 2000$ and $Ri = 1.0$.

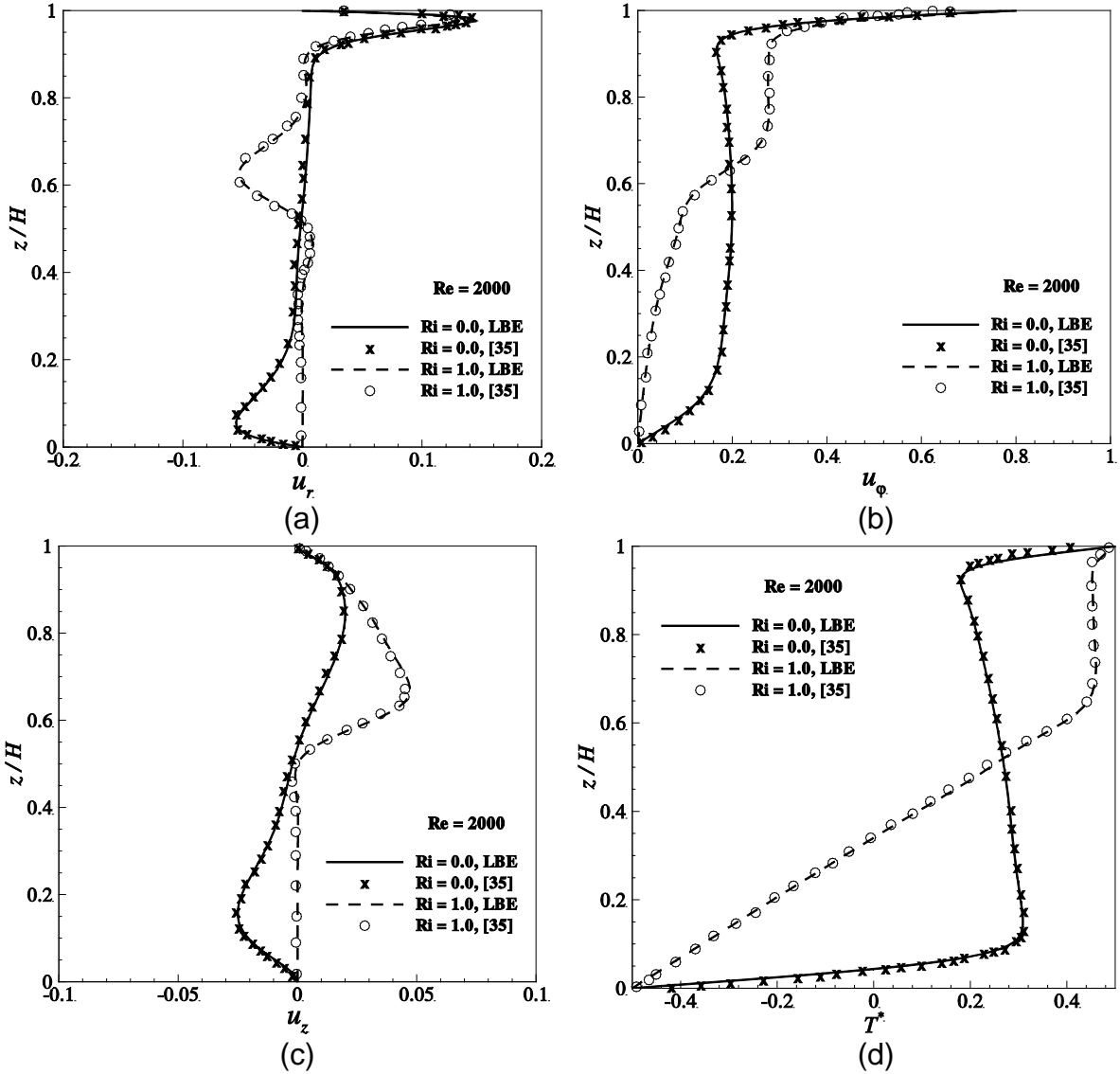


Figure 5-16. Velocity components and temperature profiles along the vertical line at $r/R = 0.8$ for $Re = 2000$: (a) radial velocity u_r , (b) azimuthal velocity u_ϕ , (c) axial velocity u_z , and (d) temperature.

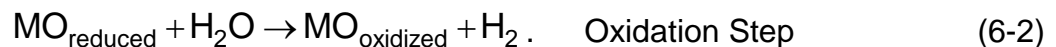
CHAPTER 6
ENERGY TRANSPORT IN A SOLAR THERMOCHEMICAL REACTOR FOR
HYDROGEN PRODUCTION*

6.1 Introduction

Thermochemical cycles using concentrated solar energy as the heat source to produce hydrogen or synthesis gas (syngas, mixture of hydrogen and carbon monoxide) have been demonstrated to be a promising and efficient strategy for renewable energy pursuit (Steinfeld 2002, Steinfeld 2005, Abanades et al. 2006, Kodama and Gokon 2007, Perkins and Weimer 2009, Loutzenhiser et al. 2010, Mehdizadeh et al. 2012). The two-step H₂O/CO₂-splitting cycle by a metal oxide process is one of most studied cycles in the literature (Steinfeld 2002, Steinfeld 2005, Abanades et al. 2006, Kodama and Gokon 2007, Loutzenhiser et al. 2010, Mehdizadeh et al. 2012).

In the two-step H₂O/CO₂-splitting reduction-oxidation (Redox) reaction, one step is known as the regeneration or thermal reduction, in which a metal oxide is reduced, releasing lattice oxygen. During the subsequent oxidation step, the reduced and activated material is oxidized by reacting with water/CO₂ to produce hydrogen/CO.

The present study focuses on hydrogen production. Denoting M as the used metal and MO the corresponding metaloxide, the reduction and oxidation steps can be represented by



The reduction step is endothermic and the oxidation step is exothermic, both steps require high temperatures and the temperature for the reduction step is normally

* The Monte Carlo ray-tracing modeling of the radiative heat transfer inside the cavity by Singh A. (Singh 2013) based on the work of Petrasch J. (2002) is greatly appreciated.

much higher than that for the oxidation step. For example, most of the operation temperatures required for the reduction step as listed in Abanades et al.'s work (2006) is greater than 1000 °C. Due to the high temperature requirement especially during the reduction step, concentrated high-flux solar energy is considered as an effective heat source for which a solar cavity-receiver configuration is usually required.

Klausner et al. (2011) have been developing a solar thermochemical reactor prototype for cyclically producing renewable and carbon-neutral fuels. Main features in their concept include: (i) a magnetically stabilized structured bed of metal/metal oxide particles to improve cyclical behavior and minimize solid particle losses, (ii) low pressure operation to bring down reduction temperatures below 1500 °C, and (iii) a windowless dual cavity reactor concept that avoids reliability issues associated with directly irradiated, windowed cavity type reactors (Klausner et al. 2011).

Heat transfer mechanisms in the reactor include radiation, conduction, convection and chemical reaction. A fundamental understanding of the energy transport in the solar cavity-receiver and the heat flux and temperature distributions on the surfaces and in the interior of the reactors (absorbers) is essential to the optimal design of the cavity-reactor.

Radiative heat transport inside the cavity can be modeled either by the radiosity analysis method (Wieckert et al. 2003, Müller et al. 2008) or using the Monte Carlo ray-tracing (MCRT) technique (Petrasch et al. 2007, Melchior and Steinfeld 2008). The MCRT technique, which is intrinsically three-dimensional, is preferred in the present work since it can be applied to simulate the radiative heat transfer in arbitrary geometric configurations and thus be used for optimal design. With the heat flux boundary

condition on the absorber surfaces obtained from the radiative heat transfer analysis, the energy transport inside the absorbers, including conduction, convection, radiation and chemical reaction in the porous bed, can be simulated. Realizing the reemission from the absorber surfaces becomes significant when the surface temperatures are high enough, this reemission should be fed back to the radiative analysis inside the cavity. Thus these two models should be coupled to balance the energy transfer in the whole cavity-reactor system.

Wickert et al. (2003) applied the radiosity method to calculate the solar energy absorption efficiency for a two-cavity configuration. Müller et al. (2008) also used the radiosity method to simulate the radiative heat transfer between the cavity wall and the absorber surfaces. Melchior and Steinfeld (2008) used the Monte Carlo method to study the radiative transfer inside a solar cylindrical cavity with diffusely or specularly reflecting inner walls, containing one single-tube or multiple-tube absorbers, and a selective window or a windowless aperture. The location and relative dimensions of the absorbers are optimized for maximum energy transfer efficiency or for maximum absorber surface temperature (Melchior and Steinfeld 2008). It is noticed that the heat transfer inside the reaction chamber or the absorbers is not fully simulated in both of the work by Wieckert et al. (2003) and by Melchior and Steinfeld (2008). Instead, they considered the net power absorbed by the reactors as a parameter and examined the energy transfer efficiency at different values of that parameter. Maag et al. (2010a, 2010b) developed a radiation/convection/conduction coupled solar-reactor heat transfer model for syngas production and methane decomposition. Their reactor model consists of a cavity-receiver model and an absorber tube model, which are coupled by the net

heat sink into each tube based on the outer surface temperatures of the tubes. A constant surface temperature was assumed on each outer tube in the coupled model (Maag et al. 2010a, 2010b) considering the high thermal conductivity of the graphite tubes.

The thermochemical reduction step in the redox cycle is very sensitive to change of temperature at high temperatures. In addition, the radiative emission from the absorber surfaces, which is directly related to the surface temperature distributions, contributes to and significantly affects the overall radiative transfer analysis inside the cavity. The simulation and determination of the actual temperature field inside the absorbers as well as on the absorber surfaces are thus necessary in the energy transport analysis of the cavity-reactor system.

A coupled radiation-convection-diffusion model is developed in this work. The boundary heat flux distributions on the surfaces are obtained from an MCRT radiation mode, and the energy equation inside the absorbers is solved with the thermal lattice Boltzmann equation (TLBE) method discussed in Chapters 3, 4 and 5. These two models are fully coupled and iteratively solved. The geometry of the curved boundary is preserved using the boundary condition treatment in Chapter 3.

6.2 Horizontal Cavity-Receiver Solar Reactor

The geometrical configuration of the present solar reactor is schematically depicted in Fig. 6-1. Its main features include a cylindrical cavity with its axis being horizontal and parallel to the central incident solar flux, a circular aperture through which the incident solar flux enters the cavity, and a series of tubular absorbers at the circumference of the cavity. A stabilized porous structure or packed bed of particles is loaded inside the absorbers for chemical reaction and it is indirectly heated by the solar

radiation. To minimize the heat loss from the outer surface of the cavity, a thick insulation layer covering the cavity is used.

6.3 Heat Transfer Analysis

A comprehensive heat transfer analysis in the high-temperature solar thermochemical reactor includes the components of radiation, conduction, convection, and chemical reaction. This study is focused on the reduction step during which concentrated solar energy is used for high temperature requirement. The University of Florida Solar Simulator is able to provide high flux up to 10 kW (Erickson 2012, Klausner 2011) and it is used as a radiation source. The distribution of the solar flux arriving at the cavity aperture from the Solar Simulator is determined utilizing an MCRT-based VEGAS code. The details about the VEGAS code can be found in (Petrasch 2002). The center of the present analysis is on the energy transfer inside the cavity reactor with a given constant input solar power and a fixed flux distribution at the aperture. An MCRT-based radiation model developed by Singh (2013) is applied to simulate the radiative transfer between the cavity wall and the absorber surfaces. The details of the radiation model are referred to (Singh 2013) and some basic concepts are highlighted here for completeness. The energy transfer inside the absorbers is modeled using the thermal lattice Boltzmann equation (TLBE) method.

6.3.1 Radiative Heat Transfer

6.3.1.1 Radiation between the cavity wall and the absorbers

Assuming the medium filling the space between the cavity wall and the absorbers is nonparticipating, the radiative heat flux on a surface using the MCRT technique is governed by (Modest 2003, Melchior and Steinfeld 2008)

$$q''(\mathbf{r}) = \varepsilon(\mathbf{r})\sigma T^4(\mathbf{r}) - \int_A \varepsilon(\mathbf{r}')\sigma T^4(\mathbf{r}') \frac{dF_{dA' \rightarrow dA}}{dA} dA', \quad (6-3)$$

where $q''(\mathbf{r})$ is the local surface heat flux in the normal direction, \mathbf{r} is a spatial vector, $\varepsilon(\mathbf{r})$ is the total hemispherical emissivity of the surface at \mathbf{r} , σ is the Stefan–Boltzmann constant, T is the surface temperature, A is the surface area of the enclosure, and $dF_{dA' \rightarrow dA}$ is the generalized radiation exchange factor between surface elements dA' and dA .

In Eq. (6-3), the first term on the right-hand side represents the emission from the surface at \mathbf{r} with temperature $T(\mathbf{r})$, and the integrand in the second term is the fraction of the energy, originally emitted from the surface at \mathbf{r}' that eventually gets absorbed at location \mathbf{r} . If the enclosure is not closed, such as the aperture in the cavity, some artificial closing surfaces must be introduced. Since the opening aperture is irradiated by the solar simulator, it is replaced by a nonreflecting surface with zero emissivity for all angles but the solar angle.

The MCRT method traces the history of a statistically meaningful random sample of photons from their points of emission to their points of absorption within or exiting from the volume (Modest 2003). The emissive power is equally distributed to the individual photon rays, which are created in random directions.

The photon rays with concentrated solar power, \dot{Q}_{solar} , enter the cavity through the aperture, and the power carried per ray is

$$\dot{Q}_{\text{ray-aperture}} = \frac{\dot{Q}_{\text{solar}}}{N_{\text{ray-aperture}}}, \quad (6-4)$$

where $N_{\text{ray-aperture}}$ is the number of rays at the aperture. After encountering multiple reflections inside the cavity the photon rays either get absorbed by the absorber surfaces or the cavity wall, or leave the cavity from the aperture. Note that the distribution of incident rays at the aperture are obtained from the VEGAS code (Petrasch 2002).

As the surface temperatures of the absorbers and the inner cavity walls increase with the irradiation absorbed, the emission from the their surfaces becomes important and it should be accounted for in the radiative transfer analysis. The absorber surfaces and the cavity inner walls are thus divided into a large number of differential elements, each assumed at a uniform temperature. The emissive power per ray from the surface element A_i is thus

$$\dot{Q}_{\text{ray-absorber}}^i = \frac{\dot{Q}_{\text{absorber}}^i}{N_{\text{ray-absorber}}^i} = \frac{\epsilon_i \sigma T_i^4 A_i}{N_{\text{ray-absorber}}^i}, \quad (6-5)$$

Both the absorber surfaces and the cavity walls are assumed to be diffusely reflecting and emitting.

6.3.1.2 Radiation in the porous structure inside the absorbers

The reactive material filled in the absorbers is in the form of optically thick porous structures thus the Rosseland diffusion approximation for the radiation inside the bed is valid (Modest 2003, Müller et al. 2008). The radiative heat transfer is then simplified to a diffusion process with an equivalent thermal conductivity

$$k_R = \frac{16n^2\sigma}{3\beta_R} T^3, \quad (6-6)$$

where n is the refractive index of the medium, and β_R is the Rosseland-mean extinction coefficient. The high value of β_R results in attenuation of the incident radiation mostly at

the surface layer of the bed. The radiative exchange inside the bed is thus mainly due to the local emission and absorption of thermal radiation, justifying the application of the Rosseland diffusion approximation for optically thick media (Müller et al. 2008).

6.3.2 Convective Heat Transfer

In the reduction step of the two-step H₂O/CO₂-splitting cycling the primary gas is the oxygen released during the reaction. Considering the oxygen is removed from the system at a very low speed, the convective heat transfer is neglected in the present simulations. The same assumption was made in those previous works (Müller et al. 2008, Loutzenhiser et al. 2010). In the subsequent oxidation step, however, as relatively high H₂O/CO₂ flow rate is passing through the bed, the convective heat transfer is significant and should be included in the overall heat transfer analysis.

6.3.3 Conductive Heat Transfer

For the reduction step, the heat transfer inside the absorbers is simplified to a heat conduction problem. Recalling Eq. (6-6), the effective thermal conductivity for heat conduction can be approximated by (Müller et al. 2008, Loutzenhiser et al. 2010)

$$k_{\text{eff}} = k_R + k_{\text{cond}} = \frac{16n^2\sigma}{3\beta_R} T^3 + k_{\text{cond}}, \quad (6-7)$$

where the thermal conductivity, k_{cond} , for the porous medium without considering radiation can be obtained either from experimental measurement of the samples at room temperature, or from tomography-based pore-scale numerical simulation.

6.3.4 Endothermic Chemical Reaction

The heat consumption due to the endothermic dissociation of the reactive material can be represented by

$$\dot{q}_{\text{chem}}''' = r_{\text{MO}}''' (\bar{h}_{\text{M}} + 0.5\bar{h}_{\text{O}_2} - \bar{h}_{\text{MO}}), \quad (6-8)$$

where r_{MO}''' is the volumetric reaction rate of the metal oxide MO such as FeO or ZnO, \bar{h} is the specific enthalpy of the reactants or products. The reaction rate is usually modeled by an Arrhenius-type rate law (Müller et al. 2008, Loutzenhiser et al. 2010). Here we follow the oxidation reaction model in (Mehdizadeh et al. 2012b) and use a similar reaction model for the reduction step

$$r_{\text{MO}}''' = k_0 \exp\left(\frac{-E_a}{RT}\right) f(x), \quad (6-9)$$

where the activation energy, E_a , for reduction is experimentally determined, the pre-exponential factor, k_0 , is a constant fitted from experimental data, and $f(x)$ is a dimensionless function that depends on the reaction mechanism, x is the mass fraction of the reacted material (Mehdizadeh et al. 2012b).

6.4 TLBE Simulation of Heat Transfer in Absorbers

The energy conservation equation for the reactive porous structure filled in the cylindrical absorbers can be written as

$$\rho c_p \frac{\partial T}{\partial t} = \frac{1}{r} \frac{\partial}{\partial r} \left(r k_{\text{eff}} \frac{\partial T}{\partial r} \right) + \frac{1}{r^2} \frac{\partial}{\partial \phi} \left(k_{\text{eff}} \frac{\partial T}{\partial \phi} \right) + \frac{\partial}{\partial z} \left(k_{\text{eff}} \frac{\partial T}{\partial z} \right) + \dot{q}_{\text{chem}}''', \quad (6-10)$$

where ρ and c_p are the density and specific heat capacity of the solid matrix, respectively, and \dot{q}_{chem}''' is the rate of volumetric heat sink given by Eq. (6-8). Eq. (6-10) is a diffusion equation and it can be solved using the cubic D3Q7 TLBE model (Yoshida and Nagaoka 2010) with the curved geometry preserved using the boundary condition treatment by Li et al. (2013a, 2013b).

6.4.1 Scaling from the physical units to the LBE units

It is realized that all the numerical tests in Chapters 3 — 5 are presented in LBE units where both the lattice spacing and the time step are unity. This serves as a clean plate on which the analysis and numerical validation are conveniently conducted. To simulate a particular real-world problem, however, the parameters/variables in physical units should be properly scaled and converted into those in LBE units that are also suitable for LBE algorithm implementation. These two sets of unit systems are connected by the same dimensionless units, such as

$$(r/R_{\text{abs}})_{\text{phys}} = r^* = (r/R_{\text{abs}})_{\text{LBE}}, \quad (6-11a)$$

$$(z/R_{\text{abs}})_{\text{phys}} = z^* = (z/R_{\text{abs}})_{\text{LBE}}, \quad (6-11b)$$

$$(T/\Delta T)_{\text{phys}} = T^* = (T/\Delta T)_{\text{LBE}}, \text{ and} \quad (6-11c)$$

$$\frac{R_{\text{abs}}}{\Delta T} \frac{\partial T}{\partial r} \Big|_{r=R_{\text{abs}}}^{\text{phys}} = \frac{\partial T^*}{\partial r^*} = \frac{R_{\text{abs}}}{\Delta T} \frac{\partial T}{\partial r} \Big|_{r=R_{\text{abs}}}^{\text{LBE}}, \quad (6-11d)$$

where ΔT is the reference temperature difference.

Introducing basic scaling factors for the characteristic length and time scales from the physical units to the LBE units as

$$L_0 \delta_x = R_{\text{abs}}^{\text{phys}} / R_{\text{abs}}^{\text{LBE}}, \text{ and } T_0 \delta_t = \delta t_{\text{phys}} / \delta t_{\text{LBE}} = t_0 / N_t, \quad (6-12)$$

where t_0 is the characteristic physical time and N_t is the number of time steps. The diffusion coefficient in LBE simulations then becomes

$$D_{\text{LBE}} = \alpha \times \frac{T_0 \delta_t}{(L_0 \delta_x)^2} = \frac{k_{\text{eff}}}{\rho c_p} \frac{T_0 \delta_t}{(L_0 \delta_x)^2}. \quad (6-13)$$

In TLBE simulations the relaxation coefficient τ_{ij} is related to the diffusion coefficient as $\tau_{ij} = \frac{1}{2}\delta_{ij} + \frac{\delta t}{\varepsilon(\delta x)^2}D_{ij}$ (see Eq. 3-14) in order to correctly recover the macroscopic convection-diffusion equation (CDE). Also as demonstrated in Figs. 3-8, 4-3 and 4-4, the errors of the LBE results increases with larger values of τ_{ij} especially for those cases with $\tau_{ij} > 1.0$. Accurate LBE simulations thus require that τ_{ij} be within a reasonable region. For high-diffusion-coefficient CDEs, the diffusion coefficient should thus be properly rescaled when the TLBE method is employed. The details about the rescaling technique are given in the following section.

6.4.2 Rescaling for high-diffusion-coefficient CDE in TLBE

In hydrodynamic LBE simulations, the macroscopic hydrodynamic equations are recovered from the kinetic-based LBE when the mean free path is much smaller than the lattice grid size. As the relaxation coefficient τ_f is defined as the ratio of the relaxation time to the lattice time step ($\tau_f = \lambda_f/\delta t$), a high τ_f value corresponds to a large relaxation time and large particle mean free path. Hence higher τ_f values would yield larger numerical errors in LBE solutions, as examined in (Chen et al. 1992, Noble et al. 1995, Mei et al. 2002, Chun and Ladd 2007).

Similarly, in thermal LBE simulations, the deviation of the TLBE results from the solutions to the CDE increases with large relaxation coefficient τ_D values (corresponding to higher diffusion coefficient in the governing CDE) as reported in (Li et al. 2013a, Yoshida and Nagaoka 2010). In this work, we show that the diffusion coefficient D in a CDE can be properly rescaled to ensure moderate τ_D values to have good numerical stability and accuracy. It should also be noted that with a gain of numerical accuracy, using smaller relaxation values of τ_f and τ_D in LBE simulations would require more lattice

time steps to reach steady-state or time-dependent solutions (Li et al. 2013a, Yoshida and Nagaoka 2010).

We rescale the large diffusion coefficient D with a parameter λ so that the general CDE (3-1) becomes

$$\frac{\partial \phi}{\partial t'} + \frac{\partial}{\partial x_j} (v'_j \phi) = \frac{\partial}{\partial x_i} (D'_{ij} \frac{\partial \phi}{\partial x_j}) + G'. \quad (6-14)$$

with

$$t' = \lambda t, \quad v'_j = v_j / \lambda, \quad D'_{ij} = D_{ij} / \lambda, \quad \text{and} \quad G' = G / \lambda. \quad (6-15)$$

Equation (6-15) shows that the time, velocity and source term are rescaled accordingly. Note that the spatial vector \mathbf{x} is not rescaled in Eq. (6-14) and the characteristic Fourier number and Péclet number remain the same after the rescaling, i.e.,

$Fo' = D' t'_c / L^2 = D t_c / L^2 = Fo$ and $Pe' = U' L / D' = U L / D = Pe$, with t_c , U and L being the respective reference time, velocity and length scales.

The Dirichlet boundary condition in Eq. (3-2) is not affected by the rescaling, while the Neumann boundary condition in Eq. (3-3) should be rescaled as (Li et al. 2013d)

$$-n_i D'_{ij} \frac{\partial \phi}{\partial x_j} + n_j \frac{v_j}{\lambda} \phi = \frac{\Phi_n}{\lambda}. \quad (6-16)$$

After the heat equation (6-10) is converted to a CDE in the LBE units, it will be rescaled according to Eq. (6-14) and solved.

6.4.3 Computational Procedure for the Coupled Model

The computational procedure for the coupled conduction-radiation model is summarized as below:

1. The incident solar power \dot{Q}_{solar} and the distributions of the rays at the aperture of the cavity is obtained from the “VEGAS” ray tracing code for the solar simulator (Petrasch 2002);
2. Start with initial temperature distributions on the absorber and cavity surfaces and the emission power from each surface is computed;
3. The MCRT radiation model (Singh 2013) is used to obtain the net heat flux, which is a combination of the absorbed and emitted radiative energy, on the absorber surfaces and the cavity walls;
4. The temperature distributions in the interior of the absorbers, the cavity and the insulation layer are simulated with the net heat flux boundary conditions using the TLBE model;
5. The heat sink due to chemical reaction is calculated with the temperature field in the absorbers obtained;
6. Temperature distributions on the absorber surfaces and the cavity walls are updated so that the radiative emission from those surfaces is updated;

Steps (3 - 6) are iteratively conducted during each time step.

6.5 Simulation Results and Discussion

Simulation results from three cases with different aspect ratios of the cavity are presented in this section. The baseline parameters for those three cases are summarized in Table 6-1. A constant solar power of $\dot{Q}_{\text{solar},1} = 10 \text{ kW}$ is applied to heat up the reactor from room temperature $27 \text{ }^\circ\text{C}$ (300 K) to the reduction temperature at $1450 \text{ }^\circ\text{C}$, then a lower solar input $\dot{Q}_{\text{solar},2}$ is chosen to maintain the temperature of the reactive material at about $1450 \text{ }^\circ\text{C}$. Considering the absorbers are uniformly distributed along the

azimuthal direction inside the cylindrical cavity, a representative absorber is selected and the heat flux boundary condition is assumed to be the average value of the heat fluxes on all the absorbers. Therefore only the interior temperature field in one absorber is simulated in the coupled model, which greatly reduces the computational time.

Figures 6-2 (a) and (b) show the evolution of the average reactor bed temperatures T_{bed} (averaged over the 3-D interior of the absorbers) with time for the three cases listed in Table 6-1. The evolution history starts from 300 K and the desirable operating temperatures, 1200 °C for the oxidation step and 1450 °C for the reduction step, are also highlighted in Fig. 6-2 (a). A 10 min reduction duration time is used and the decrease of the solar power is illustrated in Fig. 6-2 (b).

Define the solar-to-fuel efficiency η as

$$\eta = \frac{mY / V_m \Delta H_c^0}{\sum (\dot{Q}_{\text{solar},1} \Delta t_1 + \dot{Q}_{\text{solar},2} \Delta t_2 + W_{\text{pump}})}, \quad (6-17)$$

where m is the total mass of the bed material, Y is the total hydrogen yield per kg of bed material, V_m is a constant $V_m = 22.41 \text{ dm}^3/\text{mol}$, ΔH_c^0 is the standard enthalpy of combustion of hydrogen $\Delta H_c^0 = 286 \text{ kJ/mol}$, $(\dot{Q}_{\text{solar},1} \Delta t_1)$ is the input solar energy to ramp up T_{bed} from 1200 °C to 1450 °C time, $(\dot{Q}_{\text{solar},2} \Delta t_2)$ is the input solar energy to maintain the reduction temperature of 1450 °C for 10 mins (ideally the oxidation step is exothermic and no solar input is required), and W_{pump} is the energy consumption of the vacuum pump.

According to the benchmark data obtained from our experiments for Cobalt ferrite-based reactive material, a bulk hydrogen yield of $Y = 2.5 \text{ dm}^3/\text{kg}$ of total material is assumed, the efficiency for those cases are thus $\eta_1 = 11.12\%$, $\eta_2 = 9.91\%$, and $\eta_3 =$

7.30%. The calculations are illustrated in Table 6-2. For cerium-based reactive material, faster reaction and higher production yield are noticed, thus the overall efficiency is expected to be higher.

To illustrate the incident flux distributions, the contours of incident heat flux on the surface of Absorber 1 are shown in Figs. 6-3 (a), (b) and (c) for Cases I, II, and III, respectively. The incident flux remains the same during the reduction step. With the absorber surface heated up by the incident flux, its temperature increases and radiative emission from the surface becomes important.

When the average temperature of the absorbers reaches 1450 °C, the net heat flux and temperature distributions on the absorber surfaces for all three cases are shown in Figs. 6-4 and 6-5, respectively, where the results are presented in the (θ , z) coordinates (see Fig. 6-1). The heat flux and temperature distributions are symmetric about the axis at $\theta = 0$, which is consistent with the axisymmetric arrangement of the absorbers inside the cavity. Along the θ -direction, relatively higher surface temperature is observed for each case at the location near $\theta = 0$, which is exposed to the incident radiation coming through the aperture (see Fig. 6-1). In the axial z -direction, a hot spot of temperature is noticed for each case. This hot spot region corresponds to the location on the surface that absorbs high-intensity incident flux as shown in Fig. 6-3. The temperature profiles along the axial direction at $\theta = 0$ for the three cases are compared in Fig. 6-6.

To examine the interior temperature field of the absorbers at $T_{ave} = 1450$ °C, we show the temperature distributions on the x - z plane that contains the centerline of Absorber 1 for all three cases in Fig. 6-7 (the x , y , z axes for Absorber 1 are parallel to

that in the x - y - z Cartesian coordinate system for the cavity as shown in Fig. 6-1 with the origin shifted to the centerline of Absorber 1). The interior temperature distribution is essential to the understanding of the local chemical reaction rate. The temperature distributions in Fig. 6-7 implies that further effort can be devoted to minimize the temperature difference in the bed to have more uniform chemical reaction.

6.6 Summary and Conclusions

A coupled radiation-conduction model is developed for simulating the energy transport in a high-temperature solar thermochemical reactor. The radiative transfer inside the porous structures is approximated as a diffusion process with large effective thermal conductivity at high temperatures. A general technique for rescaling the high-diffusion convection diffusion equation (CDE) and the boundary conditions in the thermal lattice Boltzmann equation (TLBE) method is presented to improve numerical accuracy. Radiative transfer between the cavity wall and the absorbers is modeled with the Monte-Carlo ray tracing (MCRT) technique. As the surface temperature of the absorbers is solved, actual radiative emission from the absorber surfaces is included in the MCRT model. Simulation results for a horizontal cavity-receiver reactor prototype are presented to give insights into the reactor design.

Table 6-1. Baseline simulation parameters for cavity aspect ratio $L_{\text{cav, in}} / D_{\text{cav}} = 0.69$, 1.01, and 1.16 for Cases I, II and III, respectively.

Parameter	Symbol	Value
Maximum solar power input	$\dot{Q}_{\text{solar, max}}$	10 kW
Absorber emissivity	ϵ	0.8
Number of absorbers	n	17, 14, 13
Absorber diameter	D_{abs}	50.8 mm
Absorber length	L_{abs}	246, 305, 330 mm
Absorber thickness	t_{abs}	3.18 mm
Aperture diameter	D_{aperture}	50.0 mm
Cavity diameter	D_{cav}	355, 302, 284 mm
Cavity thickness	h_{cav}	76.2 mm
Insulation thickness	h_{ins}	127 mm
Inner cavity length	$L_{\text{cav, in}}$	246, 305, 330 mm
Outer cavity length	$L_{\text{cav, out}}$	398, 457, 482 mm
Insulation length	L_{ins}	652, 711, 736 mm
Spacing between absorber and cavity axes	H_{abs}	150, 123, 115 mm

Table 6-2. Solar-to-fuel efficiency calculations for Cases I, II and III.

	Case I ($L_{\text{cav, in}}/D_{\text{cav}}=0.69$)	Case II ($L_{\text{cav, in}}/D_{\text{cav}}=1.01$)	Case III ($L_{\text{cav, in}}/D_{\text{cav}}=1.16$)
Mass load (kg)	13.29	13.54	13.62
Benchmark H ₂ yield (liter)	33.23	33.85	34.05
HHV of H ₂ (kJ)	424.28	432.26	434.81
($\dot{Q}_{\text{solar,1}} \Delta t_1$), 1200-1450 °C (kJ)	2030.00	2690.00	4226.67
($\dot{Q}_{\text{solar,2}} \Delta t_2$), ~1450 °C (kJ)	1697.25	1582.20	1638.00
W_{pump} (kJ)	87.53	89.17	89.70
Efficiency η (Cobalt-ferrite-based)	11.12%	9.91%	7.30%

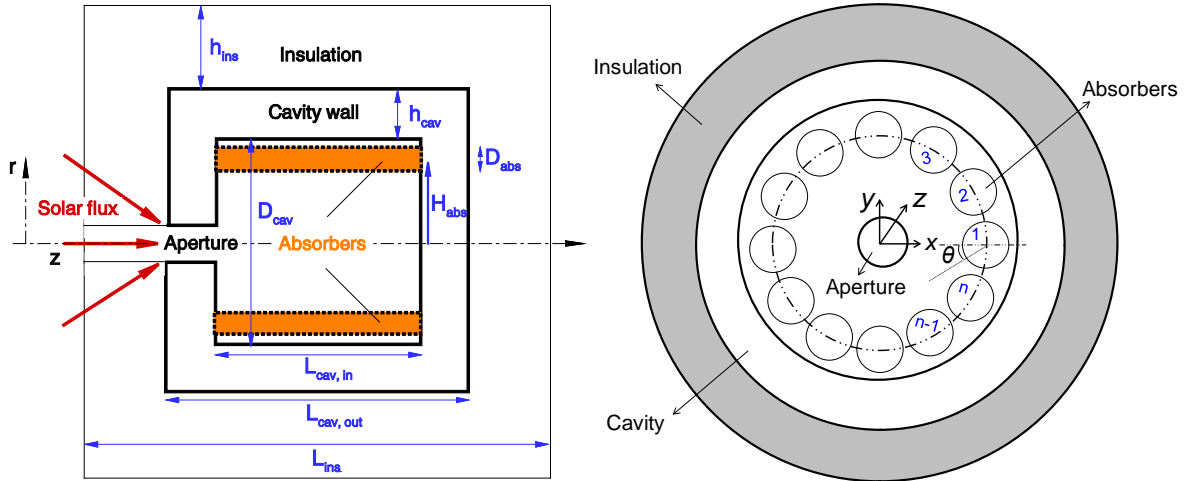


Figure 6-1. Schematic depiction of the horizontal solar reactor configuration: (a) cross section view, and (b) front view.

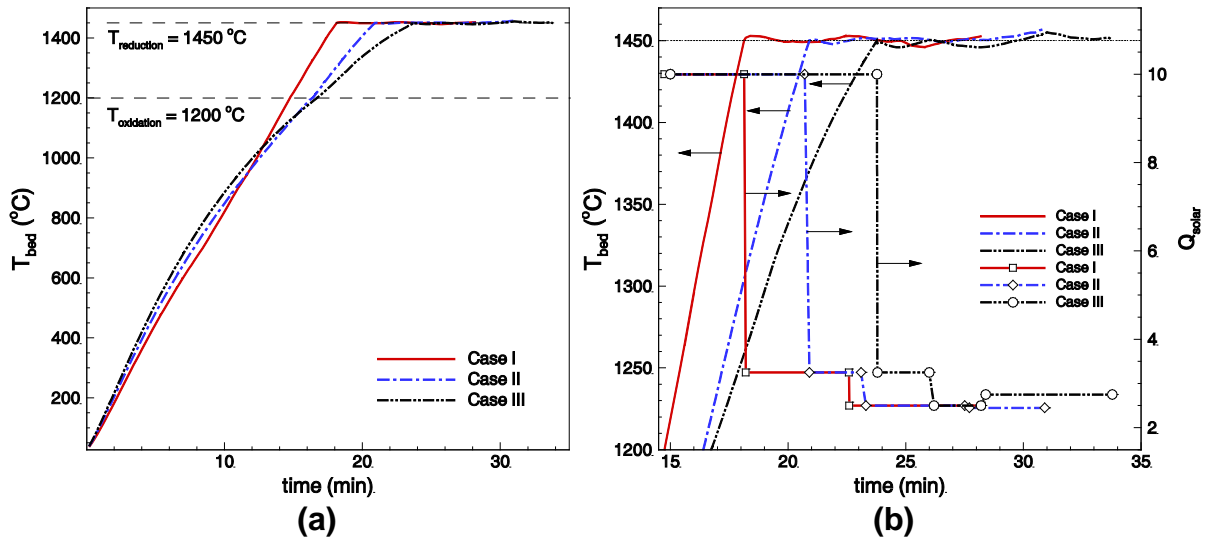


Figure 6-2. (a) Variations of the average bed temperature (T_{bed}) with time, and (b) variations of T_{bed} and solar power input (\dot{Q}_{solar}) with time at $1200 \text{ }^\circ\text{C} \leq T_{\text{bed}} \leq 1450 \text{ }^\circ\text{C}$ for Cases I, II and III.

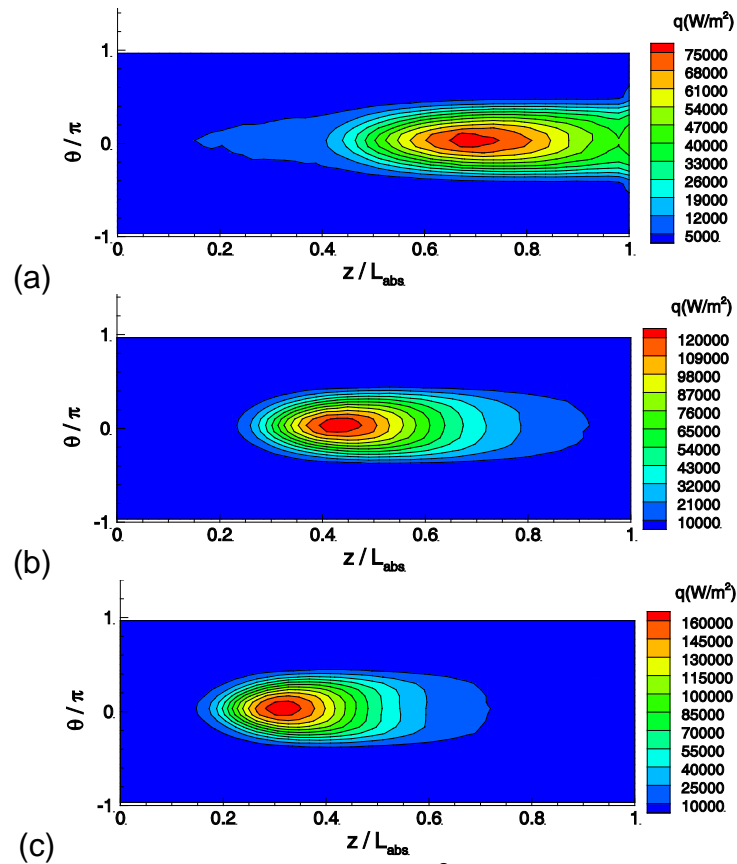


Figure 6-3. Incident heat flux distribution (in W/m²) on the surface of Absorber 1 (see Fig. 6-1) for (a) Cases I, (b) Case II, and (c) Case III.

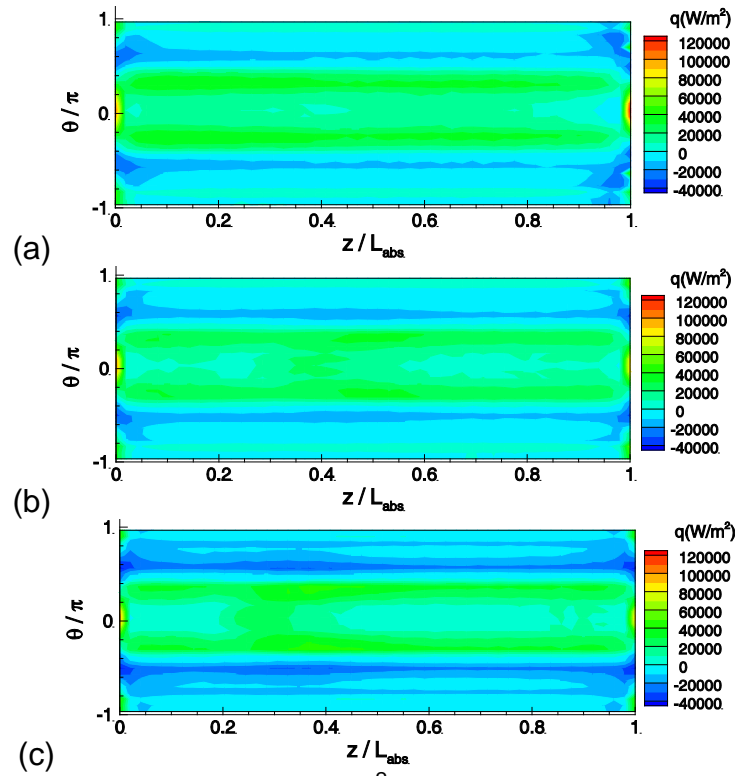


Figure 6-4. Net heat flux distribution (in W/m^2) on the surface of Absorber 1 for (a) Case I, (b) Case II, and (c) Case III.

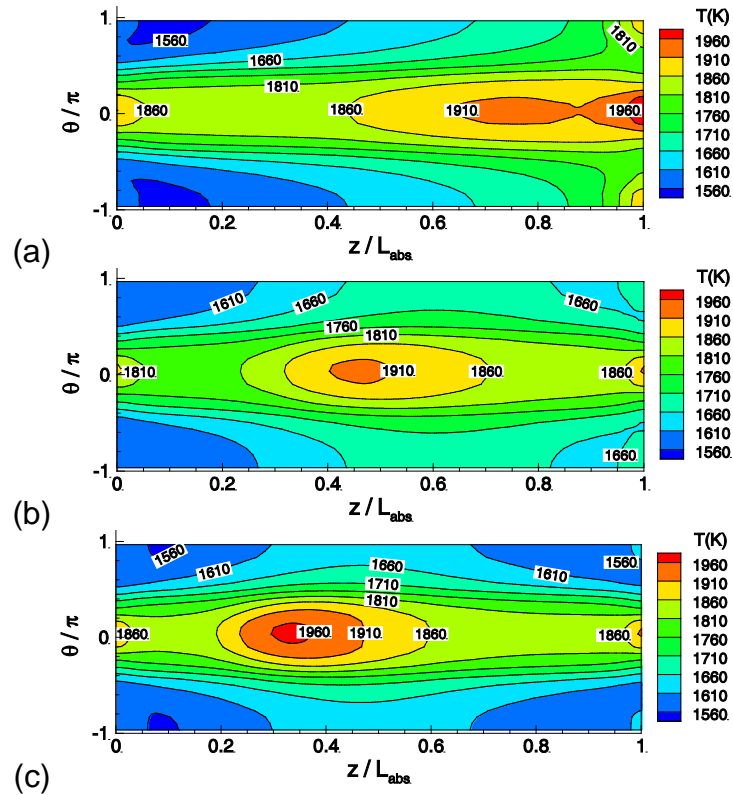


Figure 6-5. Temperature distribution (in K) on the surface of Absorber 1 for (a) Cases I, (b) Case II, and (c) Case III.

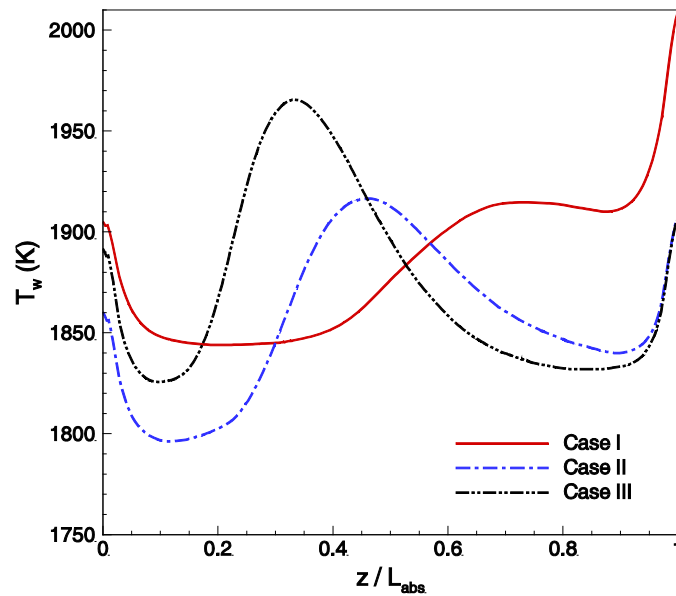


Figure 6-6. Comparison of temperature profiles (in K) along ($\theta = 0, z$) on the surface of Absorber 1 for the three cases simulated.

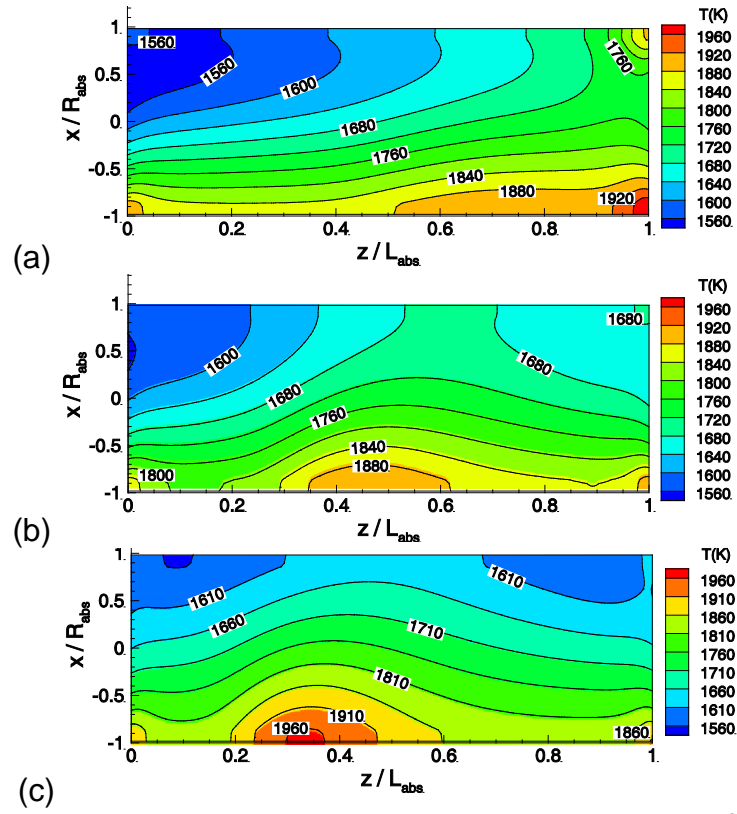


Figure 6-7. Interior temperature distribution on the central x - z plane of Absorber 1 for (a) Case I, (b) Case II, and (c) Case III.

CHAPTER 7 SUMMARY AND FUTURE WORKS

Heat transfer, as one of the most significant transport phenomena in fluid-solid flows, is studied in this dissertation. Various numerical tools have been developed/improved to efficiently and accurately evaluate the heat transfer in fluid-solid systems. Most effort is devoted to the boundary condition treatments and heat transfer evaluation in the thermal lattice Boltzmann equation (TLBE) method. The major contributions in the dissertation are summarized as follows.

Heat transfer between colliding particles of various materials is investigated:

- The singular nature of the thermal field and heat flux at the edge of the contact area is elucidated through analytical solutions.
- A self-similar solution for the thermal field during the initial period of contact is developed. And it serves as an accurate initial condition for the entire collisional period.
- A two-dimensional asymptotic analysis is presented for the thermal field and heat flux in the contact area in the small Fourier number limit.
- A closed-form expression is developed for the heat transfer prediction as a function of the Fourier number, the thermal diffusivity ratio and the thermal conductivity ratio of the impacting particles.

Boundary condition treatments in TLBE method are proposed:

- Thermal boundary condition treatments based on the “bounce-back” scheme and spatial interpolation are presented for both the Dirichlet and Neumann conditions.
- When second-order accuracy is pursued, there is an adjustable parameter for the Dirichlet problem, while the Neumann condition treatment is unique.
- Three particular schemes for the Dirichlet condition treatment are presented and their stability and accuracy are examined. All three Dirichlet schemes are stable and Scheme 2 gives smaller error in most cases investigated.
- For curved boundaries, the Dirichlet condition treatment can be applied directly and it leads to second-order accuracy of the temperature field and first-order accuracy of the boundary heat flux.

- For curved boundaries, the proposed Neumann condition treatment requires the determination of heat fluxes in the discrete velocity directions of the TLBE model. A general formula to convert the normal heat flux into the fluxes in the discrete velocity directions is derived.
- Only first-order accuracy is obtained for the temperature field with Neumann conditions due to the combined effect of the curved boundary and the heat flux conversion.
- For the special case with no tangential variation of temperature along the curved boundary, the heat flux conversion becomes exact and second-order accuracy of the temperature field can be obtained.

Heat transfer evaluation on curved boundaries in TLBE method is studied:

- An efficient and accurate approach for evaluating local and overall heat transfer rates on curved boundaries is proposed.
- The boundary heat flux in the discrete velocity directions is obtained with the temperature distribution functions at the lattice nodes close to the boundary and the given Dirichlet or mixed boundary condition.
- Based on energy conservation, the integration of the heat fluxes in the discrete velocity directions with constant effective surface area leads to the total heat transfer rate.
- There are two major benefits for the proposed heat transfer evaluation: no requirement for the normal heat flux determination and no surface area approximation.
- Numerical tests demonstrate that the heat transfer evaluation method is second-order accurate for straight walls perpendicular to one of the discrete lattice velocity vectors and first-order accurate for curved boundaries.

A Multi-relaxation-time (MRT) lattice Boltzmann (LB) model for the axisymmetric convection-diffusion equation (CDE) is proposed:

- The axisymmetric CDE is transformed to a standard CDE in the Cartesian coordinate system and the additional terms due to the coordinate transformation are treated as source terms at the macroscopic level.
- The scalar gradient in the source terms is formulated using the local moment of the non-equilibrium components of the distribution functions without the need for finite-difference type of calculations.

- For thermo-hydrodynamic problems, the proposed model can be directly coupled with hydrodynamic axisymmetric LB models on the macroscopic level without explicit coupling between the two sets of distribution functions, making the present model much easier to implement and more robust.

A coupled radiation-conduction model for energy transport in a solar reactor is developed:

- The radiative transfer inside the porous structures is approximated as a diffusion process with large effective thermal conductivity at high temperatures.
- A general technique for rescaling the high-diffusion convection diffusion equation (CDE) and the boundary conditions in the thermal lattice Boltzmann equation (TLBE) method is presented to improve numerical accuracy.
- Radiative transfer between the cavity wall and the absorbers is modeled with the Monte-Carlo ray tracing (MCRT) technique.
- The surface temperature of the absorbers is solved and actual radiative emission from the absorber surfaces is included in the MCRT model.
- Simulation results for a horizontal cavity-receiver reactor prototype are presented to provide insights into the reactor design.

Based on the material presented in this dissertation, the following are recommended as future works:

1. With curved boundaries, the boundary heat flux evaluation for Dirichlet problems and the interior and boundary temperature computations for Neumann problems become first-order accurate in the TLBE method. This has been verified with numerous numerical tests. While a thorough analysis of the convergence order for curved boundaries remains open.
2. A detailed parametric study is needed in the radiation-conduction coupled model for optimal solar thermochemical cavity-reactor design.
3. A more advanced numerical model including, i) fluid flows (especially for the oxidation step), and ii) species transport due to chemical reaction, is highly desirable to serve as a design tool for the solar thermochemical reactor.

APPENDIX A VALIDITY OF THE SEMI-INFINITE MEDIA ASSUMPTION

During the elastic collision of two particles initially at different temperatures, the deformations of the spheres in the direction normal to the contact area are very small compared with their respective radii according to the Hertzian contact theory (Timoshenko et al. 1970, Johnson 1987). The heat transfer is also limited to a small area near the contact region. Sun and Chen (1988) thus employed the semi-infinite media assumption by treating the rest of the solids in the z -direction (normal to the contact area) far away from the contact region as infinite media (see Eq. (2-15)). It is also implied that the solid in the r -direction far away from contact region is at infinity (see Eq. (2-16)). Furthermore, the surfaces near the edge of the contact area are assumed to be flat so that the surfaces outside $r = R(t)$ can be assumed to be at $z = 0$ (see Eq. (2-14)). Zhou et al. (2008) argued that for high Fourier numbers (when Fo is close to 10), the above assumptions may not be valid. Thus they treated the two colliding spheres as deforming bodies and thus maintained the geometric fidelity and the exactness of the boundary conditions using a finite-element method.

Thus it is instructive to examine the conditions needed for the semi-infinite media assumption to be valid. There are three issues of concern:

i) Is the region of influence in the z -direction much smaller than the length scale of the body in the z -direction?

ii) Is the region of the influence in the r -direction much smaller than the length scale of the body in the r -direction?

iii) Is the region of the influence in the r -direction sufficiently small so that the curvature effect of the surface near the contact region can be assumed negligible or the surface can be assumed to be flat?

These issues are addressed below based on scaling analyses and the computational results obtained in this study using the post priori method.

i) For a solid with thermal diffusivity α , the relevant length scale of the thermal diffusion in the z -direction is on the order of $O(\sqrt{\alpha t_c})$ in which t_c is the contact duration. For the rest of the solid to be treated as an infinite medium in the z -direction, it is necessary that

$$\sqrt{\alpha_i t_c} \ll R_i, (i = 1, 2) \quad (\text{A-1})$$

Examination of the temperature contours over a wide range of Fo for particles of the same material shows that the temperature contour lines in the η -direction varies very little during the entire collision period. This confirms that $\sqrt{\alpha_1 t}$ is the correct scale in the z -direction. Since $\eta = z / \sqrt{\alpha_1 t}$ is applied in this work the domain of the influence in the η -direction is limited to $\eta \sim 4 - 5$. Thus when (A-1) is satisfied, the z -direction can be treated as semi-infinite for each body.

ii) In the r -direction, the region influenced by the impact can be estimated as $O(R_c + \sqrt{\alpha t_c})$ where R_c is the maximum contact radius. In the limit of zero Fo , the region is limited precisely to the contact area, $r \leq R_c$; for large Fourier numbers, the thermal diffusion length in the r -direction is then $O(\sqrt{\alpha t_c})$ beyond the point of contact. At $Fo = 50$, the isothermal lines on the surface of particle 1 at $t^* = 0.5, 0.75, \text{ and } 0.95$ are shown in Fig. A-1, where the coordinate is transformed back to the (r, z) coordinates. The

shrink of the contact area during the decompression process renders a decrease in the length scale of the transient contact radius, which makes the thermal diffusion from the contact zone dominant. During the whole decompression process, the diffusion length in the r -direction is still on the order of $O(\sqrt{\alpha t_c})$. Thus for Eq. (2-16) to be valid, it requires that

$$R_c \ll R_i, (i = 1, 2), \text{ and} \quad (\text{A-2})$$

$$\sqrt{\alpha_i t_c} \ll R_i, (i = 1, 2) \quad (\text{A-3})$$

In the context of elastic collision, (A-2) must be satisfied. Since (A-3) is identical to (A-1), the second condition becomes identical to the first one.

iii) The spherical surface just outside the contact area can be described using the Taylor series expansion as (Timoshenko et al. 1970, Johnson 1987)

$$z \sim \frac{r^2}{2R_i} + \dots, (i = 1, 2) \quad (\text{A-4})$$

Thus for the spherical surfaces near the contact area and within the region of the thermal influence by the contact to be approximated by $z = 0$ (Eq. (2-14)), it is necessary that

$$\frac{R_c^2}{2R_i} \ll R_i \text{ and } \frac{\alpha_i t_c}{2R_i} \ll R_i, (i = 1, 2) \quad (\text{A-5})$$

based on (A-2) and (A-3).

Thus when the assumptions of the elastic collision (A-2) is satisfied, the thermal conditions in (A-1) and (A-5) simply reduce to

$$\sqrt{\alpha_i t_c} \ll R_i, (i = 1, 2) \quad (\text{A-6})$$

Recalling the definition of Fo in Eq. (2-23a), condition (A-6) can be rewritten as

$$Fo^{1/2} \frac{R_c}{R_i} \ll 1, (i = 1, 2) \quad (A-7)$$

or

$$Fo^{1/2} \frac{1}{R_i} \left(\frac{5m_{12}R_{12}^2}{4E_{12}} \right)^{1/5} v_{12}^{2/5} \ll 1 \quad (A-8)$$

For spherical particles of the same size and same material, condition (A-8) can be simplified to

$$Fo \ll \left(\frac{E}{\rho v_{12}^2} \right)^{2/5} \quad (A-9)$$

Typically $E \sim O(10^{10})$ (N/m²) or higher and $\rho \sim O(10^3)$ (kg/m³). For particle collision velocity at 10 (m/s), the above condition requires $Fo \ll \left(\frac{E}{\rho v_{12}^2} \right)^{2/5} \sim 100$ for the semi-infinite media assumption to be valid. For the physical parameters used by Zhou et al (2008) where $\rho = 1451.7$ kg/m³, $E = 193$ GPa, and the normal relative velocity $v_{12} = 0.5$ m/s, the condition (A-9) requires $Fo \ll 3090$ which is satisfied in all the simulations described in Zhou et al.'s work.

In conclusion, for practical engineering problems where condition (A-8) is satisfied, the semi-infinite media assumption is appropriate and the results of the present work can be applied. In the extreme cases where (A-8) does not hold or plastic deformation occurs, one must adopt the approach used by Zhou et al. (2008) to capture the influence of the geometry and the relevant boundary conditions.

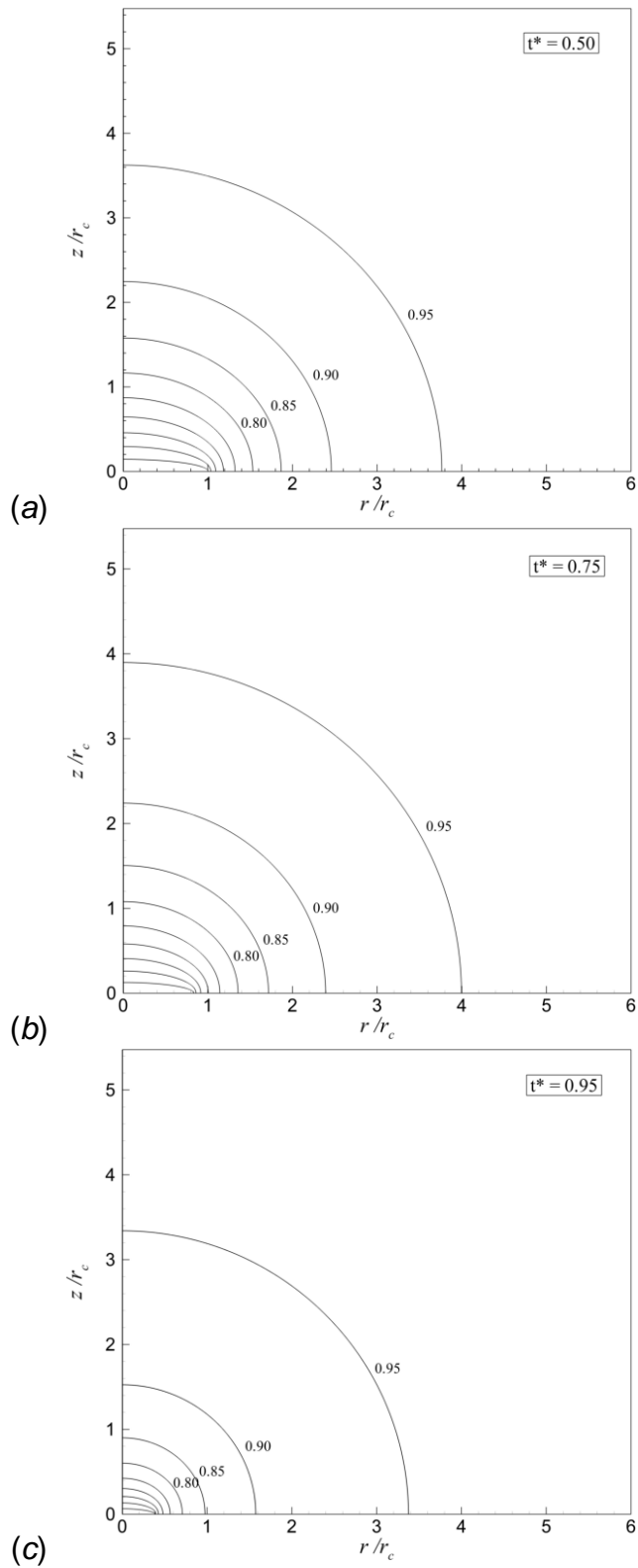


Figure A-1. Isotherms on the surface of particle 1 at $Fo = 50$ when (a) $t^* = 0.50$, (b) $t^* = 0.75$, and (c) $t^* = 0.95$.

APPENDIX B
ASYMPTOTIC ANALYSIS OF SECOND-ORDER ACCURATE BOUNDARY SCHEMES

The asymptotic analysis and diffusive scaling in (Yoshida and Nagaoka 2010) are applied here with the following dimensionless parameter introduced

$$\epsilon = \delta x / L, \quad (\text{B-1})$$

where L is the reference length. For details of the asymptotic analysis of the thermal lattice Boltzmann equation (TLBE) and the diffusive scaling please refer to the work by Yoshida and Nagaoka (2010). Here we focus on the asymptotic analysis for the present boundary condition treatments; some results given by Yoshida and Nagaoka (2010) are used directly.

The distribution function g_α and the macroscopic variable ϕ can be expanded as (the arguments of (\mathbf{x}, t) are dropped for simplicity):

$$g_\alpha = g_\alpha^{(0)} + \epsilon g_\alpha^{(1)} + \epsilon^2 g_\alpha^{(2)} + O(\epsilon^3), \quad (\text{B-2})$$

$$\phi = \phi^{(0)} + \epsilon \phi^{(1)} + \epsilon^2 \phi^{(2)} + O(\epsilon^3), \quad (\text{B-3})$$

and the spatial vectors \mathbf{x}_f and \mathbf{x}_{ff} in the field are related to the boundary vector \mathbf{x}_w by (see Fig. 3-2)

$$\mathbf{x}_f = \mathbf{x}_w - \Delta \mathbf{e}_\alpha \epsilon = \mathbf{x}_w + \Delta \mathbf{e}_{\bar{\alpha}} \epsilon, \quad (\text{B-4a})$$

$$\mathbf{x}_{ff} = \mathbf{x}_w - (1+\Delta) \mathbf{e}_\alpha \epsilon. \quad (\text{B-4b})$$

Note that the spatial vector \mathbf{x} and time t throughout this Appendix are dimensionless variables normalized by the reference length and diffusion time scales, respectively. Based on the diffusive scaling in (Yoshida and Nagaoka 2010) the present boundary condition treatments in Eqs. (3-32) and (3-38) can be rewritten in terms of \mathbf{x}_w as follows Dirichlet boundary condition:

$$g_{\bar{\alpha}}(\mathbf{x}_w + \Delta \mathbf{e}_{\bar{\alpha}} \boldsymbol{\epsilon}, t + \boldsymbol{\epsilon}^2) = c_{d1} \hat{g}_{\alpha}(\mathbf{x}_w - \Delta \mathbf{e}_{\alpha} \boldsymbol{\epsilon}, t) + c_{d2} \hat{g}_{\alpha}(\mathbf{x}_w - (1+\Delta) \mathbf{e}_{\alpha} \boldsymbol{\epsilon}, t) \\ + c_{d3} \hat{g}_{\bar{\alpha}}(\mathbf{x}_w + \Delta \mathbf{e}_{\bar{\alpha}} \boldsymbol{\epsilon}, t) + c_{d4} \boldsymbol{\epsilon} \Phi_d, \quad \text{and} \quad (\text{B-5})$$

Neumann boundary condition:

$$g_{\bar{\alpha}}(\mathbf{x}_w + \Delta \mathbf{e}_{\bar{\alpha}} \boldsymbol{\epsilon}, t + \boldsymbol{\epsilon}^2) = c_{n1} \hat{g}_{\alpha}(\mathbf{x}_w - \Delta \mathbf{e}_{\alpha} \boldsymbol{\epsilon}, t) + c_{n2} \hat{g}_{\alpha}(\mathbf{x}_w - (1+\Delta) \mathbf{e}_{\alpha} \boldsymbol{\epsilon}, t) \\ + c_{n3} \hat{g}_{\bar{\alpha}}(\mathbf{x}_w + \Delta \mathbf{e}_{\bar{\alpha}} \boldsymbol{\epsilon}, t) + c_{n4} \boldsymbol{\epsilon} \Phi_{n\bar{\alpha}} / U, \quad (\text{B-6})$$

where U is a reference speed ($U = \boldsymbol{\epsilon} \delta x / \delta t$) for diffusive scaling as defined in (Yoshida and Nagaoka 2010). The source term does not affect the boundary condition treatment; thus it is not considered here for simplicity. The post-collision distribution functions in Eqs. (B-5, B-6) are manipulated with the collision operator, and after inserting the expansion (B-2) into Eqs. (B-5, B-6) each distribution can be expressed with respect to the boundary distribution function, $\hat{g}_{\bar{\alpha}}^{(m)}(\mathbf{x}_w, t)$, or $\hat{g}_{\alpha}^{(m)}(\mathbf{x}_w, t)$ ($m = 0, 1, \text{ and } 2$) using

Taylor-series expansions as below

$$g_{\bar{\alpha}}^{(m)}(\mathbf{x}_w + \Delta \mathbf{e}_{\bar{\alpha}} \boldsymbol{\epsilon}, t + \boldsymbol{\epsilon}^2) = g_{\bar{\alpha}}^{(m)} + (\Delta \boldsymbol{\epsilon} e_{\bar{\alpha}j} \frac{\partial}{\partial x_j} + \boldsymbol{\epsilon}^2 \frac{\partial}{\partial t} + \frac{1}{2} \Delta^2 \boldsymbol{\epsilon}^2 e_{\bar{\alpha}i} e_{\bar{\alpha}j} \frac{\partial^2}{\partial x_i \partial x_j} + O(\boldsymbol{\epsilon}^3)) g_{\bar{\alpha}}^{(m)}, \quad (\text{B-7a})$$

$$\hat{g}_{\alpha}^{(m)}(\mathbf{x}_w - \Delta \mathbf{e}_{\alpha} \boldsymbol{\epsilon}, t) = g_{\alpha}^{(m)}(\mathbf{x}_w - \Delta \mathbf{e}_{\alpha} \boldsymbol{\epsilon}, t) + L g_{\alpha}^{(m)}(\mathbf{x}_w - \Delta \mathbf{e}_{\alpha} \boldsymbol{\epsilon}, t) \\ = (g_{\alpha}^{(m)} + L g_{\alpha}^{(m)}) + (-\Delta \boldsymbol{\epsilon} e_{\alpha j} \frac{\partial}{\partial x_j} + \frac{1}{2} \Delta^2 \boldsymbol{\epsilon}^2 e_{\alpha i} e_{\alpha j} \frac{\partial^2}{\partial x_i \partial x_j} + O(\boldsymbol{\epsilon}^3)) (g_{\alpha}^{(m)} + L g_{\alpha}^{(m)}), \quad (\text{B-7b})$$

$$\hat{g}_{\alpha}^{(m)}(\mathbf{x}_w - (1+\Delta) \mathbf{e}_{\alpha} \boldsymbol{\epsilon}, t) = g_{\alpha}^{(m)}(\mathbf{x}_w - (1+\Delta) \mathbf{e}_{\alpha} \boldsymbol{\epsilon}, t) + L g_{\alpha}^{(m)}(\mathbf{x}_w - (1+\Delta) \mathbf{e}_{\alpha} \boldsymbol{\epsilon}, t) \\ = (g_{\alpha}^{(m)} + L g_{\alpha}^{(m)}) + (-(1+\Delta) \boldsymbol{\epsilon} e_{\alpha j} \frac{\partial}{\partial x_j} + \frac{1}{2} (1+\Delta)^2 \boldsymbol{\epsilon}^2 e_{\alpha i} e_{\alpha j} \frac{\partial^2}{\partial x_i \partial x_j} + O(\boldsymbol{\epsilon}^3)) (g_{\alpha}^{(m)} + L g_{\alpha}^{(m)}), \quad (\text{B-7c})$$

$$\hat{g}_{\bar{\alpha}}^{(m)}(\mathbf{x}_w + \Delta \mathbf{e}_{\bar{\alpha}} \boldsymbol{\epsilon}, t) = g_{\bar{\alpha}}^{(m)}(\mathbf{x}_w + \Delta \mathbf{e}_{\bar{\alpha}} \boldsymbol{\epsilon}, t) + L g_{\bar{\alpha}}^{(m)}(\mathbf{x}_w + \Delta \mathbf{e}_{\bar{\alpha}} \boldsymbol{\epsilon}, t)$$

$$= (g_{\bar{\alpha}}^{(m)} + L g_{\bar{\alpha}}^{(m)}) + (\Delta \epsilon_{\bar{a}j} \frac{\partial}{\partial x_j} + \frac{1}{2} \Delta^2 \epsilon^2 e_{\bar{a}i} e_{\bar{a}j} \frac{\partial^2}{\partial x_i \partial x_j} + O(\epsilon^3)) (g_{\bar{\alpha}}^{(m)} + L g_{\bar{\alpha}}^{(m)}), \quad (\text{B-7d})$$

where the arguments (\mathbf{x}_w, t) on the RHS of the equations are skipped for brevity and the collision operator is

$$L \mathbf{g}^{(m)} = M^{-1} S M (Q^{(0)} + \epsilon Q^{(1)}) \mathbf{g}^{(m)}, \quad (\text{B-8})$$

with

$$Q^{(0)} = (\omega_0, \omega_1, \dots, \omega_6)^T (1, 1, \dots, 1) - I_{7 \times 7}, \text{ and} \quad (\text{B-9a})$$

$$Q^{(1)} = \frac{1}{\epsilon U} (0, u\omega_1, -u\omega_2, v\omega_3, -v\omega_4, w\omega_5, -w\omega_6)^T (1, 1, 1, 1, 1, 1), \quad (\text{B-9b})$$

Substitution of Eqs. (B-7a) through (B-7d) into the boundary schemes given by Eqs. (B-5) and (B-6) and rearranging the relevant terms according to the power of ϵ , one obtains the required conditions to satisfy the thermal boundary conditions to second-order accuracy.

Dirichlet boundary condition:

The equation of zeroth-order in ϵ is

$$(1 - c_{d3}) g_{\bar{\alpha}}^{(0)} - (c_{d1} + c_{d2}) g_{\alpha}^{(0)} = c_{d4} \epsilon \Phi_d. \quad (\text{B-10})$$

In the power of ϵ^1 , the equation is

$$(1 - c_{d3}) g_{\bar{\alpha}}^{(1)} - (c_{d1} + c_{d2}) g_{\alpha}^{(1)} + [(\Delta(1 - c_{d3}) - c_{d3}) e_{\bar{a}j} \frac{\partial g_{\bar{\alpha}}^{(0)}}{\partial x_j} + ((\Delta - 1)(c_{d1} + c_{d2}) + c_{d2}) e_{\bar{a}j} \frac{\partial g_{\alpha}^{(0)}}{\partial x_j}] = 0, \quad (\text{B-11})$$

According to Yoshida and Nagaoka (2010), the following relationships are noticed based on the respective Eqs. (50), (51) and (57)

$$g_{\bar{\alpha}}^{(0)} - g_{\alpha}^{(0)} = 0, \quad (\text{B-12})$$

$$g_{\bar{\alpha}}^{(0)} + g_{\alpha}^{(0)} = \varepsilon \phi^{(0)}, \quad (\text{B-13})$$

$$g_{\bar{\alpha}}^{(1)} + g_{\alpha}^{(1)} = \varepsilon \phi^{(1)}. \quad (\text{B-14})$$

Equations (B-12 – B-14) imply that the following relationships must hold for the coefficients in Eqs. (B-10) and (B-11)

$$\begin{cases} 1 - c_{d3} = -(c_{d1} + c_{d2}) \\ 1 - c_{d3} = c_{d4} \\ \Delta(1 - c_{d3}) - c_{d3} = (\Delta - 1)(c_{d1} + c_{d2}) + c_{d2} \\ c_{d4} \neq 0, \end{cases} \quad (\text{B-15})$$

in order to satisfy

$$\phi^{(0)} = \Phi_d, \text{ and} \quad (\text{B-16})$$

$$\phi^{(1)} = 0. \quad (\text{B-17})$$

Noting that the Dirichlet thermal boundary condition is given by

$$\phi = \Phi_d, \quad (3-2)$$

and recalling the expansion $\phi = \phi^{(0)} + \varepsilon \phi^{(1)} + \varepsilon^2 \phi^{(2)} + O(\varepsilon^3)$ in (B-3), the following is thus obtained

$$\phi^{(0)} = \Phi_d + O(\varepsilon^2). \quad (\text{B-18})$$

Equation (B-18) verifies that the Dirichlet boundary condition is satisfied up to second-order accuracy with the leading-order solution solved by $\phi^{(0)}$ in TLBE simulations. The coefficients in Eq. (B-15) cannot be uniquely determined, and leaving c_{d1} adjustable the constraints can be rewritten as

$$\left\{ \begin{array}{l} c_{d2} = -\frac{2\Delta c_{d1} + 1}{2\Delta + 1} \\ c_{d3} = \frac{c_{d1} + 2\Delta}{2\Delta + 1} \\ c_{d4} = \frac{-c_{d1} + 1}{2\Delta + 1} \\ c_{d1} \neq 1. \end{array} \right. \quad (\text{B-19})$$

Neumann boundary condition:

The Neumann boundary condition is given by Eq. (3-3). For brevity, we assume the normal direction of the physical boundary is in the same direction as the discrete velocity direction $\mathbf{e}_{\bar{\alpha}}$; thus $\Phi_{n\bar{\alpha}} = \Phi_n$ can be directly applied.

Substitution of expansions in (B-7a – B-7d) into the boundary scheme in (B-6) gives the equation of zeroth-order in ϵ as

$$(1 - c_{n3})g_{\bar{\alpha}}^{(0)} - (c_{n1} + c_{n2})g_{\alpha}^{(0)} = 0. \quad (\text{B-20})$$

In the power of ϵ^1 , the equation is

$$\begin{aligned} & (1 - c_{n3})g_{\bar{\alpha}}^{(1)} - (c_{n1} + c_{n2})g_{\alpha}^{(1)} \\ & + [(\Delta(1 - c_{n3}) - c_{n3})\mathbf{e}_{\bar{\alpha}j} \frac{\partial g_{\bar{\alpha}}^{(0)}}{\partial x_j} - ((1 - \Delta)(c_{n1} + c_{n2}) - c_{n2})\mathbf{e}_{\alpha j} \frac{\partial g_{\alpha}^{(0)}}{\partial x_j}] = c_{n4} \frac{\Phi_n}{U}, \end{aligned} \quad (\text{B-21})$$

and proceeding further to $O(\epsilon^2)$ yields

$$\begin{aligned} & [(1 - c_{n3})g_{\bar{\alpha}}^{(2)} - (c_{n1} + c_{n2})g_{\alpha}^{(2)}] + \left[(\Delta - c_{n3}(1 + \Delta))\mathbf{e}_{\bar{\alpha}j} \frac{\partial g_{\bar{\alpha}}^{(1)}}{\partial x_j} - (c_{n1} - (c_{n1} + c_{n2})\Delta)\mathbf{e}_{\alpha j} \frac{\partial g_{\alpha}^{(1)}}{\partial x_j} \right] \\ & + \left[\frac{1}{2}(\Delta^2 - c_{n3}(\Delta + 1)^2)\mathbf{e}_{\bar{\alpha}i}\mathbf{e}_{\bar{\alpha}j} \frac{\partial^2 g_{\bar{\alpha}}^{(0)}}{\partial x_i \partial x_j} - \frac{1}{2}(c_{n1}(\Delta - 1)^2 + c_{n2}\Delta^2)\mathbf{e}_{\alpha i}\mathbf{e}_{\alpha j} \frac{\partial^2 g_{\alpha}^{(0)}}{\partial x_i \partial x_j} \right] = 0. \end{aligned} \quad (\text{B-22})$$

With the expansion $\phi = \phi^{(0)} + \epsilon\phi^{(1)} + \epsilon^2\phi^{(2)} + O(\epsilon^3)$ in (B-3) one would expect that

$$-D_{ij} \frac{\partial \phi^{(0)}}{\partial x_j} + v_i \phi^{(0)} = \Phi_n, \quad (\text{B-23})$$

so that the leading-order solution of $\phi^{(0)}$ satisfies the Neumann boundary condition.

Recalling the relationship between D_{ij} and τ_{ij} in Eq. (3-14) the above (B-23) can be rewritten as

$$\left(-\tau_{ij} + \frac{1}{2} \delta_{ij}\right) \varepsilon \frac{\partial \phi^{(0)}}{\partial x_j} + \frac{v_i}{U} \phi^{(0)} = \frac{\Phi_n}{U}. \quad (\text{B-24})$$

Besides Eqs. (B-12 – B-14), the following relationships can be obtained from Eqs. (56) and (64) in Yoshida and Nagaoka (2010), respectively

$$g_{\bar{\alpha}}^{(1)} - g_{\alpha}^{(1)} = \frac{v_i}{U} \phi^{(0)} - \varepsilon \tau_{ij} \frac{\partial \phi^{(0)}}{\partial x_j}, \quad (\text{B-25})$$

$$g_{\bar{\alpha}}^{(2)} - g_{\alpha}^{(2)} = \varepsilon \frac{v_i}{U \varepsilon} \phi^{(1)} - \varepsilon \tau_{ij} \frac{\partial \phi^{(1)}}{\partial x_j}. \quad (\text{B-26})$$

Comparing Eq. (B-20) with Eq. (B-12) and combining Eqs. (B-13, B-21, B-24, and B-25) we obtain the requirements

$$\begin{cases} 1 - c_{n3} = c_{n1} + c_{n2} \\ \Delta(1 - c_{n3}) - c_{n3} = (1 - \Delta)(c_{n1} + c_{n2}) - c_{n2} \\ 1 - c_{n3} = 2[\Delta(1 - c_{n3}) - c_{n3}] \\ c_{n4} = 1 - c_{n3}. \end{cases} \quad (\text{B-27})$$

The unique solution to the coefficients in Eq. (B-27) is

$$\begin{cases} c_{n1} = 1 \\ c_{n2} = -\frac{2\Delta - 1}{2\Delta + 1} \\ c_{n3} = \frac{2\Delta - 1}{2\Delta + 1} \\ c_{n4} = \frac{2}{2\Delta + 1}. \end{cases} \quad (\text{B-28})$$

With the above coefficients and the relationships in Eqs. (B-14) and (B-26) the following can be derived from Eq. (B-22)

$$\left(-\tau_{ij} + \frac{1}{2}\delta_{ij}\right)\varepsilon_D \frac{\partial \phi^{(1)}}{\partial x_j} + \frac{v_i}{U}\phi^{(1)} = 0. \quad (\text{B-29})$$

As discussed in (Yoshida and Nagaoka 2010), since the condition for $\phi^{(1)}$ is linear and homogeneous, $\phi^{(1)}$ in (B-29) has only a trivial solution of $\phi^{(1)} \equiv 0$. Thus we have verified that the Neumann boundary condition is satisfied to second-order accuracy.

APPENDIX C
EXTENSION OF ZHOU'S BGK AXISYMMETRIC LATTICE BOLTZMANN MODEL
(ZHOU 2011) TO AN MRT LATTICE BOLTZMANN MODEL

The governing equations for the athermal incompressible axisymmetric flows in the cylindrical coordinate system can be written as

$$\frac{\partial u_j}{\partial x_j} = -\frac{u_r}{r}, \quad (\text{C-1})$$

$$\frac{\partial u_i}{\partial t} + u_j \frac{\partial u_i}{\partial x_j} = -\frac{1}{\rho} \frac{\partial p}{\partial x_i} + \nu \frac{\partial^2 u_i}{\partial x_j^2} + \frac{\nu}{r} \frac{\partial u_i}{\partial r} - \frac{\nu u_i}{r^2} \delta_{ir}, \quad (\text{C-2})$$

where i, j are the indices denoting the radial r - and axial z -directions, x_i and u_i are the components of the spatial vector $\mathbf{x}(r, z)$ and the velocity vector $\mathbf{u}(u_r, u_z)$, respectively, ρ is the density, p is the pressure, and δ_{ir} is the Kronecker's delta function.

Substitution of the continuity equation (C-1) into Eq. (C-2) gives the following momentum equation (Li et al. 2010, Zhou 2011)

$$\frac{\partial u_i}{\partial t} + \frac{\partial}{\partial x_j} (u_i u_j) = -\frac{1}{\rho} \frac{\partial p}{\partial x_i} + \nu \frac{\partial}{\partial x_j} \left(\frac{\partial u_i}{\partial x_j} + \frac{\partial u_j}{\partial x_i} \right) + \frac{\nu}{r} \left(\frac{\partial u_i}{\partial r} + \frac{\partial u_r}{\partial x_i} \right) - \frac{u_i u_r}{r} - \frac{2\nu u_i}{r^2} \delta_{ir}. \quad (\text{C-3})$$

For incompressible flows in the Cartesian coordinate system, the continuity and momentum equations recovered by the standard LBE read

$$\frac{\partial u_j}{\partial x_j} = 0, \quad (\text{C-4})$$

$$\frac{\partial u_i}{\partial t} + \frac{\partial}{\partial x_j} (u_i u_j) = -\frac{1}{\rho} \frac{\partial p}{\partial x_i} + \nu \frac{\partial}{\partial x_j} \left(\frac{\partial u_i}{\partial x_j} + \frac{\partial u_j}{\partial x_i} \right). \quad (\text{C-5})$$

As implied in Zhou's LB model (2011), Eq. (C-3) can be considered as a particular form

of Eq. (C-5) with explicit force terms $\frac{v}{r} \left(\frac{\partial u_i}{\partial r} + \frac{\partial u_r}{\partial x_i} \right)$ and $-\frac{u_i u_r}{r} - \frac{2v u_i}{r^2} \delta_{ir}$, and another

implicit source term accounting for the continuity Eq. (C-1).

The LBE for the velocity distribution function f_α in Zhou's BGK-LB model (2011) is formulated as

$$f_\alpha(\mathbf{x} + \mathbf{e}_\alpha \delta t, t + \delta t) - f_\alpha(\mathbf{x}, t) = -\frac{1}{\tau} \left[1 + \frac{(2\tau - 1) \mathbf{e}_{\alpha r} \delta t}{2r} \right] (f_\alpha - f_\alpha^{(\text{eq})}) + \omega_\alpha \theta \delta t + \frac{\delta t}{\kappa \mathbf{e}^2} \mathbf{e}_{\alpha i} F_i, \quad (\text{C-6})$$

in order to recover the axisymmetric flow equations. For brevity, the special case of $r = 0$ discussed in (Zhou 2011) is not considered here. The source or sink term θ is

$$\theta = -\rho u_r / r, \quad (\text{C-7})$$

and F_i is a force term defined by

$$F_i = -\frac{\rho u_i u_r}{r} - \frac{2\rho v u_i}{r^2} \delta_{ir}. \quad (\text{C-8})$$

For rotational flows with azimuthal velocity component u_φ , the force term in Eq. (C-8) should be modified to

$$F_i = -\frac{\rho u_i u_r}{r} - \frac{2\rho v u_i}{r^2} \delta_{ir} + \frac{\rho u_\varphi^2}{r} \delta_{ir}. \quad (\text{C-9})$$

Here we rearrange Eq. (C-6) as

$$f_\alpha(\mathbf{x} + \mathbf{e}_\alpha \delta t, t + \delta t) - f_\alpha(\mathbf{x}, t) = -\frac{1}{\tau} (f_\alpha - f_\alpha^{(\text{eq})}) - \frac{1}{r} \frac{2\tau - 1}{2\tau} \mathbf{e}_{\alpha r} \delta t (f_\alpha - f_\alpha^{(\text{eq})}) + \omega_\alpha \theta \delta t + \frac{\delta t}{\kappa \mathbf{e}^2} \mathbf{e}_{\alpha i} F_i, \quad (\text{C-10})$$

It is noted in Eq. (C-10) that the first bracketed term on the right side, $-\frac{1}{\tau} (f_\alpha - f_\alpha^{(\text{eq})})$, is

the standard BGK collision operator in the LBE method. The second bracketed term,

$-\frac{1}{r} \frac{2\tau-1}{2\tau} \mathbf{e}_{\alpha r} \delta t (f_{\alpha} - f_{\alpha}^{(\text{eq})})$, and the last term, $\frac{\delta t}{\kappa e^2} \mathbf{e}_{\alpha i} F_i$, correspond to the velocity gradient

(stress) term $\frac{v}{r} \left(\frac{\partial u_i}{\partial r} + \frac{\partial u_r}{\partial x_i} \right)$ and the force term $-\frac{u_i u_r}{r} - \frac{2v u_i}{r^2} \delta_{ir}$ in Eq. (C-3),

respectively. As discussed earlier, the source term, θ , included in Eq. (C-10) is necessary to satisfy the continuity equation (C-1). The proof for the correspondence of each term in the LBE (C-10) to their relevant terms recovered in the momentum Eq. (C-3) can be found in (Zhou 2011).

In this manner, the velocity gradient can be considered as a source term and obtained from the non-equilibrium part of the velocity distribution functions as in Eq. (C-10). This is analogous to the treatment of the scalar gradient, $\frac{D_{rr}}{r} \frac{\partial \phi}{\partial r}$, in Eq. (5-2) as a source

term obtained from the non-equilibrium distribution functions,

$-\frac{1}{r} \left(1 - \frac{1}{2\tau_{rr}} \right) \frac{\delta x}{\delta t} \sum_{\alpha=1}^m \mathbf{e}_{\alpha r} [g_{\alpha} - g_{\alpha}^{(\text{eq})}]$, in Eq. (5-6) in the present LB model for the

axisymmetric CDE.

The BGK model by Zhou (2011) can then be conveniently extended to an MRT model with the following evolution equation for f_{α}

$$f_{\alpha}(\mathbf{x} + \mathbf{e}_{\alpha} \delta t, t + \delta t) - f_{\alpha}(\mathbf{x}, t) = - \left[\mathbf{M}^{-1} \mathbf{S} (\mathbf{m} - \mathbf{m}^{(\text{eq})}) \right]_{\alpha} + \mathbf{G} \delta t. \quad (\text{C-11})$$

where \mathbf{M} is a transformation matrix converting the velocity distribution functions \mathbf{f} to their moment \mathbf{m} by $\mathbf{m} = \mathbf{M} \mathbf{f}$, $\mathbf{m}^{(\text{eq})}$ is the equilibria of the moments, and \mathbf{S} is a matrix of relaxation coefficients. According to Eq. (C-10), the combined source term \mathbf{G} in Eq. (C-11) is determined from

$$G = -\frac{1}{r} \frac{2\tau - 1}{2\tau} \mathbf{e}_{ar} (f_\alpha - f_\alpha^{(\text{eq})}) + \omega_\alpha \theta + \frac{1}{\kappa e^2} \mathbf{e}_{ai} F_i. \quad (\text{C-12})$$

The standard D2Q9 MRT-LB model in (Lallemand and Luo 2000) and (Yu et al. 2003) can be applied to simulate Eq. (C-11) and it is used in the present work.

LIST OF REFERENCES

- Abanades, S., Charvin, P., Flamant, G., and Neveu, P., 2006, "Screening of Water-Splitting Thermochemical Cycles Potentially Attractive for Hydrogen Production by Concentrated Solar Energy," *Energy*, **31**, pp. 2805-2822.
- Aidun, C. K., and Clausen, J. R., 2010, "Lattice-Boltzmann Method for Complex Flows," *Annu. Rev. Fluid Mech.*, **42**, pp. 439-472.
- Alexander, F. J., Chen, S., and Sterling, J. D., 1993, "Lattice Boltzmann Thermohydrodynamics," *Phys. Rev. E*, **47**, R2249.
- Ammar, F. B., Kaviany, M., and Barber, J. R., 1992, "Heat Transfer During Impact," *Int. J. Heat Mass Transfer*, **35**, pp. 1495-1506.
- Asinari, P., 2008, "Asymptotic Analysis of Multiple-relaxation-time Lattice Boltzmann Schemes for Mixture Modeling," *Comput. Math. Appl.*, **55**, pp. 1392-1407.
- Barber, J. R., 1989, "An Asymptotic Solution for Short-time Transient Heat Conduction between Two Similar Contacting Bodies," *Int. J. Heat Mass Transfer*, **32**, pp. 943-949.
- Behrend, O., 1995, "Solid-Fluid Boundaries in Particle Suspension Simulations via the Lattice Boltzmann Method," *Phys. Rev. E*, **52**, pp. 1164-1175.
- Bhatnagar, P. L., Gross, E. P., and Krook, M., 1954, "A Model for Collision Processes in Gases. I. Small Amplitude Processes in Charged and Neutral One-Component Systems," *Phys. Rev.*, **94**, pp. 511-525.
- Bouzidi, M., Firdaouss, M., and Lallemand, P., 2001, "Momentum Transfer of a Boltzmann-Lattice Fluid with Boundaries," *Phys. Fluids*, **13**, pp. 3452-3459.
- Chen, H., Chen, S., and Matthaeus, W. H., 1992, "Recovery of the Navier–Stokes Equations Using a Lattice-Gas Boltzmann Method," *Phys. Rev. A*, **45**, R5339.
- Chen, L., Kang, Q., He, Y. L., and Tao, W. Q. 2012, "Pore-Scale Simulation of Coupled Multiple Physicochemical Thermal Processes in Micro Reactor for Hydrogen Production Using Lattice Boltzmann Method," *Int. J. Hydrogen Energ.*, **37**, pp. 13943-13957.
- Chen, S., and Doolen, G. D., 1998, "Lattice Boltzmann Method for Fluid Flows," *Annu. Rev. Fluid Mech.*, **30**, pp. 329-364.
- Chen, S., Martinez, D., and Mei, R., 1996, "On Boundary Conditions in Lattice Boltzmann Method," *Phys. Fluids*, **8**, pp. 2527-2536.
- Chen, S., Tolke, J., Geller, S., and Krafczyk, M., 2008, "Lattice Boltzmann Model for Incompressible Axisymmetric Flows," *Phys. Rev. E*, **78**, 046703.

- Chen, S., Tolke, J., and Krafczyk, M., 2009, "Simulation of Buoyancy-Driven Flows in a Vertical Cylinder Using a Simple Lattice Boltzmann Model," *Phys. Rev. E*, **79**, 016704.
- Chen, Y., Ohashi, H., and Akiyama, M., 1994, "Thermal Lattice Bhatnagar-Gross-Krook Model without Nonlinear Deviations in Macrodynamic Equations," *Phys. Rev. E*, **50**, 2776.
- de Vahl Davis, G., and Thomas, R. W., 1969, "Natural Convection between Concentric Vertical Cylinders," *Phys. Fluids*, **12**, (suppl. 2) pp. 198-207.
- d'Humières, D., 1992, "Generalized Lattice Boltzmann Equations. In Rarefied Gas Dynamics: Theory and Simulations," *Prog. Astronaut. Aeronaut.*, **159**, pp. 450-458.
- d'Humières, D., Ginzburg, I., Krafczyk, M., Lallemand, P., and Luo, L.-S., 2002, "Multiple-relaxation-time Lattice Boltzmann Models in Three Dimensions," *Philos. T. Roy. Soc. A*, **360**, pp. 437-451.
- D'Orazio, A., Succi, S., and Arrighetti, C., 2003, "Lattice Boltzmann Simulation of Open Flows with Heat Transfer," *Phys. Fluids*, **15**, pp. 2778-2781.
- Faghri, A., and Zhang, Y., 2006, *Transport Phenomena in Multiphase Systems*, Elsevier Inc.
- Filippova, O., and Hänel, D., 1998, "Grid Refinement for Lattice-BGK Model," *J. Comput. Phys.*, **147**, pp. 219-228.
- Flekky, E. G., 1993, "Lattice Bhatnagar-Gross-Krook Models for Miscible Fluids," *Phys. Rev. E*, **47**, pp. 4247-4257.
- Garimella, S. V., and Sobhan, C. B., 2003, "Transport in Microchannels - a Critical Review," *Annu. Rev. Heat Transfer*, **13**, pp. 1-50.
- Ginzburg, I., and d'Humières, D., 1996, "Local Second-order Boundary Methods for Lattice Boltzmann Models," *J. Stat. Phys.*, **84**, pp. 927-971.
- Ginzburg, I., and d'Humières, D., 2003, "Multireflection Boundary Conditions for Lattice Boltzmann Models," *Phys. Rev. E*, **68**, 066614.
- Ginzburg, I., 2005, "Generic Boundary Conditions for Lattice Boltzmann Models and Their Application to Advection and Anisotropic Dispersion Equations," *Adv. Water Resour.*, **28**, pp. 1196-1216.
- Graebel, W. P., 2001, *Engineering Fluid Mechanics*, Taylor & Francis, New York.

- Guo, Z., Han, H., Shi, B., and Zheng, C., 2009, "Theory of the Lattice Boltzmann Equation: Lattice Boltzmann Model for Axisymmetric Flows," *Phys. Rev. E*, **79**, 046708.
- Guo, Z., and Zhao, T. S., 2002, "Lattice Boltzmann Model for Incompressible Flows through Porous Media," *Phys. Rev. E*, **66**, 036304.
- Guo, Z., Zhao, T. S., and Shi, Y., 2006, "Physical Symmetry, Spatial Accuracy, and Relaxation Time of the Lattice Boltzmann Equation for Microgas Flows," *J. Appl. Phys.*, **99**, 074903.
- Guo, Z., Zheng, C., and Shi, B., 2002, "An Extrapolation Method for Boundary Conditions in Lattice Boltzmann Method," *Phys. Fluids*, **14**, pp. 2007-2010.
- Guo, Z., Zheng, C., and Shi, B., 2007, "Thermal Lattice Boltzmann Equation for Low Mach Number Flows: Decoupling Model," *Phys. Rev. E*, **75**, 036704.
- Hahn, D. W., and Ozisik, M. N., 2012, *Heat Conduction*, 3rd ed., John Wiley & Sons, New York, USA.
- Halliday, I., Hammond, L. A., Care, C. M., Good, K., and Stevens, A., 2001, "Lattice Boltzmann Equation Hydrodynamics," *Phys. Rev. E*, **64**, 011208.
- He, X., Chen, S., and Doolen, G. D., 1998, "A Novel Thermal Model for the Lattice Boltzmann Method in Incompressible Limit," *J. Comput. Phys.*, **146**, pp. 282-300.
- He, X., and Doolen, G., 1997, "Lattice Boltzmann Method on Curvilinear Coordinates System: Flow around a Circular Cylinder," *J. Comput. Phys.*, **134**, pp. 306-315.
- He, X., Zou, Q., Luo, L.-S., and Dembo, M., 1997, "Analytic Solutions of Simple Flows and Analysis of Nonslip Boundary Conditions for the Lattice Boltzmann BGK Model," *J. Stat. Phys.* **87**, pp. 115-136.
- Heasley, J.H., 1965, "Transient Heat Flow between Contacting Solids," *Int. J. Heat Mass Transfer*, **8**, pp. 147-154.
- Huang, H., and Lu, X.-Y., 2009, "Theoretical and Numerical Study of Axisymmetric Lattice Boltzmann Models," *Phys. Rev. E*, **80**, 016701.
- Ho, C. F., Chang, C., Lin, K. H., and Lin, C. A., 2009, "Consistent Boundary Conditions for 2D and 3D Laminar Lattice Boltzmann Simulations," *Comput. Model Eng. Sci.*, **44**, 137.
- Howard, J. R., and Sutton, A. E., 1970, "An Analogue Study of Heat Transfer through Periodically Contacting Surfaces," *Int. J. Heat Mass Transfer*, **3**, pp. 173-183.
- Huang, H., Lee, T. S., and Shu, S., 2006, "Thermal Curved Boundary Treatment for the Thermal Lattice Boltzmann Equation," *Int. J. Mod. Phys. C*, **17**, pp. 631-643.

- Huang, H., Lee, T. S., and Shu, S., 2007, "Hybrid Lattice Boltzmann Finite-Difference Simulation of Axisymmetric Swirling and Rotating Flows," *Int. J. Numer. Meth. Fluids*, **53**, pp. 1707-1726.
- Iwatsu, R., 2004, "Flow Pattern and Heat Transfer of Swirling Flows in Cylindrical Container with Rotating Top and Stable Temperature Gradient," *Int. J. Heat Mass Transfer*, **47**, pp. 2755-2767.
- Jeong, H. K., Yoon, H. S., Ha, M. Y., and, Tsutahara M., 2010, "An Immersed Boundary-Thermal Lattice Boltzmann Method Using an Equilibrium Internal Energy Density Approach for the Simulation of Flows with Heat Transfer," *J. Comput. Phys.*, **229**, pp. 2526-2543.
- Johnson, K. L., 1987, *Contact Mechanics*, Cambridge University Press, Cambridge, U.K..
- Kang, Q., Lichtner, P. C., and Zhang, D., 2006, "Lattice Boltzmann Pore-Scale Model for Multicomponent Reactive Transport in Porous Media," *J. Geophys. Res.*, **111**, B05203.
- Kang, Q., Lichtner, P. C., and Zhang, D., 2007, "An Improved Lattice Boltzmann Model for Multicomponent Reactive Transport in Porous Media at the Pore Scale," *Water Resour. Res.*, **43**, W12S14.
- Kao, P. H., Ren, T. F., and Yang, R. J., 2007, "An Investigation into Fixed-Bed Microreactors Using Lattice Boltzmann Method Simulations," *Int. J. Heat Mass Transfer*, **50**, pp. 4243-4255.
- Kaviany, M., 1988, "Effect of a Moving Particle on Wall Heat Transfer in a Channel Flow," *Numer. Heat Transfer*, **12**, pp. 111-124.
- Kaviany, M., 1998, *Heat Transfer in Porous Media. Handbook of Heat Transport*, 3rd ed., McGraw-Hill, pp. 9.1–9.82.
- Klausner, J. F., Petrasch, J., Hahn, D. W., and Mei, R., 2011, "Solar thermochemical fuel production via a novel low pressure, magnetically stabilized, non-volatile iron oxide looping process," Research Proposal for *ARPA-E, DOE*.
- Kim, B. S., Lee, D. S., Ha, M. Y., and Yoon, H. S., 2008, "A Numerical Study of Natural Convection in a Square Enclosure with a Circular Cylinder at Different Vertical Locations," *Int. J. Heat Mass Transfer*, **51**, pp. 1888-1906.
- Kodama, T., and Gokon, N., 2007, "Thermochemical Cycles for High-Temperature Solar Hydrogen Production," *Chem. Rev.*, **107**, pp. 4048-4077.
- Kostoglou, M., and Konstandopoulos, A. G., 2002, "On the Transient Heat Transfer through the Solid Phase in Aggregates and Deposits," *Ind. Eng. Chem. Res.*, **41**, pp. 3317-3325.

- Kumar, R., and Kalam, M. A., 1991, "Laminar Thermal Convection between Vertical Coaxial Isothermal Cylinders," *Int. J. Heat Mass Transfer*, **34**, pp. 513-524.
- Kuo, L.-S., and Chen, P. H., 2009, "Numerical Implementation of Thermal Boundary Conditions in the Lattice Boltzmann Method," *Int. J. Heat Mass Transfer*, **52**, pp. 529-532.
- Lallemand, P., and Luo, L.-S., 2000, "Theory of the Lattice Boltzmann Method: Dispersion, Dissipation, Isotropy, Galilean Invariance, and Stability," *Phys. Rev. E*, **61**, pp. 6546-6562.
- Lallemand, P., and Luo, L.-S., 2003, "Theory of the Lattice Boltzmann Method: Acoustic and Thermal Properties in Two and Three Dimensions," *Phys. Rev. E*, **68**, 036706.
- Lätt, J., Chopard, B., Succi, S., and Toschi, F., 2006, "Numerical Analysis of the Averaged Flow Field in a Turbulent Lattice Boltzmann Simulation," *Physica A*, **362**, pp. 6-10.
- Lee, T. S., Huang, H., and Shu, C., 2006, "An Axisymmetric Incompressible Lattice Boltzmann Model for Pipe Flow," *Int. J. Mod. Phys. C*, **17**, pp. 645-661.
- Li, J., and Mason, D. J., 2000, "A Computational Investigation of Transient Heat Transfer in Pneumatic Transport of Granular Particles," *Powder Technol.*, **112**, pp. 273-282.
- Li, L., Mei, R., Klausner, J. F., and Hahn, D. W., 2012, "Heat Transfer between Colliding Surfaces and Particles," *ASME J. Heat Trans.*, **134**, 011301.
- Li, L., Mei, R., and Klausner, J. F., 2013a, "Boundary Conditions for Thermal Lattice Boltzmann Equation Method," *J. Comput. Phys.*, **237**, pp. 366-395.
- Li, L., Mei, R., and Klausner, J. F., 2013b, "Heat Transfer Evaluation on Curved Boundaries in Thermal Lattice Boltzmann Equation Method," *ASME J. Heat Trans.*, accepted for publication.
- Li, L., Mei, R., and Klausner, J. F., 2013c, "Multiple-relaxation-time Lattice Boltzmann Model for the Axisymmetric Convection Diffusion Equation," *Int. J. Heat Mass Transfer*, under review.
- Li, L., Singh, A., AuYeung, N., Mei, R., Petrasch, J., and Klausner, J. F., 2013d, "Lattice Boltzmann Simulation of High-Diffusivity Problems with Application to Energy Transport in a High-Temperature Solar Thermochemical Reactor," *Proceedings of the ASME 2013 Summer Heat Transfer Conference, HT2013*, July 14-19, Minneapolis, MN.
- Li, Q., He, Y.-L., Tang, G. H., and Tao, W. Q., 2009, "Lattice Boltzmann Model for Axisymmetric Thermal Flows," *Phys. Rev. E*, **80**, 037702.

- Li, Q., He, Y.-L., Tang, G. H., and Tao, W. Q., 2010, "Improved Axisymmetric Lattice Boltzmann Scheme," *Phys. Rev. E*, **81**, 056707.
- Liu, C. H., Lin, K. H., Mai, H. C., and Lin, C. A., 2010, "Thermal Boundary Conditions for Thermal Lattice Boltzmann Simulations," *Comput. Math. Appl.*, **59**, pp. 2178-2193.
- Loutzenhiser, P. G., Meier, A., and Steinfeld, A., 2010, "Review of the Two-step H₂O/CO₂-Splitting Solar Thermochemical Cycle Based on Zn/ZnO Redox Reactions," *Materials*, **3**, pp. 4922-4938.
- Luo, L.-S., and Girimaji, S. S., 2003, "Theory of the Lattice Boltzmann Method: Two-fluid Model for Binary Mixtures," *Phys. Rev. E*, **67**, 036302.
- Maier, R. S., and Bernard, R. S., 2010, "Lattice-Boltzmann Accuracy in Pore-Scale Flow Simulation," *J. Comput. Phys.*, **229**, pp. 233-255.
- Manjhi, N., Verma, N., Salem, K., and Mewes, D., 2006, "Lattice Boltzmann Modelling of Unsteady-state 2D Concentration Profiles in Adsorption Bed," *Chem. Eng. Sci.* **61**, pp. 2510-2521.
- Mehdizadeh, A. M., Klausner, J. F., Barde, A., and Mei R., 2012, "Enhancement of Thermochemical Hydrogen Production Using an Iron-silica Magnetically Stabilized Porous Structure," *Int. J. Hydrogen Energ.*, **37**, pp. 8954-8963.
- Mei, R., Yu, D., Shyy, W., and Luo, L.-S., 2002, "Force Evaluation in the Lattice Boltzmann Method Involving Curved Geometry," *Phys. Rev. E*, **65**, 041203.
- Mei, R., Luo, L.-S., and Shyy, W., 1999, "An Accurate Curved Boundary Treatment in the Lattice Boltzmann Method," *J. Comput. Phys.*, **155**, pp. 307-330.
- Mei, R., Shyy, W., Yu, D., and Luo, L.-S., 2000, "Lattice Boltzmann Method for 3-D Flows with Curved Boundary," *J. Comput. Phys.*, **161**, pp. 680-699.
- Melchior, T., and Steinfeld, A., 2008, "Radiative Transfer within a Cylindrical Cavity with Diffusely/Specularly Reflecting Inner Walls Containing an Array of Tubular Absorbers," *ASME J. Sol. Energ.*, **130**, 021013.
- Mezrhab, A., Moussaoui, M. A., Jami, M., Naji, H., and Bouzidi, M., 2010, "Double MRT Thermal Lattice Boltzmann Method for Simulating Convective Flows," *Phys. Lett. A*, **374**, pp. 3499-3507.
- Modest, M. F., 2003, *Radiative Heat Transfer*, 2nd ed., Academic Press, USA.
- Moukalled, F., and Acharya, S., 1996, "Natural Convection in the Annulus between Concentric Horizontal Circular and Square Cylinders," *J. Thermophys. Heat Transfer*, **10**, pp. 524-531.

- Müller, R., Lipiński, W., and Steinfeld, A., 2008, "Transient Heat Transfer in a Directly-Irradiated Solar Chemical Reactor for the Thermal Dissociation of ZnO," *Appl. Therm. Eng.*, **28**, pp. 524-531.
- Noble, D. R., Chen, S., Georgiadis, J. G., and Buckius, R. O., 1995, "A Consistent Hydrodynamic Boundary Condition for the Lattice Boltzmann Method," *Phys. Fluids*, **7**, pp. 203-209.
- Pan, C., Luo, L.-S., and Miller, C. T., 2006, "An Evaluation of Lattice Boltzmann Schemes for Porous Medium Flow Simulation," *Comput. Fluids*, **35**, pp. 898-909.
- Peng, Y., Chew, Y. T., and Shu, C., 2003, "Simplified Thermal Lattice Boltzmann Model for Incompressible Thermal Flows," *Phys. Rev. E*, **67**, 026701.
- Peng, Y., Shu, C., Chew, Y. T., and Qiu, J., 2003, "Numerical Investigation of Flows in Czochralski Crystal Growth by an Axisymmetric Lattice Boltzmann Method," *J. Comput. Phys.*, **186**, pp. 295-307.
- Perkins, C., and Weimer, A. W., 2009, "Solar-Thermal Production of Renewable Hydrogen," *AIChE J.*, **55**, pp. 286-293.
- Petrasch, J., 2002, "Thermal Modeling of Solar Chemical Reactors: Transient Behavior, Radiative Transfer," Master's thesis, ETH-Zürich.
- Petrasch, J., Coray, P., Meier, A., Brack, M., Haberling, P., Wuillemin, D., and Steinfeld, A., 2007, "A Novel 50 kW 11,000 Suns High-flux Solar Simulator Based on an Array of Xenon Arc Lamps," *ASME J. Sol. Energ.*, **129**, pp. 405-411.
- Premnath, K. N., and Abraham, J., 2007, "Three-dimensional Multi-relaxation-time (MRT) Lattice-Boltzmann Models for Multiphase Flow," *J. Comput. Phys.*, **224**, pp. 539-559.
- Qian, Y. H., d'Humières, D., and Lallemand, P., 1992, "Lattice BGK Models for Navier-Stokes Equation," *Europhys. Lett.*, **17**, pp. 479-484.
- Reis, T., and Phillips, T. N., 2007, "Modified Lattice Boltzmann Model for Axisymmetric Flows," *Phys. Rev. E*, **75**, 056703.
- Reis, T., and Phillips, T. N., 2008, "Numerical Validation of a Consistent Axisymmetric Lattice Boltzmann Model," *Phys. Rev. E*, **77**, 026703.
- Rong, F., Guo, Z., Chai, Z., and Shi, B., 2010, "A Lattice Boltzmann Model for Axisymmetric Thermal Flows through Porous Media," *Int. J. Heat Mass Transfer*, **53**, pp. 5519-5527.
- Servan-Camas, B., and Tsai, F. T.-C., 2008, "Lattice Boltzmann Method with Two Relaxation Times for Advection-Diffusion Equation: Third Order Analysis and Stability Analysis," *Adv. Water Resour.*, **31**, pp. 1113-1126.

- Shan, X., 1997, "Solution of Rayleigh-Benard Convection Using a Lattice Boltzmann Method," *Phys. Rev. E*, **55**, 2780.
- Shi, B., and Guo, Z., 2009, "Lattice Boltzmann Model for Nonlinear Convection-Diffusion Equations," *Phys. Rev. E*, **79**, 016701.
- Shu, C., and Zhu, Y. D., 2002, "Efficient Computation of Natural Convection in a Concentric Annulus between an Outer Square Cylinder and an Inner Circular Cylinder," *Int. J. Numer. Meth. Fluids*, **38**, pp. 429-445.
- Singh, A., 2013, "Multi-Scale, Multi Physics Modeling of Thermo-Chemical Iron/Iron Oxide Cycle for Fuel Production," Doctoral dissertation, University of Florida.
- Steinfeld, A., 2002, "Solar Hydrogen Production via a Two-step Water-splitting Thermochemical Cycle Based on Zn/ZnO Redox Reactions," *Int. J. Hydrogen Energ.*, **27**, pp. 611-619.
- Steinfeld, A., 2005, "Solar Thermochemical Production of Hydrogen - A Review," *Sol. Energy*, **78**, pp. 603-615.
- Succi, S., 2001, *The Lattice Boltzmann Equation for Fluid Dynamics and Beyond*. Oxford University Press, New York.
- Sullivan, S. P., Sani, F. M., Johns, M. L., and Gladden, L. F., 2005, "Simulation of Packed Bed Reactors Using Lattice Boltzmann Methods," *Chem. Eng. Sci.* **60**, pp. 3405-3418.
- Sun, J., and Chen, M. M., 1988, "A Theoretical Analysis of Heat Transfer Due to Particle Impact," *Int. J. Heat Mass Transfer*, **31**, pp. 969-975.
- Tang, G. H., Tao, W. Q., and He, Y. L., 2005, "Thermal Boundary Condition for the Thermal Lattice Boltzmann Equation," *Phys. Rev. E*, **72**, 016703.
- Timoshenko, S. P., and Goodier, J. N., 1970, *Theory of Elasticity*, 3rd ed., McGraw-Hill, New York.
- van der Sman, R. G. M., Ernst, M. H., 2000, "Convection-Diffusion Lattice Boltzmann Scheme for Irregular Lattices," *J. Comput. Phys.*, **160**, pp. 766-782.
- Venkatachalappa, M., Sankar, M., and Natarajan, A. A., 2001, "Natural Convection in an Annulus between Two Rotating Vertical Cylinders," *Acta Mech.*, **147**, pp. 173-196.
- Verma, N., Salem, K., and Mewes, D., 2007, "Simulation of Micro- and Macro-Transport in a Packed Bed of Porous Adsorbents by Lattice Boltzmann Methods," *Chem. Eng. Sci.* **62**, pp. 3685-3698.

- Verma, N., and Mewes, D., 2008, "Simulation of Temperature Fields in a Narrow Tubular Adsorber by Thermal Lattice Boltzmann Methods," *Chem. Eng. Sci.* **63**, pp. 4269-4279.
- Wang, L., Guo, Z., and Zheng, C., 2010, "Multi-relaxation-time Lattice Boltzmann Model for Axisymmetric Flows," *Comput. Fluids*, **39**, pp. 1542-1548.
- Wang, M., Wang, J., Pan, N., and Chen, S., 2007, "Mesoscopic Predictions of the Effective Thermal Conductivity for Microscale Random Porous Media," *Phys. Rev. E*, **75**, 036702.
- Wieckert, C., Meier, A., and Steinfeld, A., 2003, "Indirectly Irradiated Solar Receiver-Reactors for High-Temperature Thermochemical Processes," *ASME J. Sol. Energ.*, **125**, pp. 120-123.
- Yin, X., Le, G., and Zhang, J., 2012, "Mass and Momentum Transfer across Solid-Fluid Boundaries in the Lattice-Boltzmann Method," *Phys. Rev. E*, **86**, 026701.
- Yoshida, H., and Nagaoka, M., 2010, "Multiple-relaxation-time Lattice Boltzmann Model for the Convection and Anisotropic Diffusion Equation," *J. Comput. Phys.*, **229**, pp. 7774-7795.
- Yu, D., Mei, R., Luo, L.-S., and Shyy, W., 2003, "Viscous Flow Computations with the Method of Lattice Boltzmann Equation," *Prog. Aerosp. Sci.*, **39**, pp. 329-367.
- Yu, H., Luo, L.-S., and Girimaji, S. S., 2006, "LES of Turbulent Square Jet Flow Using an MRT Lattice Boltzmann Model," *Comput. Fluids*, **35**, pp. 957-965.
- Ziegler, D. P., 1993, "Boundary Conditions for Lattice Boltzmann Simulations," *J. Stat. Phys.*, **71**, pp. 1171-1177.
- Zheng, H. W., Shu, C., and Chew, Y. T., 2006, "A Lattice Boltzmann Model for Multiphase Flows with Large Density Ratio," *J. Comput. Phys.*, **218**, pp. 353-371.
- Zheng, L., Shi, B., Guo, Z., and Zheng, C., 2010a, "Lattice Boltzmann Equation for Axisymmetric Thermal Flows," *Comput. Fluids*, **39**, pp. 945-952.
- Zheng, L., Guo, Z., Shi, B., and Zheng, C., 2010b, "Kinetic Theory Based LBE with Viscous Dissipation and Pressure Work for Axisymmetric Thermal Flows," *J. Comput. Phys.*, **229**, pp. 5843-5856.
- Zhou, J.G., 2008, "Axisymmetric Lattice Boltzmann Method," *Phys. Rev. E*, **78**, 036701.
- Zhou, J.G., 2011, "Axisymmetric Lattice Boltzmann Method Revised," *Phys. Rev. E*, **84**, 036704.
- Zhou, J. H., Yu, A. B., and Horio, M., 2008, "Finite Element Modeling of the Transient Heat Conduction between Colliding Particles," *Chem. Eng. J.*, **139**, pp. 510-516.

Zou, Q., and He, X., 1997, "On Pressure and Velocity Boundary Conditions for the Lattice Boltzmann BGK Model," *Phys. Fluids*, **9**, pp. 1591-1598.

BIOGRAPHICAL SKETCH

Like Li was born in 1985 in Hunan, China. He received his bachelor's degree in mechanical engineering from the Central South University in Changsha, China in 2007. He was then accepted by the graduate school of Beijing University of Aeronautics and Astronautics (BUAA) with a research assistantship. In 2010, he obtained his master's degree in mechanical engineering from BUAA and flew overseas to the United States for pursuing a doctoral degree.

Like Li has been studying and working as a Ph.D. student in the Department of Mechanical and Aerospace Engineering at the University of Florida since spring 2010. His current research interests include computational modeling of heat transfer, momentum and mass transfer in fluid-solid systems.